

INITIAL SOLIDIFICATION PHENOMENA
IN THE CONTINUOUS CASTING SLAB MOULD

by

EIICHI TAKEUCHI

M.E. KYUSHU UNIVERSITY, 1977

A THESIS SUBMITTED IN PARTIAL FULFILMENT OF
THE REQUIREMENTS FOR THE DEGREE OF
DOCTOR OF PHILOSOPHY

in

THE FACULTY OF GRADUATE STUDIES
METALLURGICAL ENGINEERING

We accept this thesis as conforming
to the required standard

THE UNIVERSITY OF BRITISH COLUMBIA

October 1984

© Eiichi Takeuchi, 1984

In presenting this thesis in partial fulfilment of the requirements for an advanced degree at the University of British Columbia, I agree that the Library shall make it freely available for reference and study. I further agree that permission for extensive copying of this thesis for scholarly purposes may be granted by the head of my department or by his or her representatives. It is understood that copying or publication of this thesis for financial gain shall not be allowed without my written permission.

Eiichi TAKEUCHI

Department of Metallurgical Engineering

The University of British Columbia
1956 Main Mall
Vancouver, Canada
V6T 1Y3

Date Oct. 12, 1984

ABSTRACT

In a study of initial solidification during the continuous casting of steel slabs, the formation of oscillation marks and their effect on the surface quality of the slabs have been examined by metallographical investigation of slab samples and by performing a set of mathematical analyses.

The metallographic study of the oscillation marks has revealed that the adjacent subsurface structure may exhibit "hooks". The depth of oscillation marks exhibiting subsurface hooks is affected by the carbon content of the steel, while oscillation marks without adjacent hooks do not show the carbon dependence. Another important factor which affects the depth of oscillation marks is variation of the meniscus level. Quick upward movement of the meniscus level increases the depth of oscillation marks.

The theoretical analysis of heat flow at the meniscus indicates that the meniscus may partially freeze within the period of a typical mould oscillation cycle. Lubrication theory has shown that a significant pressure can be generated in the flux channel by the reciprocating motion of the mould relative to the shell. The shape of the meniscus has been computed as a function of the pressure developed in the mould flux. This has demonstrated that the "contact" point of the meniscus with the mould wall moves out of phase with the mould displacement by $\pi/2$, and has a greater amplitude than the stroke of mould

oscillation. Thus near the beginning of the positive strip period molten steel can overflow at the meniscus when a rigid hook-like shell exists, whilst the meniscus in the absence of a rigid shell, caused by high superheat and/or steel convection at the solidification front, is drawn toward the mould wall to form the oscillation marks without a subsurface hook. Consequently the effect of various casting variables on the depth of oscillation marks can be explained on theoretical grounds.

Positive segregation of phosphorus has been observed at the bottom of the oscillation marks and has been classified mainly into two types. One type is observed at the end of the overflow region on the subsurface hook. A heat-flow model which takes into account the shape of the oscillation marks has revealed that this type of positive segregation is caused by local delay of solidification at the bottom of the oscillation marks. Another type of positive segregation has been found in a layer on the bottom of oscillation marks without subsurface hooks. This form of segregation cannot be explained by the heat-flow model, but is likely due to a penetration mechanism in which the negative pressure in the flux channel generated during the upward motion of the mould draws out interdendritic liquid from the semi-solidified shell.

Transverse cracks are found along the bottom of oscillation marks. The surface of the transverse cracks exhibits an interdendritic appearance in the vicinity of the slab surface, which implies that the cracks are hot tears initiated in the

mould region. A heat-flow analysis predicts that deep oscillation marks cause nonuniformity of the shell in the mould, which was also observed in the metallographic investigation. According to the heat-flow analysis not only the depth but also the pitch of oscillation marks affects the shell profile. Therefore increasing the frequency of mould oscillation effectively reduces transverse cracks, by decreasing both the depth and the pitch of oscillation marks.

Table of Contents

Table of Contents	v
List of Tables	viii
List of Figures	ix
List of Symbols	xviii
Acknowledgement	xxi
 1. INTRODUCTION	 1
2. PREVIOUS WORK	6
2.1 Mould Oscillation And Mould Flux	6
2.2 Oscillation Mark Formation	8
2.2.1 The Shape Of Oscillation Marks	8
2.2.2 Subsurface Structure Of Oscillation Marks	9
2.2.3 Mechanism Of Oscillation Mark Formation.	10
2.3 Heat Transfer In The Mould Near The Mensiscus ...	13
2.3.1 Factors Affecting Mould Heat Flux	13
2.3.2 Meniscus Solidification	14
2.4 Lubrication In The Mould	16
2.4.1 Consumption Of Mould Flux	16
2.4.2 Mould Friction	18
2.5 Surface Quality Of Slabs Related To Oscillation Marks.	19
2.5.1 Transverse Cracks	19
2.5.2 Positive Segregation	22
2.6 Summary - Industrial Necessity For The Present Work	23
 3. SCOPE AND OBJECTIVES OF THE PRESENT WORK	 51
3.1 Scope Of The Present Work	51
3.2 The Objectives Of The Present Work	53
 4. FORMATION OF OSCILLATION MARKS	 55
4.1 Metallurgical Investigation	55
4.1.1 Casting Conditions Of Slab Samples	55
4.1.2 Investigation Procedure	56
4.1.3 Appearance And Pitch Of Oscillation Marks	56
4.1.4 Subsurface Structure Of Oscillation Marks	58
4.1.5 Depth Of Oscillation Marks	61
4.2 Heat Flow Analysis Of The Meniscus Region	64
4.2.1 Axial Profile Of Mould Heat Flux At The Meniscus	64
4.2.2 Temperature Distribution In The Mould Flux And Steel	67
4.3 Fluid Pressure In The Mould Flux At The Meniscus	73
4.4 Meniscus Shape	78
4.4.1 Static Shape Of Meniscus	78
4.4.2 Change Of The Meniscus Shape By Mould Oscillation	79
4.5 Mechanism Of Oscillation-Mark Formation	82
4.6 Meniscus Model Predictions	86

5. THE EFFECT OF OSCILLATION MARKS ON THE SURFACE QUALITY OF SLABS	149
5.1 Introduction	149
5.2 Metallurgical Study Of Transverse Cracks	151
5.2.1 Casting Conditions	151
5.2.2 Appearance Of Transverse Cracks	151
5.2.3 Subsurface Structure In The Vicinity Of Transverse Cracks	152
5.2.4 Surface Of Transverse Cracks	155
5.2.5 The Effect Of Oscillation-marks Shape On Local Shell Thickness.	157
5.2.6 Summary Of Metallurgical Investigation Of Transverse Cracks	158
5.3 Metallurgical Studies Of Positive Segregation Near Oscillation Marks	159
5.3.1 Casting Conditions	159
5.3.2 Metallographic Classification Of Positive Segregation	160
5.3.3 Microanalysis Of Positive Segregation By CMA ...	164
5.3.4 Positive Segregation Caused By Overflow At The Slab Corner	165
5.3.5 Summary Of Metallurgical Investigations Of Positive Segregation	167
5.4 Heat Transfer Analysis Of Solidification In The Mould In The Vicinity Of Oscillation Marks	168
5.4.1 Objectives And Description Of The Physical System	168
5.4.2 Mathematical Modeling	169
5.4.3 Calculated Results	172
5.4.3.1 Temperature Distribution In Mould Flux And Steel	172
5.4.3.2 The Effect Of Oscillation-Mark Shape On The Nonuniformity Of Shell Thickness	174
5.4.3.3 Cooling Rate Distribution Near The Oscillation Marks	176
5.5 Discussion On The Formation Of Positive Segregation	178
6. CONCLUSIONS AND SUGGESTIONS FOR FUTURE WORK	234
6.1 Conclusions	234
6.2 Suggestions For Future Work	238
BIBLIOGRAPHY	240
APPENDIX I: NODAL EQUATIONS FOR THE HEAT FLOW CALCULATION IN THE MOULD	248
APPENDIX II: NODAL EQUATIONS FOR THE TEMPERATURE DISTRIBUTION IN THE MENISCUS REGION	250
APPENDIX III: SHAPE OF MENISCUS	253
APPENDIX IV: DYNAMIC PRESSURE IN THE MOULD FLUX CHANNEL	257
APPENDIX V: COMPUTER PROGRAM FOR THE TEMPERATURE PREDICTION IN THE MENISCUS REGION	260
APPENDIX VI: COMPUTER PROGRAM FOR THE CALCULATION OF FLUID PRESSURE IN THE FLUX CHANNEL	278
APPENDIX VII: COMPUTER PROGRAM FOR THE CALCULATION OF THE CHANGE OF MENISCUS SHAPE	280

APPENDIX VIII: COMPUTER PROGRAM FOR THE CALCULATION OF
NONUNIFORMITY OF SHELL PROFILE IN THE MOULD .285

List of Tables

I.	Properties of Mould Flux	25
II.	Casting Conditions and Chemical Composition of the Slab Samples from Company A	91
III.	Casting Conditions and Chemical Composition of the Slab Samples from Company B	92
IV.	Casting Conditions and Chemical Composition of the Slab Samples from Company C	93
V.	Casting Conditions and Chemical Composition of the Slab Samples from Company D	94
VI.	Casting Conditions and Chemical Composition of the Slab Samples from Company E	95
VII.	Thermal Properties and Conditions for Calculation of Mould Heat Flux	96
VIII.	Assumed Steel Composition and Thermophysical Properties for Calculations of Temperature Distribution at the Meniscus	97
IX.	Casting Conditions of Samples for Metallurgical Study of Transverse Cracks	182
X.	Casting Conditions of Samples for Metallurgical Study of Positive Segregation	183

List of Figures

1-1	Variation of world crude-steel production and percentage of the steel continuously cast (1965-81) from McPherson et al. ¹	4
1-2	Causes and effects of the initial solidification in the slab mould.	5
2-1	Mould displacement due to oscillation.	26
2-2	Macroscopic structure and temperature distribution in the melting mould flux layer on the meniscus. ¹²	27
2-3	Effect of oscillation stroke on the depth of oscillation marks. ⁹	28
2-4	Effect of oscillation frequency on the depth of oscillation marks. ¹⁶	29
2-5	Relationship between the depth of oscillation marks and the negative strip time. ²³⁻²⁵	30
2-6	Dendrite structure in the vicinity of oscillation marks. ⁹ (1) Hook-like structure, (2) Non-hook-like structure, (3) Direction of growth of primary dendrite, (4) Casting direction.	31
2-7	Formation mechanism of oscillation marks by Sato. ³⁰	32
2-8	Formation mechanism of oscillation marks by Emi et al. ⁹	33
2-9	Schematic diagram of "mould simulator" (a) and formation mechanism of oscillation marks (b) by Kawakami et al. ³⁶	34
2-10	Change of displacement of the mould and the shell with time.	35
2-11	Calculated effect of oscillation frequency and stroke on the depth of oscillation marks by Nakato's model. ³⁹	36
2-12	Effect of the casting speed on the axial heat flux profile in the mould wall. ⁴⁰	37
2-13	Calculated temperature distribution in the mould wall and in the steel. ³²	38

2-14	Calculated shell profile with different convective heat transfer coefficients. ³⁸	39
2-15	Effect of casting speed on mould flux consumption. ⁵⁵	40
2-16	Effect of oscillation frequency on mould flux consumption. ⁸	41
2-17	Effect of viscosity of mould flux on the flux consumption. ⁵²	42
2-18	Effect of softening temperature of mould flux on the flux consumption. ⁵²	43
2-19	Transverse cracks observed on slab surface. ²⁹	44
2-20	Effect of nitrogen on the hot ductility in low carbon steel ⁸⁰ (a), and on the frequency of transverse crack formation in Nb-V steel ⁸² (b).	45
2-21	Temperature profile on the slab surface to avoid the brittle temperature range at the unbending point. ⁴	46
2-22	Relationship between the maximum content of P and the depth of oscillation marks. ²⁹	47
2-23	Mechanism of positive segregation by Tanaka et al. ²⁹	48
2-24	Types of positive segregation of stainless steel slab. ⁸⁶	49
2-25	Mechanism of positive segregation by H. Takeuchi et al. ²⁷	50
2-26	Relation between frequency of positive segregation in stainless steel slabs and negative-strip time. ⁸⁶ (Ne: Negative-strip ratio)	50
4-1	Immersion nozzle for the multi-port practice (Company D).	98
4-2	Schematic view of the electromagnetic stirrer in the mould ⁸⁸ (Company E).	99
4-3	Appearance of oscillation marks on the narrow face of a slab (Company A).	100
4-4	Effect of casting speed on the pitch of oscillation marks (Company A).	101
4-5	Appearance of oscillation marks on the narrow face of a slab (Company C).	102

4-6	Frequency of mould oscillation in each casting operation.	103
4-7	Appearance of oscillation marks on the narrow face of slab cast with (a) Bifurcated nozzle and (b) Multi-port practice (Company D).	104
4-8	Appearance of oscillation marks on the narrow face of slab cast (a) without mould EMS and (b) with mould EMS (Company E).	105
4-9	Subsurface structure near oscillation marks exhibiting "hooks" in steel slabs containing (a) 0.09%C and (b) 0.26%C (Company A). (x6)	106
4-10	Subsurface structure near oscillation marks without "hooks" in steel slabs containing (a) 0.08% C and (b) 0.26% C (Company A). (x6)	107
4-11	Change of secondary dendrite arm spacing in the casting direction C=0.09% (Company A).	108
4-12	Substance at the end of a subsurface hook (a) x 94 (b) x 2000 (Company B).	109
4-13	X-ray spectrograph of the substance near the hook (Company B).	110
4-14	Subsurface structure near oscillation marks in steel slabs from Company C. (x6)	111
4-15	Subsurface structure near oscillation marks in steel slabs cast by (a) bifurcated nozzle and (b) multi-port practice (Company D). (x6.5)	112
4-16	Subsurface structure near oscillation marks in steel slabs cast (a) without EMS-M and (b) with EMS-M (Company E). (x6)	113
4-17	Relationship between depth and pitch of oscillation marks in 0.08%-Carbon slabs (Company A).	114
4-18	Relationship between depth and pitch of oscillation marks on 0.26%-Carbon slabs (Company A).	115
4-19	Influence of carbon content of the slabs on the depth of oscillation marks (Company A).	116
4-20	Effect of Al on the shape of oscillation marks (Company A). Note: all marks are hook-like structures.	117
4-21	Effect of oscillation stroke on the depth of	

	oscillation Marks (Company C).	118
4-22	Effect of mould EMS on the depth of oscillation marks (Company E).	119
4-23	Physical system for the computation of heat transfer in the mould.	120
4-24	Temperature distribution in the mould wall and the heat flux distribution near the meniscus (Closed circles are values of mould temperature reported by Nakato et al ¹⁸).	121
4-25	Geometry and nodal system employed to predict temperature distributions in the mould flux and steel at the meniscus.	122
4-26	Flow chart for the calculation of the temperature distribution in steel and mould flux (i).	123
4-26	Flow chart for the calculation of the temperature distribution in steel and mould flux (ii).	124
4-27	Predicted temperature distribution in the mould flux and fraction solidified in the steel at the meniscus after a time of 0.3s. Superheat of steel is 5°C.	125
4-28	Predicted temperature distribution in the mould flux and fraction solidified in the steel at the meniscus after a time of 0.6s. Superheat of steel is 5°C.	126
4-29	Predicted temperature distribution in the mould flux and fraction solidified in the steel at the meniscus after a time of 0.3s. Superheat of steel is 0°C.	127
4-30	Predicted temperature distribution in the mould flux and fraction solidified in the steel at the meniscus after a time of 0.6s. Superheat of steel is 0°C.	128
4-31	Predicted temperature distribution in the mould flux and fraction solidified in the steel at the meniscus after a time of 0.3s. Superheat of steel is 20°C.	129
4-32	Predicted temperature distribution in the mould flux and fraction solidified in the steel at the meniscus after a time of 0.6s. Superheat of steel is 20°C.	130
4-35	Geometry of mould flux channel at the meniscus.	133
4-36	Predicted axial pressure profiles in the flux channel near the meniscus. Flux channel dimensions assumed to be: $h_i=0.35\text{mm}$, $h_f=0.05\text{mm}$, $l_f=10\text{mm}$	134

4-37	Predicted velocity distributions in the flux channel near the meniscus at time of maximum downward velocity of the mould. Conditions as for Fig. 4-36 and assumed flux viscosity is 5P.	135
4-38	Shear stress distribution along the shell.	136
4-39	Geometry of two-dimensional meniscus system.	137
4-40	Predicted change of meniscus shape with time resulting from sinusoidal mould oscillation ($s=8\text{mm}$, $f=100\text{cpm}$, $\sigma=1200\text{ dyne/cm}$, $\rho_s=7.2\text{ g/cm}^3$, $\rho_f=2.8\text{ g/cm}^3$).	138
4-41	Movement of "contact point" of meniscus with mould wall during mould oscillation. See caption to Fig. 4-40 for oscillation conditions.	139
4-42	Schematic representation of the formation of an oscillation mark with subsurface hook.	140
4-43	Schematic representation of the formation of an oscillation mark without subsurface hook.	141
4-44	Influence of meniscus level variation (shown as changing pitch of oscillation marks) on total force due to pressure generated in the flux channel. ...	142
4-45	Influence of oscillation stroke on total force due to pressure generated in the flux channel. $v_s=1\text{m/min}$	143
4-46	Influence of oscillation frequency on total force due to pressure generated in the flux channel. $v_s=1\text{m/min}$	144
4-47	Influence of oscillation frequency on total force due to pressure generated in the flux channel. $v_s=1.2, 1.5\text{ m/min}$	145
4-48	Influence of negative-strip time on total force due to pressure generated in the flux channel (numbers in parentheses indicate oscillation frequencies). $v_s=1\text{m/min}$	146
4-49	Influence of negative-strip time on bending moment due to pressure generated in the flux channels. $v_s=1\text{m/min}$	147
4-50	Influence of negative-strip time on total force due to pressure generated in the flux channel. $v_s=0.8, 1.0, 1.2, 1.5\text{ m/min}$	148

5-1	Effect of N content on the formation of transverse cracks. Note: equilibrium constant $K = \frac{[\%Al]}{[\%N]}$ by L.S. Darken et al. ¹⁰⁸	184
5-2	Appearance of transverse cracks (i) (Company B). .	185
5-3	Appearance of transverse cracks (ii) (Company B). .	186
5-4	Transverse cracks formed at the bottom of oscillation marks; picral etching (Company B). (x3.6)	187
5-5	Transverse cracks formed at the bottom of oscillation marks; nital etching (Company B). (x3.6)	188
5-6	Ferrite-pearlite structure (a) at the top and (b) at the bottom of an oscillation mark; nital etching (Company B). (x146)	189
5-7	Interdendritic cracks at the bottom of oscillation marks; picral etching (Company B). (a):x6.5, (b):x32.	190
5-8	Small crack observed along and near the subsurface hook; picral etching (Company B). (a):x6.5, (b):x43.	191
5-9	Transverse cracks on the surface of a slab sample from Company B. (x1.18)	192
5-10	Surface of transverse cracks [1] from Company B. (x20)	193
5-11	Surfaces of transverse crack [2] from Company B. (x20)	194
5-12	Surface of transverse crack [3] from Company B. (x40)	195
5-13	Surface of transverse crack from Company C. (a):x40, (b):x200.	196
5-14	X-ray spectrograph of adherent material on the surface of transverse crack, Company C.	197
5-15	Relationship between the depth of oscillation marks and the nonuniformity of the shell thickness (Company B).	198
5-16	Subsurface structure near positive segregation (Sample B1). (x38.7)	199
5-17	Subsurface structure near positive segregation (Sample B2). (x38.7)	200

5-18	Subsurface structure near a hook; $C \approx 0.10\%$ (Sample B3). (x38.7)	201
5-19	Subsurface structure near a hook; $C \approx 0.26\%$ (Sample B4). (x38.7)	202
5-20	Subsurface structure in the vicinity of positive segregation layer with hooks absent (Sample B5). (x38.7)	203
5-21	Relationship between the depth of oscillation marks and the thickness of segregation layer (Company A).	204
5-22	Positive segregation at the bottom of oscillation mark in stainless steel slab (Sample B6). (x6)	205
5-23	Segregation of Mn and P in the subsurface area of the oscillation mark determined by CMA (Sample B2). ...	206
5-24	Segregation of Mn and P in the subsurface area of the oscillation mark determined by CMA (Sample B3). ..	207
5-25	Segregation of Mn and P in the subsurface area of the oscillation mark determined by CMA (Sample B5). ..	208
5-26	Segregation of Ni and P in the subsurface area of the oscillation mark determined by CMA (Sample B6). ..	209
5-28	Appearance of overflow at the slab corner and the location of cross section for metallographic inspection, Company A.	211
5-29	Subsurface structure in each longitudinal cross section shown in Fig. 5-28; picral etching (Company A). (x5.4)	212
5-30	Slab corner sample for the investigation into the structure in the horizontal cross section (Company A). (x2)	213
5-31	Subsurface structure (a) in longitudinal cross section, and (b) in horizontal cross section of the sample shown in Fig. 5-30; Oberhoffer etch (Company A). (a):x6.5, (b):x6.	214
5-32	Classification of positive segregation.	215
5-33	Physical system for mathematical model of heat flow in the vicinity of the oscillation mark.	216
5-34	Coordinate of the controlled system (symmetric system).	217

5-35	Temperature distribution in mould flux and steel after 10s.	218
5-36	Temperature distribution in mould flux and steel after 48s.	219
5-37	Change of shell profile with time. ($l=1.0\text{cm}$, $d=0.10\text{cm}$, $x_1^*/x_2^*=0.5$)	220
5-38	Change of shell profile with time. ($l=1.0\text{cm}$, $d=0.15\text{cm}$, $x_1^*/x_2^*=0.5$)	220
5-39	Change of shell profile with time. ($l=2.0\text{cm}$, $d=0.10\text{cm}$, $x_1^*/x_2^*=0.5$)	221
5-40	Change of shell profile with time. ($l=2.0\text{cm}$, $d=0.15\text{cm}$, $x_1^*/x_2^*=0.5$)	222
5-41	Change of shell profile with time. ($l=2.0\text{cm}$, $d=0.10\text{cm}$, $x_1^*/x_2^*=0.3$)	223
5-42	Change of shell profile with time. ($l=2.0\text{cm}$, $d=0.10\text{cm}$, $x_1^*/x_2^*=0.7$)	224
5-43	Effect of the shape of oscillation mark on the nonuniformity of shell thickness after 10s. ($x_1^*/x_2^*=0.5$)	225
5-44	Change of temperature with time at the bottom and at the top of oscillation marks.	226
5-45	Change of cooling rate with time at the top and at the bottom of oscillation mark. ($l=2.0\text{cm}$, $d=0.10\text{cm}$) ..	227
5-46	Relationship between cooling rate and the secondary dendrite arm spacing by A. Suzuki et al. ¹⁰⁴ Note: Measured average values of secondary arm spacing at the top and at the bottom of oscillation mark are indicated.	228
5-47	Relationship between shell thickness and time. ($l=1.0\text{cm}$, $d=0.10\text{cm}$)	229
5-48	Relationship between shell thickness and time. ($l=2.0\text{cm}$, $d=0.10\text{cm}$)	230
5-49	Relationship between shell thickness and time. ($l=2.0\text{cm}$, $d=0.15\text{cm}$)	231
5-50	Relationship between P_a and negative-strip time. .	232
5-51	Relationship between permeability and fraction liquid from Piwonka et al. ¹⁰⁷	233

- A1 Typical nodes and their number of subroutines in
computer program for the calculation of temperature
distribution at the meniscus300
- A2 Typical nodes and their number of subroutines in
computer program for the calculation of nonuniformity
of shell profile in the mould.301

List of Symbols

a^2	Capillary constant (-)
C_{pf}, C_{ps}, C_{pw}	Specific heat of mould flux, steel and water, respectively (J/g°C)
C_{pE}	Specific heat between liquidus and solidus (J/g°C)
d	Depth of oscillation marks (cm)
d_f	Thickness of mould flux layer between mould and shell (cm)
d_w	Thickness of water channel in the mould (cm)
D_H	Hydraulic diameter (cm)
f	Frequency of mould oscillation (cycle/s)
f_s	Fraction solid (-)
$f(x)$	Shape of oscillation mark
q_L	Fraction liquid (-)
$h(x)$	Width of flux channel (cm)
h_i, h_f	Width of flux channel at inlet and outlet, respectively (cm)
h_w	Heat transfer coefficient between water and mould (W/cm ² °C)
h_{s-f}	Heat transfer coefficient between steel and mould flux (W/cm ² °C)
k	Permeability (cm ²)
l	Pitch of oscillation marks (cm)
l_f	Length of flux channel (cm)
l_M, l_s	Displacement of mould and shell, respectively (cm)
Δl_m	Variation of meniscus level (cm)
L	Latent heat of steel during solidification (J/g)

- L_c Length of interdendritic channel (cm)
 M_b Bending moment (dyne cm)
 P_a Average value of negative pressure in mould flux (dyne/cm²)
 P_i, P_f Pressure at inlet and outlet of flux channel, respectively (dyne/cm²)
 $P(x)$ Axial distribution of pressure in mould flux (dyne/cm²)
 ΔP Pressure difference (dyne/cm²)
 ΔP_s Static pressure difference (dyne/cm²)
 $q_0(x)$ Heat-flux distribution along mould wall (W/cm²)
 $q_f(x), q_s(x)$ Heat-flux distribution along mould wall in the region of depressed part and flat part of oscillation marks, respectively (W/cm²)
 Q_R Relative consumption of mould flux (cm³/s)
 $R(x)$ Integration of pressure in flux channel from $x=0$ to $x=x$ (dyne/cm)
 r Distance normal to meniscus (cm)
 S Stroke of mould oscillation (cm)
 s Distance along meniscus (cm)
 T_f, T_s Temperature of flux and steel, respectively (°C)
 T_{fi}, T_{si} Initial temperature of flux and steel, respectively (°C)
 T_{liq}, T_{sol} Liquidus and solidus temperature, respectively (°C)
 T_M Temperature of mould wall (°C)
 T_w Temperature of water (°C)
 T_{wi}, T_{wf} Temperature of water at inlet and outlet of water channel, respectively (°C)
 t_N, t_P Negative and positive strip time, respectively (s)

u_x	Relative velocity of mould flux (cm/s)
v_f	Velocity of mould flux (cm/s)
v_L	Velocity of interdendritic flow (cm/s)
v_M	Velocity of mould (cm/s)
v_s	Velocity of slab (cm/s)
v_w	Velocity of water in water channel (cm/s)
Δv_m	Velocity of meniscus level variation (cm/s)
X_c	Contact point of meniscus with mould wall (cm)
X_M	Length of mould (cm)
Y_H	Thickness of mould flux reducing heat-flux by half (cm)
Y_M	Thickness of mould wall (cm)
λ_f, λ_s	Thermal conductivity of mould flux and steel, respectively (W/cm°C)
λ_M	Thermal conductivity of mould wall (W/cm°C)
λ_w	Thermal conductivity of water (W/cm°C)
μ_f, μ_s	Viscosity of mould flux and steel, respectively (poise)
μ_w	Viscosity of water (poise)
ρ_f, ρ_s	Density of mould flux and steel, respectively (g/cm ³)
ρ_w	Density of water (g/cm ³)
σ	Interfacial tension between mould flux and steel (dyne/cm)
τ	Shear stress (dyne/cm ²)
ϕ	Contact angle (radian)

Acknowledgement

I wish to express my sincere gratitude to Professor J.K. Brimacombe for his invaluable guidance, assistance and encouragement that he provided throughout the course of this study.

I am also grateful to Dr. Y. Nishida of the Government Industrial Research Institute (Nagoya, Japan) and Dr. I.V. Samarasekera of Department of Metallurgical Engineering for their assistance and to Professor F. Weinberg and Professor E.B. Hawbolt for their helpful discussions.

Thanks are also extended to my fellow graduate students and faculty members of this Department.

Considerable thanks should be expressed to the Natural Sciences and Engineering Research Council of Canada and Nippon Steel Corporation for providing financial support.

Special thanks must be expressed to Dr. T. Ohashi, Dr. T. Matsumiya, and Mr. W. Yamada of Nippon Steel Corporation for their CMA measurement.

A large number of steel companies are gratefully acknowledged for providing slab samples and information.

Finally I would like to express a word of appreciation to my wife Yumiko for her hearty support.

1. INTRODUCTION

Owing to advantages of high yield, uniform quality, and high productivity, the continuous-casting process has been widely accepted by numerous steelmakers in the world. The fraction of steel that is continuously cast has been steadily increasing, while the growth of steel production has ceased after the oil crisis, see Fig. 1-1.¹ Particularly in the past decade, the continuous-casting process has undergone significant developments in both equipment and operation,^{2 3} until now it has become the dominant casting process in steelmaking.

Today continuous casting is entering a new era of development in which it is linked directly with the hot rolling process. Initially the hot-charging process⁴ has been developed prior to direct rolling, where the high temperature, as-cast slabs are transported to the reheating furnace without surface conditioning. This direct charging of the continuously cast slabs to the hot rolling mill not only minimizes the energy loss but also simplifies the intermediate process between steelmaking and hot rolling, viz cooling, inspection, and hand scarfing. However hot charging can only be successfully implemented if the cast slabs are free from surface defects. Thus considerable effort has been expended to improve the surface quality of slabs. In this regard initial solidification in the continuous-casting mould has been recognized to be a significantly important phenomenon to be understood and if possible controlled.

The factors related to initial solidification in the mould are expressed in Fig. 1-2. Initial solidification phenomena in continuous casting are characterized not only by rapid heat extraction but also by interaction between the initially solidified shell and the inflowing mould flux, giving rise to the formation of oscillation marks. Consumption of mould flux which results from this interaction is essential to lubrication and heat transfer in the mould. For example, nonuniform inflow of mould flux is thought to be one of the major causes of longitudinal surface cracks;⁵ deep oscillation marks resulting from inappropriate mould operation often lead to the formation of transverse surface cracks;⁶ also decreasing the consumption rate of mould flux with increasing casting speed has been one of the major problems with high speed casting from the standpoint of lubrication.⁷ Recently many industrial efforts, for example high frequency oscillation casting,^{8 22} have been initiated to produce slabs free from surface conditioning. However the results expected have not been achieved yet. This is because the initial solidification at the meniscus has not been well understood.

Thus the main purpose of the present work is to shed light on the initial solidification in the continuous-casting slab mould, especially from the process standpoint, in order to suggest the optimum mould operation for the high surface quality of slabs. The subjects treated are firstly the formation mechanism of oscillation marks and secondly the effect of oscillation marks on the surface quality of slabs. The approach

taken has involved metallurgical investigations of many slab samples continuously cast under different conditions, and the formulation of several mathematical models.

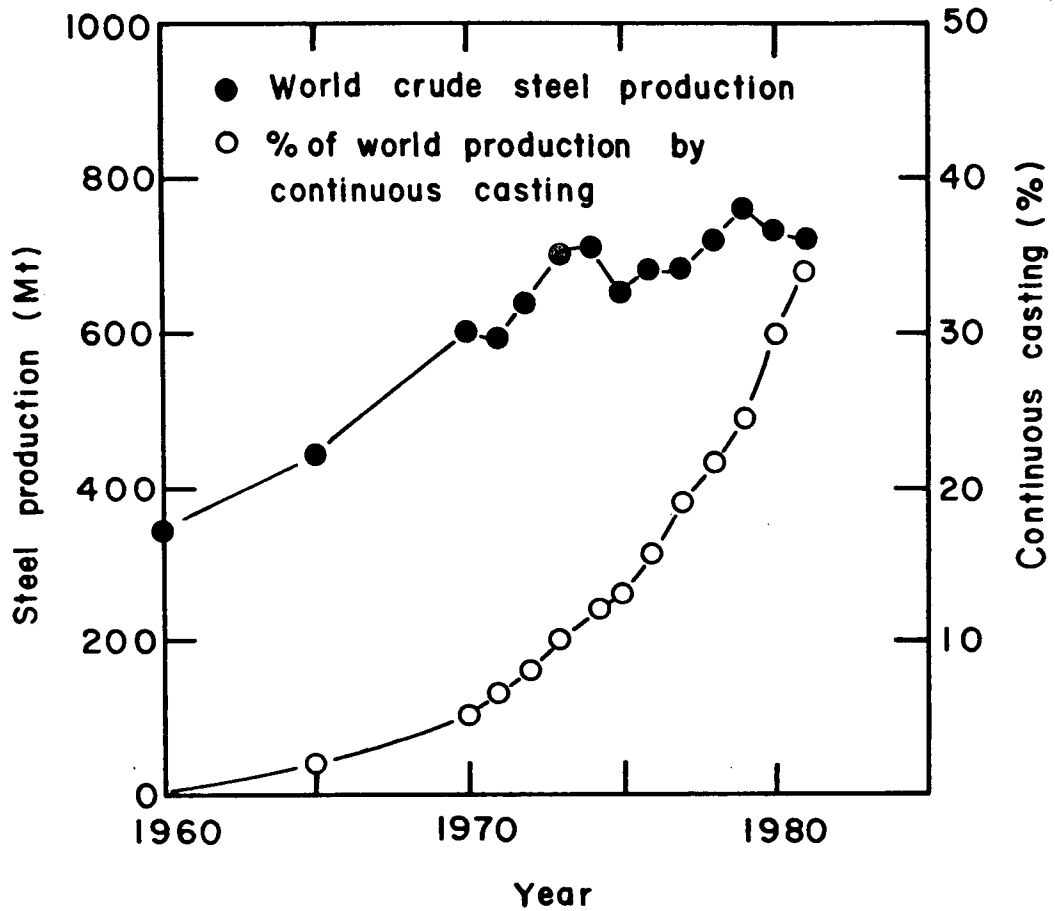


Fig. 1-1 Variation of world crude-steel production and percentage of the steel continuously cast (1965-81) from McPherson et al.¹

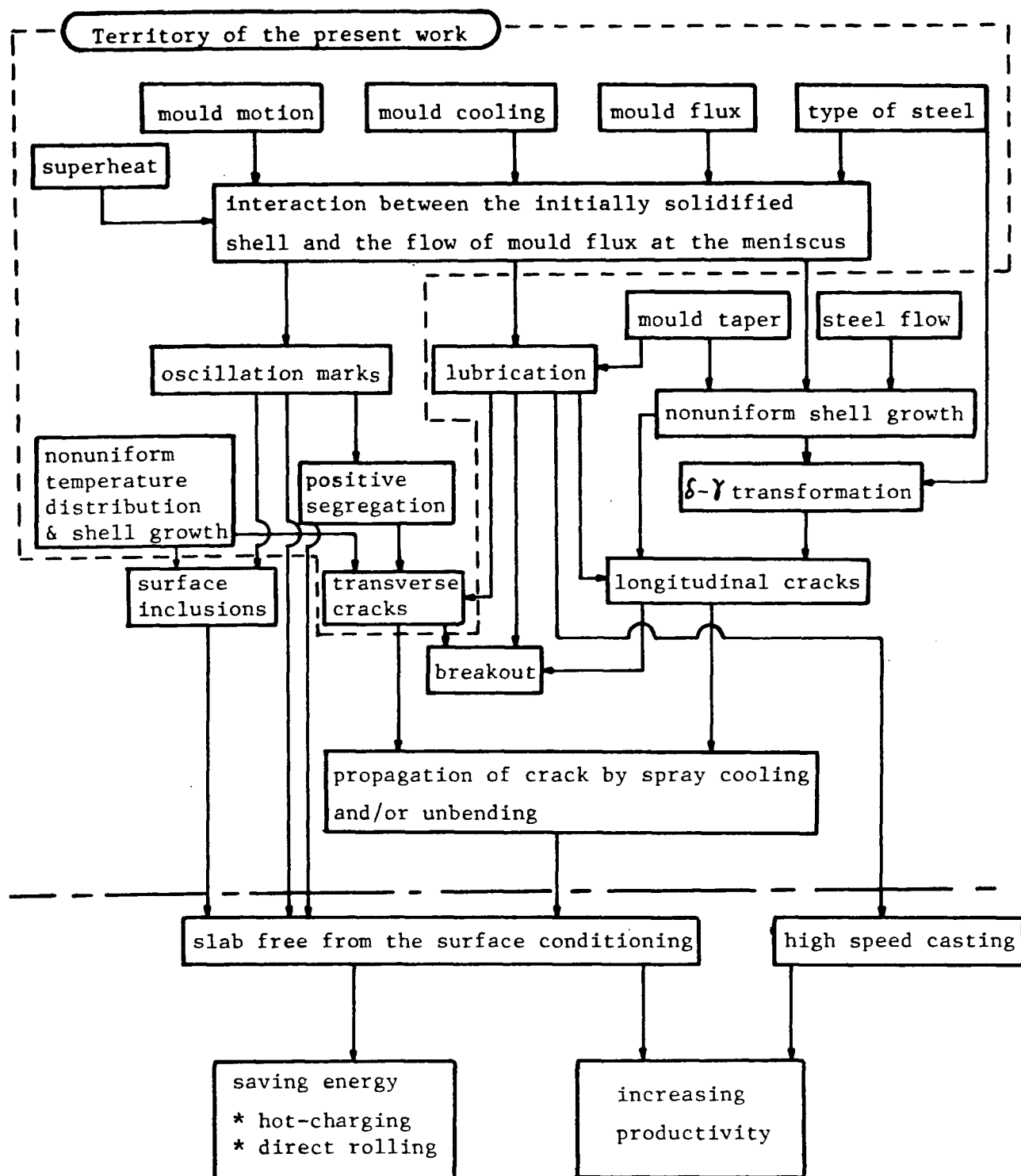


Fig. 1-2 Causes and effects of the initial solidification in the slab mould.

2. PREVIOUS WORK

2.1 Mould Oscillation And Mould Flux

Mould oscillation in the presence of an adequate lubricant plays one of the most essential parts in the continuous casting of steel. It prevents the sticking of steel on the mould wall and makes continuous casting possible. Fig. 2-1 shows a typical mould movement as a function of time.⁹ In general the mould oscillation is sinusoidal and, hence the displacement and the speed of the mould are expressed by Eqs. (2-1) and (2-2) respectively.

$$x = \frac{s}{2} \sin(2\pi ft) \quad (2-1)$$

$$v_M = \pi s f \cos(2\pi ft) \quad (2-2)$$

There is a certain period in each cycle of the mould oscillation in which the downward velocity of the mould exceeds the withdrawal rate of the strand. This is called the negative-strip time, while the remaining period in each cycle is referred to as positive-strip time, expressed by Eqs. (2-3) and (2-4) respectively.

$$t_N = \frac{60}{\pi f} \arccos\left(\frac{v}{\pi s f}\right) \quad (2-3)$$

$$t_p = \frac{60}{\pi f} \arccos\left(-\frac{v}{\pi s f}\right) \quad (2-4)$$

Rapeseed oil was first used as mould lubricant in continuous slab casting, but later mould flux was applied for the improvement of slab quality. The mould flux in continuous casting performs the following functions;^{10 11}

- i) lubrication (better than rapeseed oil)
- ii) heat transfer between mould wall and steel
- iii) dissolution of inclusions floating from the molten steel pool
- iv) thermal insulation at the meniscus
- v) prevention of reoxidation of steel at the meniscus

Mould flux is synthesized mainly from 1) SiO_2 - CaO - Al_2O_3 system as the base material, 2) CaF_2 , Na_2O , K_2O , etc. to control the fluidity, and 3) carbon and/or graphite particles as skeleton material. Today mould flux is used mostly in a prefused granular form, which ensures the most uniform melting behavior at the meniscus,¹² see Fig. 2-2. An adequate thickness of molten flux (6-15mm)^{12 13} is necessary for the uniform inflow of the lubricant into the "gap" between the mould wall and newly forming steel shell.

For the purpose of theoretical analysis of the melting behavior of mould flux on the meniscus and the inflow of mould flux into the gap between the mould wall and the shell, several thermophysical properties are required. However few studies have been reported on the measurement of the properties of mould flux, except for the viscosity.^{10 14}

As for the other properties, e.g. density, interfacial tension, specific heat, and thermal conductivity, the properties of blast

furnace slag which are better characterized, are generally employed in place of the missing data for mould flux. The properties of blast furnace slag are summarized in Table 2-1.

2.2 Oscillation Mark Formation

2.2.1 The Shape Of Oscillation Marks

The use of mould flux has brought about numerous advantages in the continuous casting process; however at the same time, oscillation marks themselves have become a more serious problem.²⁰ Oscillation marks are formed periodically and uniformly normal to the casting direction around the slab surface. The pitch of oscillation marks can be expressed simply by Eq. (2-5),⁹ which implies that the marks are formed in each cycle of the mould oscillation.

$$1 = \frac{v_s}{f} \quad (2-5)$$

As one of the indices of surface quality, the depth of oscillation marks has been discussed often in relation to the mould oscillation. The depth of oscillation marks increases with increasing oscillation stroke length,⁹ Fig. 2-3, and decreases with increasing oscillation frequency,^{8 21 22} Fig. 2-4. The longer the oscillation stroke, the larger is the effect of oscillation frequency on the depth of oscillation marks.²¹ In more general terms the mark depth has been related to the negative-strip time as expressed by Eq. (2-3). The

relationship between the depth of oscillation marks and the negative-strip time in different plants is summarized in Fig. 2-5.²³⁻²⁵ It is seen that the depth of oscillation marks increases with increasing negative-strip time. The effect of mould flux properties and casting speed on the depth of oscillation marks has not been determined clearly.

2.2.2 Subsurface Structure Of Oscillation Marks

Oscillation marks can be classified according to the adjacent solidified structure. Emi et al.⁹ have discerned two types of oscillation marks based on the presence or absence of a small "hook" in the subsurface structure adjacent to each oscillation mark, Fig. 2-6. The hooks are believed to be a manifestation of liquid metal overflowing the top of the shell which is inclined toward the molten pool. The absence of hooks, it has been suggested, is due to the top of the inclined shell being pushed back toward the mould wall by the ferrostatic pressure.

Details of the subsurface structure adjacent to oscillation mark were examined by Saucedo et al.²⁶ The secondary dendrite-arm spacing was measured and was found to be smaller at the top than at the bottom of the oscillation marks; this finding was taken as evidence that the area at the bottom of oscillation marks was solidified at a reduced rate away from the mould wall. Thus they suggested the possibility of meniscus solidification.

Recently positive segregation of solute elements in the vicinity of the bottom of oscillation marks has been reported,²⁷²⁹ and this will be described later.

2.2.3 Mechanism Of Oscillation Mark Formation

Several mechanisms have been proposed to explain the formation of oscillation marks. Sato³⁰ has suggested, as did Savage and Pritchard in 1954³¹ for the formation of reciprocation marks in steel billets, that the shell "sticks" to the mould wall such that on the upstroke of the mould, the shell ruptures allowing liquid steel to partially fill the gap created. This event is followed by a "healing" period while the mould moves downward, see Fig. 2-7. This mechanism is difficult to justify, however, because the oscillation marks on a slab surface are relatively straight and horizontal which would hardly be possible if the rupture mechanism predominated. Emi et al⁹ have proposed a mechanism, in which the top edge of the shell is pushed toward the molten steel by liquid flux during the negative-strip period of the mould oscillation, see Fig. 2-8. The mould flux is "pumped" into the channel between the steel and the mould by a frozen slag rim attached to the mould wall. At the end of the negative-strip period, when the mould and strand are moving downward with the same velocity, the flux pressure is released and ferrostatic pressure either causes molten steel to overflow the partially solidified meniscus to form a hook or the meniscus is pushed back toward the mould wall such that a hook is not created. Thus the hook adjacent to

oscillation marks is a manifestation of molten steel overflowing a partially solidified meniscus as suggested earlier. Similar concepts have been invoked by others.^{26 32-35} Based on experimental results obtained with a "mould simulator", Kawakami et al.³⁶ have suggested that oscillation marks arise from the interaction of a viscous layer of mould flux which moves with the mould wall, and during the negative-strip time, physically bends the top of the solidifying shell. Molten steel then overflows the bent shell. The sequence of events leading to the formation of oscillation marks according to this mechanism is shown schematically in Fig. 2-9. Using the same type of "mould simulator", H. Takeuchi et al.³⁷ have proposed a slightly different mechanism. They theorized that a solidified slag rim at the meniscus, which moves with the mould wall, pushes the top of the shell directly toward the meniscus. Even though the solid slag rim and/or viscous flux layer are affected by heat flow at the meniscus, no thermal analysis was done in these studies.

These reported mechanisms are essentially conceptual in nature and have been applied only in a qualitative manner to rationalize the influence of oscillation characteristics on the pitch and the depth of oscillation marks. Owing to the complexity of the meniscus phenomena, only a few theoretical approaches have been made on the mechanism of oscillation-mark formation. Based on results of an investigation of the subsurface structure adjacent to oscillation marks, as mentioned before, Saucedo et al.³⁸ formulated a two-dimensional, heat-

transfer model of solidification in the meniscus region. This heat flow analysis is to be discussed in a later section. However the mould oscillation effect was not taken into account in their model. Based on a modification of their conceptual model, Fig. 2-8, Nakato et al.³⁹ proposed a simple mathematical model to explain the effect of mould oscillation conditions on the depth of oscillation marks. Their assumptions were as follows; 1) the top of the shell is deformed directly by a solid slag rim which moves with the oscillating mould (similar to Takeuchi's model³⁷), 2) the extent of deformation of the shell, viz the depth of oscillation mark, is proportional to the maximum displacement of the mould relative to the shell, see Fig.2-10. The maximum displacement is given by Eq. (2-6).

$$d \propto \Delta l_{\max} = \frac{s}{2} \sin(2\pi f t_{\max}) - v_s t_{\max} \quad (2-6)$$

$$t_{\max} = \frac{1}{2\pi f} \arccos\left(\frac{v_s}{\pi f s}\right) \quad (2-7)$$

According to the results predicted with this model shown in Fig. 2-11, the depth of oscillation marks increase with increasing oscillation stroke. This tendency is consistent with the plant data in Fig. 2-3. However the calculated effect of oscillation frequency on the depth of oscillation mark, viz the mark depth increases with increasing oscillation frequency, is opposite to observations made in plant, Fig. 2-4.

2.3 Heat Transfer In The Mould Near The Mensiscus

2.3.1 Factors Affecting Mould Heat Flux

Mould heat transfer has been determined from the temperature distribution in the mould measured with a large number of thermocouples embedded in the copper plates of the mould wall.^{10 40-43} In addition mould heat transfer has been characterized by the temperature change of mould cooling water and/or by the calculated thermal resistance between steel shell and mould wall.^{18 45} From these thermal investigations, the following subjects have been clarified. The most important factor influencing the heat flux extracted from the mould wall is the carbon content of the steel,^{40 44} which has been discussed frequently in relation to the formation of surface cracks. Near 0.10-0.15%C the solidified shell experiences volume shrinkage due to the δ - γ transformation, which gives rise to air gaps between the mould and shell. Furthermore the ferritic solidification structure, with much less micro segregation, has a high strength which may contribute to partial contact with the mould wall.⁴¹ Therefore air gaps formed between the shell and the mould wall reduce local heat flux, which may prevent local shell growth and lead to the initiation of surface cracks. Selection of a suitable mould flux partially relieves the nonuniformity of heat extraction.⁴⁷ Casting speed also has a large influence on the heat flux,⁴⁰ because it changes not only the shell thickness, viz air gap formation, but also the flow

rate of molten steel at the solidification front⁴⁸ and the inflow of the mould flux into the "gap" between mould wall and the shell.¹⁸ Fig. 2-12 shows the effect of casting speed on the heat flux profile in the mould.⁴⁰ Unfortunately, in obtaining these axial distributions of heat flux, from thermocouple readings, one-dimensional heat conduction through the thickness of the mould wall has been assumed whereas, as Samarasekera and Brimacombe⁴⁶ have shown, the axial component of heat conduction in the meniscus region is large. Implicit neglect of axial heat conduction means that reported data for heat flux at the meniscus are lower than the actual values. Another deficiency, from the standpoint of characterizing heat flux in the meniscus region, is the absence of heat flux data over the length of the mould wall above and adjacent to the meniscus. Thus the heat flux profiles reported in the literature are inadequate for the prediction of the temperature distribution in the mould flux and the steel at the meniscus. Knowledge of mould flux temperature at the meniscus is very important because it affects the viscosity, consequently the flow of mould flux into the gap between the mould wall and the shell.

2.3.2 Meniscus Solidification

Solidification in the meniscus region has been investigated theoretically by Tomono et al.³² and Saucedo et al.³⁸ The main assumptions in the first authors' computation are as follows:

- i) no mould flux and mould oscillation
- ii) one-dimensional unsteady-state heat flow in the steel

- iii) two-dimensional steady-state heat flow in the mould wall
- iv) temperature of mould wall-water interface at 100°C
- v) specified thickness of air gap between mould and shell

One of their calculated results is shown in Fig. 2-13. Unfortunately, the temperature distribution in the mould wall is completely different from actual measured values.⁴²

Saucedo et al.³⁸ presented a two-dimensional heat transfer model, which is more acceptable than the former case. Their computation is based mainly on the following assumptions;

- i) no mould flux and mould oscillation
- ii) two-dimensional unsteady state heat flow in the steel
- iii) heat transfer coefficient assumed for the mould/steel boundary condition
- iv) solidified shell is rigid if fraction solid exceeds 0.2.

Fig. 2-14 shows one of their calculated results, the effect of convective heat-transfer coefficient on the shell profile. According to their results, partial solidification of the meniscus may be possible. Moreover the amount of heat extracted from the mould wall, carbon content, and superheat of the molten steel have a strong effect on this phenomenon. Although they suggested that the meniscus solidification is the major cause of oscillation mark formation, their assumptions especially on the rigidity of the solidified shell leave room for argument.

Another point to be noted is that they overestimated the heat flux from the meniscus by using square nodes in their finite-difference analysis to approximate the curvature of the meniscus. A more precise model should be developed to estimate the temperature distribution not only in the steel but also in the mould flux.

2.4 Lubrication In The Mould

2.4.1 Consumption Of Mould Flux

Numerous industrial trials have been conducted to determine the most suitable lubrication conditions for the production of slabs with high surface quality^{9 10 47 49-65} especially in the case of high speed casting.^{12 55 56} In general a large consumption of mould flux is expected to provide good lubrication in the mould. However it has been found that increasing the casting speed decreases the mould flux consumption,^{50 55} as shown in Fig. 2-15. Furthermore increasing the oscillation frequency, even though it reduces the depth of oscillation marks,²¹ also decreases the flux consumption,^{8 9} Fig. 2-16. Low flux consumption causes a high friction force⁶⁶ between the steel shell and mould wall, which gives rise to surface cracks,⁵¹ and in the worst case the sticking of the shell to the mould wall.⁶⁷ In order to compensate for the reduced flux consumption, improvements to the flux properties, such as viscosity and solidifying temperature,

have been made recently in many casting plants.^{47 52 55 60 61 68} The effect of the viscosity and softening temperature of mould flux on the flux consumption are shown in Figs. 2-17 and 2-18,⁵² respectively. Quantities of Li_2O ,⁵⁵ BaO and/or B_2O_3 ,^{52 61} are added to conventional mould fluxes to decrease their viscosity and softening temperature without at the same time increasing erosion of immersion nozzles.

Several theoretical approaches have been attempted to understand the process of flux consumption,^{16 69-71} and lubrication in the mould. Kor,⁶⁹ for example, calculated the velocity distribution in the flux film between the mould wall and the shell to estimate the shear stress acting on the shell surface, viz friction force, using the following equation.

$$\rho_f \frac{\partial u}{\partial t} = - \frac{\partial p}{\partial x} + \frac{\partial^2 u}{\partial y^2} \mu_f \quad (2-8)$$

The major assumption on which his model is based is that the mould wall and the solidified shell are parallel, and the distance between them, viz the thickness of mould flux layer, is constant. As a result, for example, the time independent terms of the average velocity of mould flux were expressed by Eq. (2-9).

$$\bar{v}_f = \frac{v_s}{2} + \frac{(\rho_s - \rho_f) g d_f^2}{12 \mu_f} \quad (2-9)$$

According to Eq. (2-9), flux consumption increases with increasing casting speed whereas the opposite effect has been observed in plant, Fig. 2-15. The problem could be due to the simple assumptions as described above; also the effect of

oscillation conditions and casting speed on the inflow of mould flux into the gap between mould wall and shell at the meniscus, which will determine the thickness of flux layer, is not taken into account.

2.4.2 Mould Friction

In the upper part of the mould, the friction force acting on the steel shell depends on the viscosity of the mould flux and velocity distribution in the liquid flux film.^{14 69}

$$\tau = -\mu_f \frac{\partial u_x}{\partial y} \quad (2-10)$$

However over most of the mould length, solid-solid friction⁴⁸ additionally complicates the shell behavior and makes the theoretical analysis of mould friction much more difficult. Recently measurements of the mould friction force using strain gauges, etc. have been carried out in many plants.^{51 54 60 67 72-74} Although the analysis of this sort of measurement has not been well established,⁷³⁻⁷⁵ it offers a method of determining optimum conditions of mould operation. Many experimental results reveal that a large friction force may cause breakouts and/or surface cracks, such as longitudinal cracks and transverse cracks. The mould friction decreases with decreasing casting speed, oscillation frequency and the softening temperature of mould flux, which is consistent with the consumption of mould flux.

2.5 Surface Quality Of Slabs Related To Oscillation Marks.

2.5.1 Transverse Cracks

Transverse cracks are one of the most common surface defects on continuously cast slabs, and therefore have attracted numerous studies. Transverse cracks are observed both on the wide and the narrow side and/or even at the corner of slabs,²⁹ see Fig. 2-19. They are perpendicular to the casting direction, and appear usually along the bottom of oscillation marks. Fine transverse cracks along oscillation marks are difficult to detect on the as-cast slab surface. Hence in the case of steels sensitive to transverse cracks such as micro-alloy grades,⁷⁶⁻⁷⁸ a careful visual inspection is necessary to find these fine cracks, and this seriously reduces the productivity of continuous casting.

In general transverse cracks form on the inside radius (loose) side of the strand in a curved continuous casting machine which has a single bending point between the curved region and straightening rolls. In a vertical bending continuous casting machine having an additional upper bending point, the cracks may form on either the loose or the fixed side of the strand.⁷⁹ These results suggest that transverse cracks are formed by tensile strain applied on the strand at the straightening point.^{76 79} Ductility measurements have been performed in the temperature range from 1000°C to 600°C and low strain rate $\dot{\epsilon} \approx 5 \times 10^{-3} \text{s}^{-1}$ which is close to 10^{-4}s^{-1} at the

bending point,⁸⁰ and it has been determined that transverse cracks are closely related to intergranular embrittlement associated with the A_r transformation in the temperature range from 700°C to 900°C.⁸⁰ In the case of plain carbon steel, the embrittlement is caused by film-like proeutectoid ferrite precipitating along the austenite grain boundaries. Imposed strain then concentrates in the ferrite layer to cause intergranular cracks. In addition, precipitation of AlN ⁸¹ and Nb, V carbonitride^{82 83} further decreases the ductility of steel in the same temperature range. Nitrogen reduces the ductility of steel and increases the frequency of transverse cracks as shown in Fig 2-20 (a) and(b) respectively.

In actual casting operations, decreasing these harmful alloying elements (Al,N,Nb,V) and controlling the slab surface temperature above 900°C to avoid the brittle temperature range at the straightening point have been reported to be effective in the prevention of transverse crack formation, Fig. 2-21.⁴ Prior to the development of the "hot charging" practice, the slab surface was cooled down below the brittle temperature range, viz about 600°C at the unbending point.⁷⁶

Sugitani⁸⁴ has proposed the following mechanism for transverse crack formation based on their experimental results. The surface region of slab is subjected to a repeated rise and fall of temperature in the spray cooling zone owing to changing heat extraction rates associated with rolls and sprays. If this temperature fluctuation is very large, it causes many fine

transverse cracks to form on the surface of slabs containing high Al, Nb, and/or V. These fine cracks propagate to generate large transverse cracks during unbending. This mechanism is supported by the investigation results of Yamaki et al.⁸⁵ They have examined slabs obtained from an interrupted cast and found that fine cracks appeared over the whole surface of the slabs before the unbending point.

With respect to the effect of oscillation marks on the formation of transverse cracks, it has been suggested that the bottom of oscillation marks acts as a notch to enhance cracking at the unbending point, because reducing the depth of oscillation marks decreases the formation of transverse cracks, and the cracks are usually found on the loose side of the slab where tensile strain is generated at the bending point.⁷⁹ However it seems unreasonable that the oscillation marks simply create a notch effect, because usually the bottom of oscillation marks is rounded and furthermore the depth of marks is reduced by support rolls. On the other hand Tanaka et al.²⁹ metallographically investigated the bottom of oscillation marks, and found fine cracks initiated in regions of positive segregation along the subsurface hooks; these may offer sites for transverse cracks.

2.5.2 Positive Segregation

Recently positive segregation of solute elements at the bottom of oscillation marks has been examined in relation to surface defects on slabs.

In the case of a plain-carbon steel, positive segregation of P and Mn has been detected along the hook in the subsurface structure of oscillation marks.^{28 29} This type of segregation is more severe at the corner than at the center of slabs. The maximum content of phosphorus determined by EPMA in the segregation region increases with increasing depth of oscillation marks, as shown in Fig. 2-22. Below the positive segregation along the hook, negative segregation was found. From these results the mechanism for positive segregation has been proposed as follows. Interdendritic liquid having a high solute content in the top of the shell is squeezed out as the shell is bent during the downward motion of the mould, see Fig. 2-23. Fine cracks have been observed in the zone of positive segregation of P, and therefore this region was considered to offer a good site for transverse crack formation.

In addition, the same type of positive segregation has been found at the bottom of oscillation marks in austenitic stainless-steel slabs.²⁷ Intensive segregation often gives rise to surface defects on products rolled from the slab without surface conditioning,⁸⁶ hence it has become one of the troublesome defects affecting the "hot charging" of stainless-steel slabs. Surface segregation on stainless steel slabs is

classified into the following two types: A) segregation at the overflow part on the hook, B) segregation layer at the surface of oscillation marks without hooks, see Fig. 2-24.

The segregation of Ni and Si was determined in both types of segregation zone, and the segregation ratio of these elements was found to be close to the inverse of the partition coefficient of each. Thus it has been proposed that the concentrated liquid at the solidification front is transported to the surface of the slab by overflow (type A) or by bleeding (type B), see Fig. 2-25. The frequency of the positive segregation increases with increasing negative-strip time, as shown Fig. 2-26.

2.6 Summary - Industrial Necessity For The Present Work

The oscillation marks formed on the surface of slabs are not only the site of transverse cracks⁶ but themselves are unfavorable for the establishment of hot-charging.^{8,6} High-frequency and short-stroke mould oscillation, giving short negative-strip time, has been found to reduce the depth of oscillation marks.^{8,22} However mould oscillation of short negative-strip decreases the consumption of mould flux, which increases the mould friction.^{5,5} High friction force generates tensile strain in the shell solidifying in the mould, which leads to longitudinal and/or transverse cracks^{5,1} and, in the worst case, breakouts.^{6,7} As the countermeasure to this problem, ultra-low viscosity mould flux has been developed

recently.^{52 55 61}

Further industrial development can be achieved more efficiently if the initial-solidification phenomena at the meniscus are better understood. Since the meniscus phenomena are characterized by the formation of oscillation marks, a study of the oscillation-mark formation ought to provide the necessary information. However all models of oscillation-mark formation that have been reported up to now are too conceptual to contribute to the improvement of mould operation.^{9 30 36} Therefore the present study has been undertaken as the first theoretical study of the meniscus phenomena by metallographic investigation of subsurface structure of slabs followed by several mathematical analyses.

Table I - Properties of Molten Oxide Mixture

Property	Measured Value	Ref
Density	2.8 g/cm ³ CaO-SiO ₂ -Al ₂ O ₃ , CaO/SiO ₂ =1 at 1500°C	15
Inter-facial tension	1120 a), 1250 b) dyn/cm a) CaO=47%, SiO ₂ =37%, Al ₂ O ₃ =16% b) CaO=45%, SiO ₂ =34%, Al ₂ O ₃ =21% C=0.04%, Mn=0.04%, Si=0.03%, P=0.01%, S=0.02% at 1500-1580°C	15
viscosity	$\log \mu_f = 0.578 \times 10^4 / T - 2.979$ μ_f : viscosity of mould flux (P) T: temperature of mould flux (K)	16
Specific Heat	1.13 a), 1.30 b) J/g°C CaO=52%, SiO ₂ =43%, Al ₂ O ₃ =5% a) at 1000°C, b) at 1500°C	17
Thermal Conductivity	1.26 W/mK CaO=40%, SiO ₂ =40%, Al ₂ O ₃ =20% at 1360°C	18
	2.34 W/mK mould flux (Kawasaki Steel) at 1000 - 1500°C	19

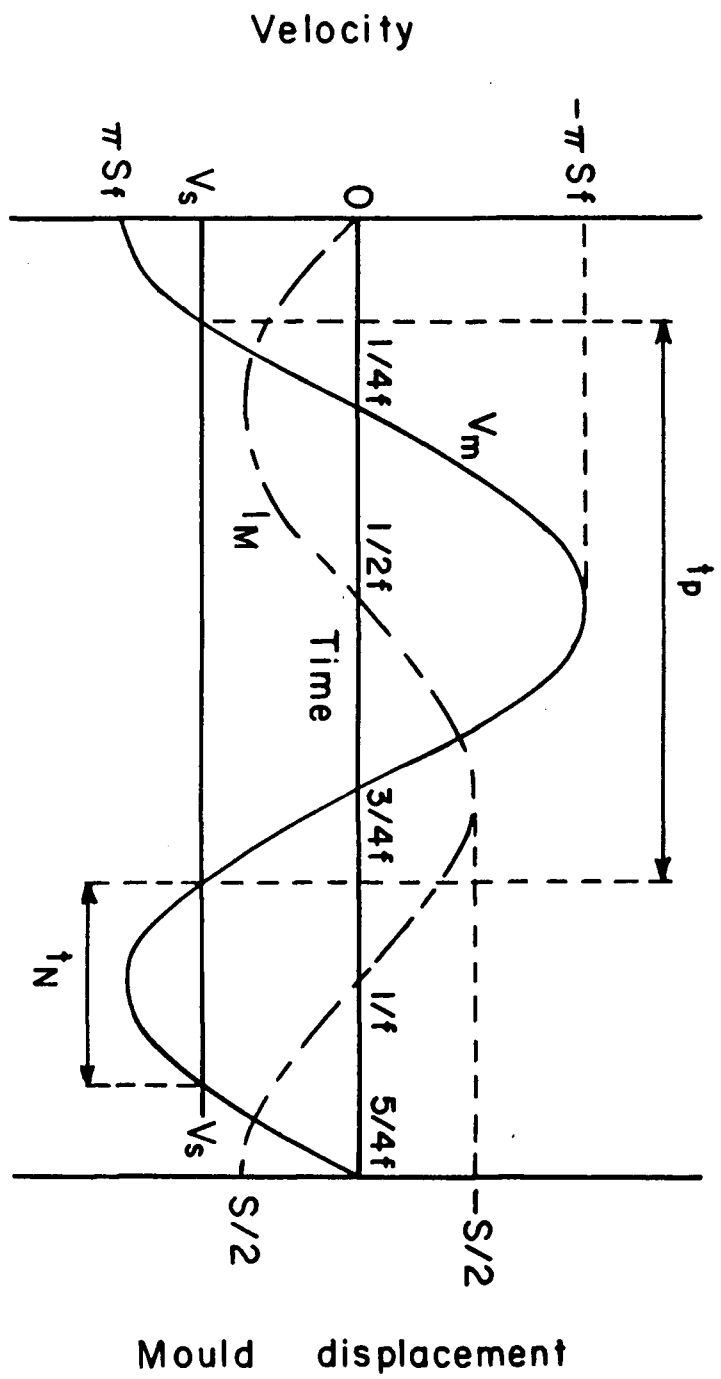


Fig. 2-1 Mould displacement due to oscillation.

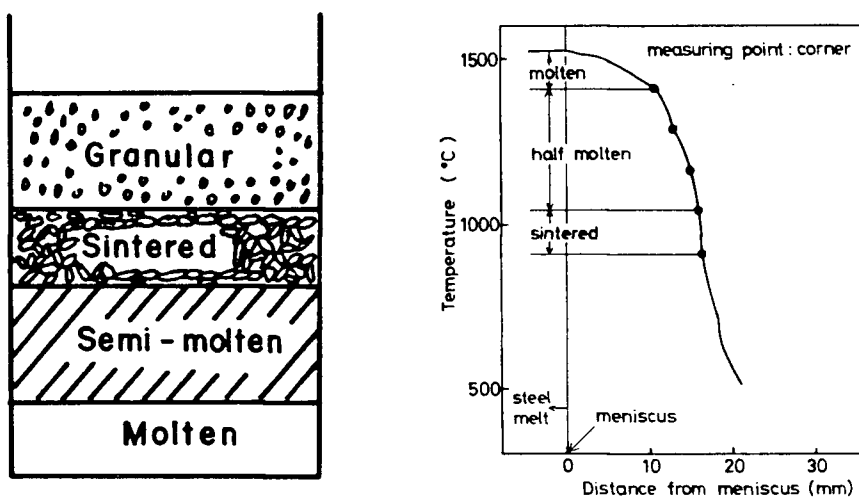


Fig. 2-2 Macroscopic structure and temperature distribution in the melting mould flux layer on the meniscus.¹²

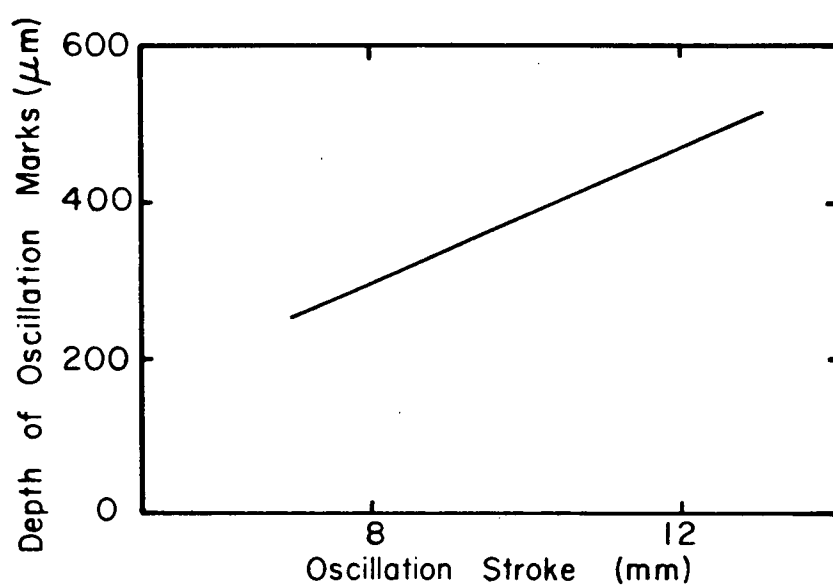


Fig. 2-3 Effect of oscillation stroke on the depth of oscillation marks.⁹

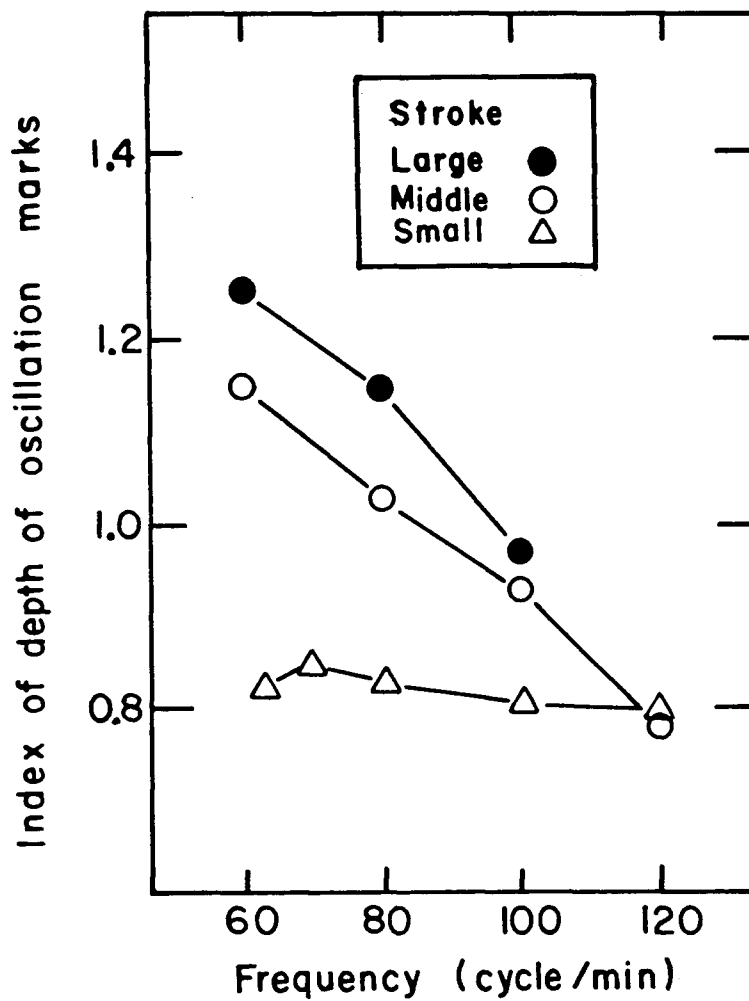


Fig. 2-4 Effect of oscillation frequency on the depth of oscillation marks.¹⁶

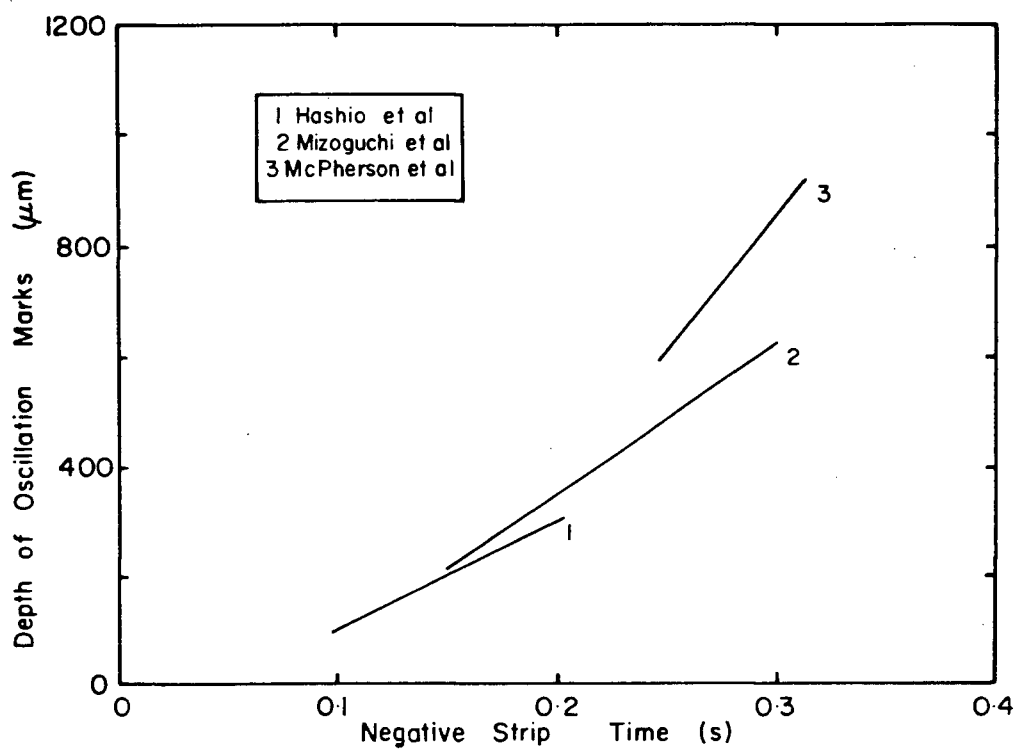


Fig. 2-5 Relationship between the depth of oscillation marks and the negative strip time.²³⁻²⁵

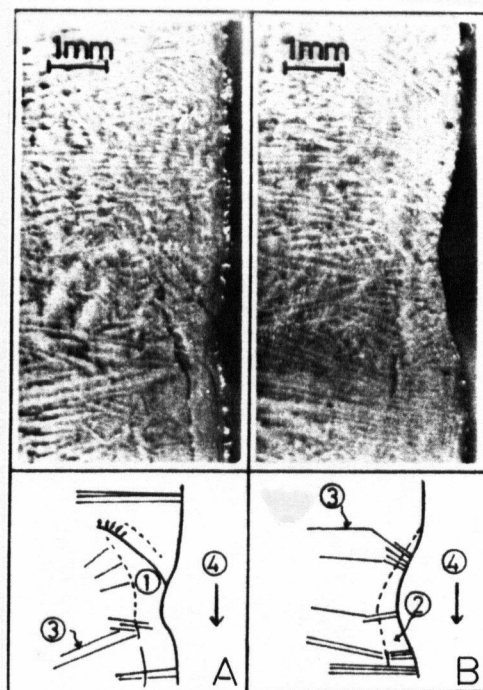


Fig. 2-6 Dendrite structure in the vicinity of oscillation marks.⁹ (1) Hook-like structure, (2) Non-hook-like structure, (3) Direction of growth of primary dendrite, (4) Casting direction.

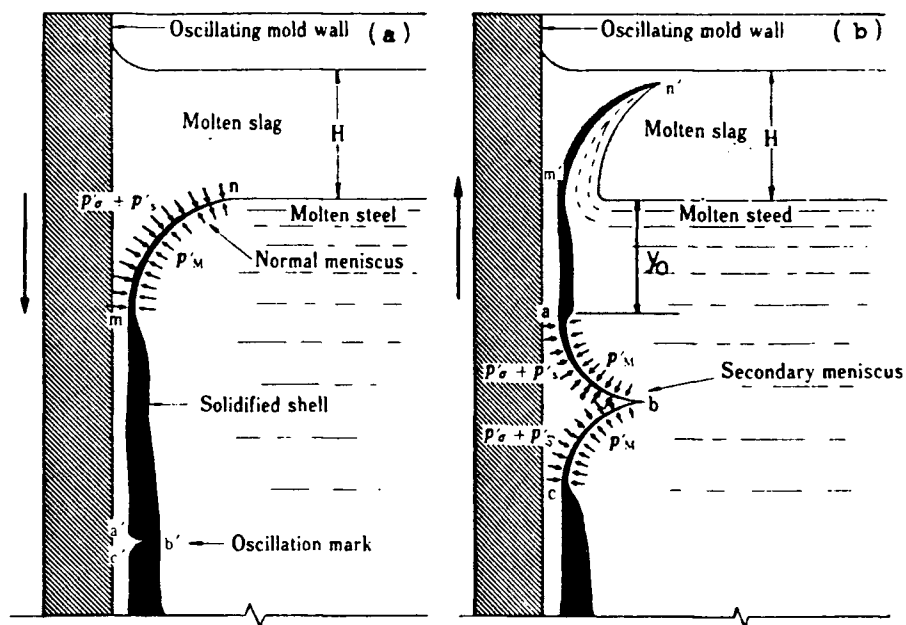


Fig. 2-7 Formation mechanism of oscillation marks by Sato.³⁰

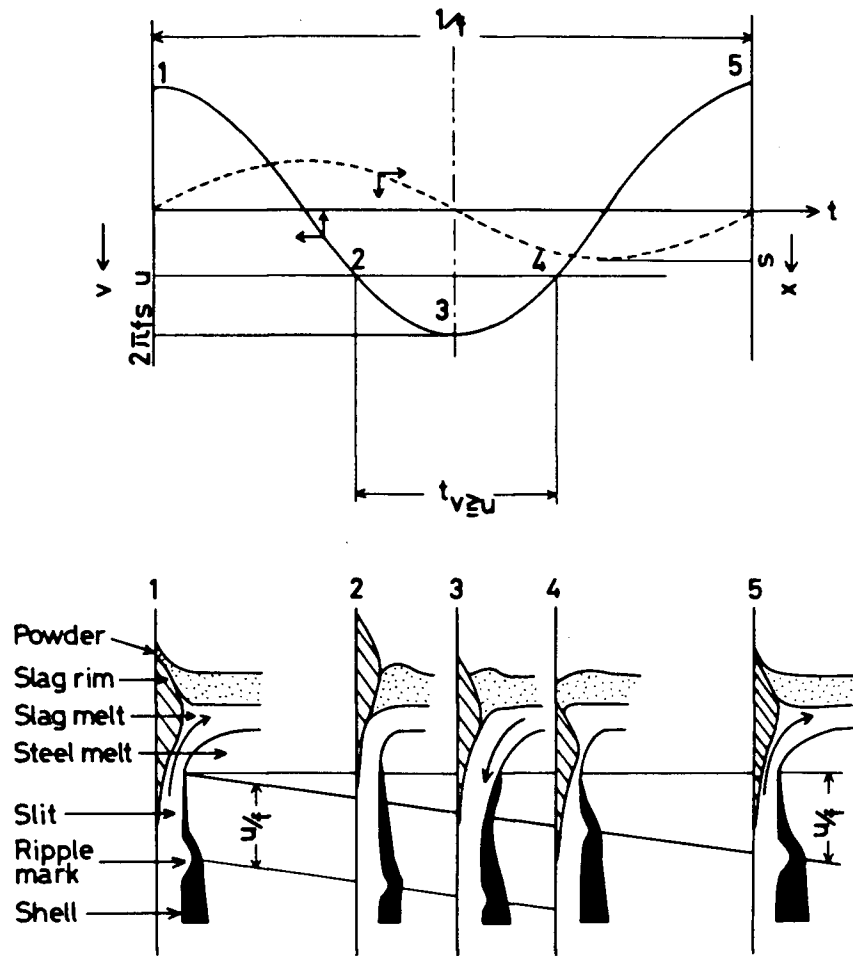


Fig. 2-8 Formation mechanism of oscillation marks by Emi et al.⁹

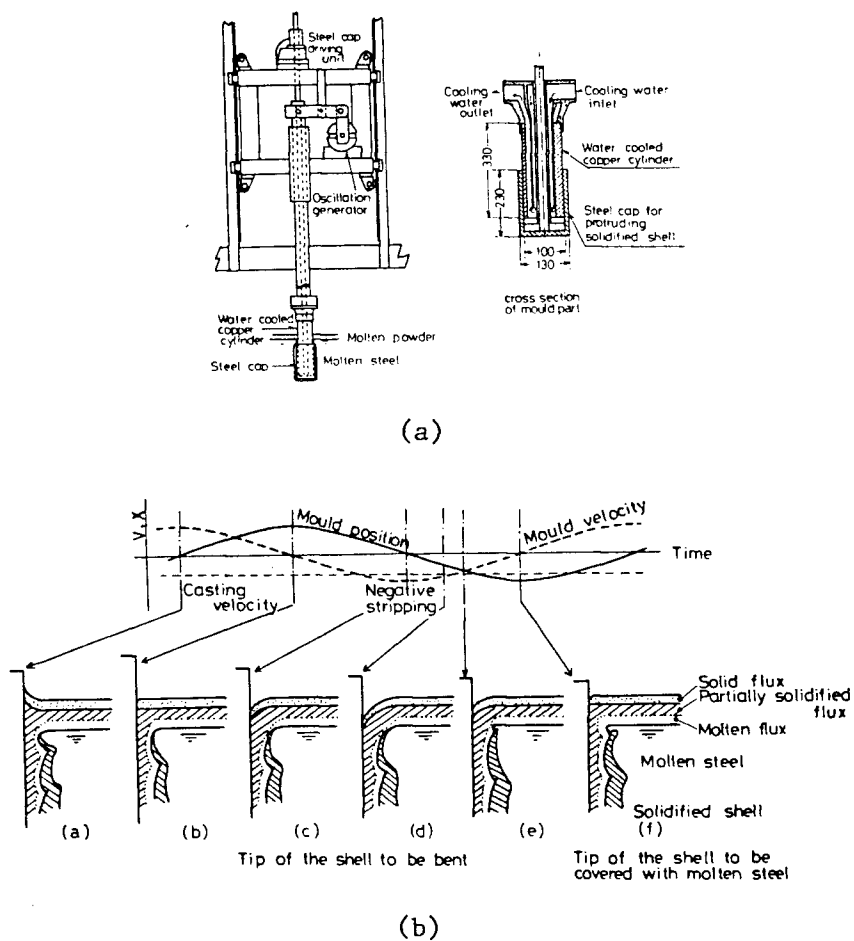


Fig. 2-9

Schematic diagram of "mould simulator" (a) and formation mechanism of oscillation marks (b) by Kawakami et al.³⁶

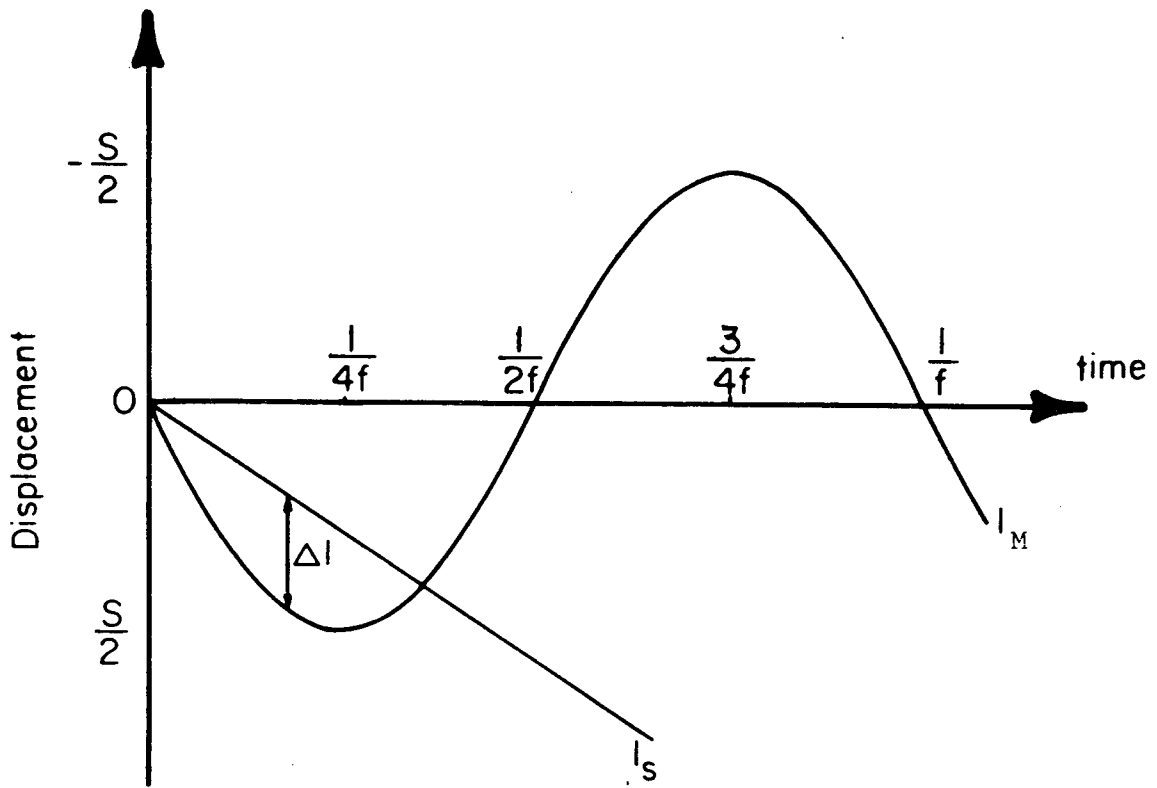


Fig. 2-10 Change of displacement of the mould and the shell with time.

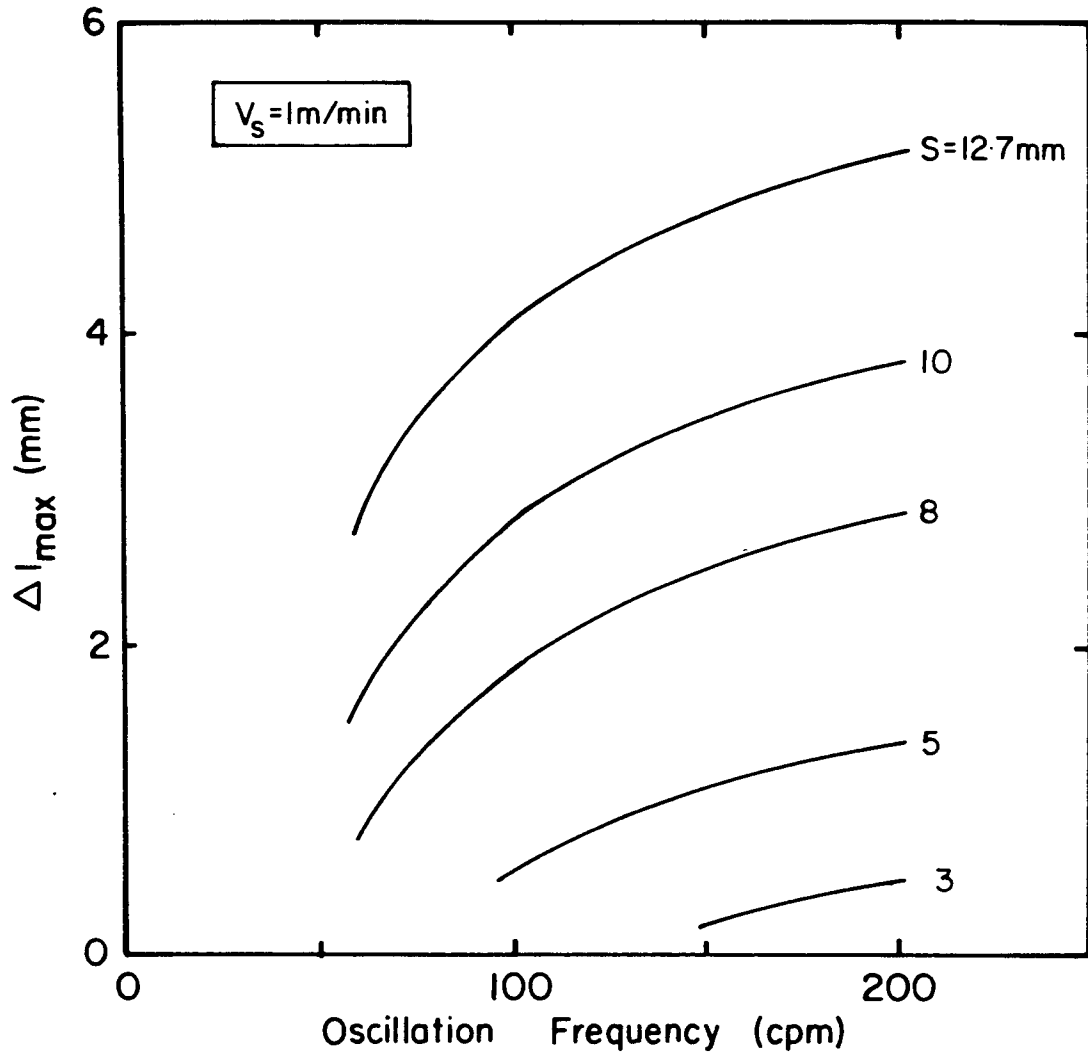


Fig. 2-11 Calculated effect of oscillation frequency and stroke on the depth of oscillation marks by Nakato's model.³⁹

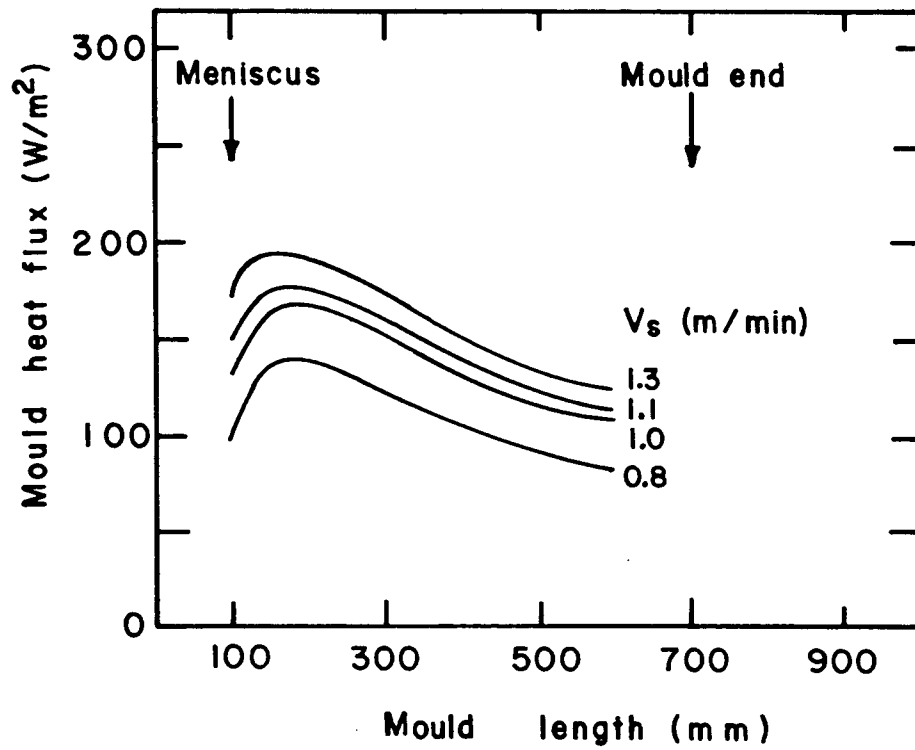


Fig. 2-12 Effect of the casting speed on the axial heat flux profile in the mould wall.⁴⁰

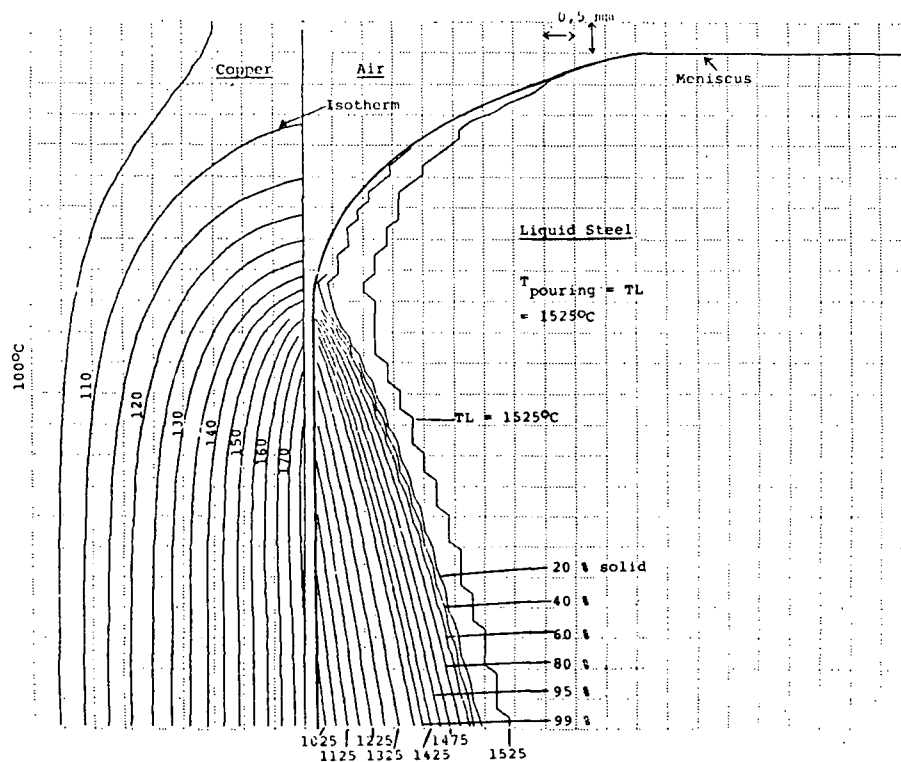


Fig. 2-13 Calculated temperature distribution in the mould wall and in the steel.³²

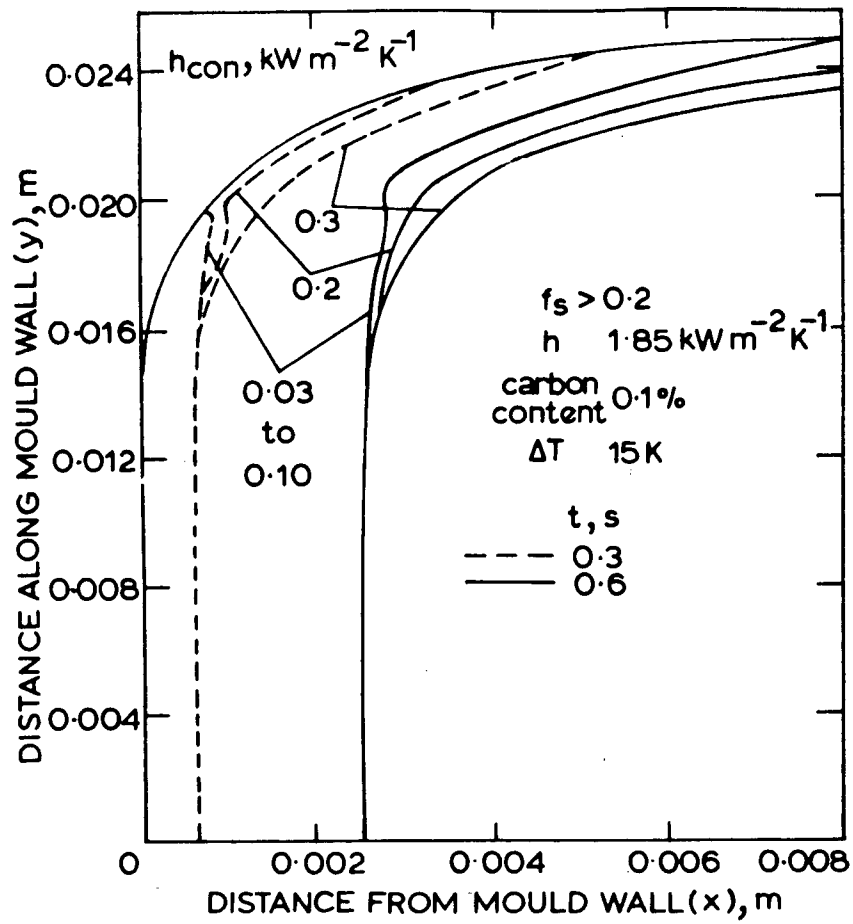


Fig. 2-14 Calculated shell profile with different convective heat transfer coefficients (h_{con}).³⁸

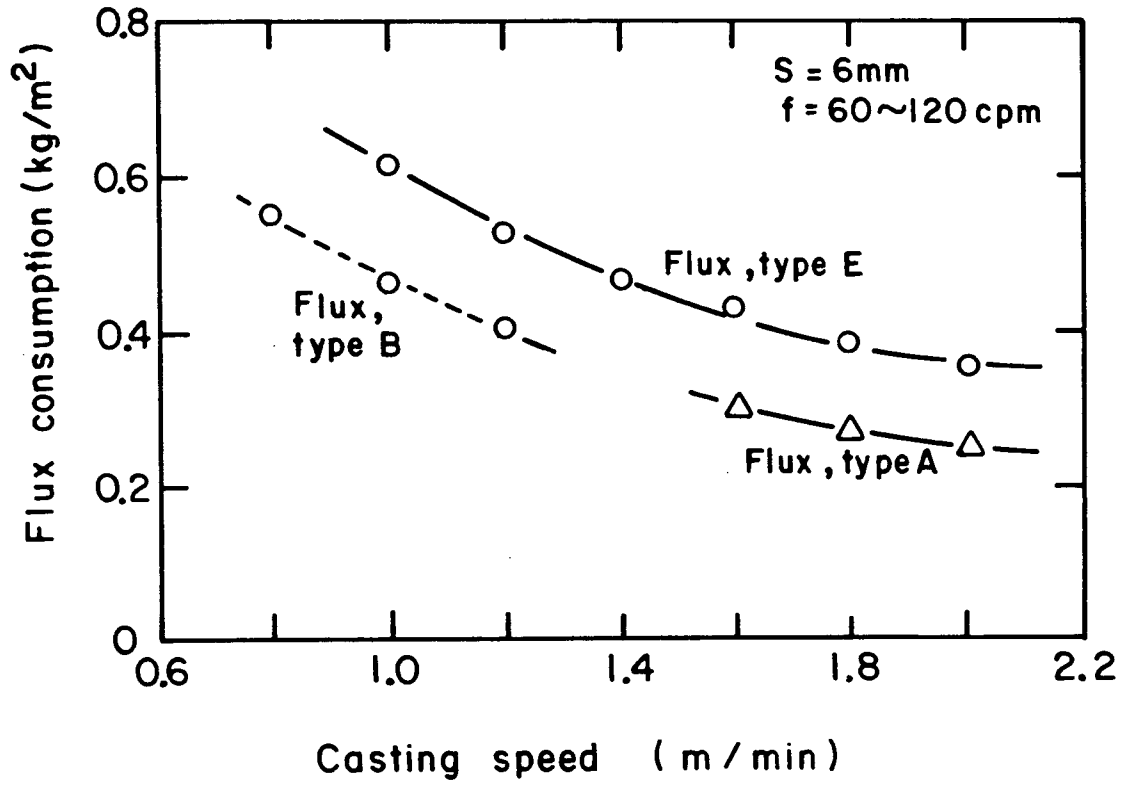


Fig. 2-15 Effect of casting speed on mould flux consumption.⁵⁵

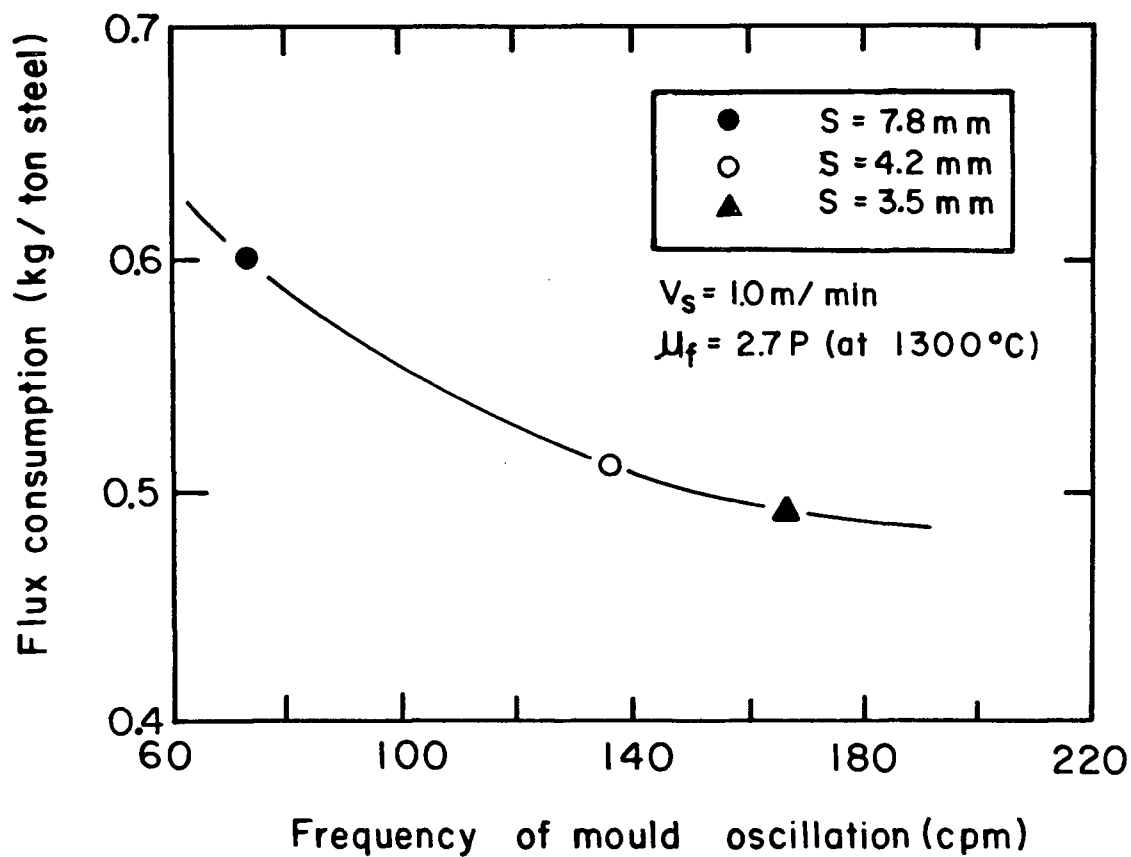


Fig. 2-16 Effect of oscillation frequency on mould flux consumption.⁸

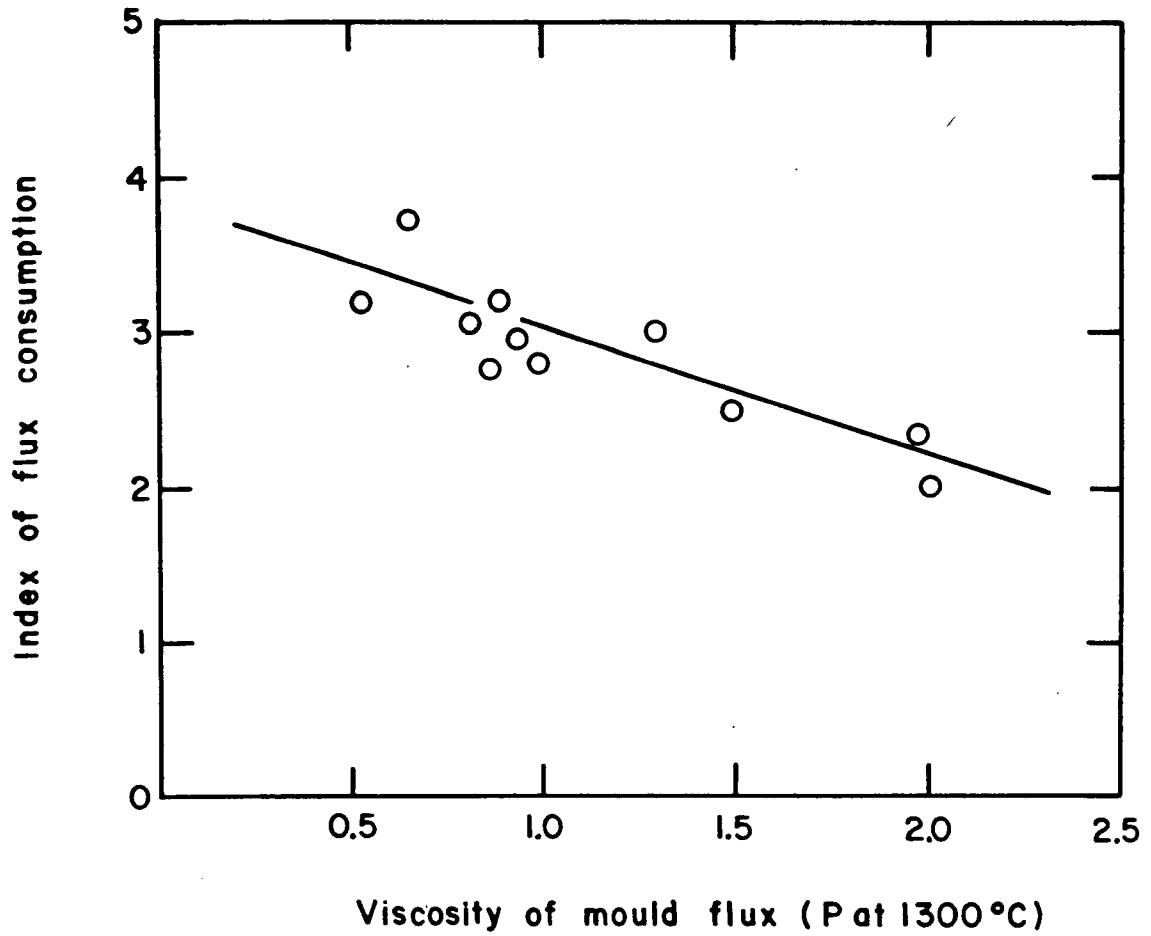


Fig. 2-17 Effect of viscosity of mould flux on the flux consumption.⁵²

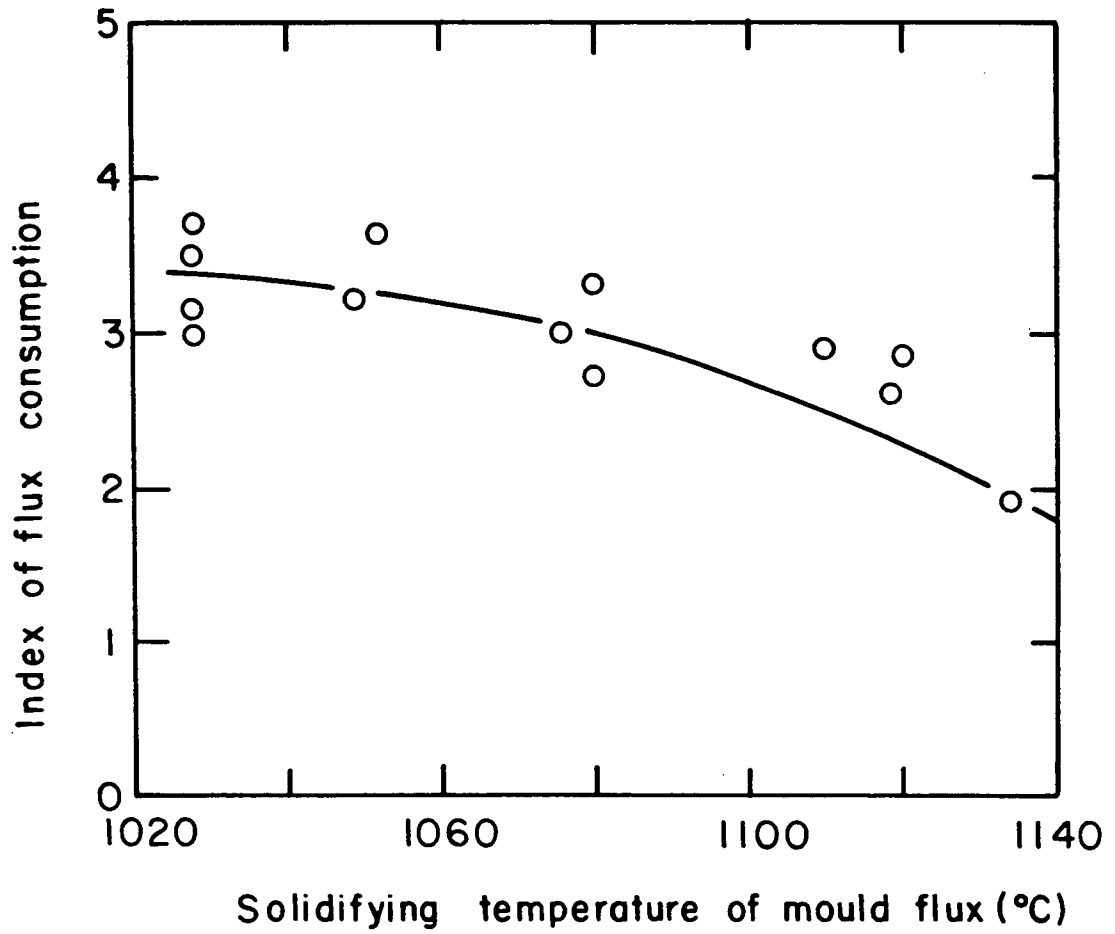


Fig. 2-18 Effect of softening temperature of mould flux on the flux consumption.⁵²

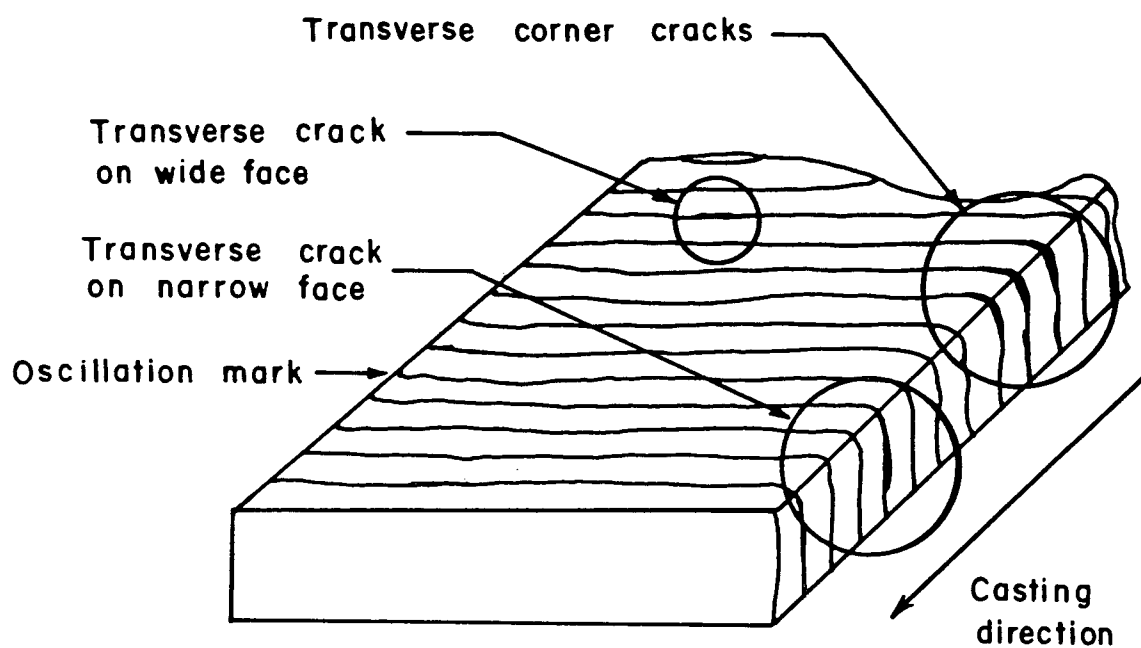
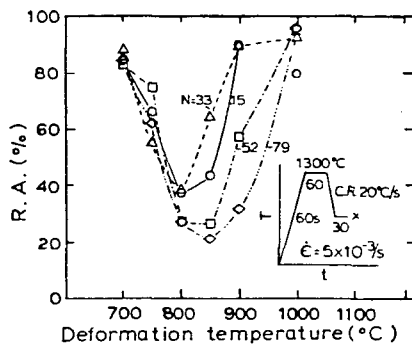
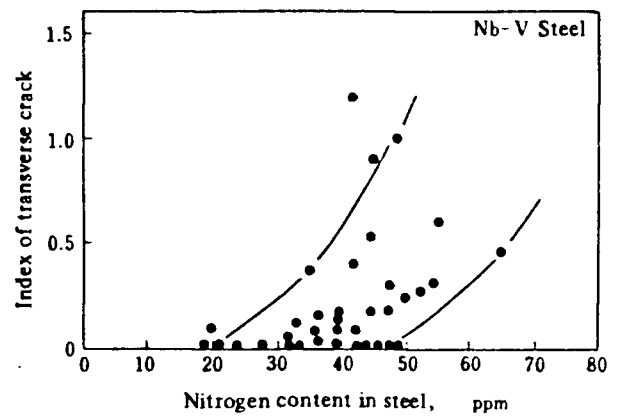


Fig. 2-19 Transverse cracks observed on slab surface.²⁹



	C	Si	Mn	P	S	Al	N
○	0.13	0.07	0.35	0.002	0.003	0.004	0.0015
△	"	"	"	"	"	"	0.0033
□	"	"	"	0.003	0.004	—	0.0052
◇	"	"	"	"	"	—	0.0079

(a)



(b)

Fig. 2-20 Effect of nitrogen on the hot ductility in low carbon steel⁸⁰(a), and on the frequency of transverse crack formation in Nb-V steel⁸²(b).

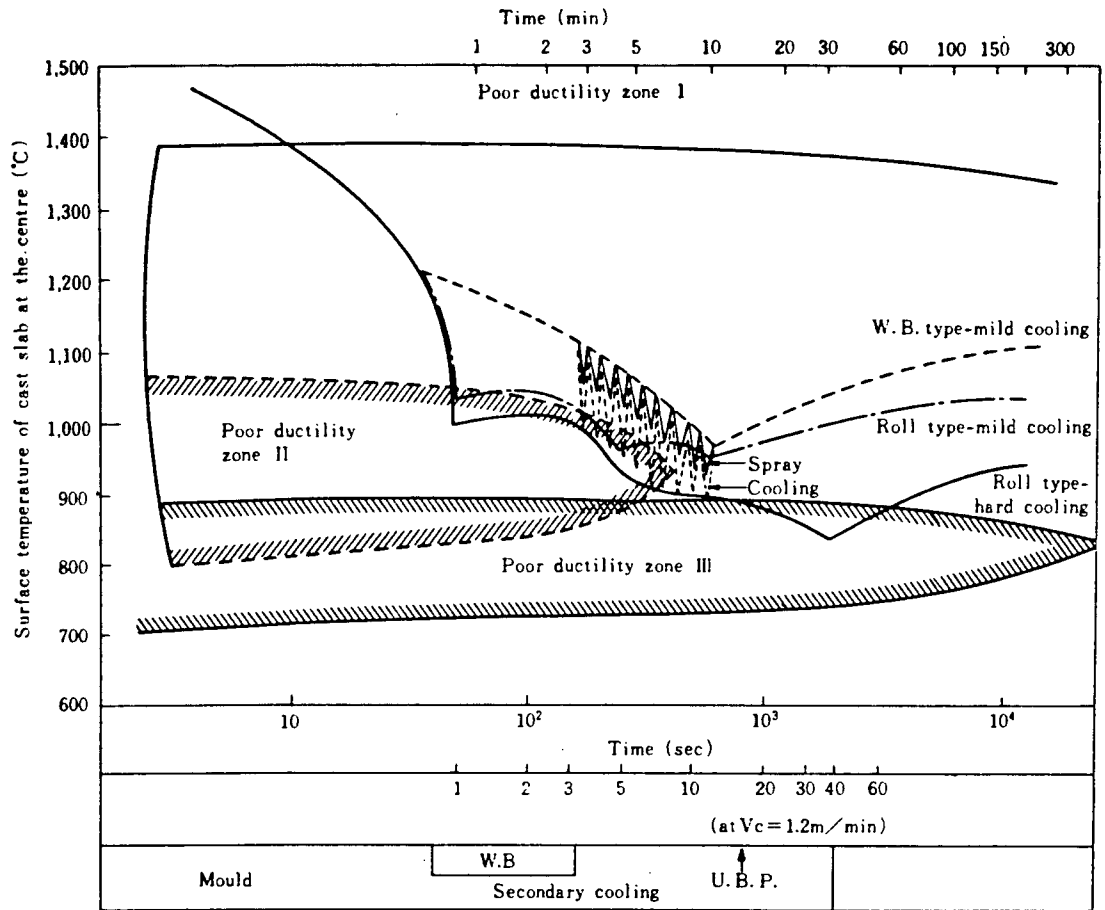


Fig. 2-21 Temperature profile on the slab surface to avoid the brittle temperature range at the unbending point.⁴

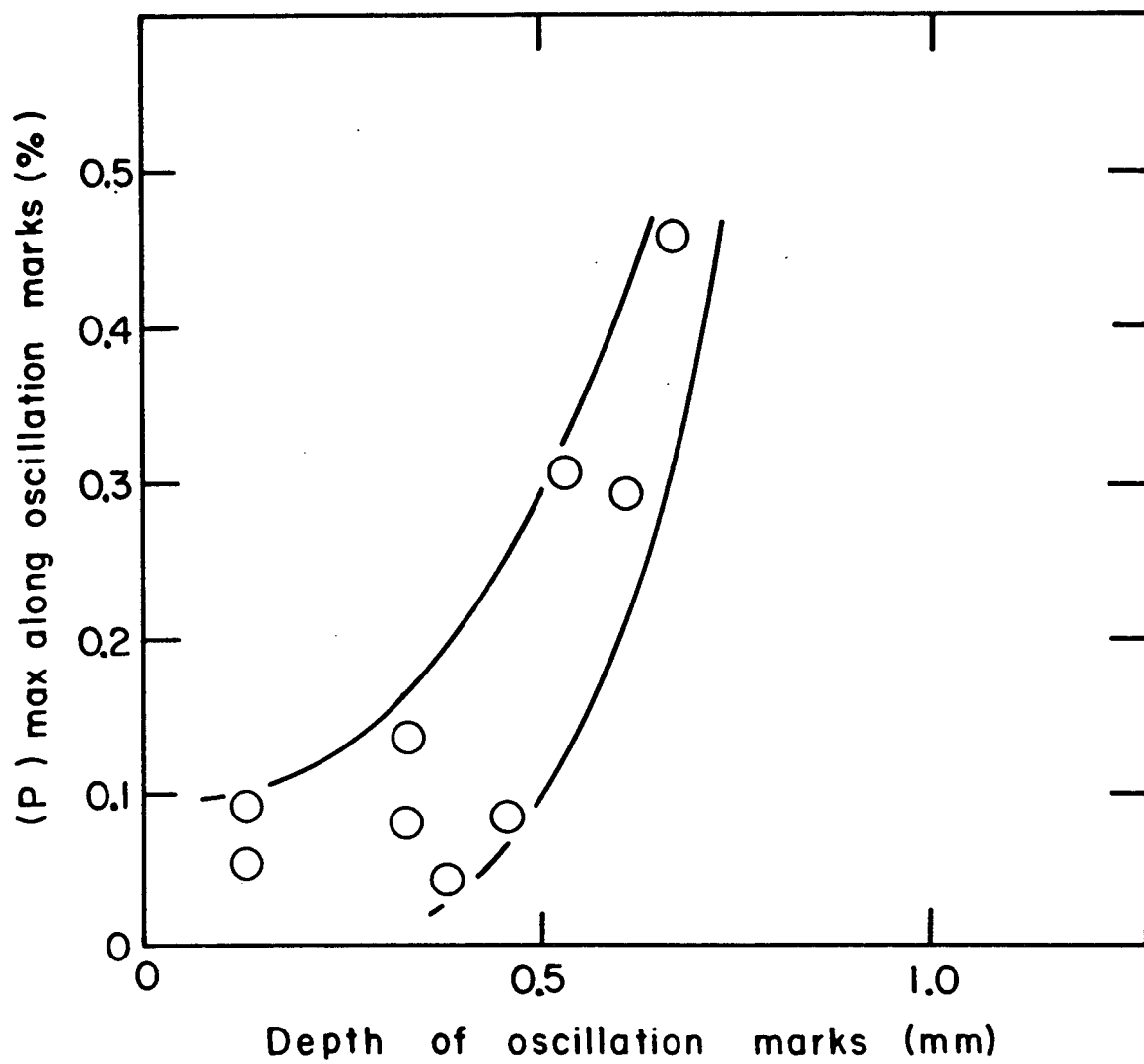


Fig. 2-22 Relationship between the maximum content of P and the depth of oscillation marks.²⁹

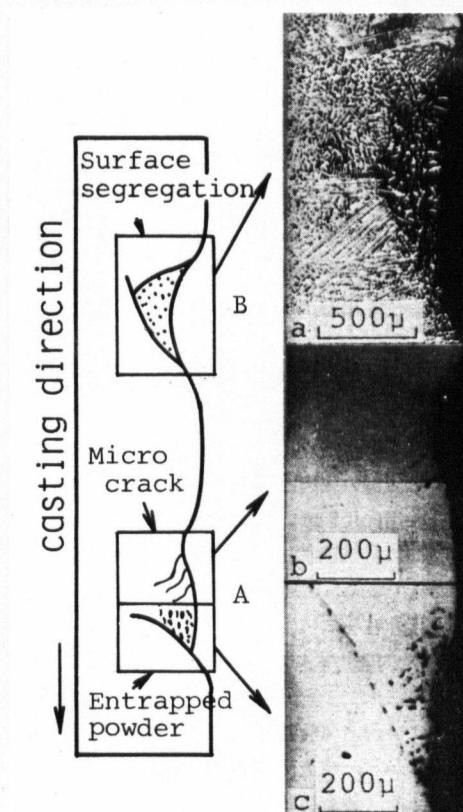


Fig. 2-24 Types of positive segregation of stainless steel slab.⁸⁶

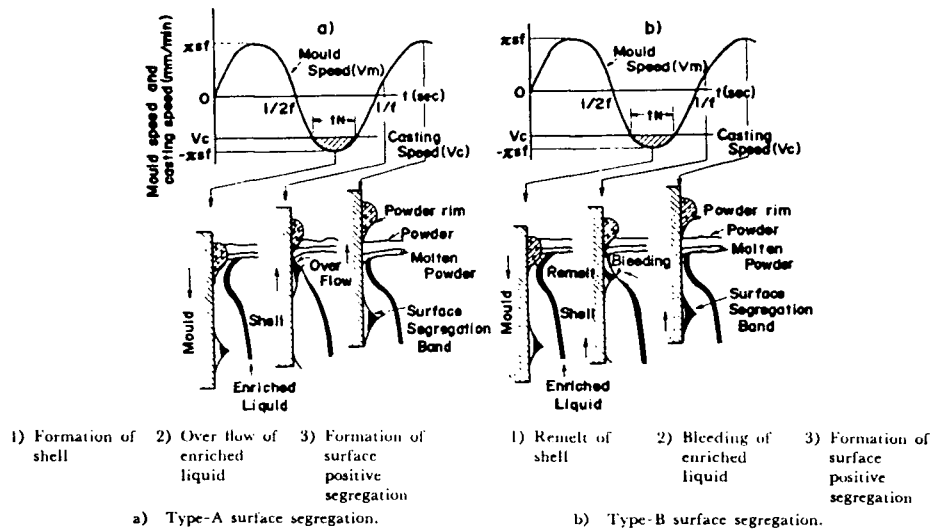


Fig. 2-25 Mechanism of positive segregation by H. Takeuchi et al.²⁷

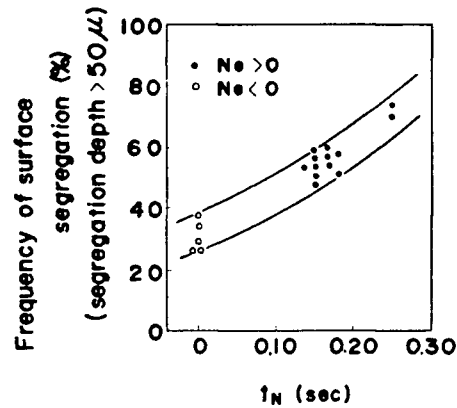


Fig. 2-26 Relation between frequency of positive segregation in stainless steel slabs and negative-strip time.^{8,6} (N_e : Negative-strip ratio)

3. SCOPE AND OBJECTIVES OF THE PRESENT WORK

3.1 Scope Of The Present Work

The present work has been undertaken to shed light on the initial solidification phenomena in the continuous casting mould, through the study of the formation of oscillation marks. An attempt is made to overcome some of the deficiencies of earlier investigations and to establish a stronger theoretical foundation for the formation of oscillation marks than hitherto has been reported. The approach taken has been to examine oscillation marks metallographically from a large number of slab samples and thereby to observe, at first hand, the geometry of the marks, the adjacent surface structure and the influence of casting variables on the metallographic aspects of oscillation marks. Next a series of theoretical analyses have been undertaken to examine three of the phenomena that are important in the meniscus region.

- i) heat flow involving steel, mould flux, and the mould wall
- ii) flow of molten mould flux into the gap between the steel and the mould wall, and the generation of pressure gradients in the flux due to mould oscillation
- iii) deformation of the meniscus as a result of the pressure gradient in the adjacent mould flux.

This approach reveals the importance of previously unreported factors like the geometry of the flux channel near the meniscus, and the deformation of the meniscus shape by the oscillation-generated flux pressure. Finally the analysis of heat transfer and fluid flow are combined in an overall model of the meniscus that predicts trends that are in agreement with industrial findings. The results of each sub-study are first presented followed by a discussion of mechanism of oscillation mark formation and a presentation of the overall model predictions.

In the next stage of the work, additional studies have been made on the mechanism of transverse-crack formation and positive segregation, especially in relation to oscillation marks. Firstly both defects have been studied metallographically which included an investigation of the etched subsurface structure and of the surface of the transverse cracks by SEM. Also the types of segregation have been classified with the aid of several etching methods; and the extent of positive segregation has been determined by CMA (Computer aided Micro Analyzer). Secondly a two-dimensional heat transfer model which accounts for the shape of the oscillation marks has been developed to explain the metallurgical relationships of both defects to the oscillation marks. Particularly regarding positive segregation, a mechanism has been proposed based on the mechanism of oscillation mark formation in this study. Finally a theoretical discussion is presented which explains how decreasing the depth of oscillation marks contributes to reducing the surface defects.

3.2 The Objectives Of The Present Work

The objectives of the present work can be summarized as follows:

- I. To determine the important factors which affect the shape of oscillation marks by metallographic investigation of slab samples.
- II. To develop a theoretical model of the oscillation mark formation, which predicts the shape of the mark as a function of process variables. This involves,
 - (1) Calculation of the heat-flux profile using a two-dimensional heat-transfer model and inplant measurement of mould wall temperature.
 - (2) Development of a two-dimensional, unsteady-state heat-transfer model to estimate the temperature distribution in the steel and in the mould flux close to the meniscus.
 - (3) Development of a fluid-flow model to calculate the fluid pressure generated in the flux channel at the meniscus.
 - (4) Calculation of the change of the meniscus shape with mould oscillation to obtain insight into steel overflow at the meniscus and the formation of subsurface hooks adjacent to oscillation marks.
 - (5) Theoretical explanation of the effect of process factors which have been already reported and also

found in metallographic investigation in the present work.

- III. To determine the effect of oscillation marks on the morphology of transverse cracks and positive segregation, by metallographic investigations of slab samples.
- IV. To explain theoretically the formation of positive segregation based on the mechanism of oscillation mark formation proposed in this investigation.
- V. To develop a two-dimensional heat transfer model, which incorporates the shape of oscillation marks, to explain the temperature history in each part of oscillation marks, and consequently nonuniformity of shell growth in the mould.

4. FORMATION OF OSCILLATION MARKS

4.1 Metallurgical Investigation

4.1.1 Casting Conditions Of Slab Samples

The metallographic study of oscillation marks has been made mainly on the slab samples from Company A. The casting conditions and composition of slab samples of Company A are presented in Table II. Note that the carbon content of the steel ranges from 0.08 to 0.26% and that the steel has either been Si-killed or Al-killed. The same type of mould flux was used for all the heats, and metal-level control was implemented.

In addition slab samples from Company B to E were examined to determine the effect of different casting conditions on the subsurface structure of oscillation marks. The casting conditions of slab samples from these companies are presented in Table III to VI. The characteristics of the casting conditions of these companies are as follows:

Company B: high nitrogen content in the steel,

Company C: large extent of meniscus level variation,

Company D: multi-port practice and ordinary bifurcated immersion nozzle, see Fig. 4-1,

Company E: electromagnetic stirring in the mould, see Fig. 4-2.

4.1.2 Investigation Procedure

Samples for the present study were cut out from the narrow face of the slabs because, unlike the broad face, it is not deformed by the support rolls in the casting machine. The surface of the slab samples was sand-blasted to remove the oxide film before examination. Firstly the pitch of the oscillation marks was measured at the center and the corner of the as-cut samples. Then the steel samples were cut longitudinally perpendicular to the oscillation marks to reveal the profile of the slab surface and the subsurface structure. The longitudinal sections so obtained were machined flat, polished and etched with either picric acid or nital. The subsurface structure was examined and photographed using a standard optical microscope. The depth of oscillation marks was measured from the base of the mark to the level of a rule resting on the slab surface.

4.1.3 Appearance And Pitch Of Oscillation Marks

The narrow face of a typical slab, exhibiting oscillation marks, is shown in Fig. 4-3 (Company A). The marks are seen to be evenly spaced and closely parallel across the face.

Fig. 4-4 shows the pitch of oscillation marks measured over 20 cm in the casting direction, plotted against casting speed. There is not much difference in the pitch between center and corner. The average value of the pitch of the oscillation marks is about 16mm which corresponds closely to that calculated from Eq. (2-5), as expected. The value was not observed to increase

with the casting speed because mould frequency was linked to the casting speed. However, the variation in the measured pitch, expressed as a standard deviation, was found to increase from 0.7 to 5.2 mm with increasing casting speed from 0.89 to 1.25 m/min. The results were the same for the center and corner of the slab face. Presumably the increased variability of pitch is caused by sudden small changes in meniscus level due to flow variation and turbulence, that are more difficult to control at the higher casting speeds, even though the meniscus level controller was in use.

On the surface of slab samples from Company B, numerous severe transverse cracks were observed along the oscillation marks. The cracks are related to the high content of nitrogen in the steel slabs. The results of the investigation will be presented in the following chapter.

Slabs from Company C exhibit irregular oscillation marks as shown in Fig. 4-5. This is caused by large variation in meniscus level due to steel flowing turbulently from the upward inclined ports of the immersion nozzle. The measured pitch of the oscillation marks is smaller than that calculated from Eq. (2-5) possibly because surface waves generated by the metal stream impinging close to the meniscus, disrupted the phenomena resulting from mould oscillation, eg. overflow at the meniscus.

The casting conditions of Company D are characterized by a low-frequency mould oscillation, see Fig. 4-6, which gives rise to oscillation marks having a long pitch. In this case

indistinct marks were found between the regular oscillation marks as shown in Fig. 4-7. The depth of these marks is much less than that of the regular oscillation marks. When a bifurcated nozzle is employed the oscillation marks are straight and distinctive, Fig. 4-7(a). On the other hand, they are relatively disordered, and do not appear as straight lines on the slab surface when a multi-port nozzle is used, Fig. 4-7(b). The indistinct marks between regular oscillation marks show the same tendency. In the case of the multi-port practice these disordered marks are caused by the upward directed stream of steel which disturbs the meniscus.

Fig. 4-8(a) and (b) show the surfaces of slabs which have been produced at Company E with and without electromagagnetic stirring in the mould respectively. It is clearly observed that the depth of the oscillation marks was reduced by the electromagetic stirring which produced a liquid flow velocity of about 0.8m/s.

4.1.4 Subsurface Structure Of Oscillation Marks

Oscillation marks were found with and without hooks in the adjacent subsurface structure, as reported by Emi et al.⁹ although the majority exhibit hooks. A study of slab samples from Company A revealed an effect of the carbon content of the steel on the subsurface structure. Typical subsurface structures associated with the two types of oscillation marks in low-carbon (0.08-0.09%) and medium-carbon (0.26%) slabs are

shown in Figs. 4-9 and 10. It is seen that oscillation marks accompanied by hooks in 0.09%C slabs, Fig. 4-9(a), are deeper and the trough associated with each mark is longer than those in the 0.26%C slabs, Fig. 4-9(b). This difference is not found in the case of oscillation marks without hooks, Fig. 4-10. Moreover, hooks in the subsurface of 0.09%C slabs form a smaller angle with the surface than in the 0.26%C slabs. The dendrite orientation adjacent to the oscillation marks is similar to that described by Emi et al.⁹, viz. that dendrites initially grow normal either to the hooks when they are present or to the curved surface of the oscillation mark when the hooks are absent. In either case, the dendrites then change orientation within a short distance to become roughly perpendicular to the mould wall. Fig. 4-11 shows the change of the dendrite arm spacing about 1mm from the slab surface along the casting direction in a 0.09%-carbon slab. Although there is scatter in the measured values, the secondary dendrite arm spacings are smaller near the top of the mark than near the bottom. This indicates that the solidification rate is greater at the top than at the bottom of the oscillation marks. Slab samples free of subsurface hooks characteristically also contained small spherical blowholes, that are likely trapped argon gas that was injected through the submerged nozzle.

Fig. 4-12(a) shows the subsurface structure of a slab sample from Company B. A non-metallic substance was found at the end of the subsurface as indicated by the arrow. Enhanced magnification of the substance shown in Fig. 4-12(b), suggests

that it is an oxide and x-ray analysis using the SEM clearly indicates it is entrapped mould flux because Na and K present in the mould powder were detected, see Fig. 4-13. These results suggest that the outside of the hook once had been covered by mould flux, a part of which was trapped by overflowing steel.

Slab samples from Company C are characterized by irregular oscillation marks on the slab surface. The subsurface structure adjacent to these marks does not exhibit the presence of hooks, see Fig. 4-14.

Figures 4-15(a) and (b) show the subsurface structure in slab samples from Company D, produced with the conventional bifurcated immersion nozzle and with the multi-port practice respectively. Long subsurface hooks can be seen in the slab sample cast with the bifurcated immersion nozzle (25 degree downward), Fig. 4-15(a), as compared with the sample from the slab produced using the multiport nozzle with the ports angled 15° upward, Fig. 4-15(b). Such long hooks are undesirable because they may entrap inclusions rising in the mould pool and thereby reduce the surface quality of the slabs. The difference in the nature of the hooks with the two types of nozzles is most likely caused by dissimilar flow patterns and differences in the convection of superheat to the newly solidifying shell at the meniscus. In the case of the bifurcated nozzle with downward angled ports, convection at the meniscus should be relatively mild so that solidification of the meniscus is favoured. On the other hand, the multiport nozzle with its six upward flowing

metal streams creates greater turbulent convection at the meniscus and the extent of initial solidification is reduced.

As mentioned in the previous section, overflow marks are observed between successive oscillation marks. The subsurface structure of these marks does not exhibit any hooks which suggests that these marks are different from the oscillation marks.

Slab samples from Company E were produced with an in-mould electromagnetic stirrer (EMS). The subsurface structure of samples without and with mould EMS are presented in Figs. 4-16(a) and (b) respectively. The type of steel cast is a pseudo-rimmed steel which contains only a trace of Al. Because of the high oxygen content of the steel, CO blowholes, that are clearly distinguished from the Ar blowholes, were formed commencing just beneath the surface of slabs cast without mould EMS, Fig. 4-16(a). However CO blowholes are suppressed in the subsurface layer when mould EMS is employed, Fig. 4-16(b). It is also observed that the hooks become shorter, and consequently the depth of oscillation marks is reduced with mould EMS.

4.1.5 Depth Of Oscillation Marks

Slab samples from Company A first were examined for the shape of oscillation marks, which had been produced under nearly identical casting conditions with respect to the casting speed, mould oscillation, and mould flux. Figs. 4-17 and 4-18 show the depth plotted against the pitch of the oscillation marks

measured in the 0.08 and 0.26%-carbon slabs respectively. The depth of oscillation marks and its dependence on the pitch is the same for marks with and without hooks in the low-carbon slabs, Fig. 4-17, and for marks without hooks in the higher carbon slab, Fig. 4-18. The depth of oscillation marks increases with increasing pitch and the deviation of the pitch when subsurface hooks are absent is larger than that when hooks are present. As mentioned before, such variations of pitch indicate rapid changes in the meniscus level. Therefore it can be deduced that the subsurface structure is more likely to exhibit hooks when the meniscus level is stable than when it changes rapidly. The depth of oscillation marks with and without hooks is similar in the lower carbon steel slab ($C=0.08\%$), while in the higher carbon steel slab ($C=0.26\%$), the depth is greater when hooks are absent.

The effect of carbon content of the slabs on the depth of oscillation marks is shown in Fig. 4-19. Some scatter in the data, which chiefly depends on the meniscus level variation, is evident but nonetheless the depth of the oscillation marks exhibiting subsurface hooks is seen to be dependent on carbon content. Of the five steel grades studied, the deepest oscillation marks are found in 0.09% carbon slabs and these also exhibit the greatest scatter. In contrast, the depth of oscillation marks without subsurface hooks has no apparent dependence on carbon content over the range studied. The reason for this behaviour is discussed later.

Further investigation was made into the shape of oscillation marks on slab samples, which have the same carbon content but are deoxidized differently viz. Al- or Si- killed. The results are shown in Fig. 4-20. Thus the same tendency is observed between the depth and pitch of oscillation marks for the Al-killed and Si-killed steels. However the actual depth and the dependence of depth on pitch for the Al-killed steel is greater than that for the Si-killed steel. This finding may be due to the increased viscosity of mould flux during the casting of Al-killed steel caused by absorption of alumina inclusions.^{14 62 89} The more viscous flux gives rise to deeper oscillation marks.

Next slab samples from Company C were examined to find the relation between the depth of the oscillation marks and mould oscillation parameters. The effect of oscillation stroke on the mark depth is shown in Fig. 4-21. Although meniscus level variation leads to broad scatter in the depth of the oscillation marks, as expected, a greater oscillation stroke, viz. longer negative strip time, gives rise to deeper oscillation marks.

Finally the effect of electromagnetically driven flow at the meniscus on the depth of oscillation marks was determined from the slab samples cast at Company E. The mark depth decreases with increasing flow-velocity of steel, as shown in Fig. 4-22. A decrease in the variation of the mark depth is also achieved apparently by applying mould EMS.

4.2 Heat Flow Analysis Of The Meniscus Region

The temperature distribution in the three phases at the meniscus - steel, mould flux, and mould wall - has been studied mathematically to shed light on viscosity variation in the mould flux close to the meniscus due to heat flow, and the extent to which the meniscus may solidify. These phenomena figure importantly in the formation of the oscillation marks, as previous investigations^{9 26 32-34 36} have pointed out. Some of the shortcomings of earlier predictions of heat flow^{32 38} have been overcome by characterizing the axial mould heat-extraction profile in the meniscus region from measured mould temperatures, using a two-dimensional model of the mould wall which accounts for vertical as well as through-thickness heat conduction. Moreover, the mathematical model of heat conduction in the mould flux and steel is also fully two dimensional.

4.2.1 Axial Profile Of Mould Heat Flux At The Meniscus

The mould heat-flux profile has been calculated from the mould temperatures measured by Nakato et al¹⁸ during the casting of slabs for heavy plate. Their values of mould temperature close to the meniscus are shown as closed circles on the left hand side of Fig. 4-24. The mould heat-flux profile was determined using the mathematical model of the mould wall reported by Samarasekera and Brimacombe.⁴⁶ The two-dimensional model is based on assumptions of steady-state heat conduction and negligible oscillation effects. Fig. 4-23 shows the longitudinal mid-plane of the slab mould considered in the

computation. The governing equation for heat conduction in the mould wall can be described as follows:

$$\frac{\partial^2 T_M}{\partial x^2} + \frac{\partial^2 T_M}{\partial y^2} = 0 \quad (4-1)$$

The mould wall is sufficiently thick, so that nonuniformity of temperature distribution in the transverse (z) direction can be assumed negligible. Assuming that the cooling water is in plug flow, heat transfer in the water channel can be expressed by the following:

$$\rho_w v_w d_w C_{pw} \frac{\partial T_w}{\partial x} - h_w(x) \{T_M(x,0) - T_w(x)\} = 0 \quad (4-2)$$

Eqs (4-1) and (4-2) can be solved numerically to determine both the temperature distribution in the mould wall and the heat flux across the mould wall. The boundary conditions of the system are as follows:

$$(i) \ x=0, \ 0 \leq y \leq y_M ; \ - \lambda_M \frac{\partial T_M}{\partial x} = 0 \quad (4-3)$$

$$(ii) \ x=x_M, \ 0 \leq y \leq y_M ; \ - \lambda_M \frac{\partial T_M}{\partial x} = 0 \quad (4-4)$$

$$(iii) \ y=0, \ 0 \leq x \leq x_M ; \ - \lambda_M \frac{\partial T_M}{\partial y} = h_w (T_w - T_o) \quad (4-5)$$

$$(iv) \ y=y_M, \ 0 \leq x \leq x_M ; \ - \lambda_M \frac{\partial T_M}{\partial y} = q_o(x) \quad (4-6)$$

$$(v) \ x=x_M ; \ T_w = T_{wi} \quad (4-7)$$

$$(vi) \ x=0 ; \ T_w = T_{wf} \quad (4-8)$$

Another assumption, on which the model is based, is that radiation is neglected in the mould flux. The heat-transfer coefficient between water and mould wall is expressed by the following empirical equation;⁹

$$h_w = 0.23 \frac{\lambda_w}{D_H} \left(\frac{\rho_w v_w D_H}{\mu_w} \right)^{0.8} \left(\frac{C_{pw} \mu_w}{\lambda_w} \right)^{0.4} \quad (4-9)$$

An assumed heat flux profile, which defines the boundary conditions at the hot face of the mould, viz $q_0(x)$, was input to the model and the two-dimensional temperature distribution was calculated, then compared to the local values measured by Nakato et al.¹⁸ The heat-flux profile next was adjusted to obtain a better fit and the process was repeated until predicted and measured temperature were in close agreement. Data used in this calculation are presented in Table VII. The results of the temperature fitting and the heat flux profile determined are shown in Fig. 4-24. The heat flux is seen to have a maximum value of 2500kW/m² at 5mm below the meniscus, while in the mould flux region, it is 700 kW/m². It is also interesting that the maximum mould temperature is located at about 35mm below the meniscus which is 30mm below the level of peak heat flux. This difference results from the significant vertical heat conduction in the meniscus region. These data are used for the boundary conditions in the following computation.

4.2.2 Temperature Distribution In The Mould Flux And Steel

To predict the temperature distribution in the meniscus area, an approach similar to that of Tomono et al.³² and Saucedo et al.³⁸ has been adopted in which, due to the influence of mould oscillation on local fluid flow, temperature gradients in the mould flux and steel are assumed to be destroyed periodically. This event is followed by an interval in which heat is conducted in unsteady state through the phases. The concept is analogous to the "surface renewal" theory proposed for mass-transfer systems by Higbie^{91 92} many years ago. During the unsteady-state period, the phases are assumed to be stagnant which includes neglecting the downward motion of steel. In this calculation this period is assumed to commence at the end of the negative-strip time interval of the mould oscillation cycle because "overflow" at the meniscus, which acts to destroy local temperature gradients, occurs at this time as described previously.^{9 36} Thus the time for unsteady-state heat conduction is taken to be the positive-strip period of the mould oscillation cycle given by Eq. (2-4). Typical positive-strip times are in the range of 0.2 to 0.7s.

Fig. 4-25 shows the geometry of the system considered in the calculations. The shape of the meniscus has been calculated from equilibrium considerations; meniscus shape will be discussed later. A simplified equation has been adopted for the heat flow calculation.

$$x - x_1 = (x_2 - x_1) \sqrt{y - y_1} \quad (4-10)$$

The equations governing heat conduction in the steel and mould flux are respectively,

$$\frac{\partial T_s}{\partial t} = \frac{\lambda_s}{\rho_s C_{ps}} \left(\frac{\partial^2 T_s}{\partial x^2} + \frac{\partial^2 T_s}{\partial y^2} \right) \quad (4-11)$$

$$\frac{\partial T_f}{\partial t} = \frac{\lambda_f}{\rho_f C_{pf}} \left(\frac{\partial^2 T_f}{\partial x^2} + \frac{\partial^2 T_f}{\partial y^2} \right) \quad (4-12)$$

The initial conditions are;

$$(i) \quad t=0, \quad x \geq x_1, \quad x \geq x_2, \quad y \geq 0 ; \quad T_s = T_{si} \quad (4-13)$$

$$(ii) \quad t=0, \quad 0 \leq x \leq x_1, \quad x_2, \quad y \geq 0 ; \quad T_f = T_{fi} \quad (4-14)$$

and the boundary conditions are;

$$(iii) \quad t \geq 0, \quad x_2 \leq x \leq x_3, \quad y = 0 ; \quad -\lambda_s \frac{\partial T_s}{\partial y} = q_o(x) \quad (4-15)$$

$$(iv) \quad t \geq 0, \quad (x_2, 0) \rightarrow (x_1, y_1) ;$$

$$-\lambda_s \frac{\partial T_s}{\partial r} = -\lambda_f \frac{\partial T_f}{\partial r} = h_{s-f} (T_s - T_f) \quad (4-16)$$

$$y_1 < y \leq y_2, \quad x = x_1 ;$$

$$-\lambda_s \frac{\partial T_s}{\partial x} = -\lambda_f \frac{\partial T_f}{\partial x} = h_{s-f} (T_s - T_f) \quad (4-17)$$

$$(v) \quad t \geq 0, \quad x = x_3, \quad 0 \leq y \leq y_2 ; \quad -\lambda_s \frac{\partial T_s}{\partial x} = 0 \quad (4-18)$$

$$(vi) \quad t \geq 0, \quad x_1 \leq x \leq x_3, \quad y = y_2 ; \quad T_s = T_{si} \quad (4-19)$$

$$(vii) \quad t \geq 0, \quad 0 \leq x \leq x_2, \quad y = 0 ; \quad -\lambda_f \frac{\partial T_f}{\partial y} = q_o(x) \quad (4-20)$$

$q_o(x)$ changes from $q_o(x_1)$ to $q_o(x_2)$ in inverse proportion to the

distance between mould wall and meniscus;

$$(viii) \quad t \geq 0, \quad x_1 \leq x \leq x_2, \quad y = 0 ;$$

$$-\lambda_f \frac{\partial T_f}{\partial y} = \frac{q_o(x_2) q_o(x_1) (x_2 - x_1)^2}{\{x_2 \sqrt{q_o(x_2)} + x_1 \sqrt{q_o(x_1)} - x(\sqrt{q_o(x_2)} - \sqrt{q_o(x_1)})\}^2} \quad (4-21)$$

$$(ix) \quad t \geq 0, \quad x = 0, \quad 0 \leq y \leq y_2 ; \quad -\lambda_f \frac{\partial T_f}{\partial x} = 0 \quad (4-22)$$

$$(x) \quad t \geq 0, \quad 0 \leq x \leq x_1, \quad y = y_1 ; \quad T_f = T_{fi} \quad (4-23)$$

Equations (4-11) and (4-12) were solved, subject to the initial and boundary conditions, using the explicit finite-difference method.⁹³ Triangular volume elements have been employed to simulate the curvature of the mould flux/steel meniscus, especially close to the mould wall; the type of nodes required for the calculation are shown in Fig. 4-25. Nodal equations for each type of node are given in Appendix II. The release of the latent heat of solidification has been incorporated by adjusting the specific heat between the solidus and the liquidus temperature.

$$C_{pE} = C_p + \frac{L}{T_{liq} - T_{sol}} \quad (4-24)$$

Computations have been performed for a plate-grade steel using the heat-flux profile presented in Fig. 4-22, which was calculated from the mould wall temperature measured during the casting of the same type of steel. Fig. 4-26 shows the simplified flow diagram of the computer program that is presented in Appendix V. The composition of the steel and data

employed in the computation are given in Table VIII. Note that the initial temperature of the mould flux was assumed to be 1500°C from the reported data which are shown in Fig. 2-4.

Computed results are shown in Figs. 4-27 - 4-34, expressed as isotherms in the mould flux and fraction solidified, f_s , in the steel. The fraction solid is calculated from the lever rule, assuming that the solidus and liquidus lines are straight over the temperature range of interest.

$$f_s = \frac{T_{liq} - T_{i,j}}{T_{liq} - T_{sol}} \quad (4-25)$$

Figures 4-27 and 4-28 show the predicted temperature distribution when the superheat of steel is taken to be 5°C in the vicinity of the meniscus, after a period of 0.3s and 0.6s respectively. Thus the solidifying shell is predicted to be only partially solid with $f_s=0.6$ located at about 0.1mm from the mould wall and $f_s=0.2$ situated at about 0.6-0.7mm. These positions are similar to those reported by Saucedo et al.³⁸ although they also predicted solidification farther along the meniscus. That the region of $f_s=1$ is negligibly small does not mean that the semi-solid shell has no rigidity. Saucedo et al.³⁸ have suggested that the shell may exhibit rigidity if f_s is as low as 0.2 whereas Matsumiya et al.⁹⁴ have used a value of 0.85 for a rigidity criterion. The critical f remains unknown but it is possible that the shell formed in 0.3 or 0.4s could act as a solid. This suggests that the overflow mechanism that gives rise to subsurface hooks is plausible; but because the extent of the predicted meniscus solidification is considerably less than

the depth of the observed hooks, 1.5 to 2.0 mm in Fig. 4-9, it does not, by itself, adequately account for the formation of oscillation marks.

The effect of the superheat of the steel on the meniscus solidification also has been examined. Steel necessarily has a certain degree of superheat in the tundish, which is generally controlled to within 20-30°C, depending on the casting conditions. Higher superheats are avoided because the internal quality of the slab is affected deleteriously, viz reduction of equiaxed zone. This superheat is reduced during passage of the steel through the immersion nozzle; and also in the meniscus area further reduction of steel temperature can be expected. If the steel temperature decreases below the liquidus at the meniscus, the surface of the mould pool near the mould wall begins to solidify. From these considerations the superheat at the meniscus has been estimated to be 5°C for normal casting conditions.

Figs. 4-29 - 4-32 show the temperature distribution at the meniscus when the superheat is 0°C and 20°C, after a period of 0.3s and 0.6s. In the case of no superheat, Figs. 4-29 and 4-30, the hook may grow relatively longer. In the subsurface structure of Company D, long hooks were observed, see Fig. 4-15(a). Taking into account that the measured steel temperature at the meniscus in the casting of this sample is close to the liquidus temperature of steel, see Table IV, the long hooks are undoubtedly due to meniscus solidification. As shown in Figs.

4-31 and 4-32 high superheat reduces the length of the hook.

These calculations have been performed assuming that the molten steel is stagnant which effectively minimizes the extraction of superheat and maximizes the growth of the solid shell. However convection in the molten steel is generated at the meniscus by electromagnetically stirring, by the input streams discharging from the immersion nozzle and/or by inert gas that is injected into the immersion nozzle and entrained by the flowing steel. These effects have been modelled crudely by increasing the thermal conductivity of the stagnant steel by a factor of four. The calculation of the temperature distribution in the meniscus region has been repeated and the results are shown in Figs. 4-33 and 4-34, when the superheat of steel is 5°C . The fraction solid predicted is seen to be diminished significantly, more than that in the case of high superheat as shown in Figs. 4-31 and 4-32. Thus strong convection will cause the shell to behave more like a liquid than a solid. Under these conditions flow of molten steel over a partially solidified rigid meniscus will not take place, and subsurface hooks will not form. As mentioned previously, the length of hooks is significantly decreased by mould EMS (Company E) or by multi-port practice (Company D); rapid variation of the meniscus level, which causes steel flow in the meniscus region, brings about oscillation marks without hooks (Company A).

Thus from these calculations, it can be argued that the presence or absence of subsurface hook depends on the local extraction of superheat at the meniscus which is governed by the magnitude of superheat and the convection in the molten steel. This argument will be taken up later.

Another important aspect of the predictions shown in Figs. 4-27 - 4-34 is the low temperature zone of the mould flux adjacent to the mould wall. Since the viscosity of typical mould fluxes increases sharply with temperature below 1000-1200°C,¹⁴ a very thin zone of high viscosity flux must exist against the mould wall. As shall be seen, this high viscosity flux plays an important role in the formation of oscillation marks.

4.3 Fluid Pressure In The Mould Flux At The Meniscus

It has already been seen that a simple overflow mechanism cannot explain the depth of the subsurface hooks; and therefore other factors must also play a role in the formation of oscillation marks. The most obvious is the mould flux and, in particular, its behaviour as it flows, under the influence of mould oscillation and strand withdrawal, into the gap between the solidified shell at the meniscus and the mould wall. Previously the action of the mould flux, specifically its lubricity, has been characterized in terms of the shear stress¹⁴ ⁶⁹ that acts on the strand. While this may be important for overall mould lubrication, it will be shown here that the shear

stress is not very significant at the meniscus as compared to the pressure generated in the mould flux by mould oscillation. This pressure, which has not been considered previously, arises because the flux channel narrows in width as the meniscus curves toward the mould wall, as shown schematically in Fig. 4-35. In this part of the study, the flux pressure has been estimated roughly from fluid flow principles originally applied to lubrication problems by Reynolds and others.⁹⁶

The following assumptions have been made to predict the pressure and velocity distribution in the flux channel:

- [i] Steady state is assumed which is equivalent to saying that the pressure and velocity gradient are instantaneously established;
- [ii] Inertial forces are neglected because fluid velocities are low and the flux velocity is high;
- [iii] The flux behaves as a Newtonian fluid;
- [iv] The meniscus in the region of interest is covered with a rigid "solid" skin; and the shape of the flux channel does not change significantly;
- [v] Flux velocities in the transverse direction (u_z) and normal to the mould wall (u_y) are negligible. u_y is negligible because the angle formed by the meniscus with the vertical is small;
- [vi] The density and viscosity of the mould flux are constant.

The latter assumption is, admittedly, very restrictive because the large temperature gradients across the flux channel will result in a correspondingly steep viscosity gradient. It would be preferable to couple the heat and fluid flows and solve simultaneously for the temperature, velocity and pressure distributions, but at this early stage in the development of the model, this added complexity is unwarranted. It does mean, however, that the flux pressures predicted are only very approximate relative to real values.

Under these assumed conditions, fluid flow in the flux channel is governed by the following equation of motion,

$$\frac{dp}{dx} = \mu_f \frac{\partial^2 u_x}{\partial y^2} + \rho_f g \quad (4-26)$$

and equation of continuity.

$$\frac{\partial Q_R}{\partial x} = \frac{d}{dx} \left(\int_0^h u_x dy \right) = 0 \quad (4-27)$$

where Q_R is a relative consumption rate of mould flux. It should be noted that, because the rigid meniscus skin is moving downward with the strand, u_x is a relative velocity expressed as

$$u_x = v_f - v_s \quad (4-28)$$

Where v_f and v_s are flux and strand velocity respectively, both of which are defined relative to a fixed reference frame. The boundary conditions, subject to which Eqs. (4-26) and (4-27) are solved, are

$$(i) \quad 0 \leq x \leq l_f, \quad y = 0, \quad u_x = v_m - v_s \quad (4-29)$$

$$(ii) \quad 0 \leq x \leq l_f, \quad y = h(x), \quad u_x = 0 \quad (4-30)$$

$$(iii) \quad x = 0, \quad 0 \leq y \leq h_i, \quad P = P_i \quad (4-31)$$

$$(iv) \quad x = l_f, \quad 0 \leq y \leq h_f, \quad P = P_f \quad (4-32)$$

Note that B.C. [i] and [ii] are a statement of the "no slip" condition which is correct provided that the rigid skin assumed to cover the meniscus in the flux channel, behaves as a solid.

The solution to Eqs. (4-26) and (4-27) is described briefly in the Appendix IV. For the case where the part of the meniscus under consideration is taken to be linear, and bounded by the coordinates $(0, h_i)$ and (l_f, h_f) , see Fig. 4-35, the pressure gradient in the mould flux is given by:

$$P(x) - P_i = \left\{ \rho_f g l_f + \frac{6\mu_f l_f (v_m - v_s)}{h h_i} \right\} \frac{h_i - h}{h_i - h_f} - \frac{h_i^2 - h^2}{h_i^2 - h_f^2} \left\{ \left(\frac{h_f}{h} \right)^2 (\rho_f g l_f + P_i - P_f) + \left(\frac{6\mu_f l_f}{h^2} \right) \left(\frac{h_f}{h_i} \right) (v_m - v_s) \right\} \quad (4-33)$$

and the velocity distribution is

$$u_x = (v_m - v_s) \left(1 - \frac{y}{h} \right) - \left\{ 3(v_m - v_s) - \frac{(\rho_f g l_f + P_i - P_f) h_i^2 h_f^2 + 6\mu_f l_f (v_m - v_s) h_i h_f}{\mu_f l_f h (h_i + h_f)} \right\} \left(\frac{y}{h} - \frac{y^2}{h^2} \right) \quad (4-34)$$

Fig. 4-36 shows the pressure distribution calculated from Eq.

(4-33) for different flux viscosities and for both upward and downward mould velocities. A mould oscillation frequency of 100 cpm, a stroke length of 8mm and a casting speed of 1.0 m/min have been assumed for the calculation. The length of the flux channel has been determined from the pitch of the oscillation marks while the value of the lower channel width, h_f , has been estimated from calculated values of the minimum thickness of mould flux based on measured flux consumption rates.⁹ In Fig. 4-36 the mould flux is seen to develop a positive pressure on the down stroke, and a negative pressure on the up stroke of the mould. A maximum in the flux pressure is predicted toward the bottom of the flux channel for both upward and downward mould velocities. As expected the magnitude of the peak pressure increases with increasing flux viscosity. Interestingly the maximum value of negative pressure on the upstroke is greater than that of the positive pressure on the downstroke, because on the upstroke the motion of the mould relative to the strand is greater. These positive and negative pressures are much larger than the local ferrostatic pressure.

Fig. 4-37 shows the velocity distribution in the flux channel, as calculated from Eq. (4-34), at the maximum downward velocity of the mould. The conditions assumed are the same as applied in the pressure calculations; and the flux viscosity is 5P. As expected, a downward velocity is predicted near the mould wall, and a flow reversal is seen near the steel in the upper region of the flux channel.

The shear stress acting on the meniscus (assumed to have a rigid solidified skin) has been calculated from the velocity distribution in Fig. 4-37, as follows

$$\tau = -\mu_f \left(\frac{\partial u}{\partial y} \right)_{y=h} \quad (4-35)$$

The calculated shear stresses are shown in Fig. 4-38. This shear stress in the flux layer, between mould wall and the shell, has been discussed as an index for the surface quality of slabs.^{6,9} However the values obtained are an order of magnitude less than the pressure shown in Fig. 4-36; and therefore the shear stress will have only a minor effect on meniscus behaviour.

4.4 Meniscus Shape

4.4.1 Static Shape Of Meniscus

The shape of meniscus, especially in the vicinity of the mould wall, is important to understand the initial solidification phenomena in the continuous-casting mould. Thus a two-dimensional meniscus, as shown in Fig. 4-39, has been considered. The meniscus shape can be determined by a force balance at the interface between liquid steel and liquid mould flux. Especially in the case of a static meniscus, the meniscus shape depends on both the density of mould flux and molten steel, as well as the interfacial tension. An analytical

solution for this case was given by Matijevic⁹⁷ and Bikerman,⁹⁸ as follows; (see Appendix III for the derivation).

$$y = -\sqrt{2a^2 - x^2} + \frac{\sqrt{2a^2}}{2} \ln\left(\frac{\sqrt{2a^2} + \sqrt{2a^2 - x^2}}{x}\right) + 0.3768a \quad (4-36)$$

where a^2 , the capillary constant, is defined as

$$a^2 = \frac{2\sigma}{(\rho_s - \rho_f)g} \quad (4-37)$$

"a" gives the vertical distance between the horizontal meniscus level and the "contact" point of the meniscus with the mould wall. As mentioned before, little work has been done on the properties of mould flux. Therefore the properties of blast furnace slag, which has similar chemical components to that of mould flux, was substituted for the calculation of the meniscus shape.

4.4.2 Change Of The Meniscus Shape By Mould Oscillation

The shape of the meniscus depends on the pressure acting on the solidified skin and, more conventionally, on the balance of forces acting at the interface between the mould flux and molten steel. It is clear from the previous section that an important force that cannot be ignored is the fluid pressure generated in the mould flux channel. Thus, in this part of the study, a mathematical relationship has been developed to predict the meniscus shape resulting from the flux pressure developed at different stages of the mould oscillation cycle.

To simplify the calculations, the meniscus is assumed to be free of a rigid skin and to attain its equilibrium shape instantaneously. The equation governing the shape of the meniscus under the influence of fluid pressure, is also derived in the Appendix III, and is as follows:

$$\frac{dy}{dx} = - \frac{2\sigma(\rho_s - \rho_f)gx^2 - 4\sigma\{R(x) + \sigma\}}{[\rho_s - \rho_f]^2 g^2 x^4 - 4(\rho_s - \rho_f)\{R(x) + \sigma\}gx^2 + 4R(x)\{R(x) + 2\sigma\}]^{1/2}} \quad (4-38)$$

$$R(x) = \int_0^x \{P(x) - \rho_f gx\} dx \quad (4-39)$$

$P(x)$ is the axial pressure distribution in the mould flux calculated from Eqs. (4-26) and (4-27), assuming complete slip at the meniscus, i.e. at $y=h(x)$, $v_f=0$ and $y=0$, $v_f=v_M$. It may be noted that if $R(x)=0$, i.e. no dynamic pressure, Eq. (4-38) reduces to the analytical solution for a static meniscus, Eq. (4-36).

The "contact" point of the meniscus with the mould wall, x_c , as defined by $\phi=\pi/2$, was calculated from Eq. (A-3-11). Note that x_c corresponds to "a" when the fluid pressure of the mould flux is equal to zero.

$$x_c = \frac{2\sigma}{(\rho_s - \rho_f)g} \left(1 + \frac{R(x_c)}{\sigma} \right)^{0.5} \quad (4-40)$$

The meniscus shape was calculated at selected points in the mould oscillation cycle by the following iterative procedure:

- [i] $P(x)$ and $R(x)$ were computed initially assuming a quadratic relationship for the meniscus, Eq. (4-39)

approximated from Eq. (4-36).

[ii] To simplify the calculation, $R(x)$ was fitted to a quadratic equation, and the meniscus profile and contact point were computed from Eqs. (4-38) and (4-40) respectively.

[iii] The newly calculated meniscus profile was approximated by a new quadratic equation: $P(x)$ and $R(x)$ were recalculated; then the meniscus profile and contact point were recomputed.

[iv] The process was repeated until successive calculations of the meniscus shape differed negligibly.

In this way the generation of flux pressure, due to mould oscillation, and the meniscus shape have been coupled.

Figure 4-40 shows the meniscus profiles predicted at different times in a sinusoidal mould oscillation cycle having a frequency of 100 cpm and a stroke length of 8mm. The initial time corresponds to the mould being at the top of its stroke when $v_M=0$. At this time, there is no oscillation-generated pressure in the flux if the meniscus is completely liquid because v_s is effectively zero. Thus at $t=0$, the meniscus profile shown is that predicted from Eq. (4-36). At 0.15s the mould has reached its maximum downward velocity and the meniscus profile and "contact" point have been depressed by the positive pressure generated in the flux. At 0.3s, the mould has travelled to the bottom of its stroke when $V_M=0$, and oscillation-generated pressure in the flux has disappeared

leaving the meniscus again with an equilibrium shape predicted by Eq. (4-36). Beyond 0.3s, the mould moves upward, generating a negative pressure in the flux and drawing the meniscus and contact point also upward.

Figure 4-41 shows the movement of the contact point of the meniscus with the mould wall during the mould oscillation. It is seen that the contact point, which is responding to the mould velocity, moves out of phase with the mould displacement by $\pi/2$. Moreover the amplitude of the contact point movement is greater than that of the mould displacement; and after 0.3s the contact point rises above its initial level. Thus at this time, which corresponds to the end of the negative-strip period or just beyond it, the molten steel surges toward the mould wall; and if a thin rigid skin covers part of the meniscus, overflow may occur. This timing of the overflow of the steel is in agreement with the observations made using a "mould simulator" by Kawakami et al.³⁶

4.5 Mechanism Of Oscillation-Mark Formation

In order to facilitate the mathematical analysis of fluid flow and meniscus shape in the preceding sections, the meniscus has been assumed respectively to be covered partially with a rigid skin or to behave as a liquid. The heat-flow analysis has shown that both cases are possible depending on the superheat and local convection, Figs. 4-27 - 4-34. The presence of the meniscus skin and the generation of pressure in the flux channel

are the bases for the mechanism of oscillation mark formation.

Figs. 4-42 and 4-43 provide a schematic representation of the formation of the two types of oscillation marks, i.e. with and without adjacent subsurface hooks respectively. In both cases the meniscus responds to the mould oscillation and flux pressure in the same manner. As described earlier, during the negative-strip time (Stages 1-3), when the mould is moving downward more rapidly than the strand, the meniscus is pushed by the positive pressure generated in the mould flux, away from the mould wall. Then in the ensuing positive-strip period (Stages 4-7), the meniscus is drawn back toward the mould wall by the negative pressure. It is most unlikely that the partially solidified meniscus is drawn back uniformly, however, because the upper part of the meniscus skin is farthest from the cooling influence of the mould wall and therefore should be the hottest and weakest. As a result the upper part of the skin is expected to be drawn back more by the negative flux pressure and the inertial force of the surging liquid steel. The difference between the two types of oscillation marks then arises because of differences in the mechanical strength of the meniscus skin. In the case of oscillation marks with subsurface hooks, the skin is relatively strong, owing to a greater thickness (low superheat, stagnant liquid) and/or low carbon content. Thus the top of the skin resists being drawn back fully toward the mould wall, and liquid steel overflows it (Stage 4, Fig. 4-42) to form a subsurface hook. On the other hand, with oscillation marks having no subsurface hooks, the skin is weak and behaves

more like a liquid. Thus at the beginning of positive strip the top of the skin is easily pulled back with the liquid toward the mould so that overflow does not occur (Stage 4, Fig. 4-43).

This mechanism is consistent with results from the metallurgical study of oscillation marks reported in a previous section. Turning first to the subsurface hooks, they are significantly longer, Fig. 4-9, than was predicted by the heat-flow model, Fig. 4-27. This is explained by the fact that the meniscus skin is pushed toward the steel by the flux pressure, Fig. 4-42, before overflow occurs. The hooks in 0.09%-carbon slabs form a smaller angle with the surface than hooks in 0.26%-carbon slabs, Fig. 4-9, probably because the mechanical strength of the lower carbon meniscus skin is greater⁴¹ and more resistant to the flux pressures. Even then it is difficult to rationalize the presence of hooks in the 0.26%-carbon slabs that are nearly perpendicular to the slab surface, unless the combination of flux pressure and overflow can deform them to this extent. Slabs that do not exhibit subsurface hooks characteristically contained inert gas blowholes. This indicates that convection was created close to the meniscus by rising gas bubbles which, as shown in Fig. 4-33, reduce the thickness and strength of the meniscus skin so that it can be drawn back toward the mould wall without overflow at the beginning of positive strip.

Another finding is that the depth of oscillation marks with subsurface hooks is greater in 0.09%-carbon slabs than in slabs containing 0.26% carbon. Again this may be related to the greater strength expected for the lower carbon meniscus skin. At the beginning of the positive-strip time, when negative flux pressures are developing, the entire meniscus skin in the 0.26%-carbon slab may be sufficiently weak to be drawn back toward the mould wall. In contrast, the meniscus skin in the 0.1%-carbon slab may have sufficient strength to resist the negative flux pressure except near the top which bends partially back toward the mould before overflow occurs. That the depth of oscillation marks without subsurface hooks does not depend on the carbon content of the steel, Fig. 4-19, can be explained by a similar argument based on mechanical properties. In this case, owing to a high superheat or enhanced convection, the meniscus skin is sufficiently thin and weak that it does not develop the mechanical rigidity of a solid but behaves more like a liquid; thus it responds in the same manner to flux pressure irrespective of the carbon content of the steel.

The finding that the depth of oscillation marks with subsurface hooks in aluminum-killed steel is slightly greater than in silicon-killed steels may be due to an increase in mould flux viscosity as alumina, floating out of the steel, is absorbed by the flux. The increase in slag viscosity increases the pressure generated in the mould flux, Fig. 4-20, which in turn should increase the deformation of the meniscus during negative strip, and the depth of oscillation marks.

The electromagnetically driven flow decreases the depth of oscillation marks, Fig. 4-22. It was mentioned earlier that the steel convection suppresses meniscus solidification. Furthermore a temperature increase at the meniscus due to electromagnetic stirring was observed in this experiment^{8,8} as a result of mixing of steel in the mould. This should increase the temperature in the mould flux layer which in turn decreases the viscosity of mould flux and the flux pressure and thereby reduces the depth of oscillation marks.

4.6 Meniscus Model Predictions

The final stage in this study has been to combine the mathematical analyses of heat flow and flux pressure in a first-generation meniscus model and to calculate approximately the effect of the following variables on the oscillation mark formation: stroke length, oscillation frequency, negative strip time, mould flux viscosity and meniscus level variation. In the model, the heat flow analysis is applied first to predict the temperature of the mould flux adjacent to the mould wall during the positive-strip period of the oscillation cycle. The average temperature of the flux within $500\mu\text{m}$ of the mould wall, a typical depth of oscillation mark, and over a height at the meniscus equivalent to the oscillation stroke length then is calculated since this flux will enter the flux channel on the succeeding downstroke of the mould. The viscosity of the flux is computed from the empirical relationship¹⁶

$$\log \mu_f = 0.578 \times 10^4 \left(\frac{1}{T_f + 273} \right) - 2.979 \quad (4-41)$$

Next the fluid flow analysis is applied to predict the pressure generated in the mould flux, assuming that the length of the flux channel is equal to the pitch of oscillation marks and that the top and bottom width are 0.35 and 0.05 mm respectively. The top channel width of 0.35mm is in the range of the depth of oscillation marks, while the bottom width has been estimated from the minimum thickness of mould flux film calculated from mould flux consumption. The total flux pressure force, integrated over the channel length, has been computed at the maximum downward velocity of the mould; this has been used as a measure of the deformation of the partially solidified meniscus, and of the depth of oscillation marks.

Fig. 4-44 shows the effect of changing meniscus level, expressed in terms of the pitch of the oscillation marks, on the total force generated in two mould fluxes having different viscosities. A sudden rise in meniscus level lengthens the pitch of the oscillation marks and at the same time has the effect of raising the mould velocity. This relationship can be expressed by the following equation:

$$\Delta l = - \frac{\Delta v}{f} \quad (4-42)$$

Thus as the pitch of the oscillation marks increases, the total force acting on the partially solidified meniscus increases and the depth of oscillation marks also should increase. This effect has been seen in Figs. 4-17 and 4-18. This phenomenon

has been reported to be a problem when casting with high oscillation frequencies.^{6,1} Also in Fig. 4-44, raising the flux viscosity is predicted to increase the total pressure force, as was suggested earlier with respect to the casting of aluminum-vs silicon-killed steels.

Figure 4-45 shows the effect of oscillation stroke on the total flux pressure force for two oscillation frequencies. In both cases the total force increases almost linearly with increasing stroke length which is in reasonable agreement with the measured relationship, Fig. 4-21, and with the reported relationship by Emi et al.,⁹ Fig. 2-3. This influence is caused by the increased mould speed as the stroke length is increased at constant frequency.

Figure 4-46 shows the effect of oscillation frequency on the flux pressure force for several different stroke lengths. With longer strokes, raising the oscillation frequency markedly reduces the total pressure force; but when short oscillation strokes are employed, frequency has only a minor effect. The same tendency, with respect to the depth of the oscillation marks, has been reported by Kuwano et al.^{2,1} for the casting of stainless steel and by others^{8, 22} working with high oscillation frequencies. Varying the frequency affects the total pressure force by changing both the pitch of the oscillation marks and the mould velocity. At low frequencies, the high total pressure force results from the long pitch of the oscillation marks and the correspondingly long flux channel. However, because the

velocity of the mould is also low, a low total pressure force can be attained at high casting speeds, where $v_M - v_s$ is small, depending on the stroke length of the mould. Such an effect is shown in Fig. 4-47.

The negative-strip time, as defined by Eq. (2-3), has been calculated for all seventeen conditions indicated above; and its effect on the total pressure force generated in the flux channel, assuming a casting speed of 1.0 m/min, is shown in Fig. 4-48. A single correlation thus is found, in which with only minor variations, the total pressure force increases with negative-strip time. The same relationship, between oscillation mark depth and t_N , has been reported by McPherson et al.²⁴ Hashio et al.²³ and Mizoguchi et al.²⁴, see Fig. 2-5. Assuming that the fulcrum of bending deformation of the meniscus is at the outlet of the flux channel, the bending moment can be calculated as follows:

$$M_b = \int_{l_i}^{l_f} P(x)(x-l_f)dx \quad (4-43)$$

The relation between the negative strip time and the calculated bending moment is shown in Fig. 4-49, which shows a similar tendency to that in Fig. 4-48. However the total pressure force seems to be a more suitable index of the mark depth, because the rigidity of the initially solidified shell at the meniscus is not understood completely yet. Finally a series of plots of total pressure force vs negative-strip time has been calculated for different casting speeds and are shown in Fig. 4-50. The

solid lines reveal the effect of casting speed on the total pressure force. At low frequencies and with short strokes, the force decreases with increasing casting speed: but with higher frequencies and longer strokes it increases with casting speed. It should be noted that in this calculation the effect of the casting speed on the temperature distribution in the meniscus region was not taken into account, owing to a paucity of data. In general increasing casting speed increases the meniscus temperature which reduces the viscosity of mould flux. This tends to reduce the differences between the relationships for various casting speeds, shown in Fig. 4-50.

These predictions obviously have value only in revealing trends in the depth of oscillation marks as a function of oscillation variables. However the knowledge gained should be useful in the selection of mould conditions that minimize the depth of oscillation marks so that high surface quality can be achieved.

Table II - Casting Conditions and Chemical Composition of the Slab Samples from Company A

	C	Mn	Si	P	S	Al
Chemical	0.08	0.58	0.20	0.007	0.009	0.001
Composition	-0.26	-0.89	-0.24	-0.009	-0.019	-0.033

Temperature (in tundish): 1529 - 1549°C

Casting speed: 0.89 - 1.25 m/min

Immersion nozzle: bifurcated, 25° down

Casting

Mould size: 1829 - 1930mm x 178 - 203mm

Conditions

Mould oscillation: 12.7mm stroke,
40 - 90cpm frequency

Viscosity of mould flux: 5.45 poise at 1200°C

2.65 poise at 1300°C

Type of machine: Vertical type with unbending
(9mR)

Table III - Casting Conditions and Chemical Composition of the Slab Samples from Company B

	C	Mn	Si	P	S	Al	N
Chemical	0.07	0.25	0.03	0.006	0.012	0.042	0.0047
Composition	-0.10	-0.41	-0.06	-0.007	-0.016	-0.056	-0.0164

Casting Conditions	Temperature (in tundish): 1529 - 1549°C
	Casting speed: 1.37 - 1.57 m/min
	Immersion nozzle: bifurcated, 7.5° up
	Mould size: 985 - 1035mm x 180mm
	Mould oscillation: 11mm stroke, 95cpm frequency
	Viscosity of mould flux: not available
	(softening point 1065°C, melting point 1140°C)
Type of machine: Vertical type with unbending (9mR)	

Table IV - Casting Conditions and Chemical Composition of the Slab Samples from Company C

	C	Mn	Si	P	S	Al	N
Chemical	0.05	0.26	0.021	0.003	0.009	0.046	0.0050
Composition	-0.07	-0.33	-0.026	-0.005	-0.013	-0.063	-0.0080

Casting Conditions
 Temperature (in tundish): 1546 - 1555°C
 Casting speed: 0.85 - 0.91 m/min
 Immersion nozzle: bifurcated, 15° up
 Mould size: 1480 - 1880mm x 240mm
 Mould oscillation: 5.8 - 15mm stroke,
 60 - 95cpm frequency
 Viscosity of mould flux:
 type1/ 1.0 poise at 1250°C
 0.6 poise at 1300°C
 type2/ 4.9 poise at 1250°C
 2.9 poise at 1300°C
 Type of machine: Vertical type with unbending
 (10.5mR)

Table V - Casting Conditions and Chemical Composition of the Slab Samples from Company D

	C	Mn	Si	P	S	Al
Chemical Composition	0.043 -0.080	0.19 -1.05	0.013 -0.20	0.009 -0.015	0.011 -0.014	0.043 -0.070

Temperature (in tundish): 1541 - 1554°C
(in mould) : 1515 - 1523°C

Casting speed: 0.97 - 1.52 m/min

Immersion nozzle: 1) multi-port practice

2) bifurcated, 25° down

Casting

Mould size: 889 - 1346mm x 235mm

Conditions

Mould oscillation: 19.8mm stroke,
35 - 65cpm frequency

Viscosity of mould flux: 60 - 65 cp at 1300°C

Type of machine: Vertical type with unbending
(13mR)

* Schematic view of the immersion nozzle for the multi-port practice is in Fig. 4-1.

Table VI - Casting Conditions and Chemical Composition of the Slab Samples from Company E

	C	Mn	Si	P	S	Al
Chemical Composition	0.04	0.14	0.02	0.020	0.014	0.001
Casting Conditions	Temperature (in tundish): 1572°C					
	Casting speed: 0.70 m/min					
	Immersion nozzle: bifurcated, 45° down					
	Mould size: 1600mm x 250mm					
	Mould oscillation: 7.0mm stroke, 100cpm frequency					
	Viscosity of mould flux: not available					
	Type of machine: Vertical type with unbending (10.5mR)					
	Stirring force (flow velocity of steel) :0 - 1m/s					

* Schematic view of the electromagnetic stirrer in the mould is in Fig. 4-2

Table VII - Thermal Properties and Conditions for Calculation of Mould Heat Flux

Specific heat of water⁹⁹: 4.18 J/g°C
Viscosity of water⁹⁹: 0.83 x 10⁻²P
Density of water⁹⁹: 0.995 g/cm³
Thermal conductivity of water⁹⁹: 6.15 x 10⁻³W/cm°C
Water temperature at the inlet of water channel¹⁰⁰: 21°C
Water temperature at the outlet of water channel¹⁰⁰: 32°C
Flow velocity of water¹⁰⁰: 500cm/s
Hydraulic diameter of water channel¹⁰⁰: 1cm
Water channel gap width¹⁰⁰: 1.5cm

Thermal conductivity of mould wall¹⁸: 3.25 W/cm°C
Thickness of mould wall¹⁸: 4.8 cm
Length of mould wall¹⁸: 80 cm
Distance of mould flux surface from the mould top¹⁸: 8 cm
Distance of meniscus from the mould top¹⁸: 12 cm

Table VIII - Assumed Steel Composition and Thermophysical Properties for Calculations of Temperature Distribution at the Meniscus

	C	Mn	Si	P	S	Al
Chemical Composition (%)	0.16	0.80	0.15	0.02	0.02	0.05

Steel liquidus : 1517°C

Steel solidus : 1456°C

Steel superheat: 5°C

Steel specific heat: 0.67 J/g°C

Steel thermal conductivity¹⁸: 0.465 W/cm°C

Steel density: 7.2 g/cm

Initial flux temperature¹²: 1500°C

Flux specific heat: 1.26 J/g°C

Flux thermal conductivity¹⁸: 0.023 W/cm°C

Flux density¹⁸: 2.8g/cm³

Calculated from following equations:¹⁰¹

$$T_{\text{liq}} = 1536 - \{78[\%C] + 7.6[\%Si] + 4.9[\%Mn] + 34.4[\%P] + 38[\%S] + 4.7[\%Cu] + 3.1[\%Ni] + 1.3[\%Cr] + 3.6[\%Al]\}$$

$$T_{\text{sol}} = 1536 - \{415.5[\%C] + 12.3[\%Si] + 6.8[\%Mn] + 124.5[\%P] + 183.9[\%S] + 4.3[\%Ni] + 1.4[\%Cr] + 4.1[\%Al]\}$$

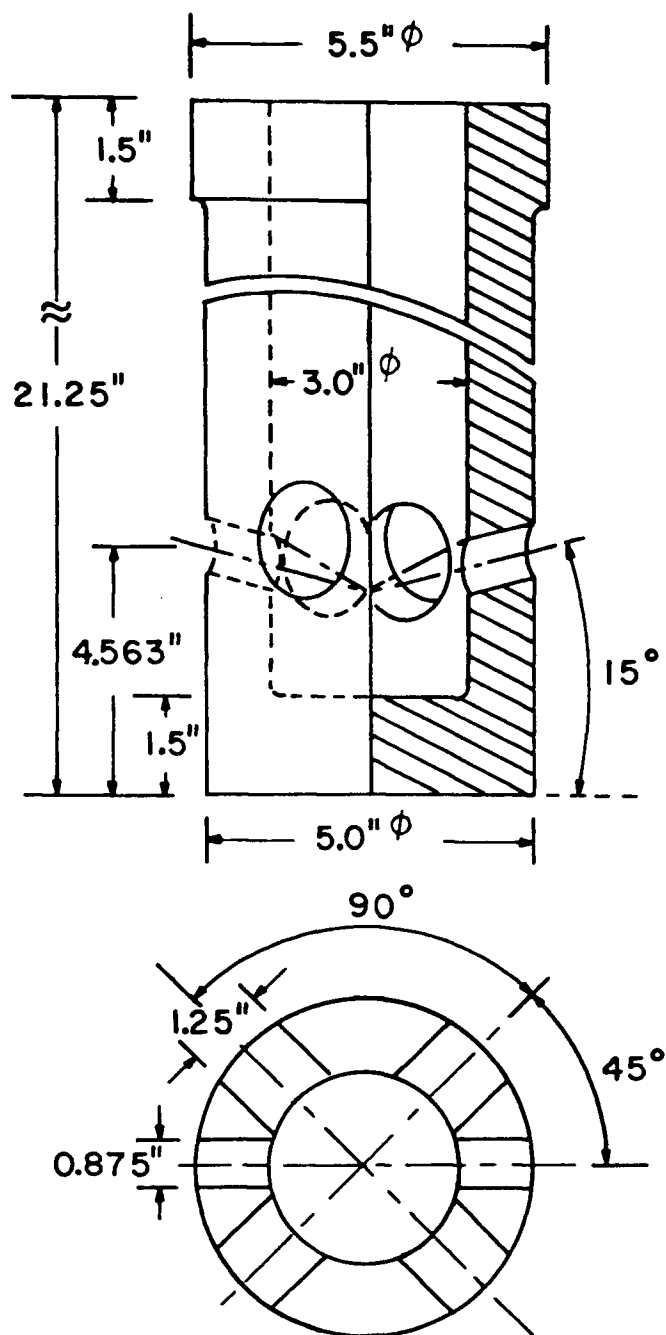


Fig. 4-1

Immersion nozzle for the multi-port practice
(Company D).

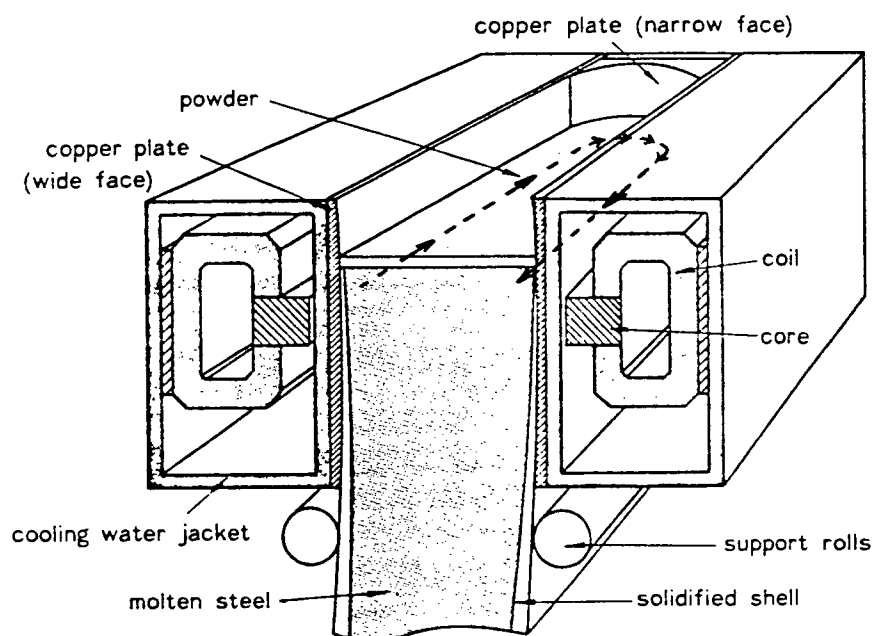


Fig. 4-2 Schematic view of the electromagnetic stirrer in the mould⁸⁸ (Company E).

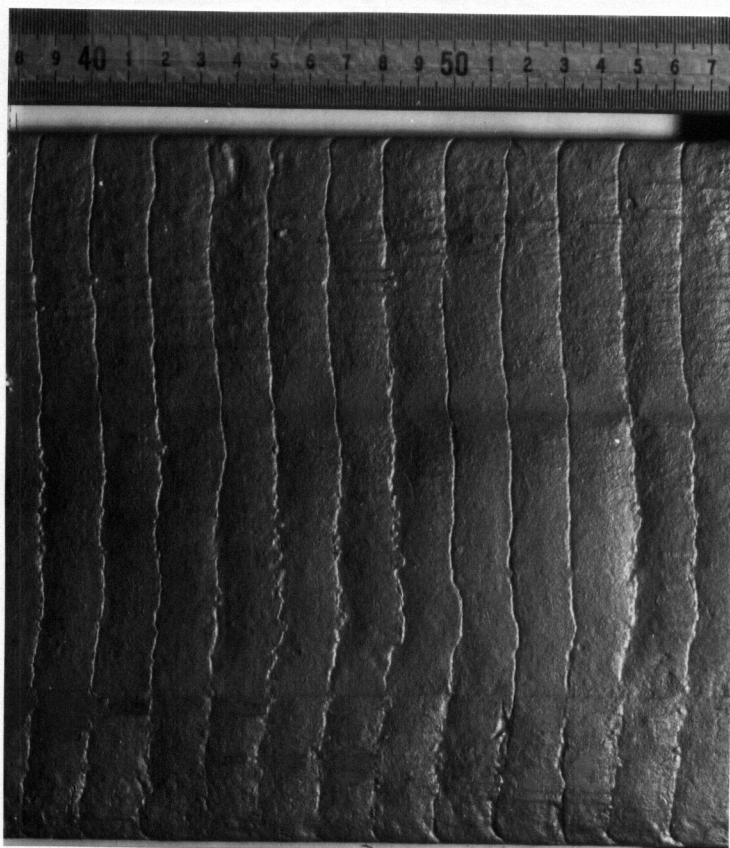


Fig. 4-3 Appearance of oscillation marks on the narrow face of a slab (Company A).

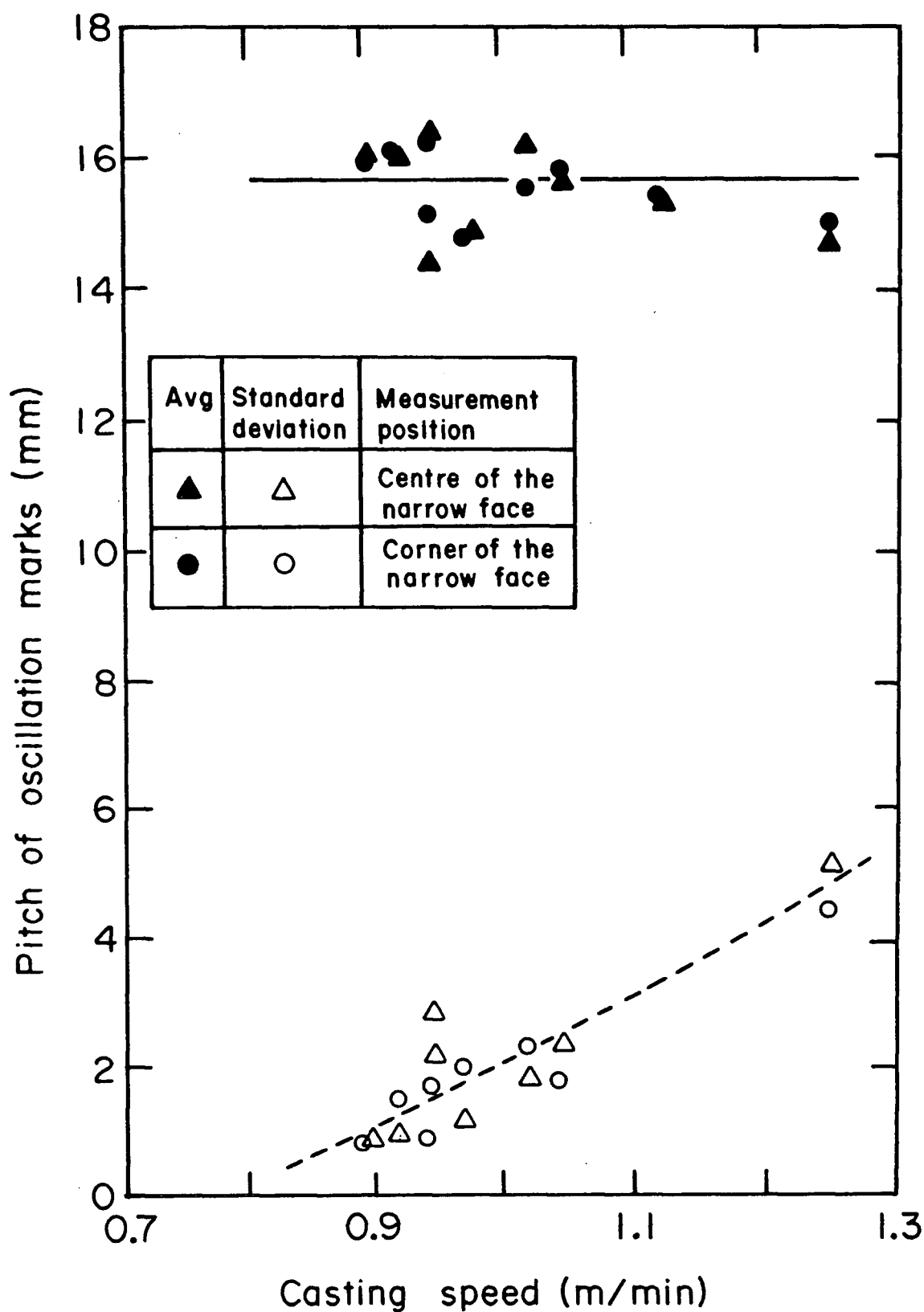


Fig. 4-4 Effect of casting speed on the pitch of oscillation marks (Company A).



Fig. 4-5 Appearance of oscillation marks on the narrow face of a slab (Company C).

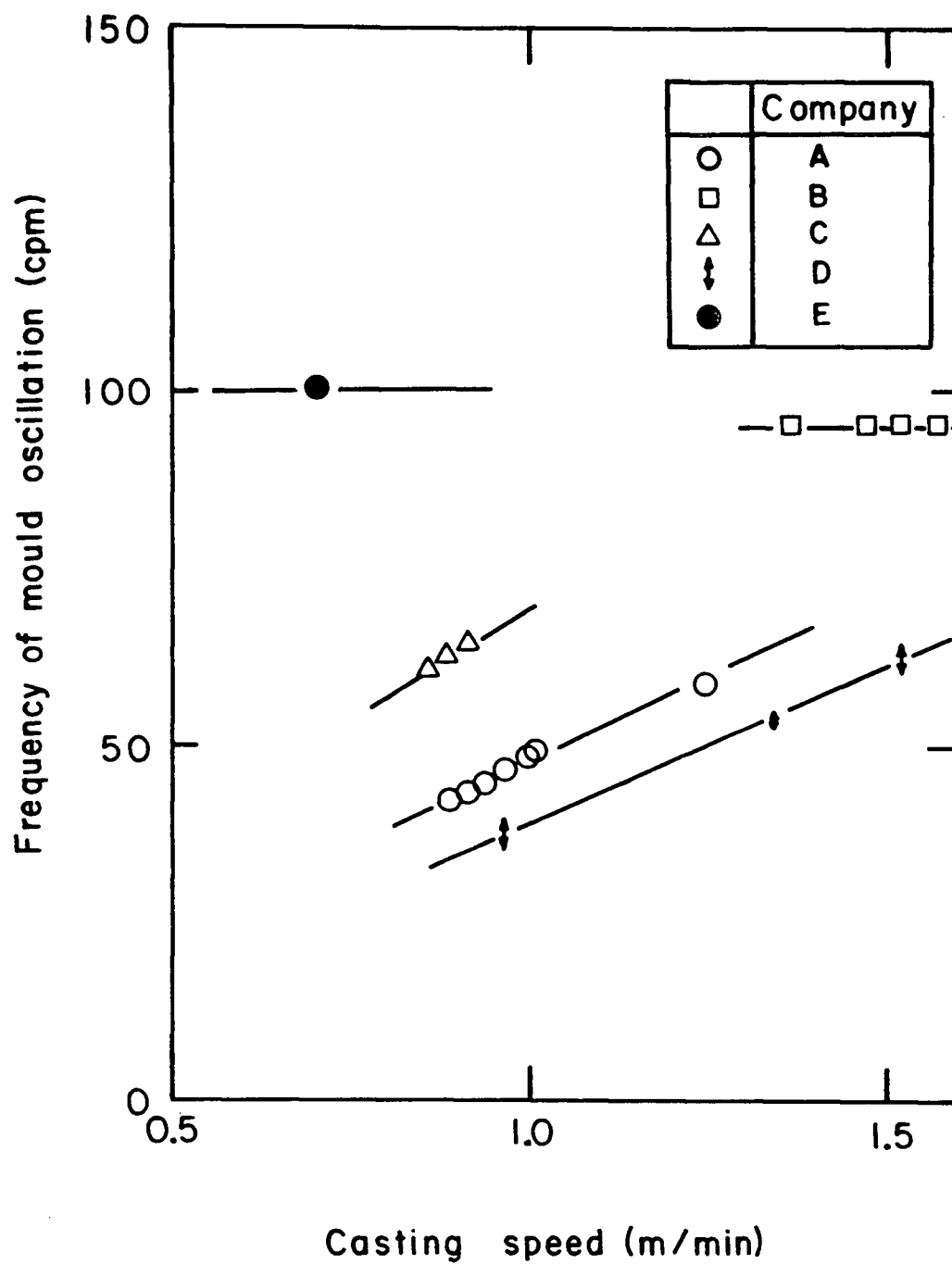
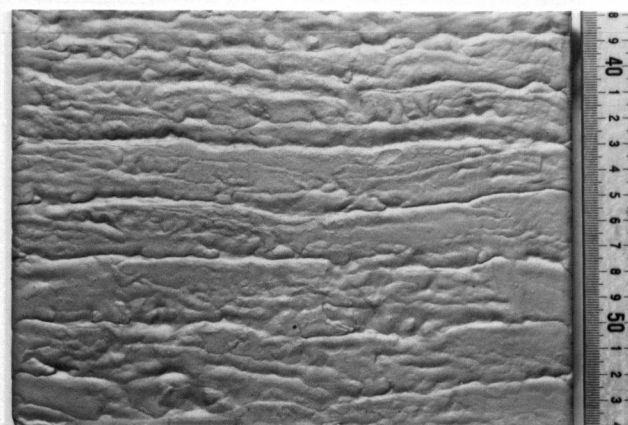
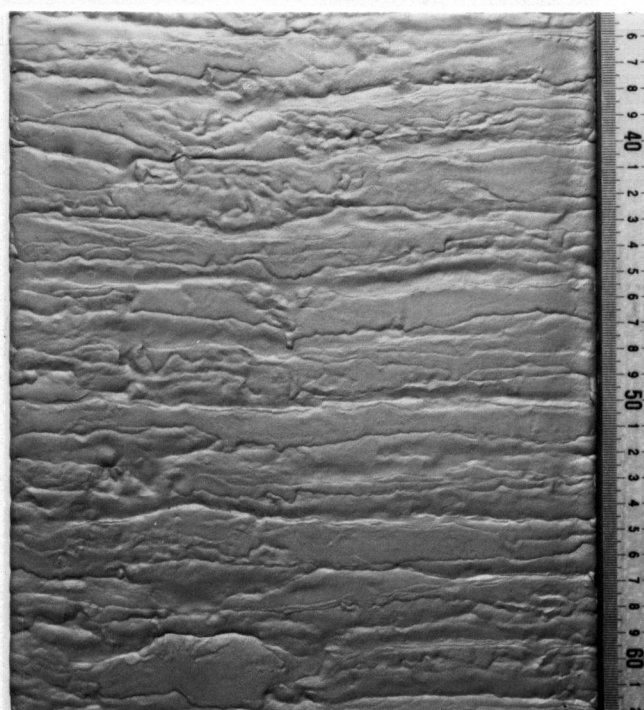


Fig. 4-6 Frequency of mould oscillation in each casting operation.

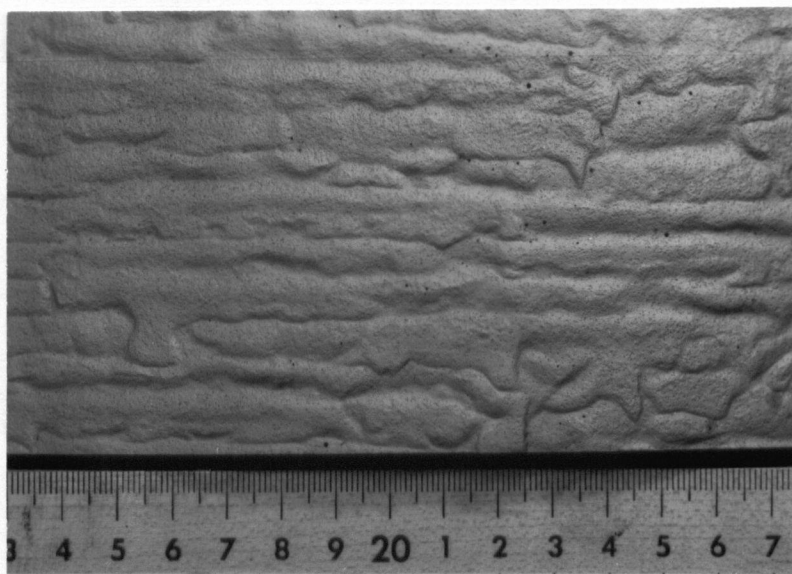


(a)

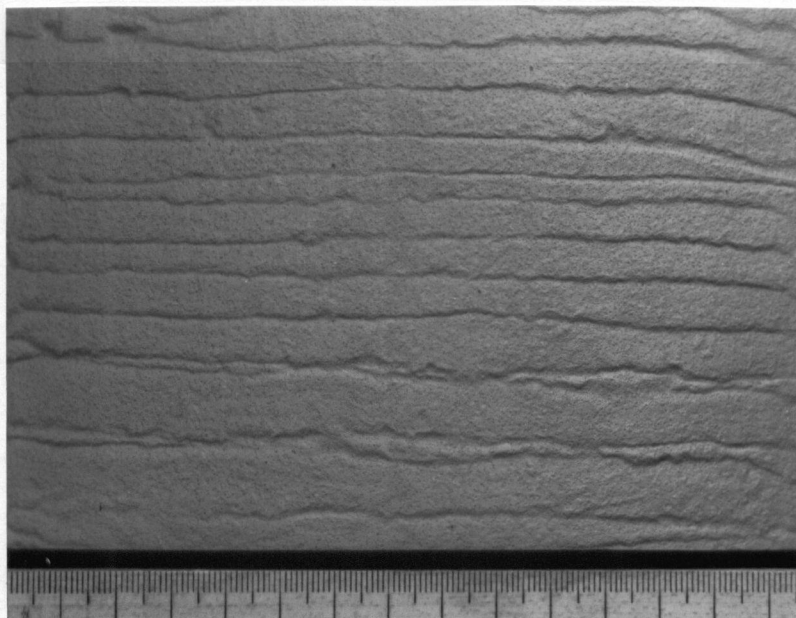


(b)

Fig. 4-7 Appearance of oscillation marks on the narrow face of slab cast with (a) Bifurcated nozzle and (b) Multi-port practice (Company D).

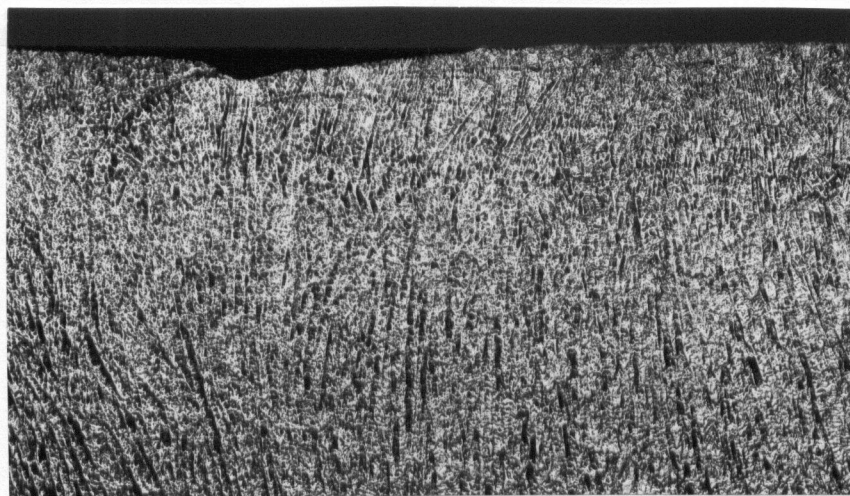


(a)

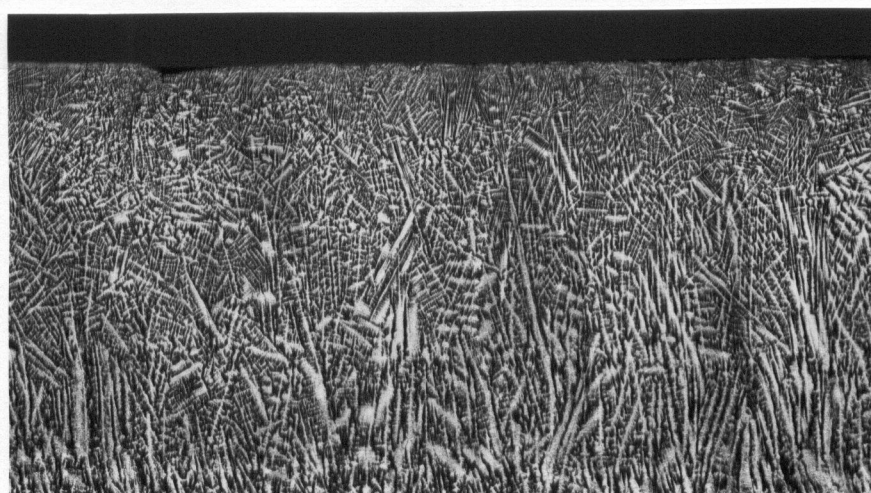


(b)

Fig. 4-8 Appearance of oscillation marks on the narrow face of slab cast (a) without mould EMS and (b) with mould EMS (Company E).

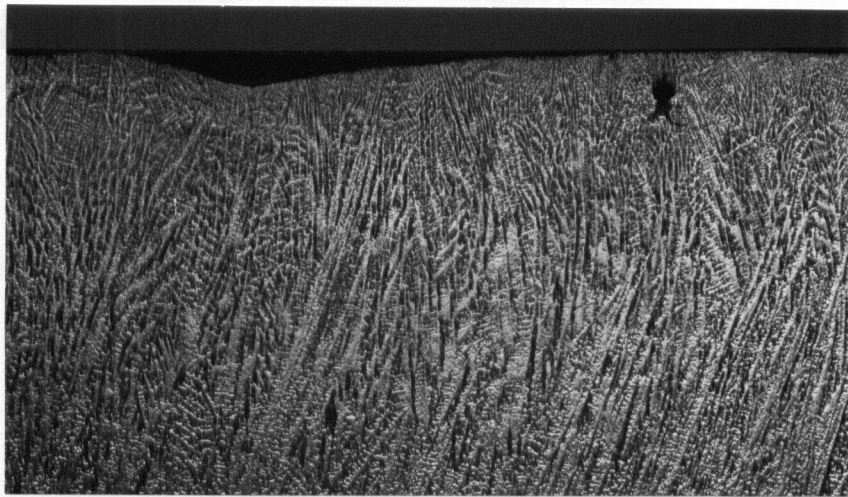


(a)

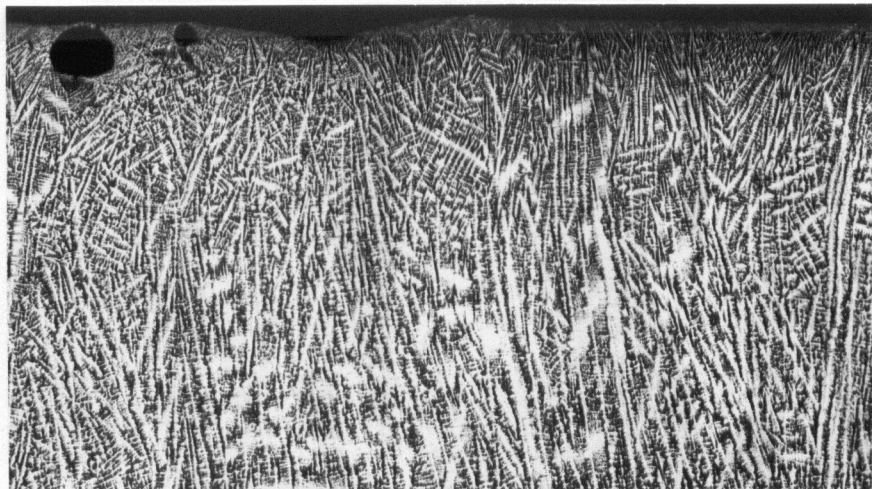


(b)

Fig. 4-9 Subsurface structure near oscillation marks exhibiting "hooks" in steel slabs containing (a) 0.09%C and (b) 0.26%C (Company A). (x6)



(a)



(b)

Fig. 4-10 Subsurface structure near oscillation marks without "hooks" in steel slabs containing (a) 0.08% C and (b) 0.26% C (Company A). (x6)

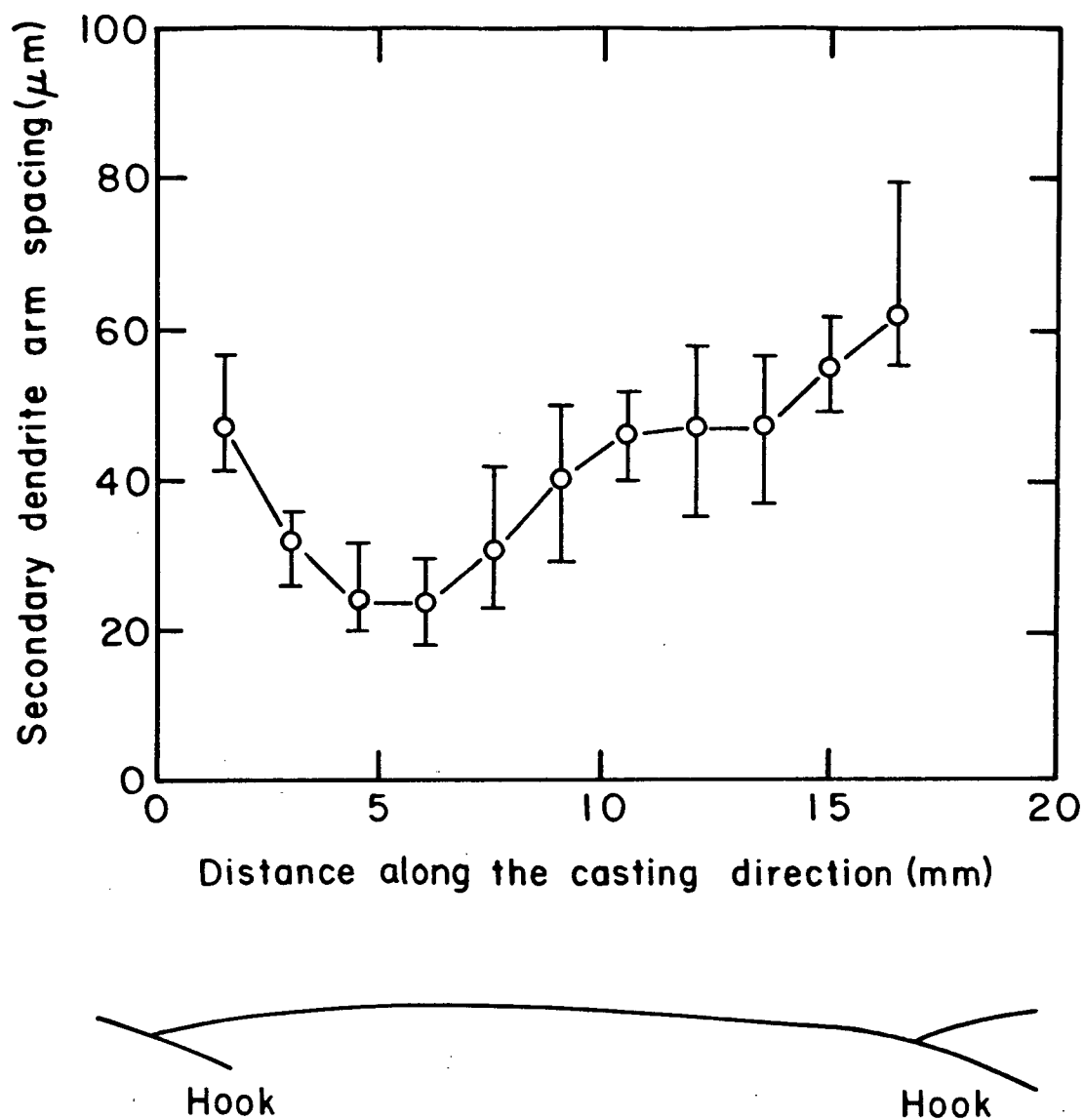
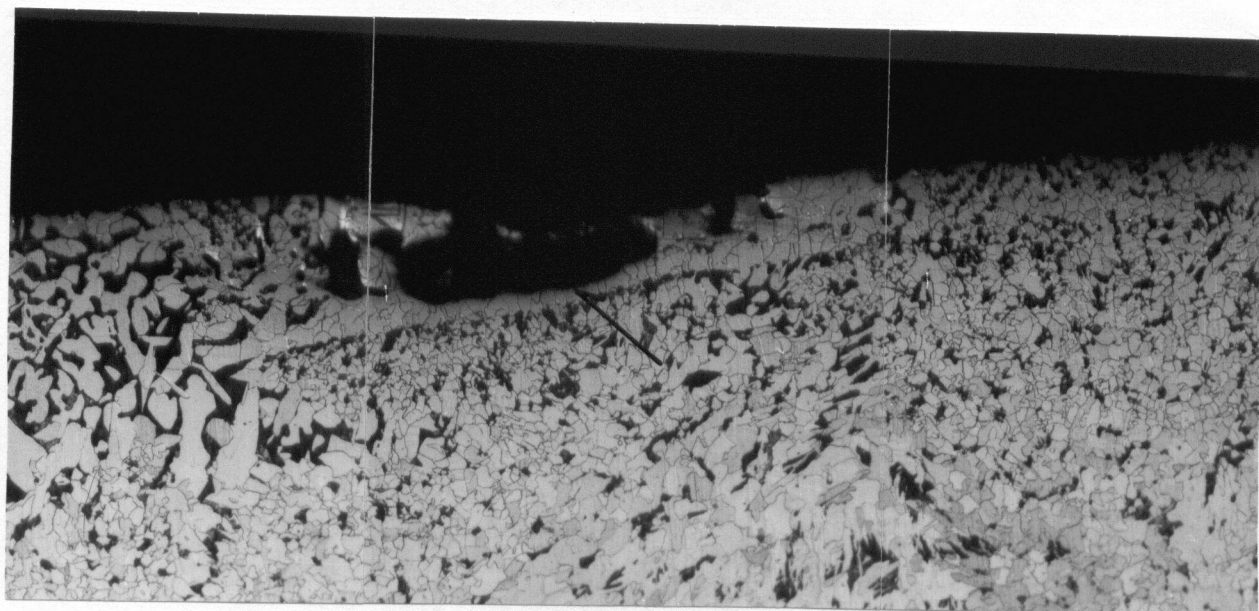
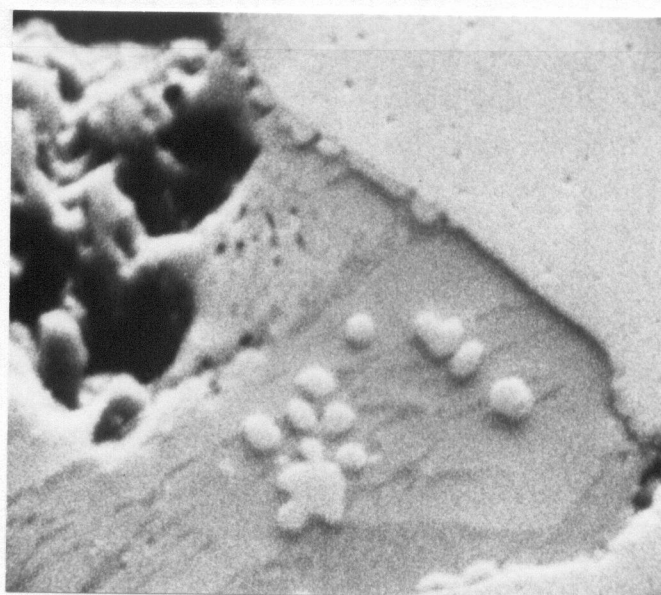


Fig. 4-11 Change of secondary dendrite arm spacing along the casting direction $C=0.09\%$ (Company A).



(a)



(b)

Fig. 4-12 Substance at the end of a subsurface hook (a) x 94
(b) x 2000 (Company B).

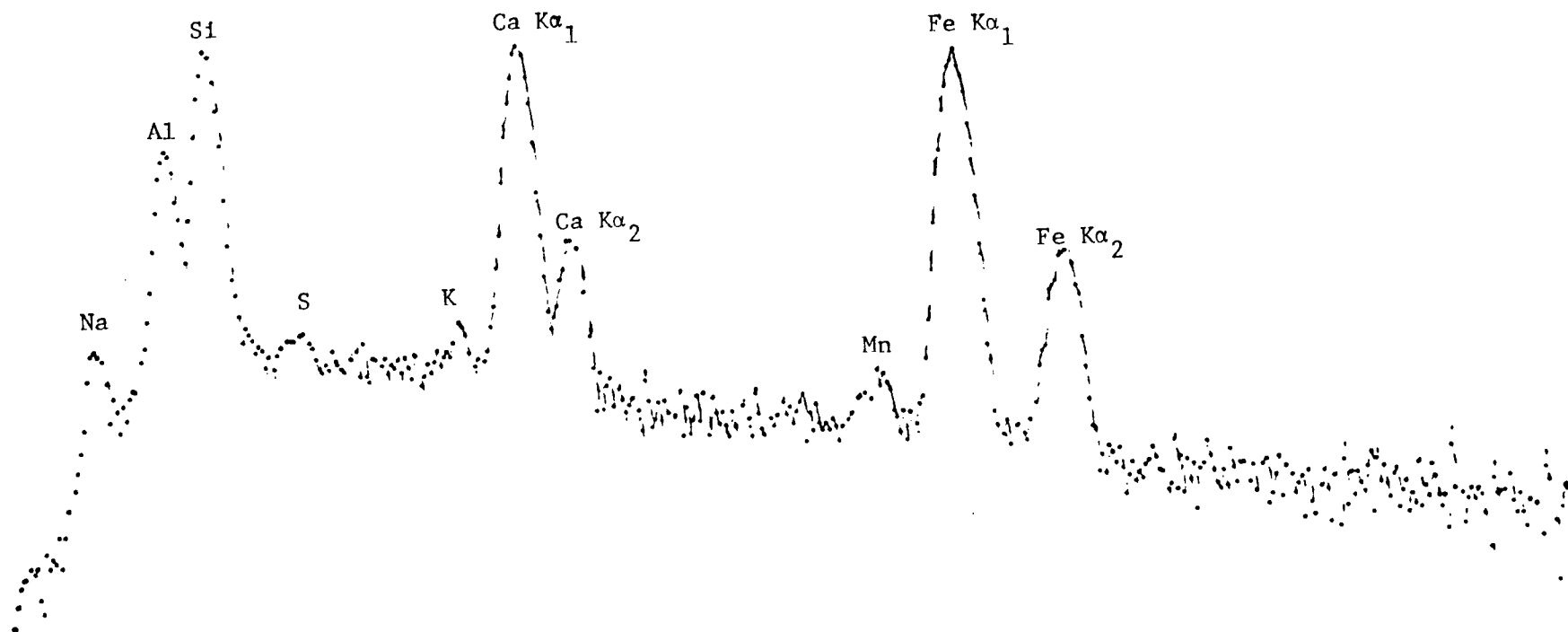
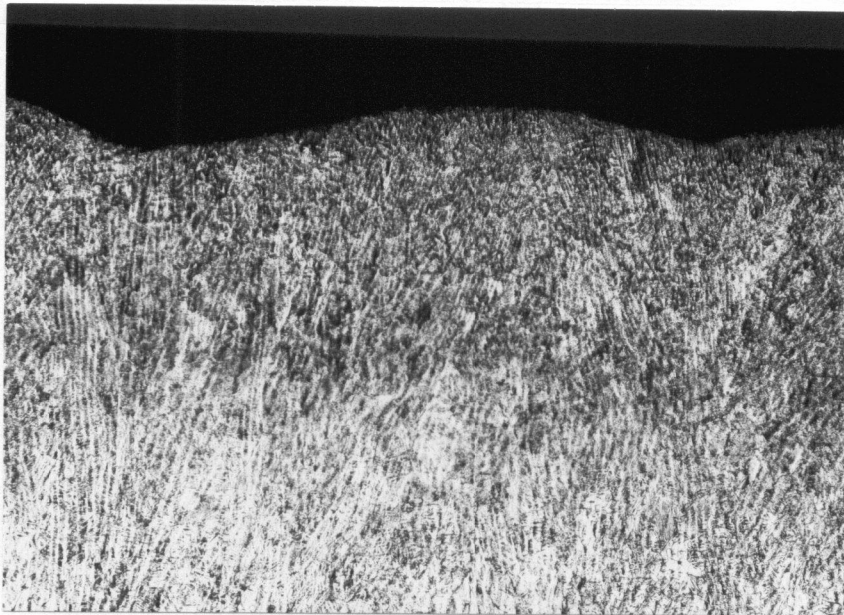
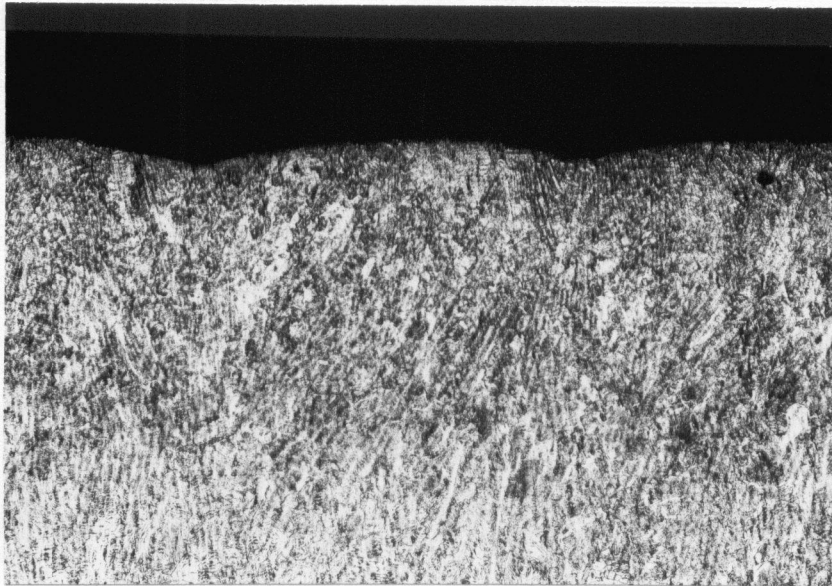


Fig. 4-13 X-ray spectrograph of the substance near the hook
(Company B).

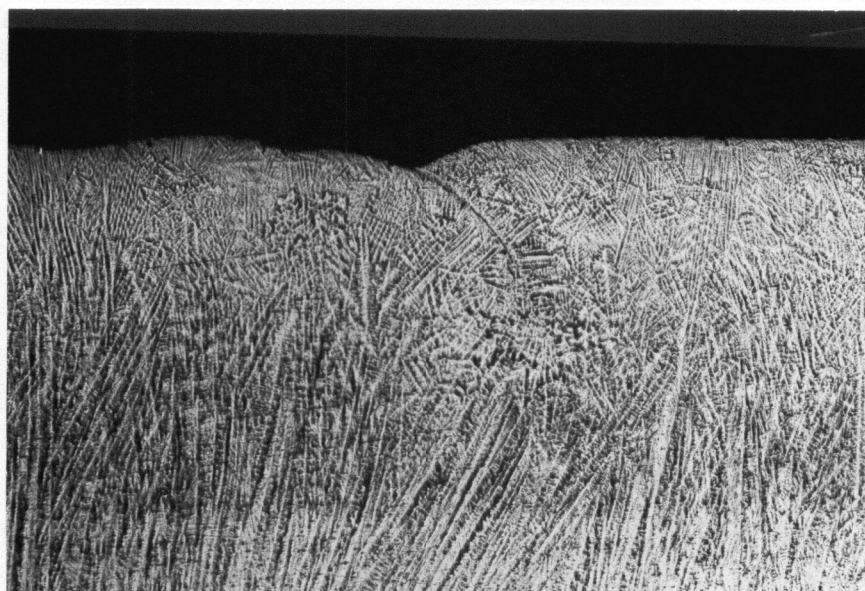


(a)

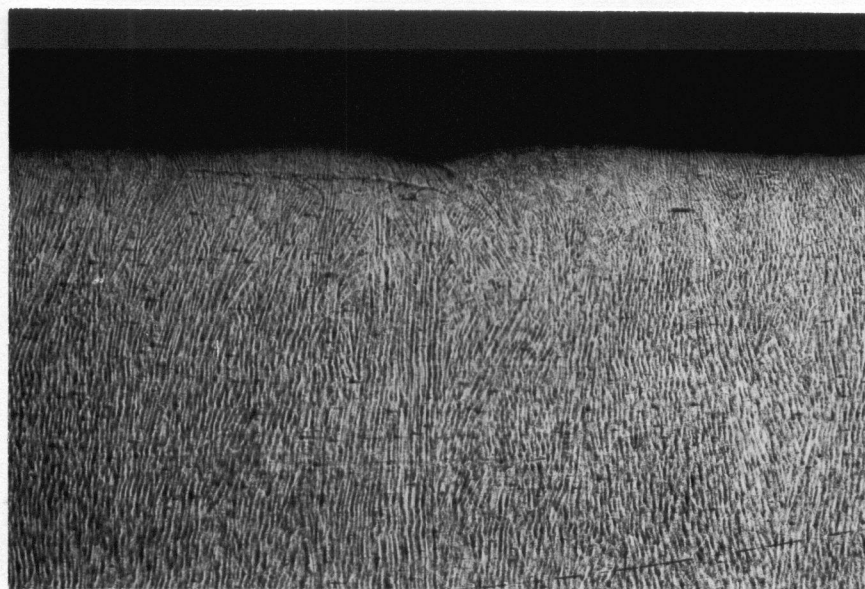


(b)

Fig. 4-14 Subsurface structure near oscillation marks in steel slabs from Company C. (x6)

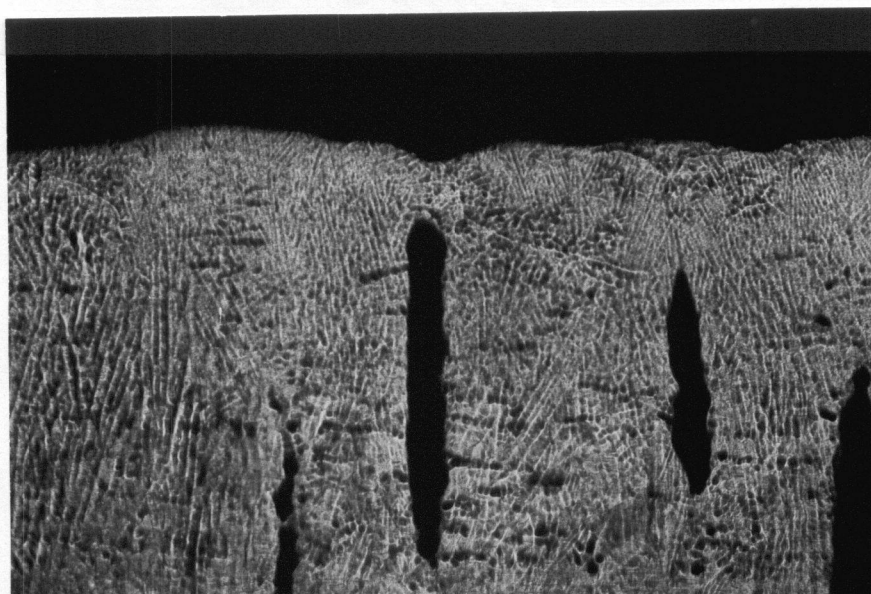


(a)

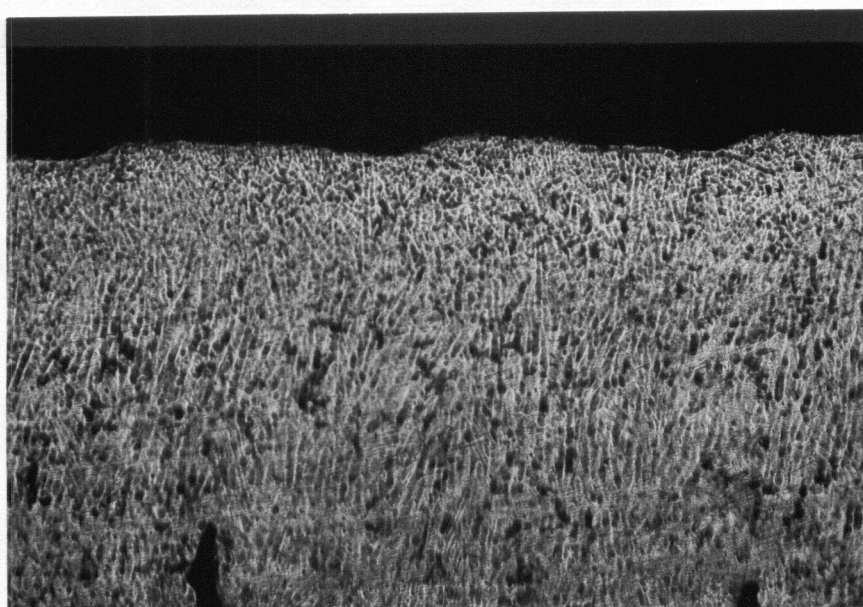


(b)

Fig. 4-15 Subsurface structure near oscillation marks in steel slabs cast by (a) bifurcated nozzle and (b) multi-port practice (Company D). (x6.5)



(a)



(b)

Fig. 4-16 Subsurface structure near oscillation marks in steel slabs cast (a) without EMS-M and (b) with EMS-M (Company E). (x6)

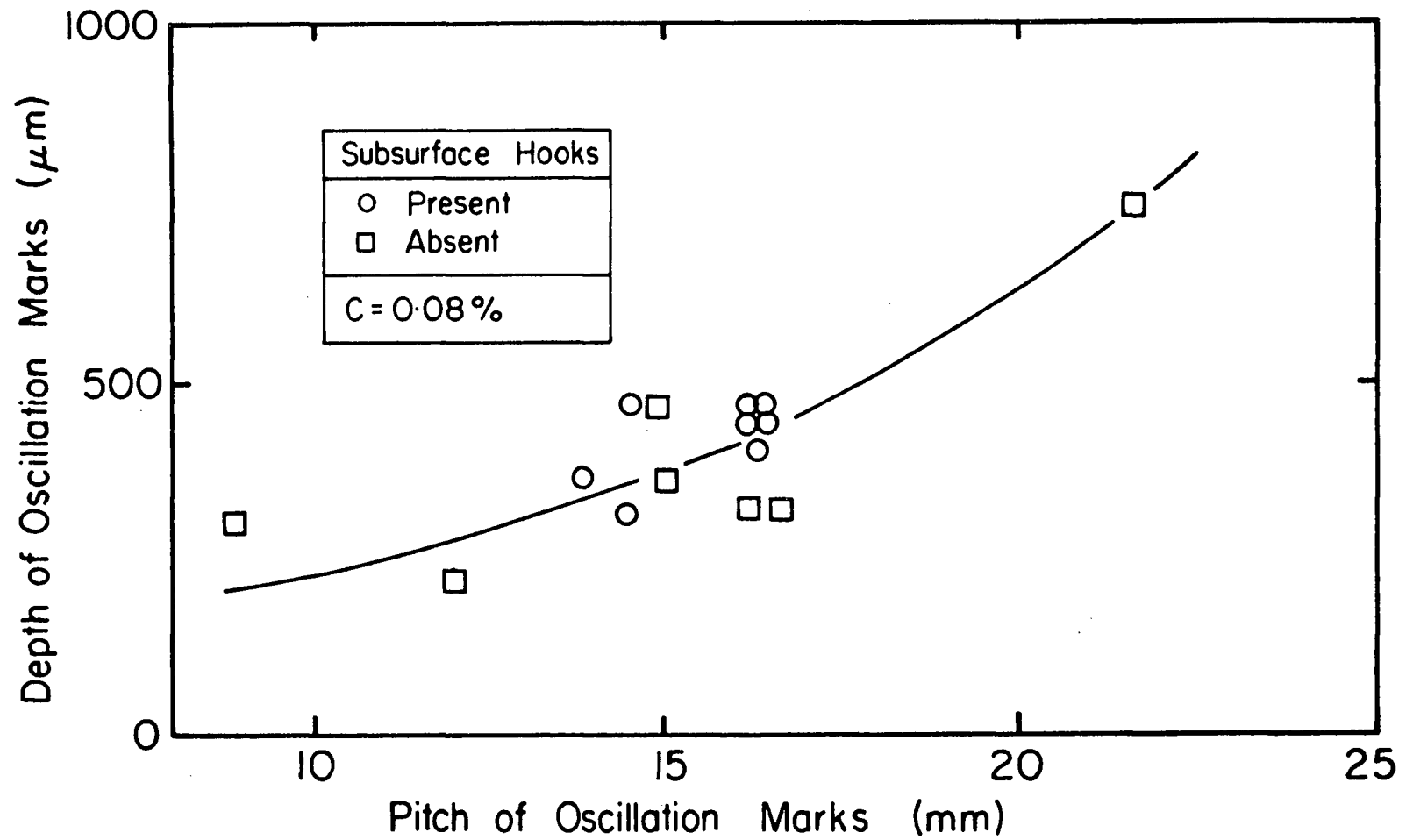


Fig. 4-17 Relationship between depth and pitch of oscillation marks in 0.08%-Carbon slabs (Company A).

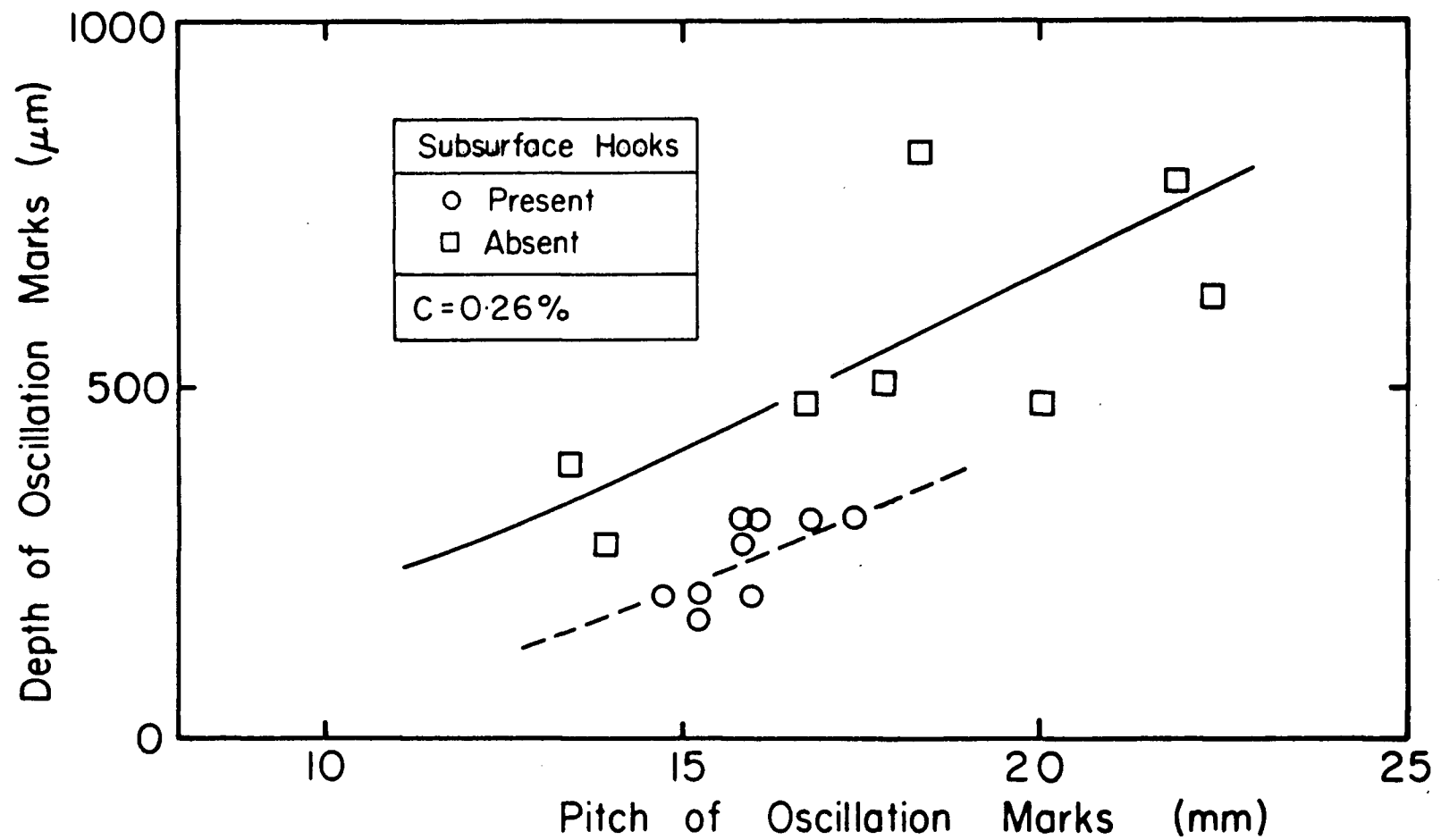


Fig. 4-18 Relationship between depth and pitch of oscillation marks on 0.26%-Carbon slabs (Company A).

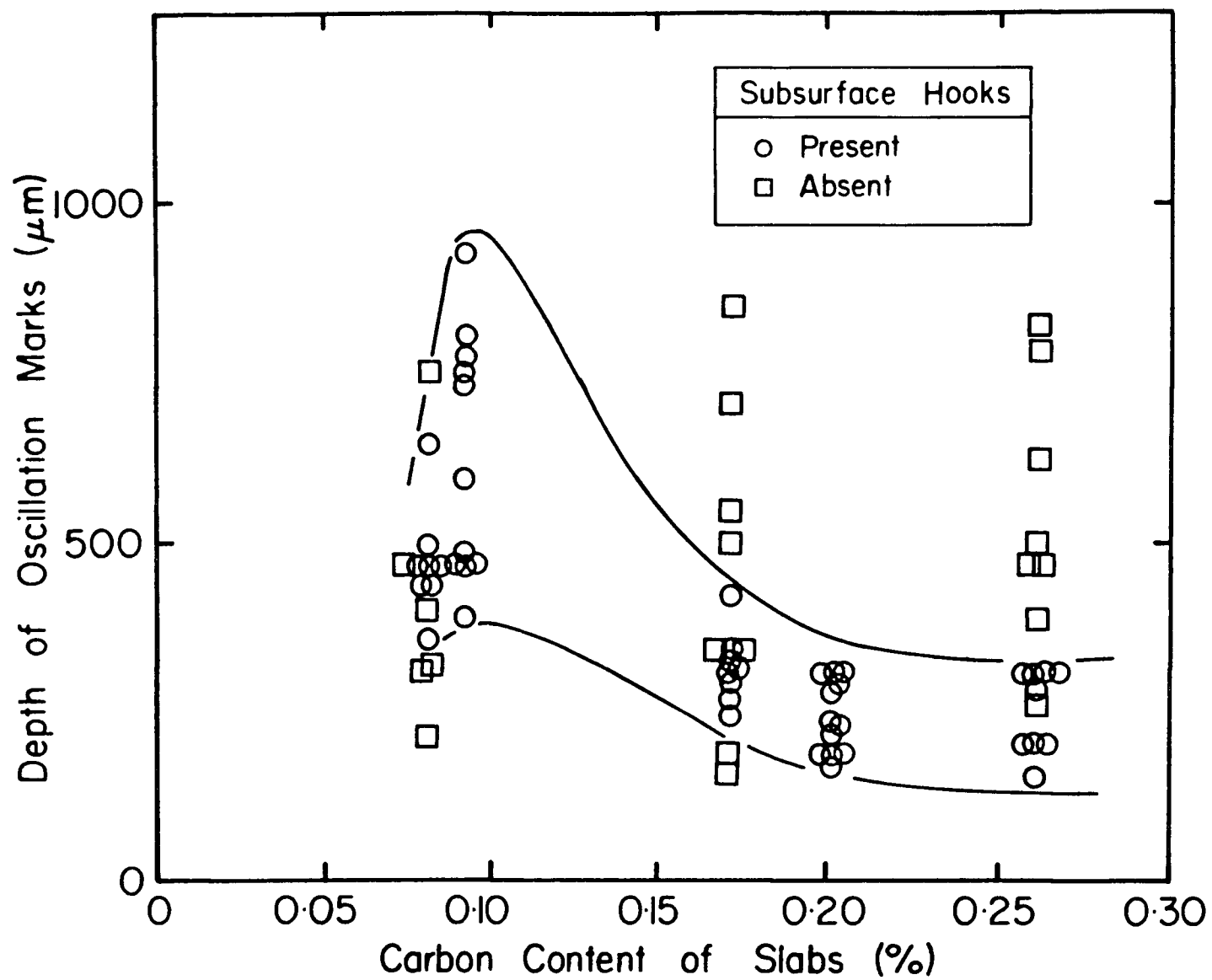


Fig. 4-19 Influence of carbon content of the slabs on the depth of oscillation marks (Company A).

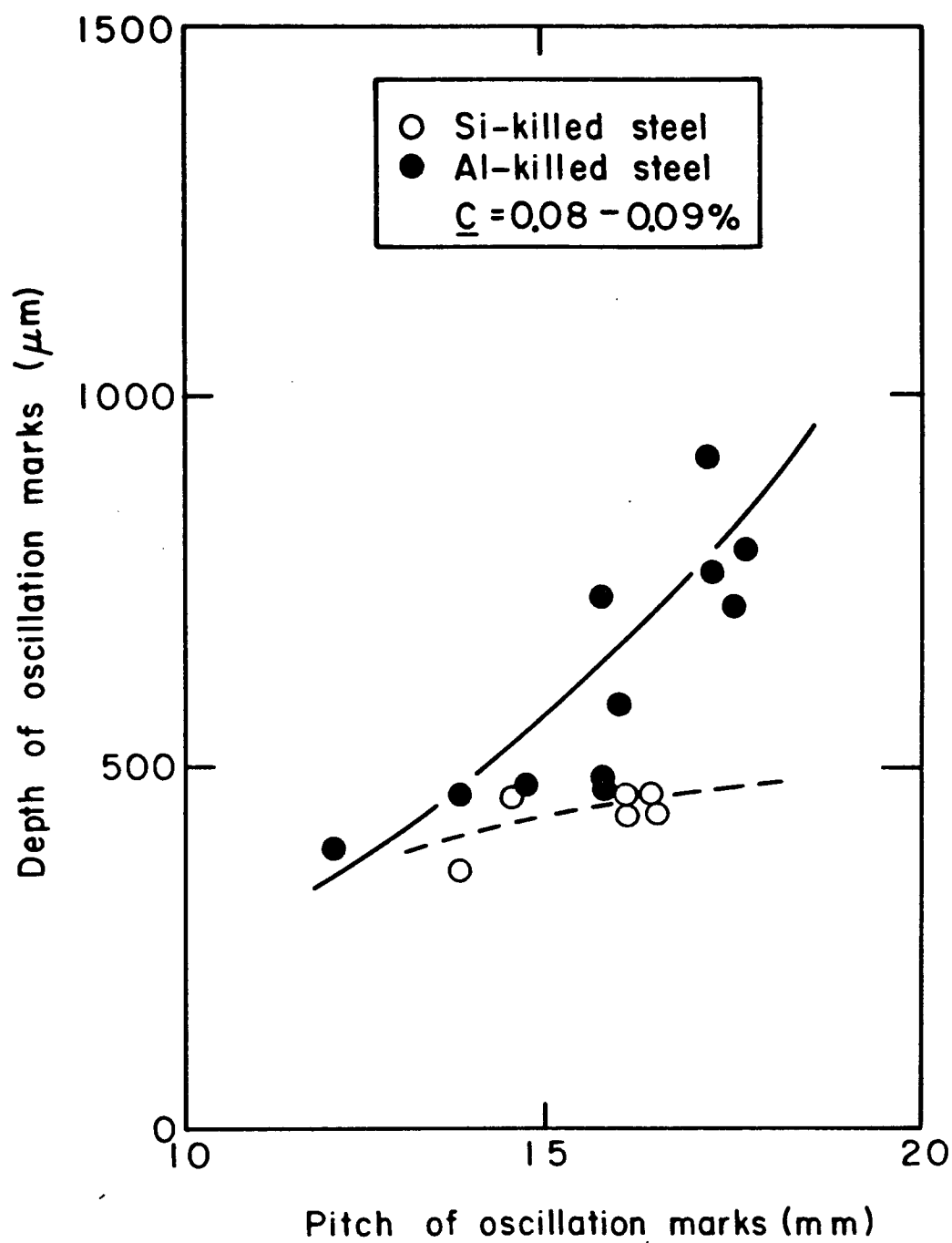


Fig. 4-20 Effect of Al on the shape of oscillation marks (Company A).
Note: all marks are hook-like structures.

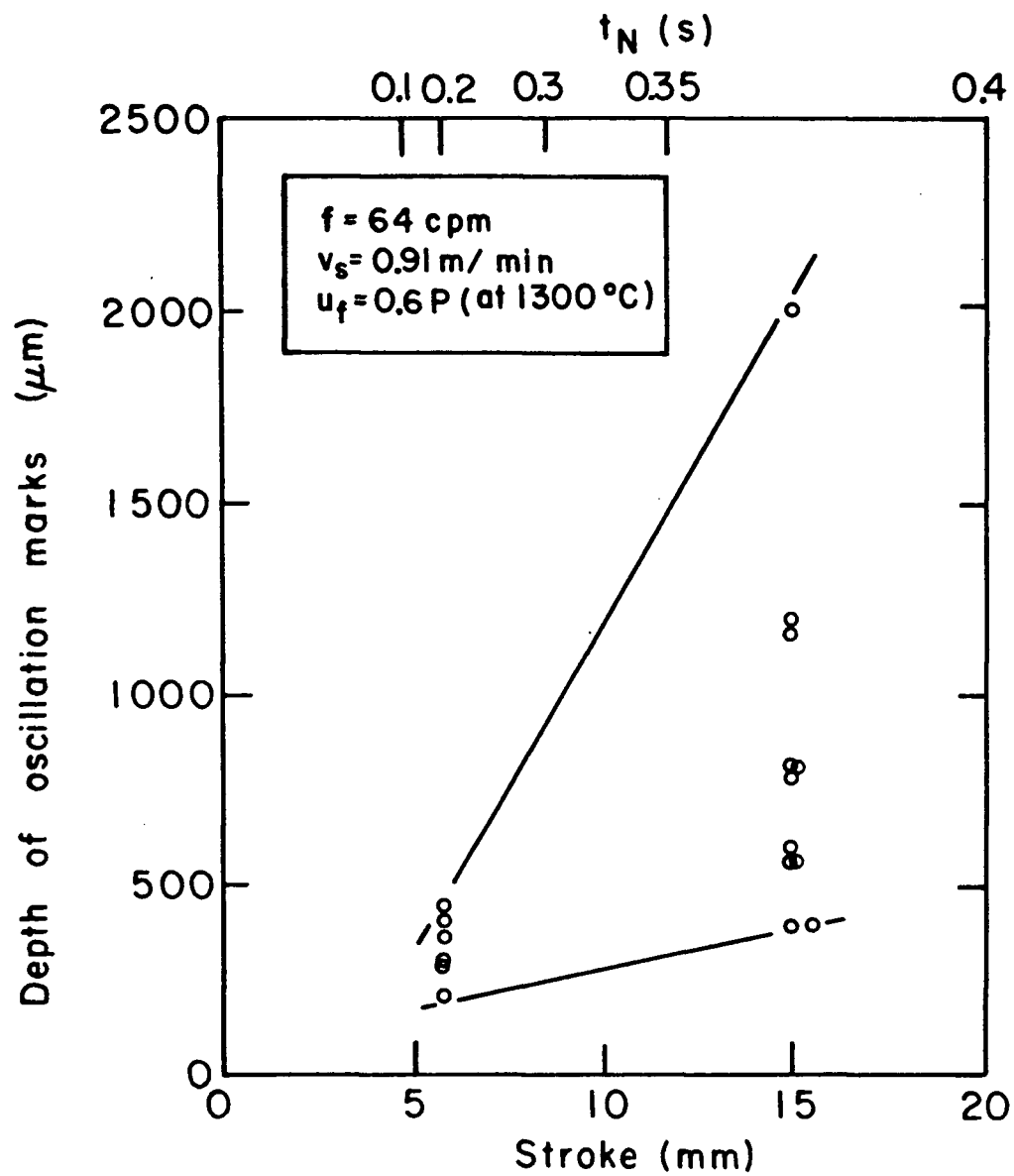


Fig. 4-21 Effect of oscillation stroke on the depth of oscillation Marks (Company C).

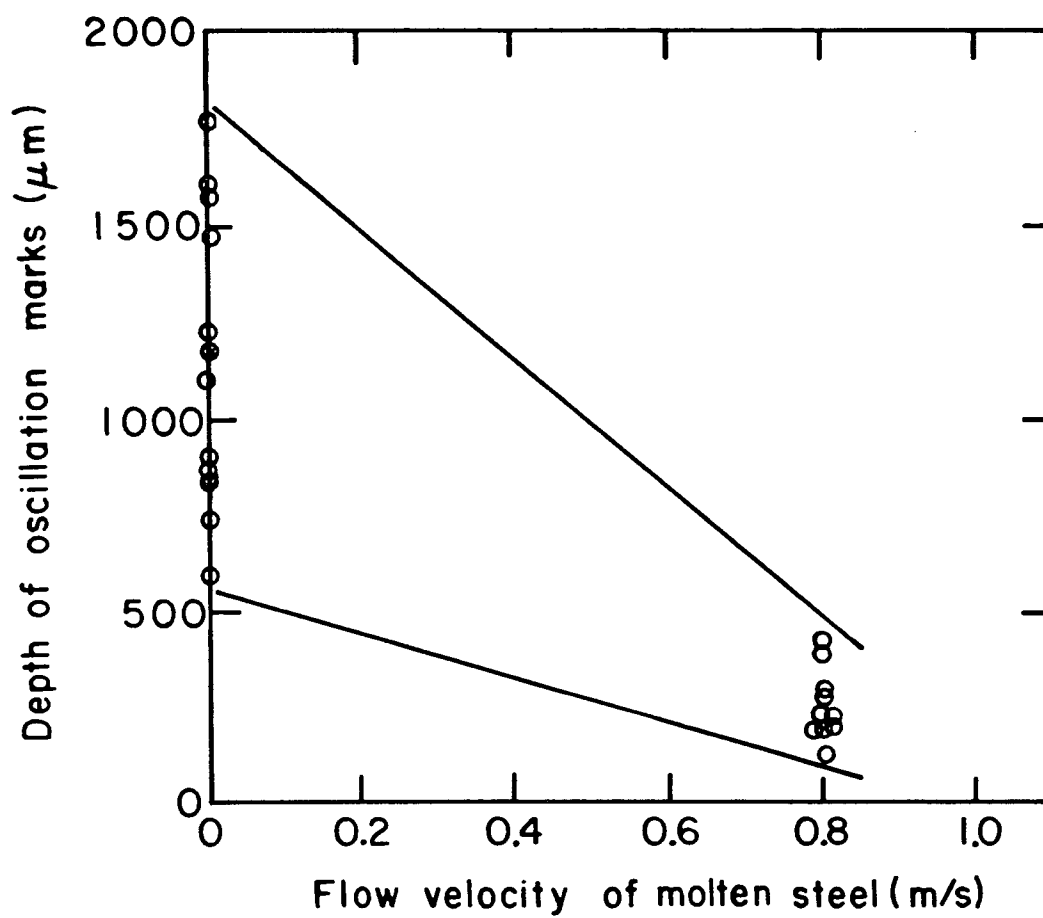


Fig. 4-22 Effect of mould EMS on the depth of oscillation marks (Company E).

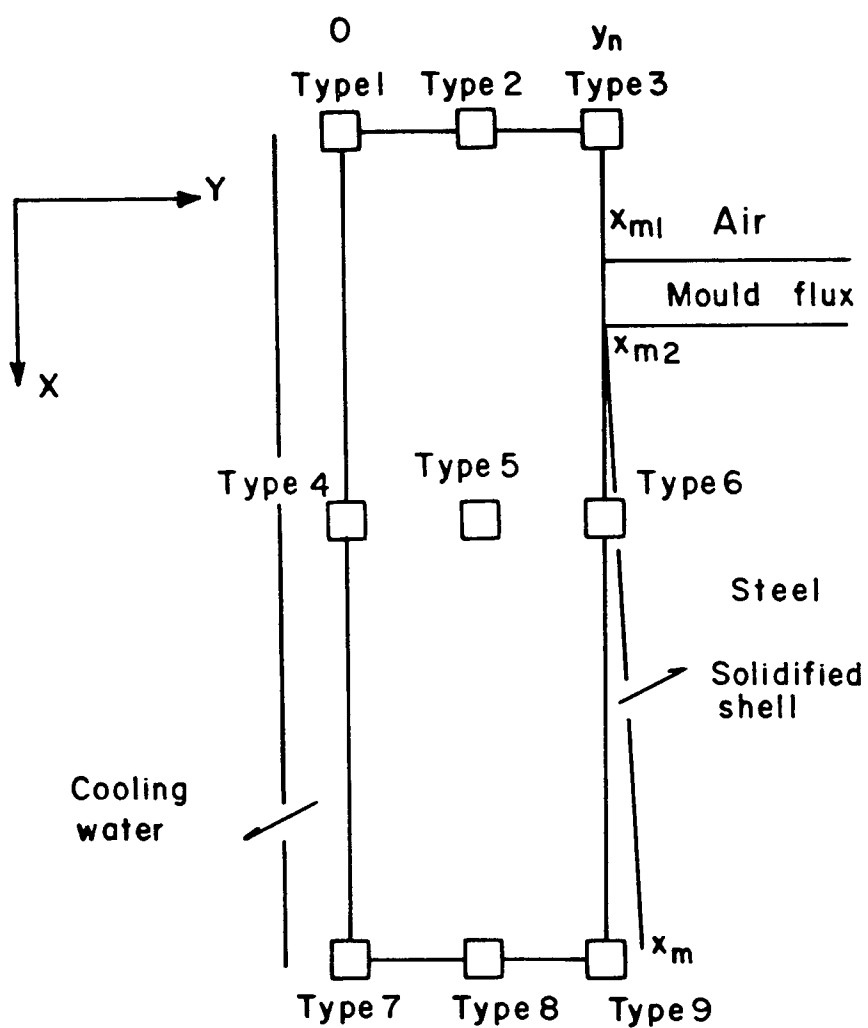


Fig. 4-23 Physical system for the computation of heat transfer in the mould.

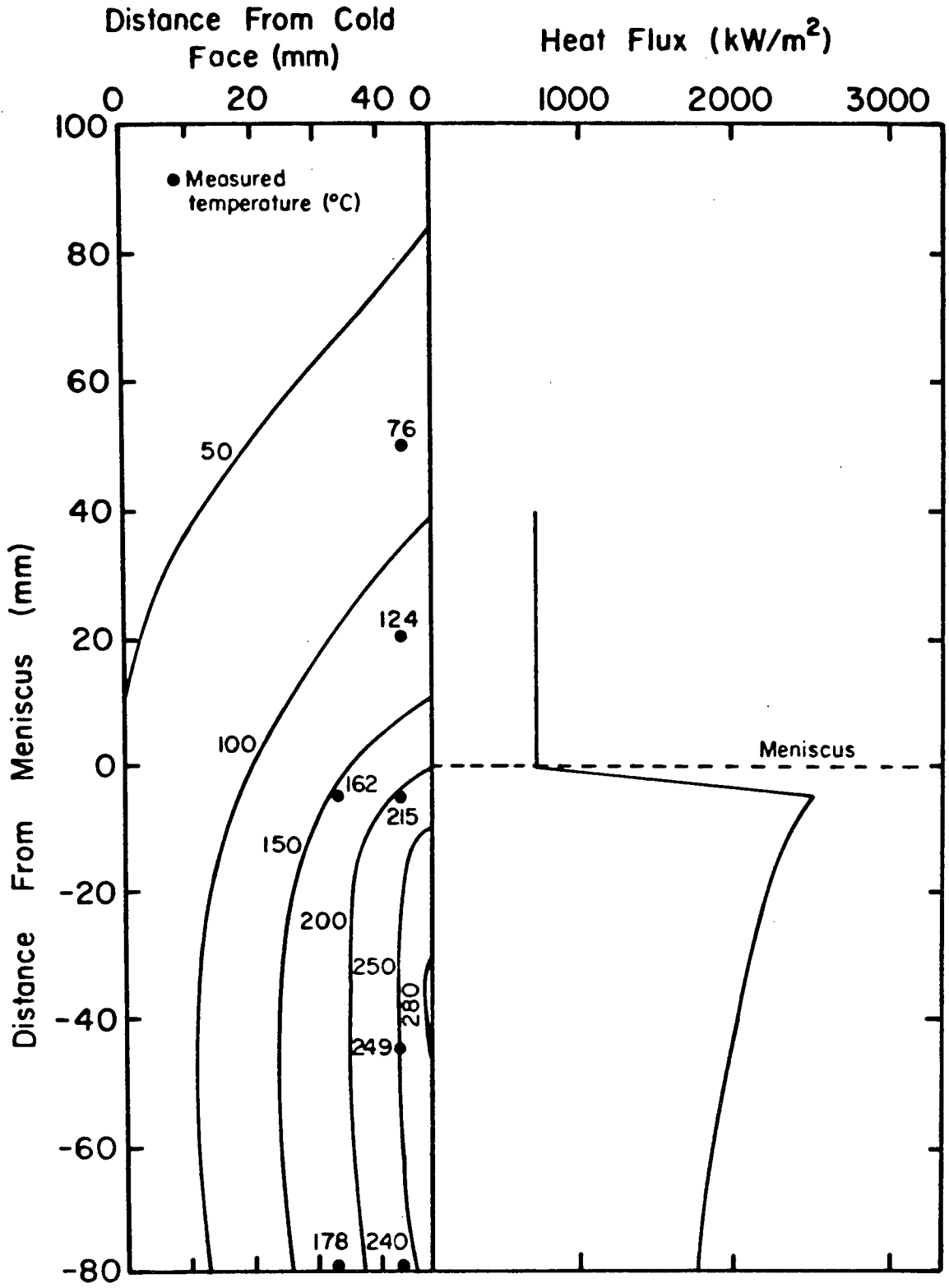


Fig. 4-24 Temperature distribution in the mould wall and the heat flux distribution near the meniscus (Closed circles are values of mould temperature reported by Nakato et al¹⁸).

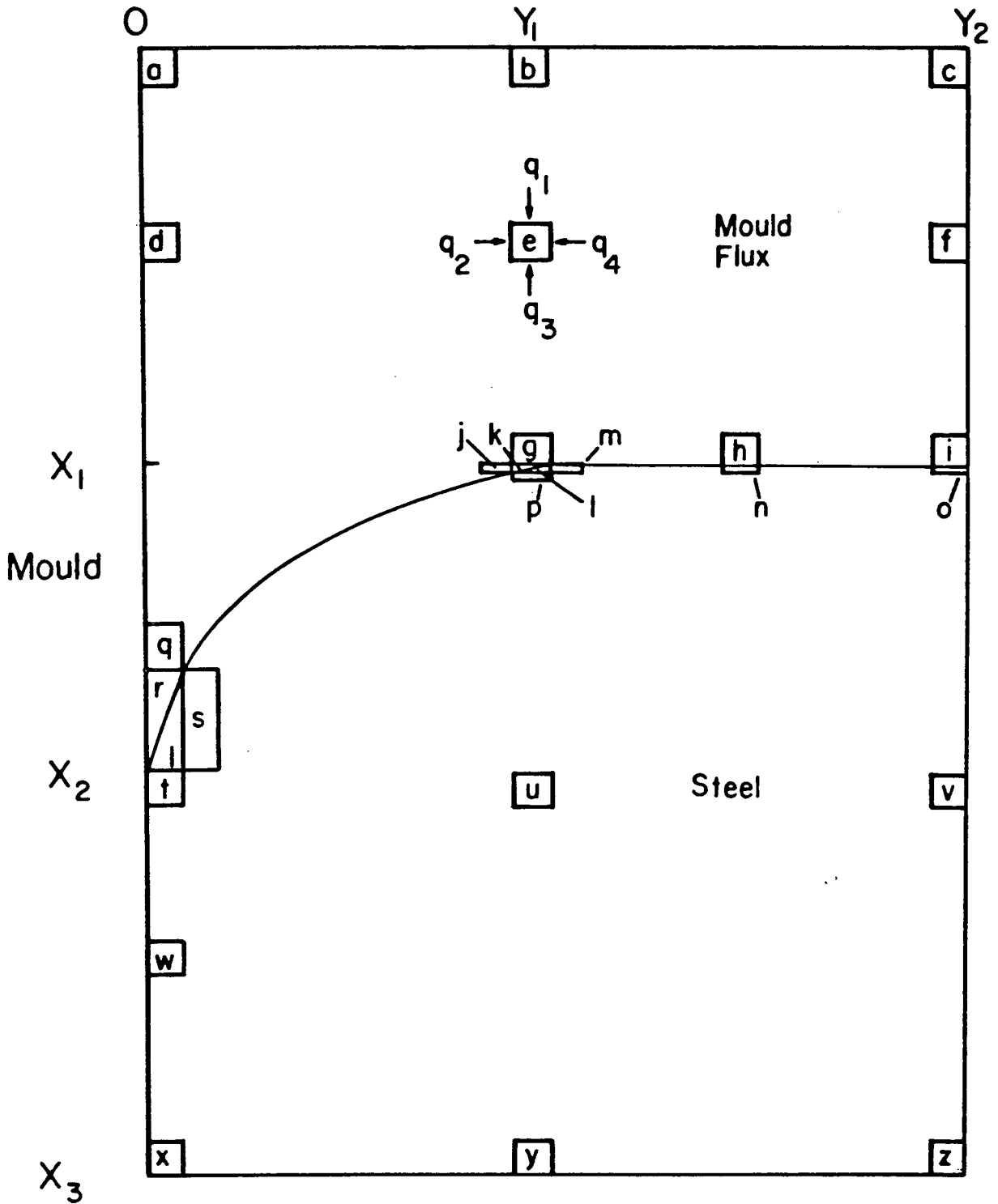


Fig. 4-25 Geometry and nodal system employed to predict temperature distributions in the mould flux and steel at the meniscus.

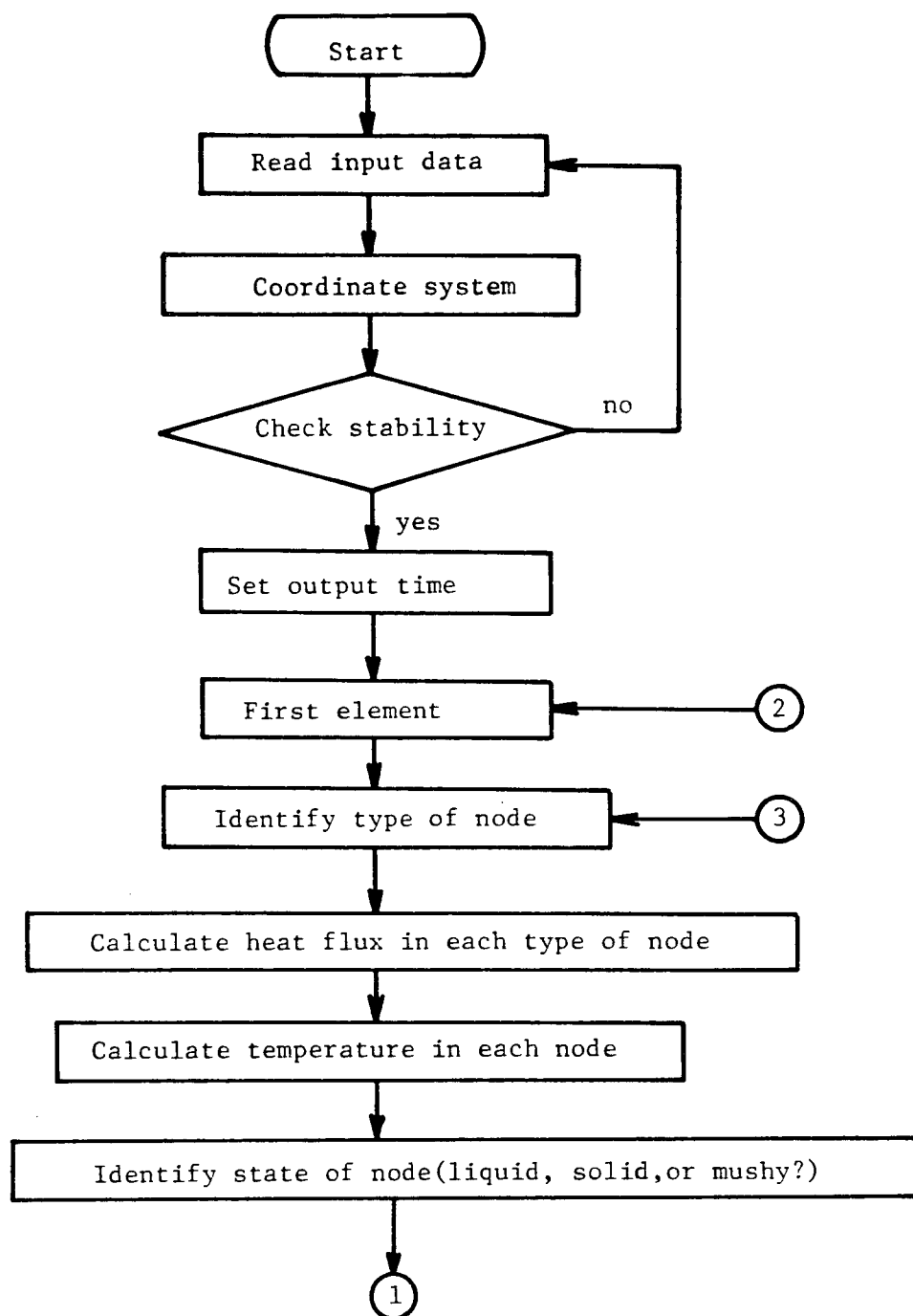


Fig. 4-26 Flow chart for the calculation of the temperature distribution in steel and mould flux (i).

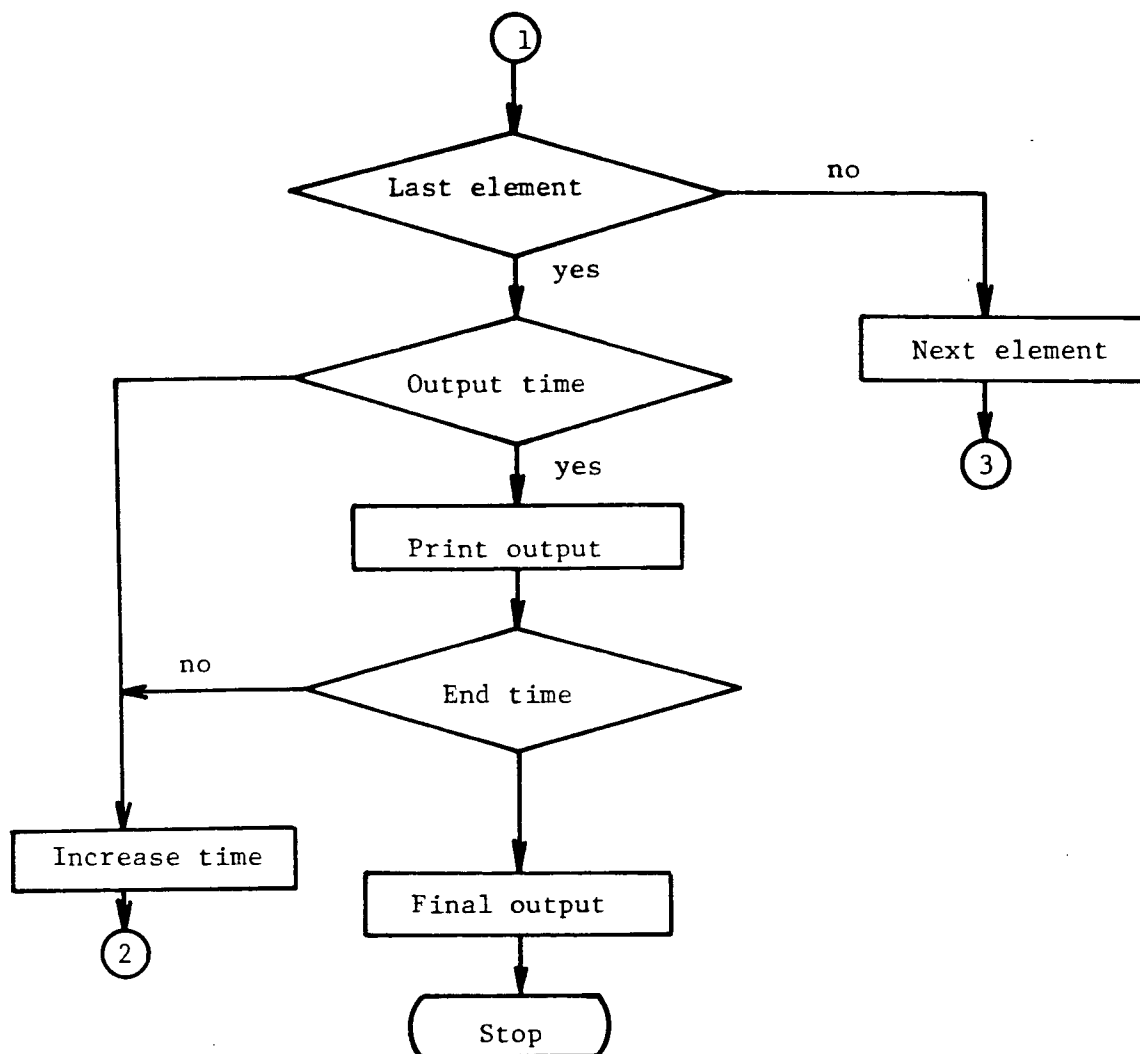


Fig. 4-26 Flow chart for the calculation of the temperature distribution in steel and mould flux (ii).

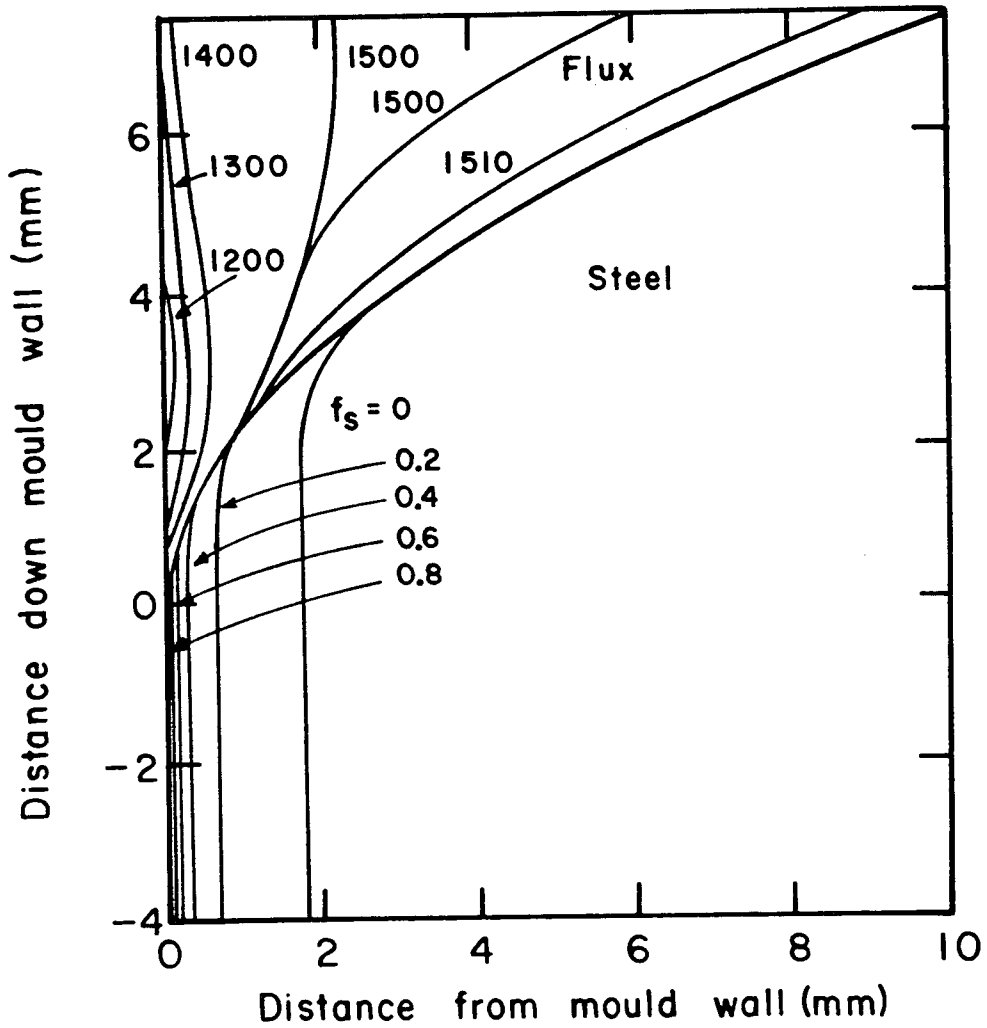


Fig. 4-27 Predicted temperature distribution in the mould flux and fraction solidified in the steel at the meniscus after a time of 0.3s. Superheat of steel is 5°C.

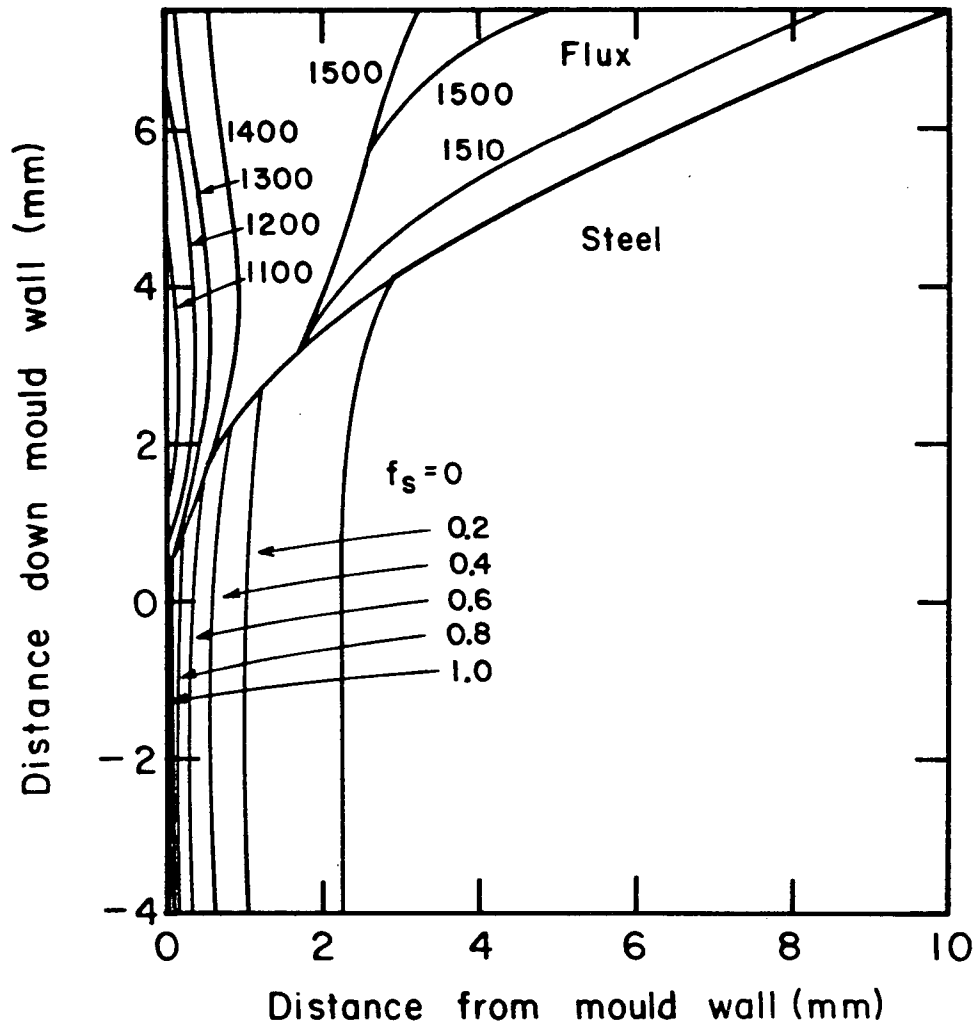


Fig. 4-28 Predicted temperature distribution in the mould flux and fraction solidified in the steel at the meniscus after a time of 0.6s. Superheat of steel is 5°C.

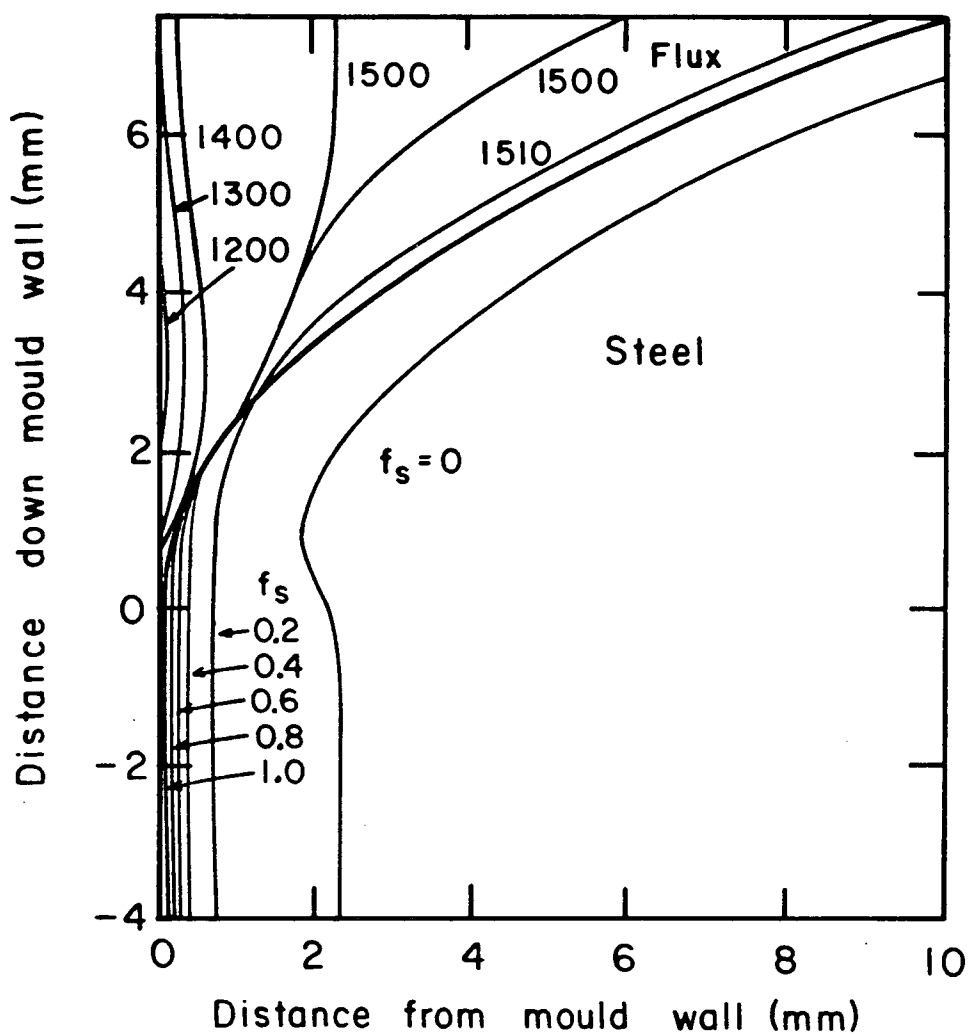


Fig. 4-29 Predicted temperature distribution in the mould flux and fraction solidified in the steel at the meniscus after a time of 0.3s. Superheat of steel is 0°C.

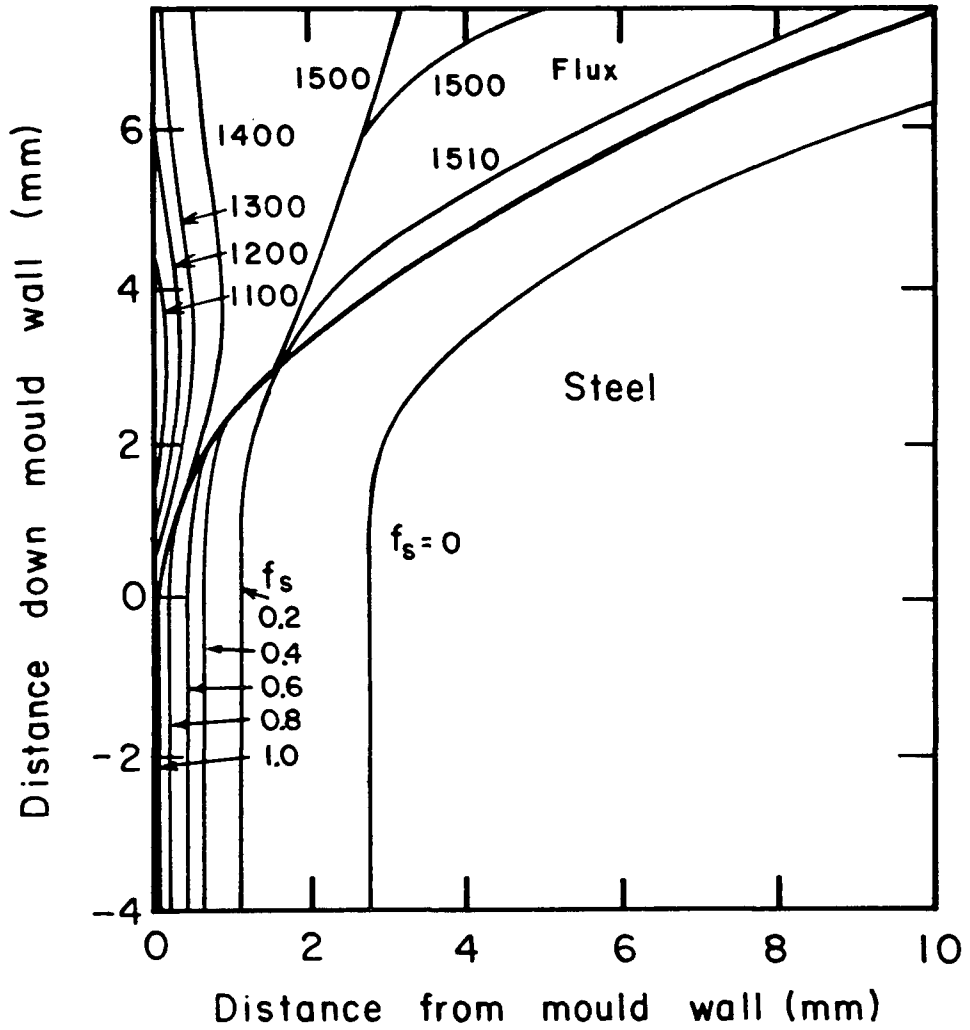


Fig. 4-30 Predicted temperature distribution in the mould flux and fraction solidified in the steel at the meniscus after a time of 0.6s. Superheat of steel is 0°C.

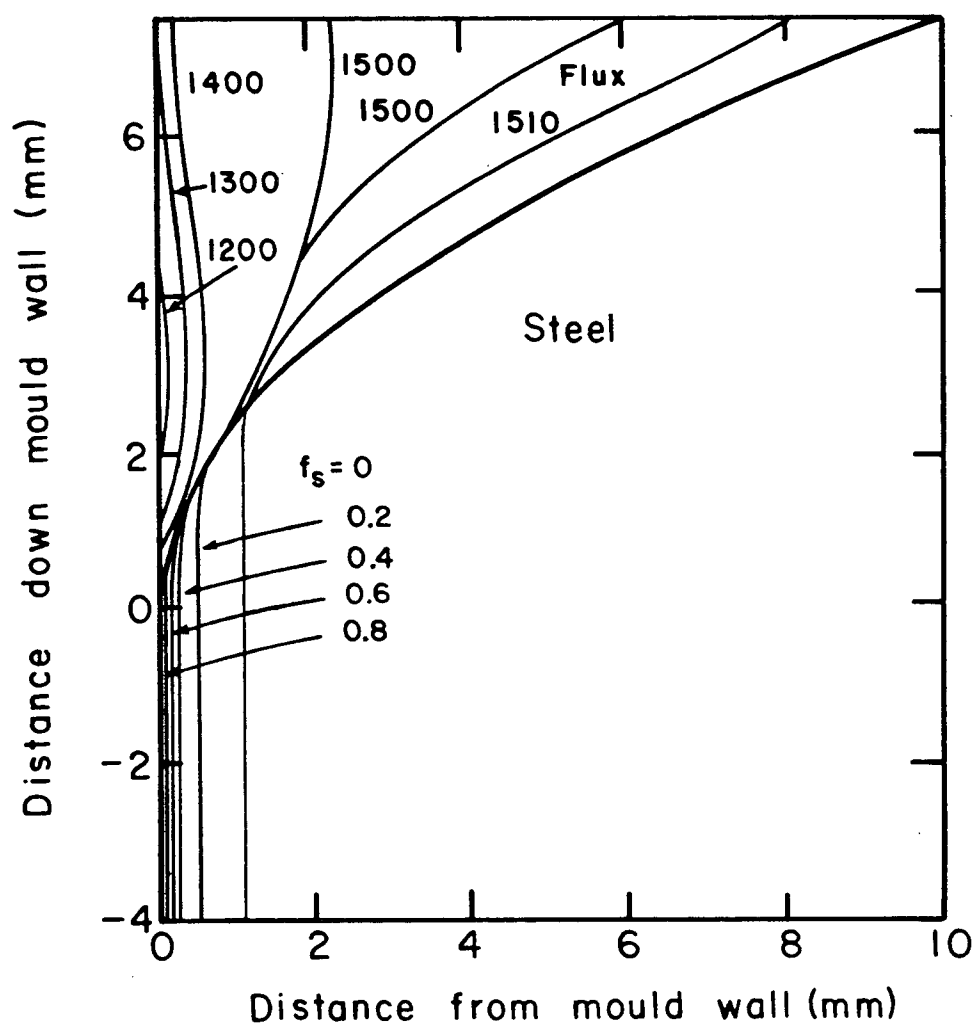


Fig. 4-31 Predicted temperature distribution in the mould flux and fraction solidified in the steel at the meniscus after a time of 0.3s. Superheat of steel is 20°C.

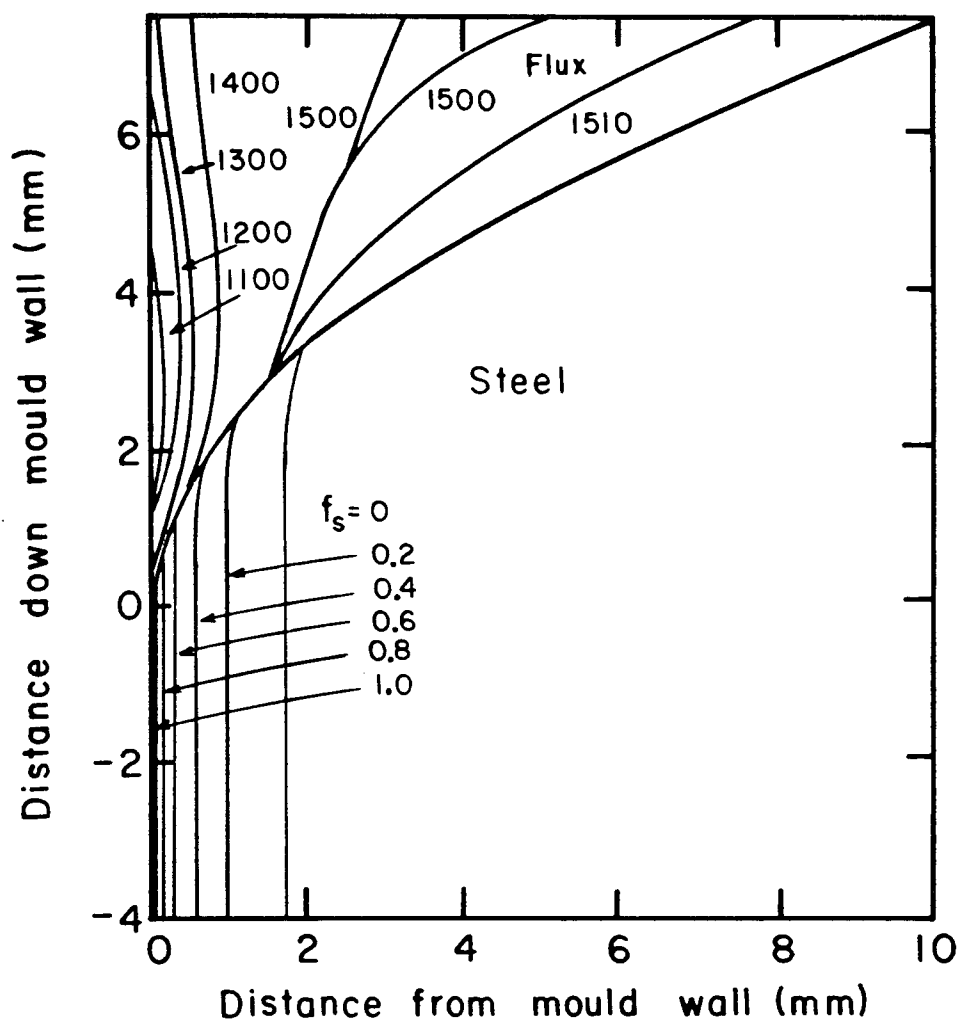


Fig. 4-32 Predicted temperature distribution in the mould flux and fraction solidified in the steel at the meniscus after a time of 0.6s. Superheat of steel is 20°C.

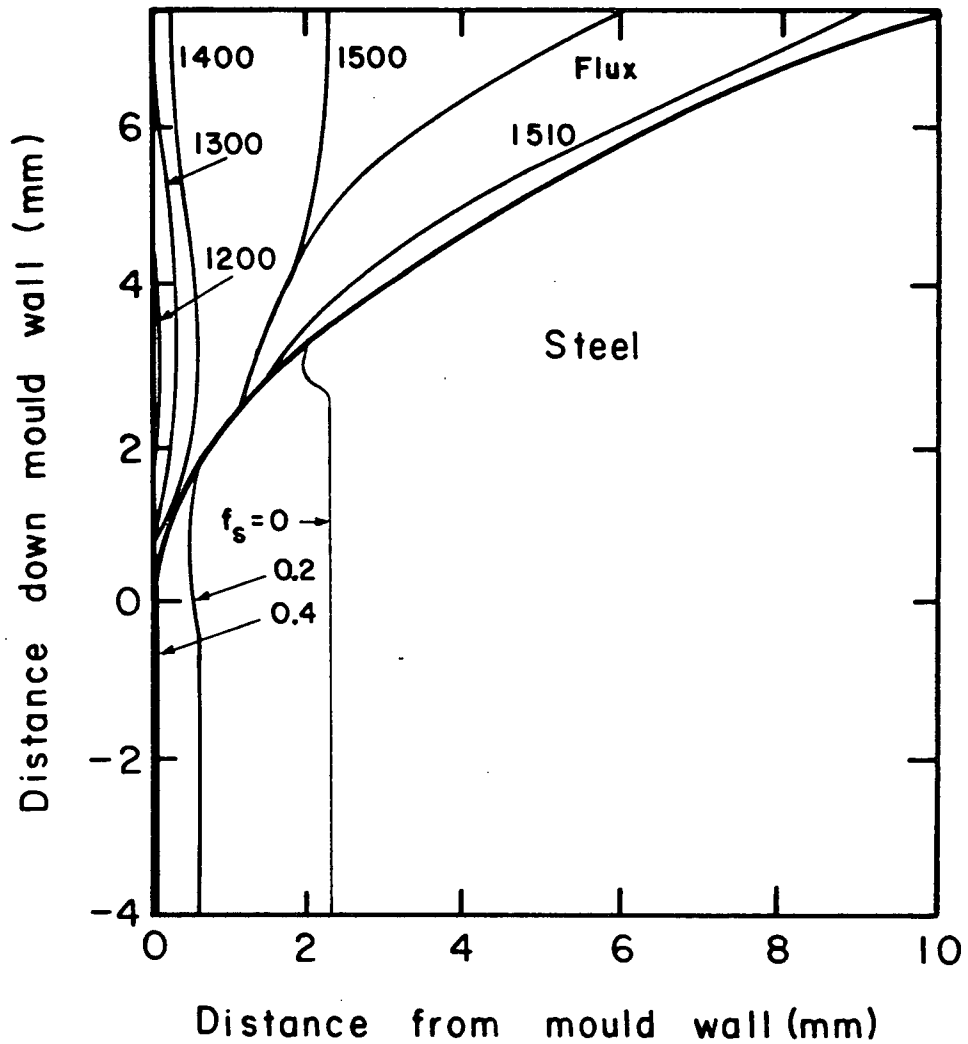


Fig. 4-33 Predicted temperature distribution in the mould flux and fraction solidified in the steel at the meniscus after a time of 0.3s. Convection in molten steel incorporated by artificially raising liquid conductivity four fold.

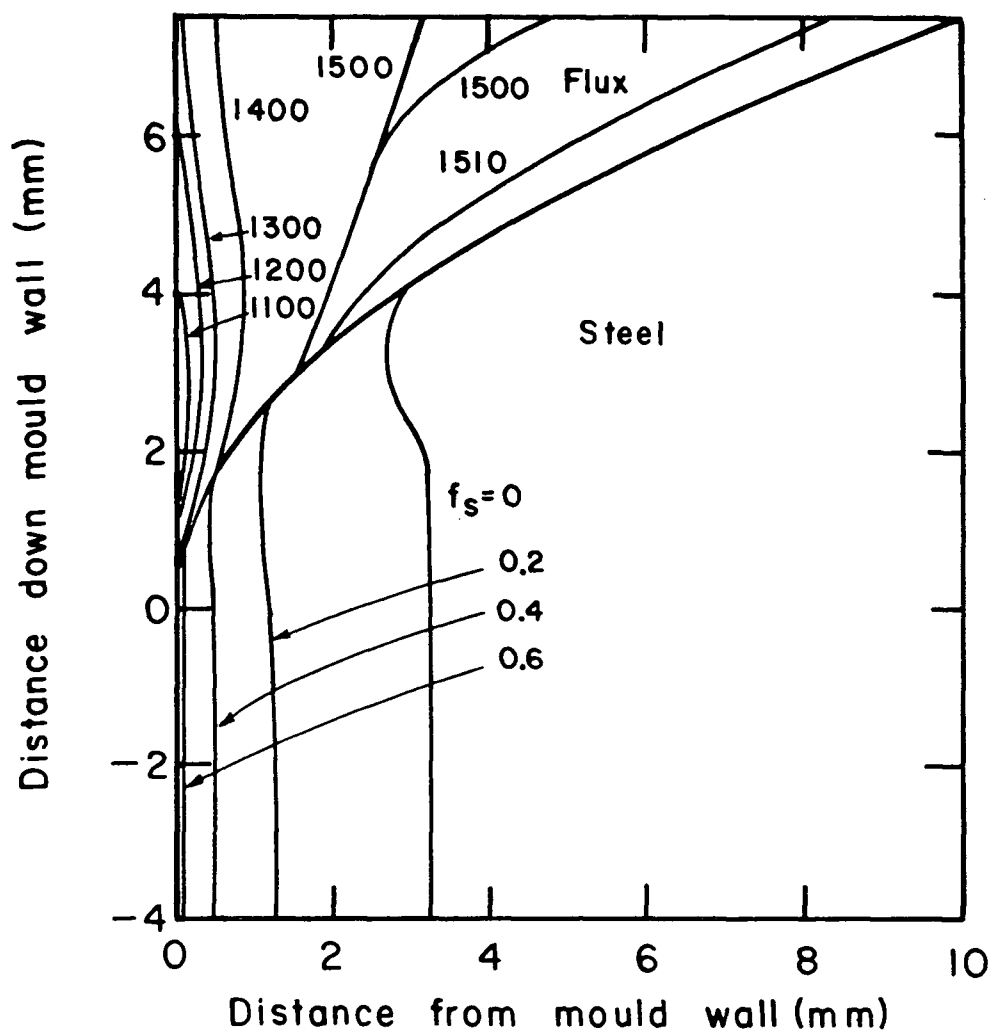


Fig. 4-34 Predicted temperature distribution in the mould flux and fraction solidified in the steel at the meniscus after a time of 0.6s. Convection in molten steel incorporated by artificially raising liquid conductivity four fold.

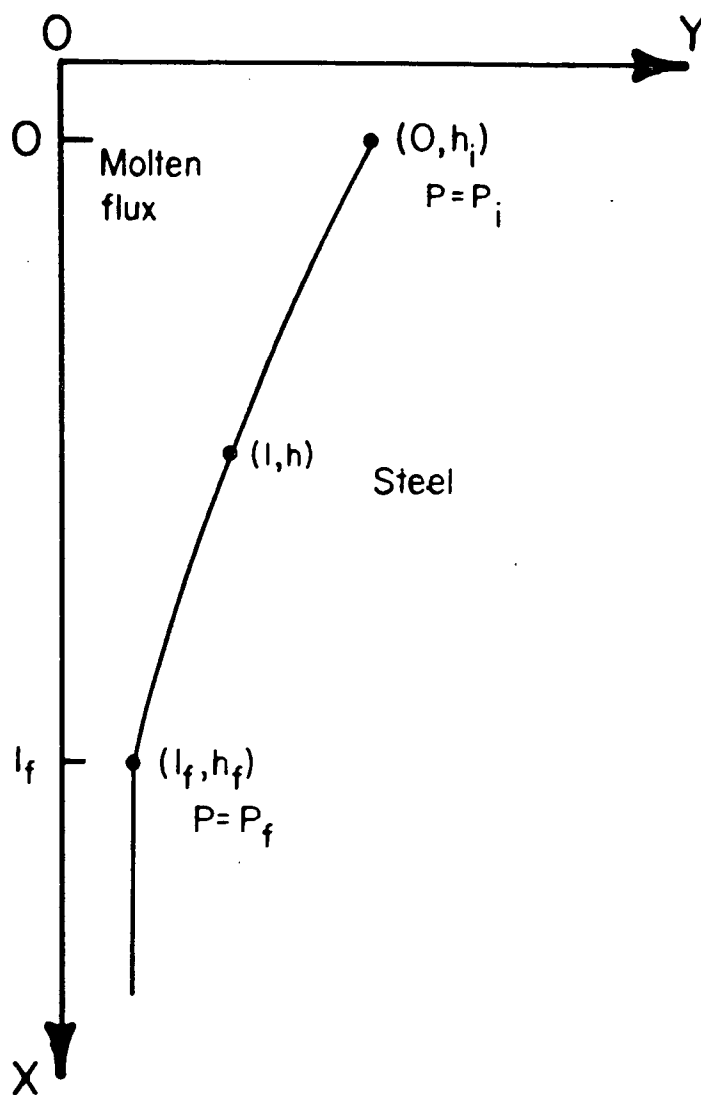


Fig. 4-35 Geometry of mould flux channel at the meniscus.

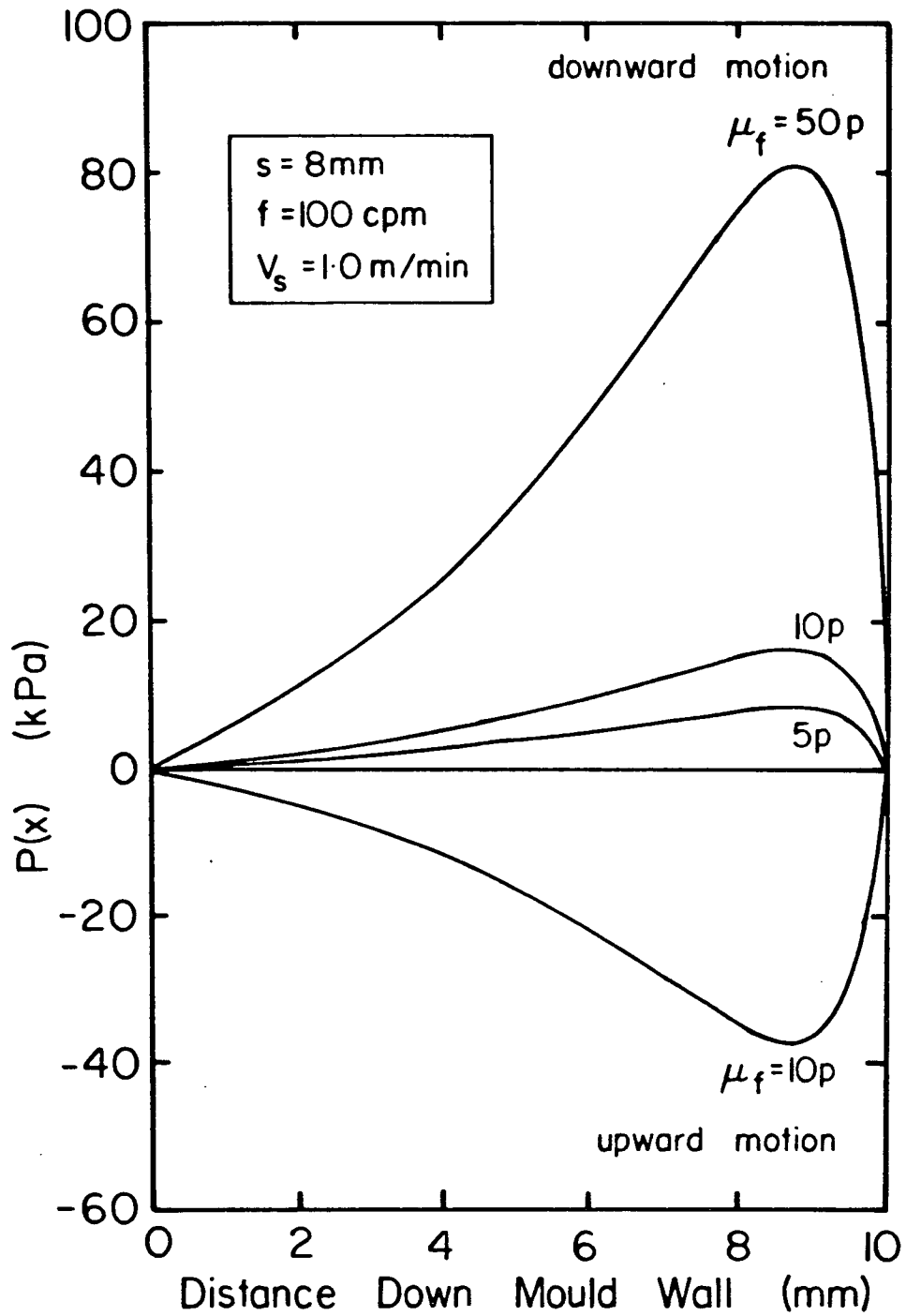


Fig. 4-36 Predicted axial pressure profiles in the flux channel near the meniscus. Flux channel dimensions assumed to be: $h_i = 0.35\text{mm}$, $h_f = 0.05\text{mm}$, $l_f = 10\text{mm}$.

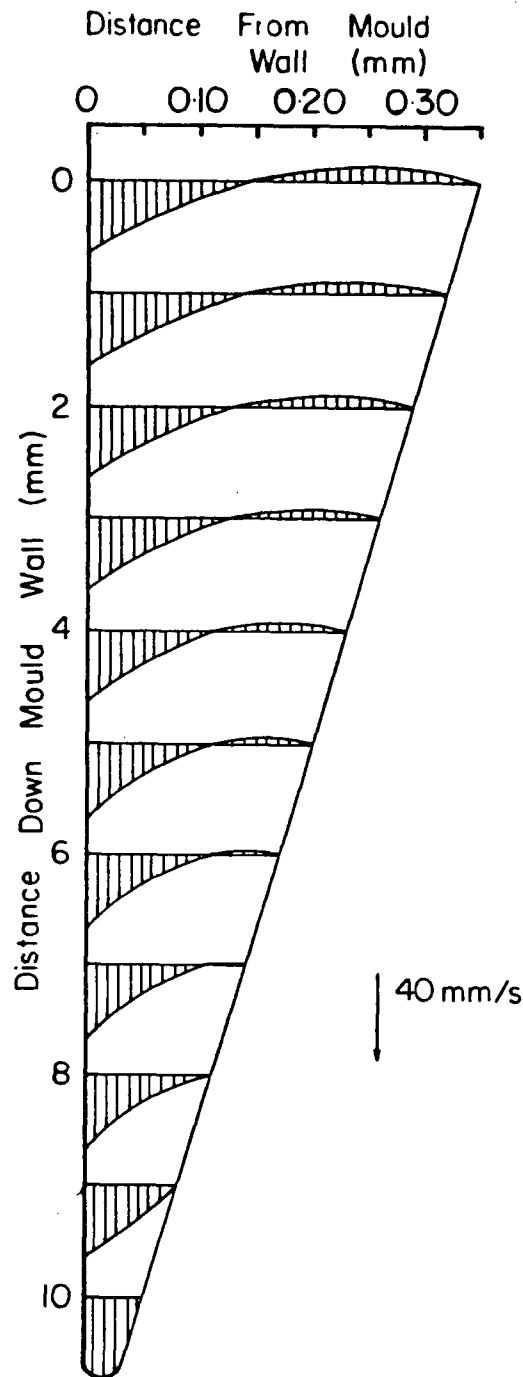


Fig. 4-37 Predicted velocity distributions in the flux channel near the meniscus at time of maximum downward velocity of the mould. Conditions as for Fig. 4-36 and assumed flux viscosity is 5P.

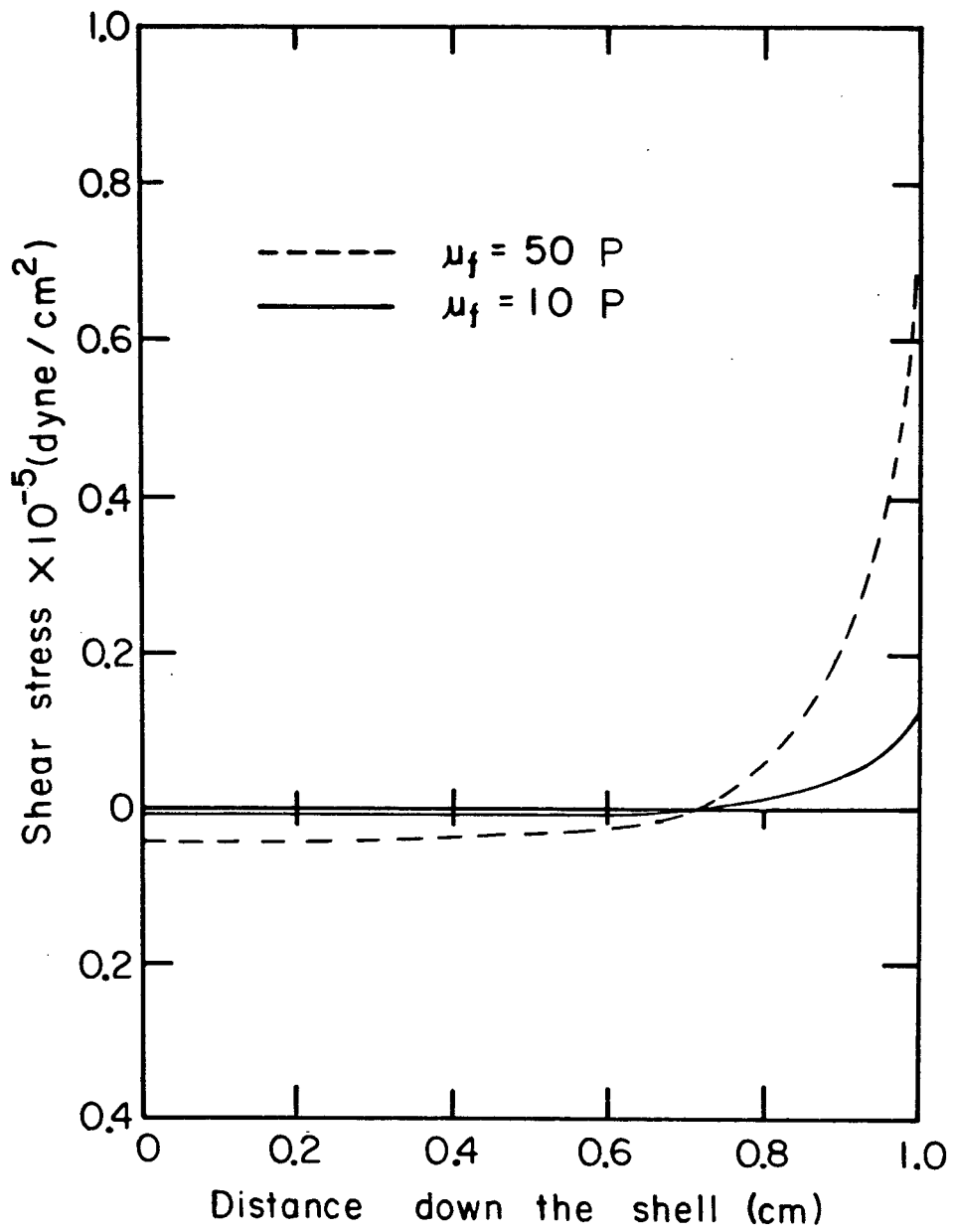


Fig. 4-38 Shear stress distribution along the shell.

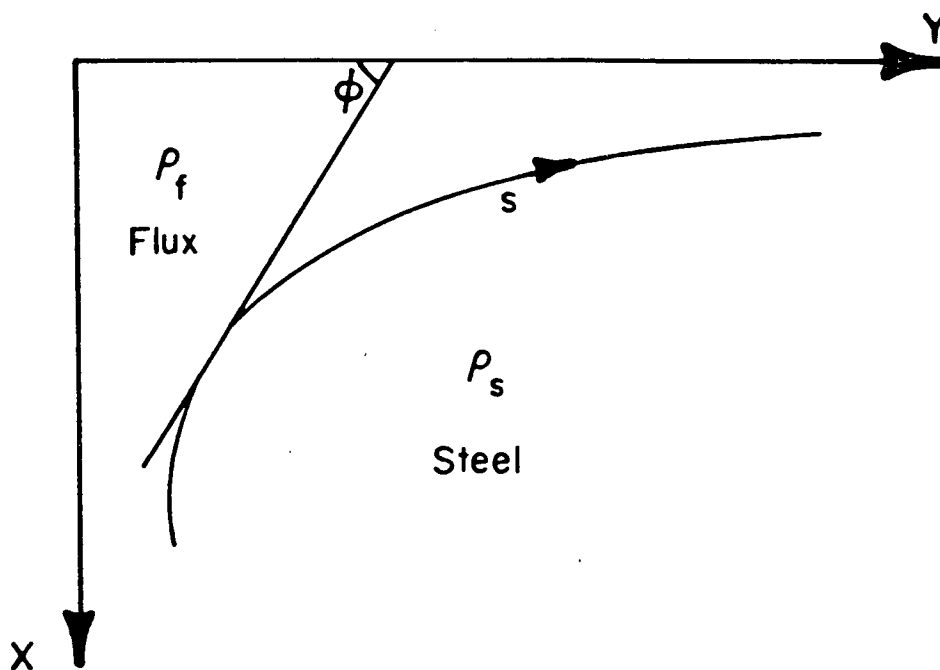


Fig. 4-39 Geometry of two-dimensional meniscus system.

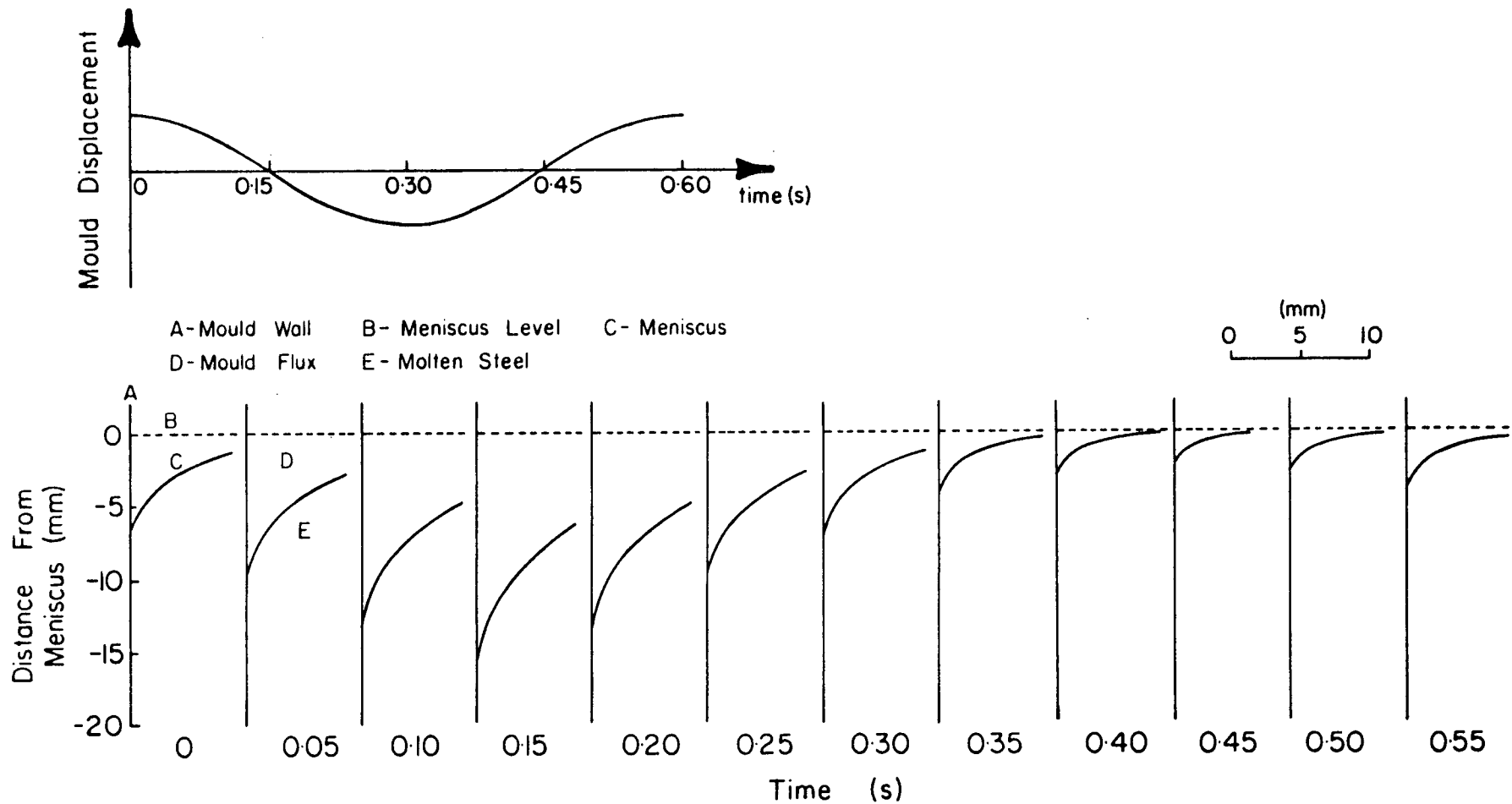


Fig. 4-40 Predicted change of meniscus shape with time resulting from sinusoidal mould oscillation ($s=8\text{mm}$, $f=100\text{cpm}$, $\sigma=1200\text{ dyne/cm}$, $\rho_s=7.2\text{ g/cm}^3$, $\rho_f=2.8\text{ g/cm}^3$).

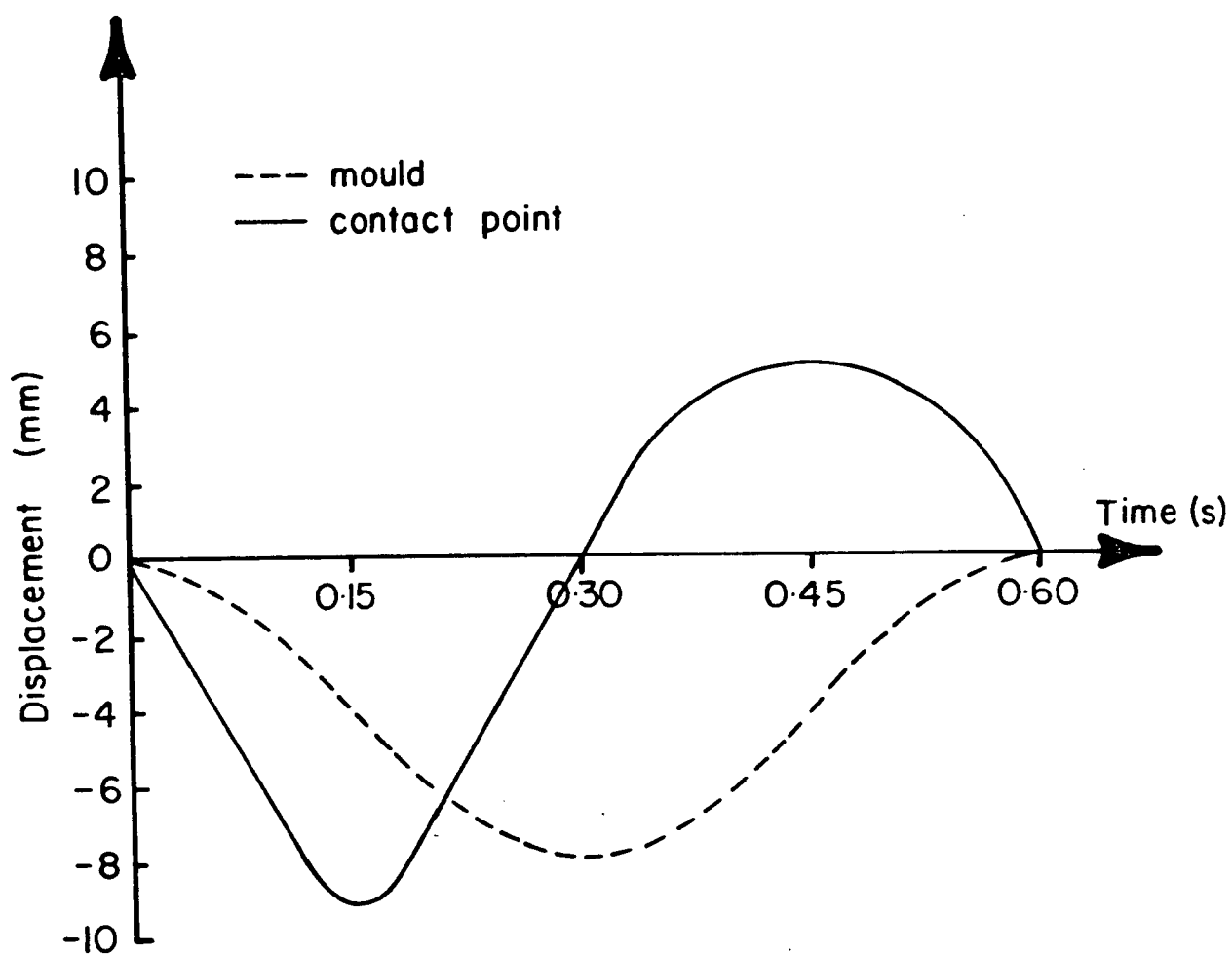


Fig. 4-41 Movement of "contact point" of meniscus with mould wall during mould oscillation. See caption to Fig. 4-40 for oscillation conditions.

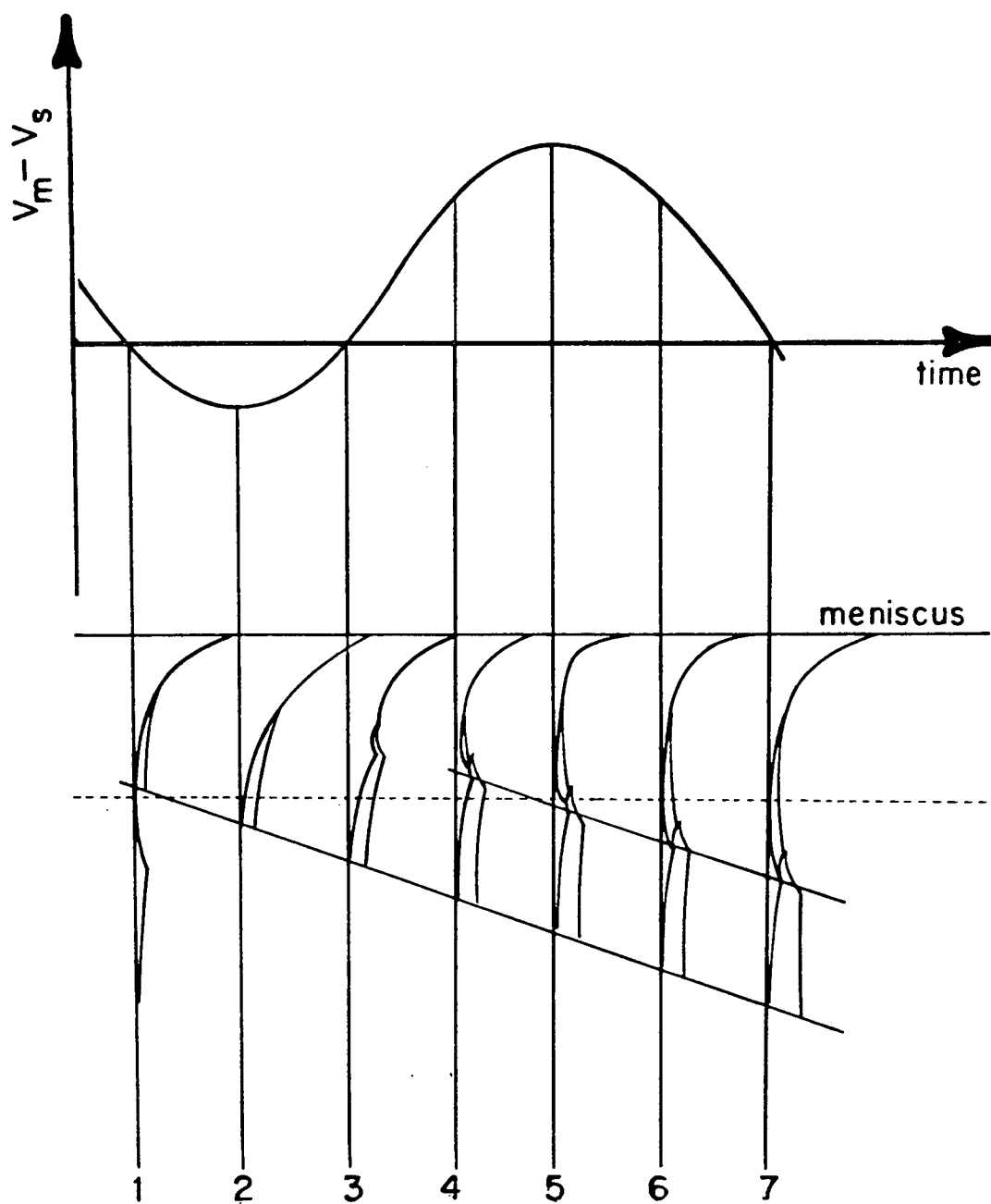


Fig. 4-42 Schematic representation of the formation of an oscillation mark with subsurface hook.

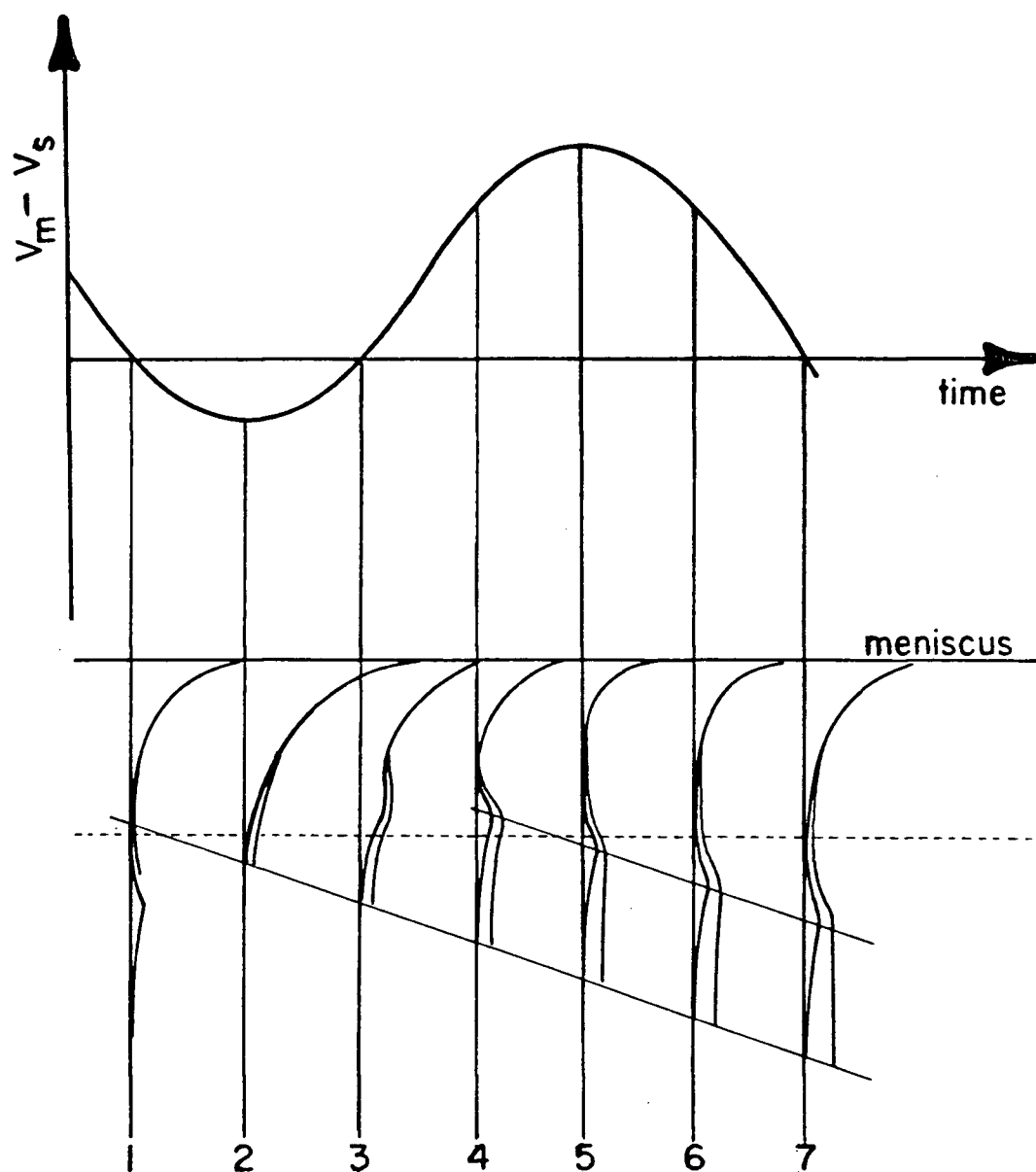


Fig. 4-43 Schematic representation of the formation of an oscillation mark without subsurface hook.

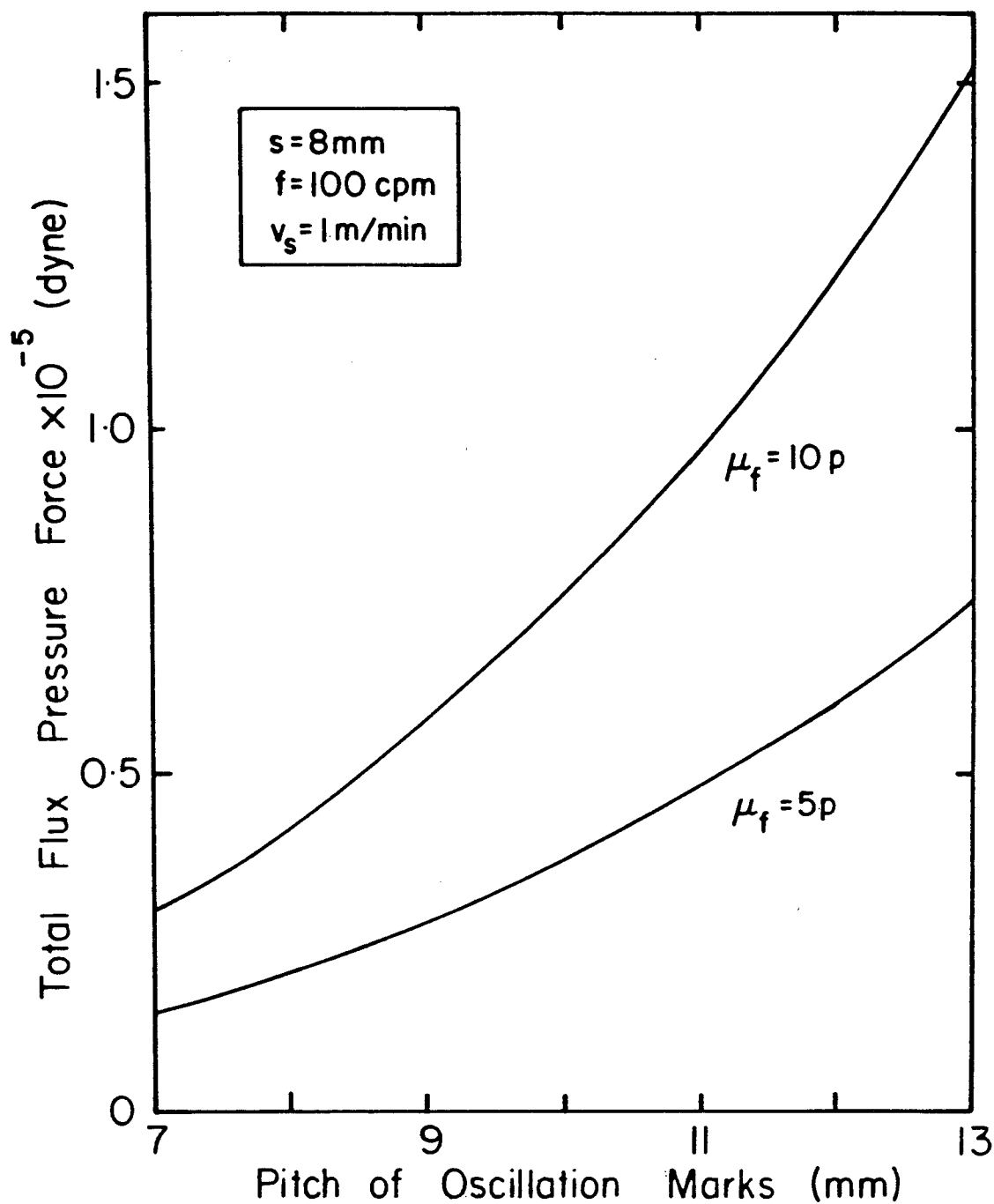


Fig. 4-44 Influence of meniscus level variation (shown as changing pitch of oscillation marks) on total force due to pressure generated in the flux channel.

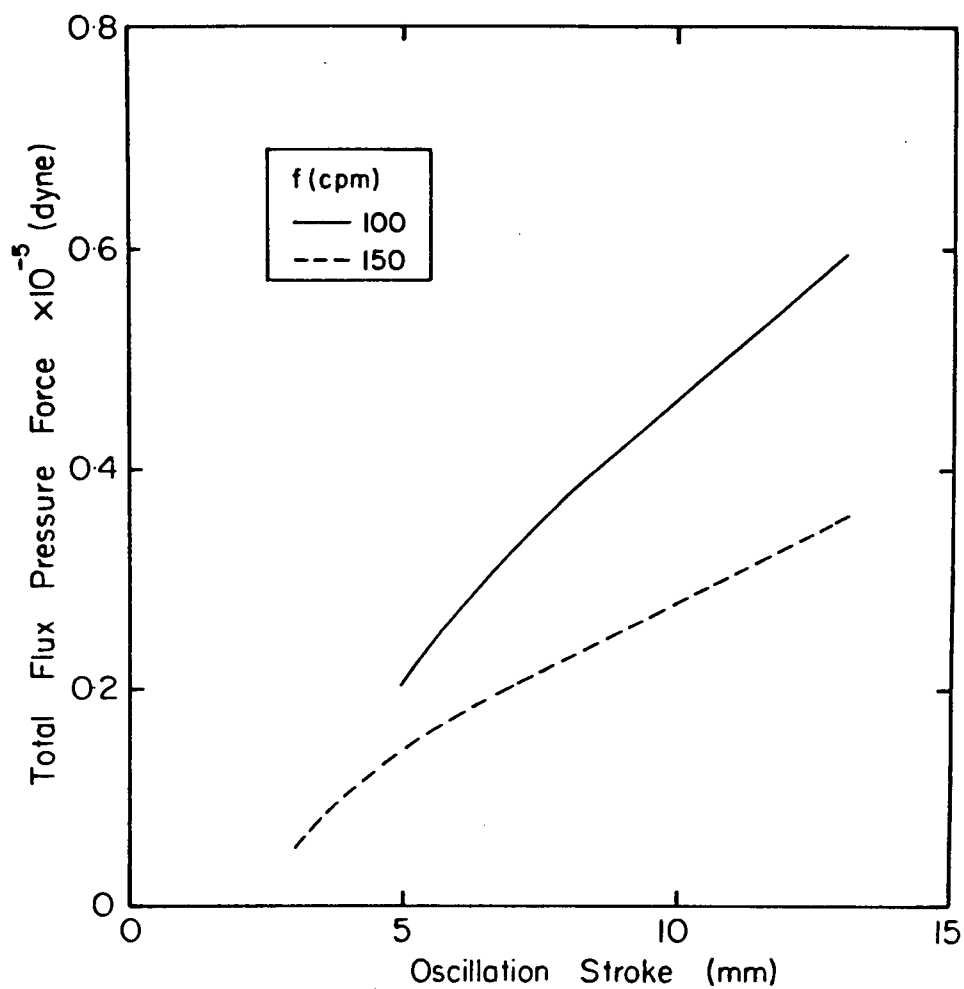


Fig. 4-45 Influence of oscillation stroke on total force due to pressure generated in the flux channel.
 $v_s=1\text{m/min.}$

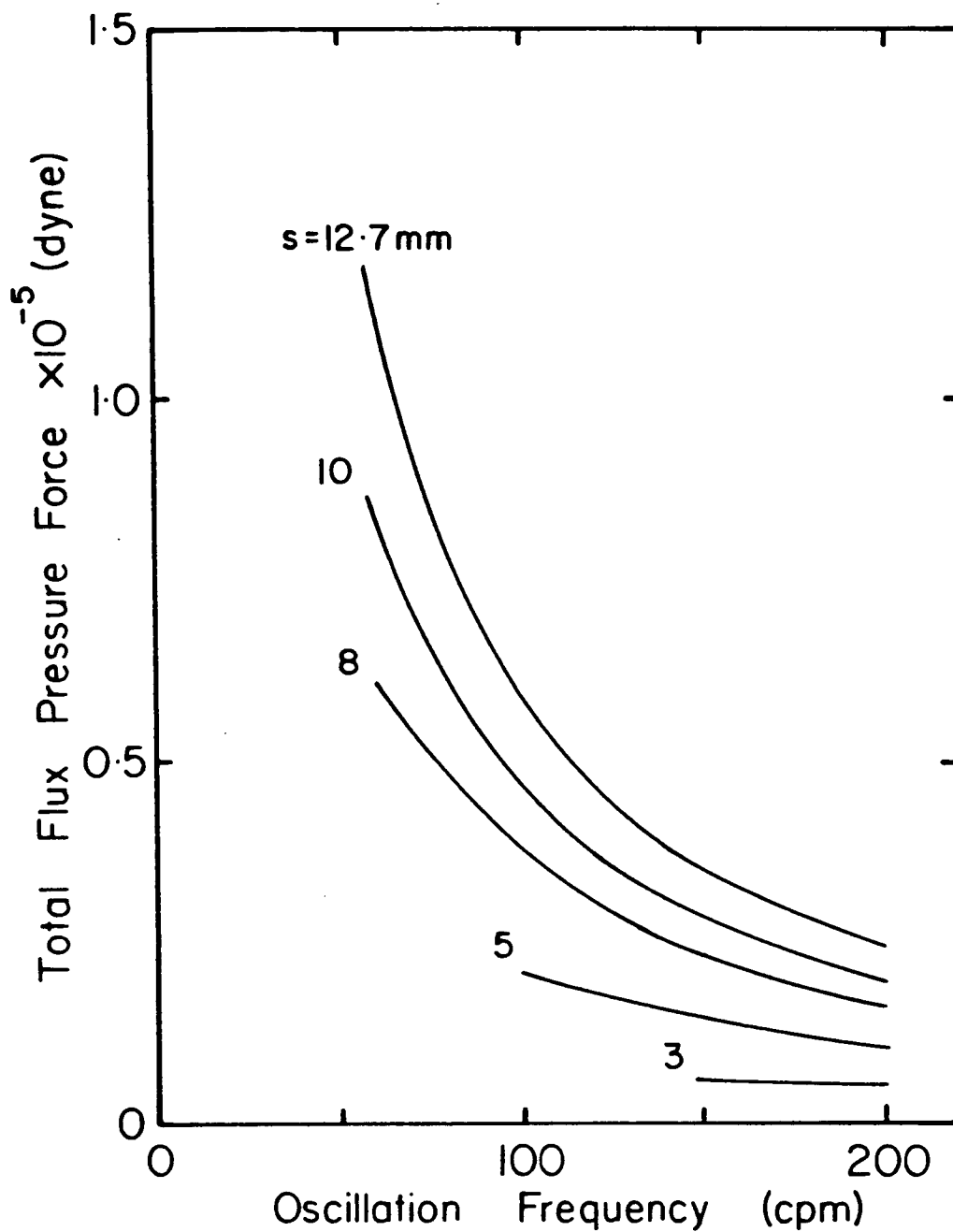


Fig. 4-46 Influence of oscillation frequency on total force due to pressure generated in the flux channel. $v_s=1\text{m/min.}$

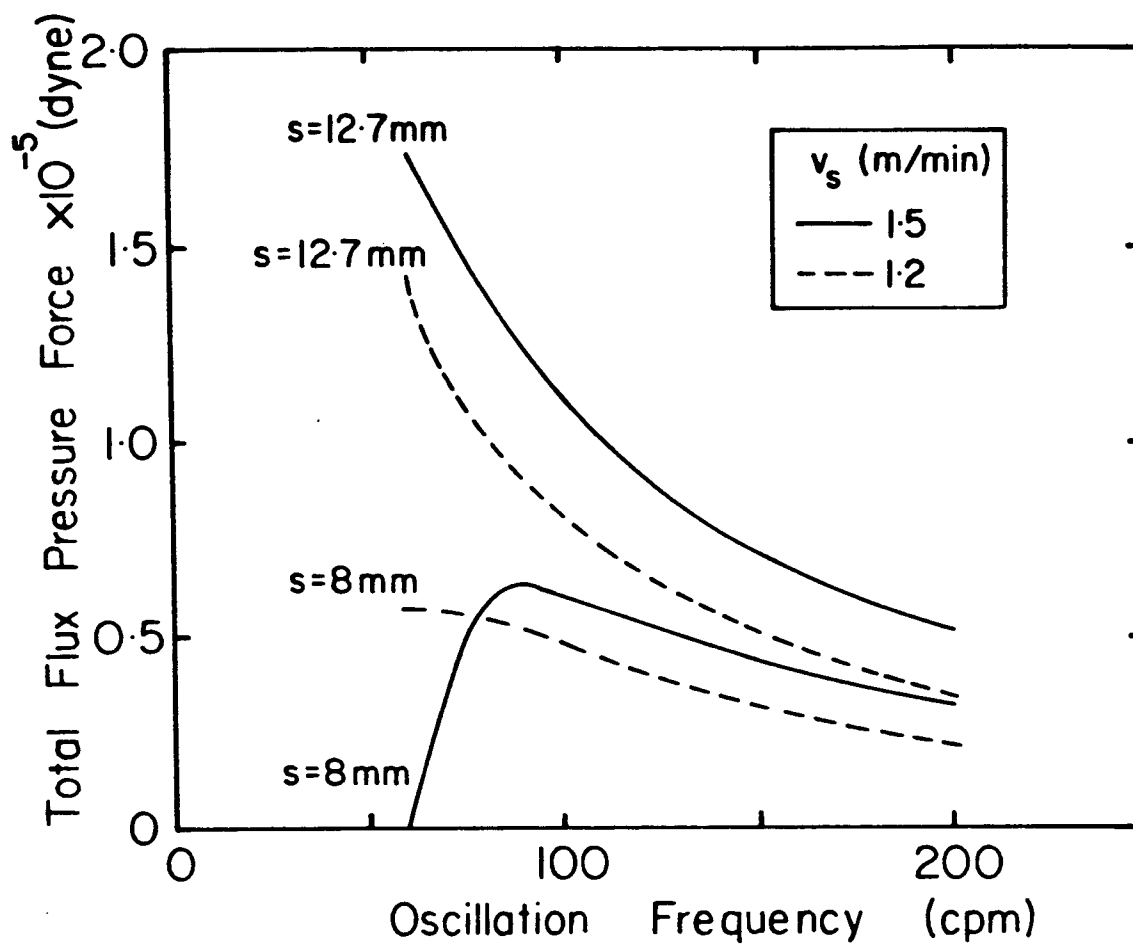


Fig. 4-47 Influence of oscillation frequency on total force due to pressure generated in the flux channel.
 $v_s = 1.2, 1.5$ m/min.

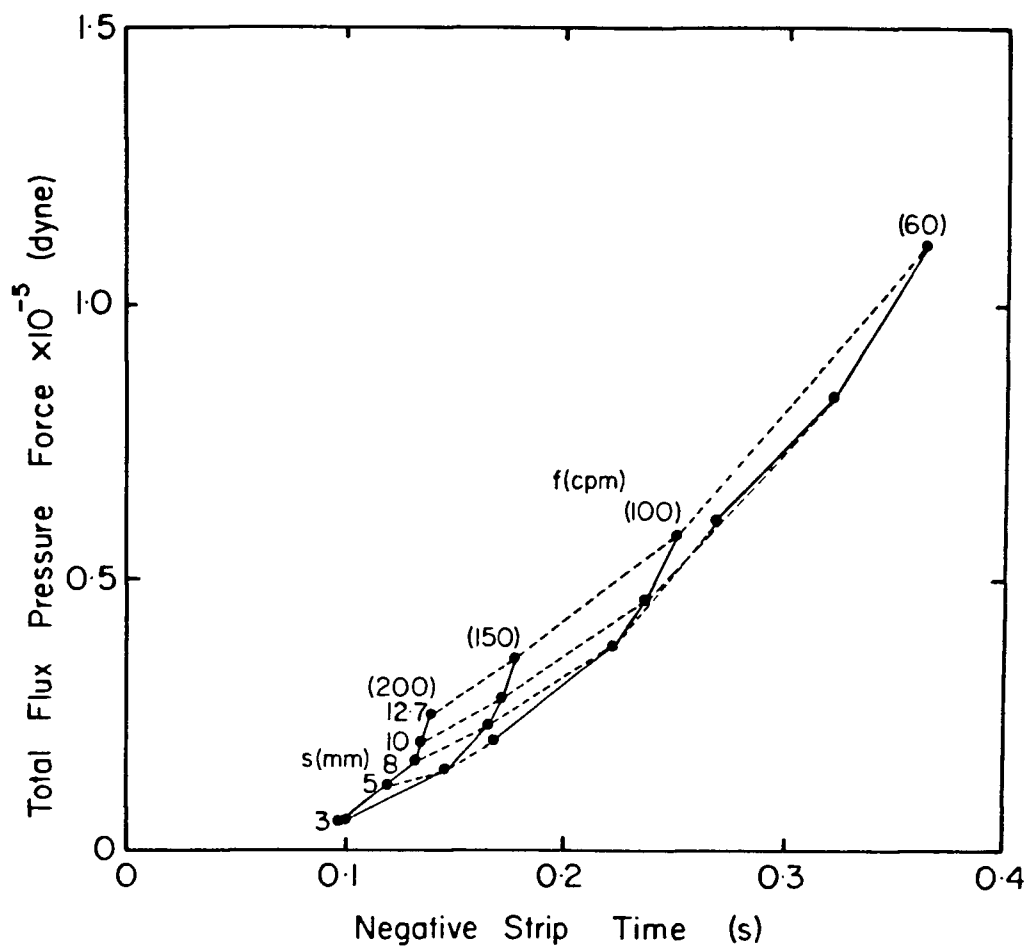


Fig. 4-48 Influence of negative-strip time on total force due to pressure generated in the flux channel (numbers in parantheses indicate oscillation frequencies). $v_s = 1\text{m/min.}$

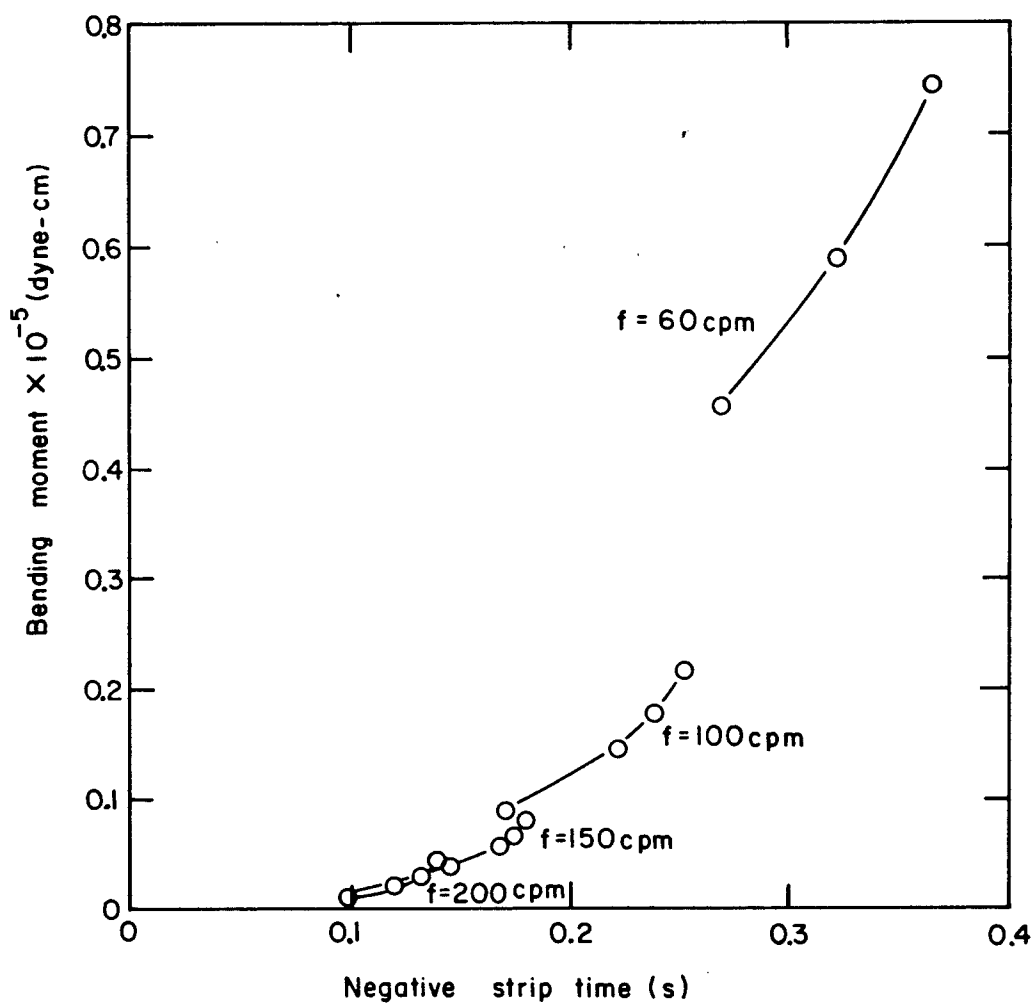


Fig. 4-49 Influence of negative-strip time on bending moment due to pressure generated in the flux channels.
 $v_s = 1\text{m/min.}$

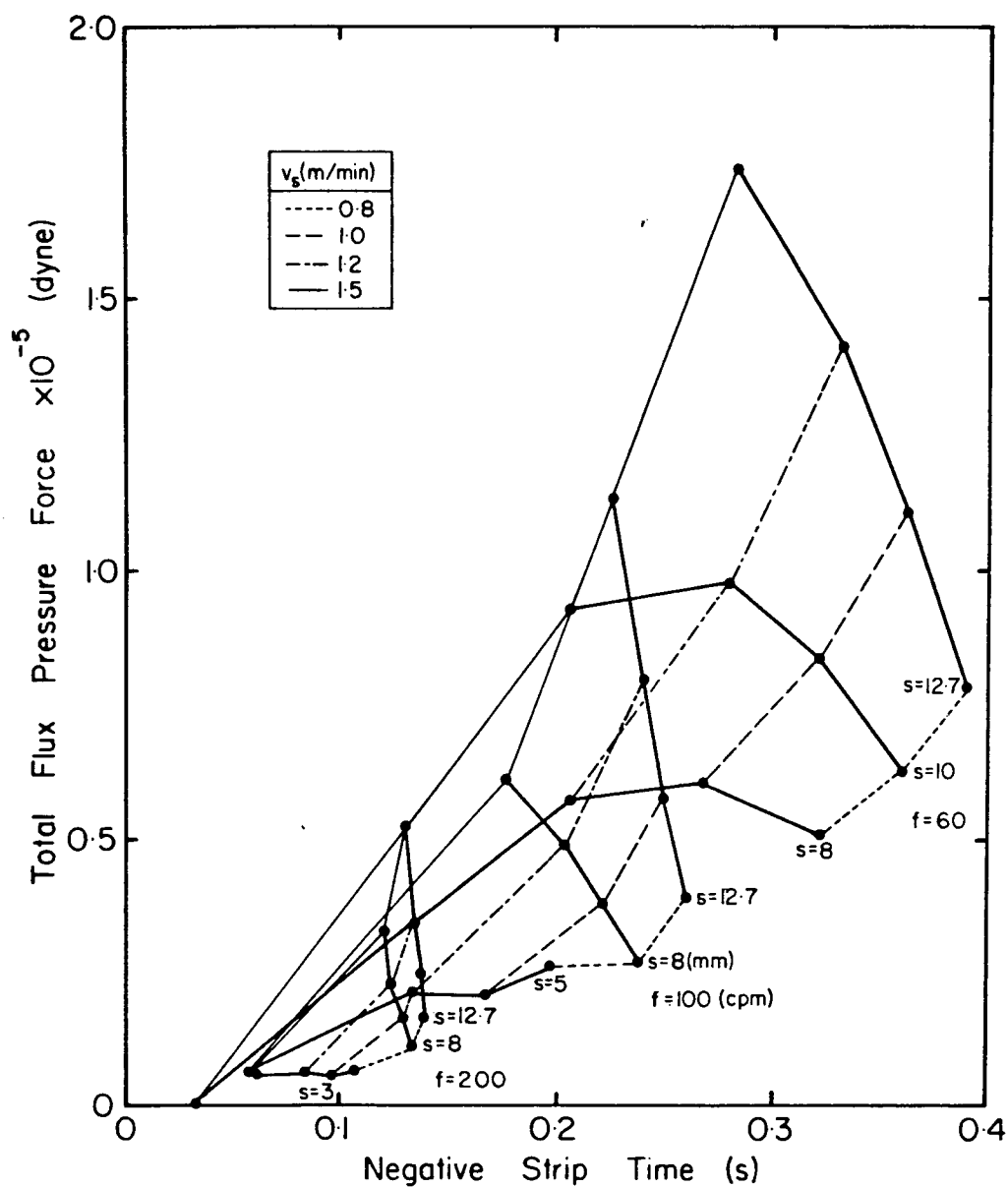


Fig. 4-50 Influence of negative-strip time on total force due to pressure generated in the flux channel. $v_s=0.8, 1.0, 1.2, 1.5$ m/min.

5. THE EFFECT OF OSCILLATION MARKS ON THE SURFACE QUALITY OF SLABS

5.1 Introduction

Transverse cracks and positive segregation of solute elements are commonly encountered surface defects associated with oscillation marks. The defects are usually observed near the bottom of the oscillation marks. Improvement in the surface quality of slabs therefore is dependent on the control of oscillation marks which in turn are affected by mould operation. For example it has been reported that the defects are reduced in frequency and severity by decreasing the depth of oscillation marks. ^{6 8 6}

Transverse cracks are one of the most common surface defects on continuously cast slabs and thus have been the subject of numerous studies. Most proposed mechanisms of crack initiation involve secondary cooling, as summarized in Chapter 2, viz fine surface cracks caused by thermal stress,^{8 4} and austenitic intergranular embrittlement associated with Ar₃ transformation^{8 0} and with precipitation of nitride^{8 1} and/or carbonitride. ^{8 2 8 3} It is believed that these events are then followed by the formation of cracks at the straightening point of the cast machine where the oscillation marks serve as a notch. ^{7 9} However, as presented in the previous chapter, the bottom of the oscillation marks is not sharp, and furthermore

the surface of slabs are usually almost flattened by support rolls. Thus the fact that transverse cracks are formed along the bottom of oscillation marks cannot be explained reasonably by the proposed mechanisms.

Regarding positive segregation, P and Ni have been reported to segregate in the vicinity of the bottom of oscillation marks in plain carbon steel slabs^{28 29} and in stainless steel slabs,²⁷ respectively. This mechanism of positive segregation has been explained only in a qualitative manner as resulting from squeezing out of interdendritic solute-rich liquid when the top of the shell is deformed during mould oscillation. ^{27 29} Such an imprecise mechanism is hardly surprising because the mechanism of oscillation-mark formation hitherto had not been understood fundamentally.

The purpose of the present work is to clarify the effect of oscillation marks on the formation of transverse cracks and also of positive segregation by metallographic investigation of these defects, and by theoretical approaches using heat flow analysis and applying the mechanism of oscillation mark formation proposed in the previous chapter.

5.2 Metallurgical Study Of Transverse Cracks

5.2.1 Casting Conditions

The casting conditions and the compositions of slab samples from Company B and C for the metallographic study of transverse cracks are shown in Table IX. The types of steel slab investigated for this defect are plain, low C, Al-killed steel with relatively high N content. For the purpose of investigating the relation between the formation of transverse cracks and the oscillation marks, slab samples from Company B with distinctly periodic oscillation marks were mainly examined. Small samples were cut out from the narrow side of the slabs, where oscillation marks had not been deformed by the support rolls.

5.2.2 Appearance Of Transverse Cracks

The oxidized surface layer on the narrow side of the slabs was first removed by sandblasting to reveal the existence of transverse cracks. In general fine transverse cracks are hard to detect on the surface of as-cast slabs, which makes transverse cracks much more troublesome in a casting operation. Fig. 5-1 shows the effect of N on the transverse crack formation. Thus the cracks were observed on the surface of slabs which have more than 60 ppm of N. This content of N for the crack formation is roughly consistent with the industrial data reported by Mukai et al. ⁷⁹

As mentioned in the previous chapter, oscillation marks on the slabs of Company C are disordered because of the large meniscus level variation. Therefore slab samples from Company C were considered to be unsuitable for the purpose of this investigation. Hereafter, investigation results of slab samples from Company B are described.

Figs. 5-2 and 5-3 show the appearance of transverse cracks formed on the narrow side of the slabs. Fine transverse cracks were observed not only at the bottom but also near the top of the oscillation marks. However, rows of relatively large transverse cracks along the bottom of oscillation marks, on the loose (inside radius) side of the slabs are more characteristic. Due to the tensile strain generated on the loose side of the slabs at the unbending point, large transverse cracks are frequently observed on this side of the slabs.

5.2.3 Subsurface Structure In The Vicinity Of Transverse Cracks

Small samples were cut longitudinally from the slab perpendicular to the oscillation marks, in the same way as described earlier for the metallographic study of oscillation marks. The longitudinal cross sections of the samples were machined flat, polished and etched with Picral, Nital and Oberhoffer's reagents to inspect the subsurface structure in the vicinity of transverse cracks. Fig. 5-4 shows the dendritic structure of a longitudinal cross section from the slab appearing in Fig. 5-2. It clearly indicates that the transverse

cracks form along the bottom of oscillation marks. The austenitic structure developed in the subsurface region, and the cracks propagated along the austenite grain boundaries. However, some intergranular cracks, which did not propagate to the slab surface, also were observed in the subsurface. Fig. 5-5 shows a Nital-etched cross section of another sample cut from the slab in Fig. 5-2, and proeutectoid ferrite can be seen along the austenite grain boundaries. As H. Suzuki has reported, transverse cracks appear to propagate along the grain-boundary proeutectoid ferrite.

The difference in austenite grain size is not clear between the top and bottom of oscillation marks in Fig. 5-5; but it is evident from Figs. 5-6(a) and (b) which show the magnified solidification structure of Fig. 5-5 near the top and the bottom respectively of an oscillation mark. There is a significant difference in grain size at these locations; the ferrite-pearlite structure is much coarser at the bottom than at the top of the oscillation mark. This finding is considered to be an important factor which controls the location of transverse cracks because along the bottom of oscillation marks transverse cracks are likely to propagate in the brittle zone consisting of the coarser structure. This phenomenon cannot be explained by the cooling rate in the spray zone but must be related to events in the mould because in addition, as was shown in the previous chapter, there is a large difference in the dendrite arm spacing between the top and the bottom of oscillation marks. The gap created by each oscillation mark apparently increases the

thermal resistance for heat extraction from the slab surface which causes locally high temperature and results in a nonuniform structure in the mould. At the same time the cooling rate is reduced leading to a coarser dendritic structure. This argument thus links the coarse dendrite structure to the coarse austenite structure, and consequently to the coarse ferrite-pearlite structure, from which it can be inferred that the nonuniform cooling in the mould region is responsible for the nonuniform subsurface structure. This phenomenon is pursued further in a later section with the aid of a heat transfer analysis.

Next, the primary solidification structure near the transverse cracks was examined in detail. Fig. 5-7 shows the dendritic structure near the bottom of an oscillation mark which does not exhibit a subsurface hook. Dendrites develop normal to the slab surface, and at the bottom of the marks, fine cracks, which are not open to the surface, are observed between the dendrites. These fine cracks are interdendritic, as will be proven later, and clearly indicate that they were formed in the mould region. Formation of these interdendritic fine cracks is explained as follows; the solidifying shell in the mould region is subjected to various kinds of stress and/or strain, viz i) mould friction force may operate on the shell surface when the lubrication by mould flux is insufficient, or ii) shell shrinkage due to δ - γ transformation may occur nonuniformly in the approximate carbon range 0.10% to 0.15%. These stresses and strains concentrate at the bottom of oscillation marks, where

the shell is thinner, owing to the low heat extraction, and hot tears result.

Another type of fine crack was also found at the bottom of oscillation marks which exhibited subsurface hooks, Fig. 5-8. These fine cracks have been generated along the hook where positively segregated P gave rise to a brittle structure. Tanaka et al²⁹ have also reported this type of fine crack along the hook of the oscillation marks at slab corners.

Thus as described above, transverse cracks may be initiated in the mould: 1) between dendrites or in regions of positive segregation of the bottom of oscillation marks, 2) in regions of positive segregation in the vicinity of oscillation marks, and 3) in a coarse solidification structure. These subsurface characteristics also provide good sites for transverse crack formation along the oscillation marks in the secondary cooling zone and/or at the unbending point of the strand.

5.2.4 Surface Of Transverse Cracks

The surface of the cracks was examined by breaking open a crack-containing steel section at -196°C after immersion in liquid nitrogen. The crack containing sample was cut out from the narrow side of the slabs and was characterized by three different types of cracks. These will be referred to as Cracks [1], [2], and [3] as shown in Fig. 5-9. Crack [1] forms partially along the bottom of oscillation marks but gradually deviates from the bottom; Crack [2] forms along the mark; Crack

[3] does not open to the slab surface but can be observed in the cross section. The fractured samples were immersed in a solution of 3ml HCl, 4ml 2Butyne-1, 4-Diol and 50ml distilled water in an ultrasonic cleaner to remove the oxide film from the crack surface. ¹⁰² While removing the oxide, the solution does not seriously alter the original structure. The crack surface then was observed with a scanning-electron microscope. Fig. 5-10 shows the surface of Crack [1]. The smooth surface of this crack clearly reveals the angular appearance of austenite grain boundaries. The surface in the lower part of Fig. 5-10 is characteristic of the low-temperature faceted, brittle fracture and can be distinguished from the original cracked surface. Fig. 5-11 shows the surface of Crack [2]. This crack surface also exhibits mostly austenite grain boundaries as in Fig. 5-11(a); however the partially undulating surface in Fig. 5-11(b) indicates the crack is interdendritic in some locations. Fig. 5-12 shows the surface of Crack [3]. The upper undulating surface is evidently interdendritic. The lower crack surface shows relatively flat faces which indicates austenite grain boundaries. This type of cracks corresponds to the crack observed on the cross section of the slab shown in Fig. 5-7. The crack propagation seen may occur not only toward the inside of slabs but also along the bottom of oscillation marks where the positive segregation and coarse grains cause a brittle structure. Interdendritic fine cracks which act as initiation sites are not necessarily located continuously along the bottom of oscillation marks.

Fig. 5-13 shows another crack surface in a sample from Company C. A low magnification micrograph, Fig. 5-13(a), shows the crack surface consists mostly of austenite grain boundaries. In this case adherent material was observed on the crack surface before cleaning. Therefore the surface was subjected to X-ray analysis using a SEM to determine the chemical composition of the material. Potassium detected in the X-ray spectrograph clearly indicated that the adherent material was mould flux. It should be noted that the mould flux used in this experiment does not contain sodium. Subsequently, this crack surface was further examined with a SEM at relatively high magnification and a region containing small interdendritic cracks was found close to the surface, Fig. 5-13(b). This observation suggests that the cracks were possibly initiated by interdendritic cracks which must have opened to the slab surface in the mould. This crack was then expanded and propagated in the sub-mould region at the austenite grain boundaries to form transverse cracks along the oscillation marks.

5.2.5 The Effect Of Oscillation-marks Shape On Local Shell Thickness.

Fig. 5-15 shows the relationship between the depth of oscillation marks and the nonuniformity of the shell thickness which was estimated from the white band caused by the input stream from the immersion nozzle. Samples examined were taken from a 0.10%C slab from Company B. It is seen that deep oscillation marks give rise to a locally thin shell. This

relationship is examined theoretically using a two-dimensional heat transfer model in a later section. It may also be noted that cracks are associated with the deepest oscillation marks; no cracks or only fine subsurface cracks were found with shallow oscillation marks.

It is well known that the shell shrinkage due to δ - γ transformation prevents uniform heat extraction in the mould which causes locally reduced shell thickness. The present work shows that the oscillation marks create a large local thermal resistance between mould wall and shell surface also to cause nonuniformity of the shell profile.

5.2.6 Summary Of Metallurgical Investigation Of Transverse Cracks

From this metallurgical investigation, the formation mechanism of transverse cracks along oscillation marks can be explained as follows:

- 1) Firstly the large gap between the solidified shell and the mould wall at the bottom of oscillation marks locally reduces heat extraction and the rate of solidification.
- 2) Secondly friction force between the solidified shell and the mould wall via the mould flux, coupled with strain due to volume shrinkage caused by δ - γ transformation in the range from 0.10-0.15% carbon content in steel, concentrate at the thinner part of the shell, namely at the bottom of oscillation marks, to form interdendritic cracks.
- 3) Finally below the mould these fine cracks propagate both

toward the inside of the slab and along the bottom of oscillation marks where the structure is most brittle owing to positive segregation of P and coarse grains. Embrittlement of austenite grain boundaries is due to the precipitation of both a proeutectoid ferrite film and AlN.

5.3 Metallurgical Studies Of Positive Segregation Near Oscillation Marks

5.3.1 Casting Conditions

A metallographic investigation was made into the positive segregation at the bottom of oscillation marks both in plain low-C, Al-killed steel slabs and in stainless steel slabs. Samples for the plain carbon slabs are from Companies A and B; the stainless steel samples are from Company F. Small samples were cut from the narrow side of the slabs in the same way as those for the transverse-crack study. The casting conditions and chemical composition of samples examined are shown in Table X. The etching reagents used for the plain-carbon steel samples is the same as those used for the metallurgical investigation of transverse cracks. A solution of $\text{FeCl}_3(5\text{g}) + \text{CuCl}_2(5\text{g}) + \text{HCl}(100\text{ml}) + \text{C}_2\text{H}_5\text{OH}(80\text{ml}) + \text{H}_2\text{O}(300\text{ml})^{103}$ was used for the etching of the stainless steel samples.

5.3.2 Metallographic Classification Of Positive Segregation

In general, positive segregation of solute elements, especially P, is observed near the bottom of oscillation marks. As shown in Chapter 2, the region of positive segregation in the subsurface structure containing hooks is along the hook or between the hook and the slab surface. When hooks are absent from the subsurface structure, the segregation is found outside of the bottom of the oscillation marks. In this section the characteristics of positive segregation are classified in association with the various types of subsurface structure observed near the oscillation marks. Typical etched structures near the bottom of oscillation marks are shown in Fig. 5-16 - 5-20. A, B, and C indicate the use of Picral, Oberhoffer, and Nital etches respectively. The black region in A, corresponding to the white region in B, clearly indicates phosphorus segregation. In C black or gray areas indicate pearlite grains, while the white areas indicate proeutectoid ferrite grains.

Fig. 5-16 and 5-17 show the positive segregation formed at the bottom of oscillation marks which have adjacent subsurface hooks. Sample B1, Fig. 5-16, and sample B2, Fig. 5-17, are from Company A and Company B respectively. The samples exhibit two common characteristics: deep oscillation marks and a hook oriented at a shallow angle to the surface. Both observations can be attributed to the low carbon content ($C \approx 0.10\%$) as was seen in an earlier chapter. A large region of segregation exists between the hook and the surface of the slab. Another

interesting characteristic was found in the subsurface structure in Fig.5-17C. The top half of the hook disappears then reappears, and it looks as if one or more channels cross the hook. The existence of these channels across the hook suggests that steel (interdenritic liquid) flows from the inside to the outside of the shell. The force causing the flow is likely to be the negative pressure generated in the flux channel during the positive strip period of the mould oscillation cycle. This will be discussed in a later section.

Sample B3 was cut from the same slab as Sample B1 and it too exhibits hooks in the subsurface structure. However the hooks are located closer to the top of the oscillation marks rather than at the bottom. Although the hook is clearly delineated in Fig. 5-18A, it is not distinct in Figs. 5-18B and 5-18C. Only a weak segregation line similar to an interdendritic segregation is observed. The major difference between Sample B1 and Sample B3 is the location of the hook and therefore of the overflow of liquid steel. This difference can be explained based on the mechanism of oscillation mark formation proposed in the previous chapter. In the case of Sample B1 the meniscus shell is more rigid (thicker) and resists being pulled back toward the mould wall by the negative pressure in the mould flux and overflow occurs early in the positive-strip period. However in the case of Sample B3, the shell is drawn back by the negative pressure because of relatively lower rigidity of the meniscus shell (likely thinner) before molten steel overflows the hook. Consequently the hook is closer to

the top of the oscillation mark in Sample B3 owing to this delay of overflow.

Specifically, the overflow region in Sample B1 is farther from the mould wall than in Sample B3, which implies that the thermal resistance between mould wall and the bottom of oscillation marks of Sample B3 is less than that of Sample B1. This suggests that the heat transfer may have a strong effect on the positive segregation.

Fig 5-19 shows the subsurface structure of Sample B4. This has a higher carbon content ($C=0.26\%$, Company A), and therefore the depth of oscillation marks is shallower. Also, as seen earlier the hook forms a large angle with the surface as compared with lower carbon steels. However, the location of the positive segregation is almost the same as that of Sample B3, namely in the form of a weak segregation line along the hook. In addition to the discontinuity of the primary solidification structure characterized by the hook, another discontinuity is observed in the secondary solidification structure, viz the proeutectoid ferrite precipitated along the austenite grain boundaries. Note that the grain-boundary ferrite was hardly observed in the sample with $C \leq 0.20\%$, because at lower carbon contents the ferrite precipitates more easily within the austenite grain.

Fig. 5-20 shows the positive segregation at the bottom of an oscillation mark in Sample B5 which does not have adjacent subsurface hooks. The casting conditions of Sample B5 are the

same as those of Sample B4. The solidified layer adjacent to the bottom of the oscillation marks can be distinguished from the structure beneath, Fig. 5-20, and exhibits a high phosphorus content. Because overflow at the meniscus does not give rise to this type of structure, it is reasonable to infer that the segregation occurs by penetration of interdendritic liquid through the semi-solidified shell, as proposed in the case of Sample B2.

Fig. 5-21 shows the dependence of the thickness of this segregation layer on the depth of oscillation marks. Thus the thickness of the layer increases with increasing depth of oscillation marks. As proposed before, the negative pressure generated in the mould flux during the upward motion of the mould is also considered to be a strong driving force for this type of segregation. The relationship shown in Fig. 5-21 is to be discussed later.

Fig. 5-22 shows the positive segregation observed at the bottom of oscillation marks in the stainless steel slabs. This type of segregation is similar to that seen in Sample B5, which is characterized by the absence of subsurface hooks. As shown in the next section, Ni is chiefly segregated in the white region, the mechanism of which is thought to be the same as that in Sample B5.

5.3.3 Microanalysis Of Positive Segregation By CMA

Segregation of elements in the subsurface area of oscillation marks have been investigated with a CMA (Computer aided X-ray Micro Analyzer).⁸⁷ The principle of measurement of CMA is similar to that of EPMA. However CMA is capable of characterizing a relatively large area of sample (max. 90x90 mm) with highly computerized functions, while ordinary EPMA can determine a small area (max. 0.25x0.25mm). In this study, the analysis area is 3x3mm; the beam diameter is 10 μ m.

Figures 5-23 to 5-25 show the distribution of Mn and P in the subsurface area of the oscillation marks. The respective subsurface structures are shown in Fig. 5-17, 5-18, and 5-20. Positive segregations of Mn and P are clearly observed at the end of the overflow region in Fig. 5-23 (Sample B2), while only a weak segregation of P is detected along the hook in Fig. 5-24 (Sample B3). Fig. 5-25 reveals the segregation of both elements along the periphery of the bottom of the oscillation mark (Sample B5). Fig. 5-26 shows the segregation of Ni and P in the overflow region at the bottom of the oscillation marks. The respective subsurface structure is shown in Fig. 5-22 (Sample B6).

Fig. 5-27(A) and (B) show the contour maps of segregation in the areas which are considered in Fig. 5-23 and 5-25 respectively. The highest segregation ratios of Mn(1.4) and P(3.0) approximately correspond to the reciprocal numbers of equilibrium partition ratios of Mn (0.73)¹⁰⁹ and P(0.28),¹⁰⁹

respectively.

5.3.4 Positive Segregation Caused By Overflow At The Slab Corner

The investigation of positive segregation at the bottom of oscillation marks suggests that heat transfer plays an important role in the segregation mechanism. However it is not easy to discuss the heat transfer effect independently of interdendritic flow which is evident from the metallographic investigation of longitudinal cross sections of samples. To clarify the effect of heat transfer on positive segregation, samples in the vicinity of the slab corner were examined metallographically. In general, periodical overflow of molten steel is observed at the slab corner, but the steel overflows not only in the casting direction but also laterally into the bottom of oscillation marks, Fig. 5-28.

Fig. 5-29 shows the longitudinal cross section close to the corner of the sample etched by Picral seen in Fig. 5-28. The casting conditions of this sample are the same as those of Sample B5. The depth of the oscillation mark, which does not include the thickness of the solidified layer on the bottom, tends to increase toward the corner of the slab. The shell at the bottom of the oscillation mark is discontinuous in Sections #4 and #5, although Sections #1 - #3 show the typical subsurface structures in the absence of hooks.

With respect to positive segregation, no segregation could be found in Section #4 and #5 which are located closest to the slab corner. However Section #3 which is the end of the overflow to the bottom of the oscillation mark unambiguously indicates some segregation. To check the result, a transverse cross section of a slab corner at the bottom of oscillation marks was taken from the same type of samples as Sample B5. Fig. 5-31(a) and (b) show the dendritic structure etched by Oberhoffer's reagent in the longitudinal cross section and in the transverse section respectively, see Fig. 5-30. Fig. 5-31(a) shows that the oscillation mark is not accompanied by a subsurface hook, while Fig. 5-31(b) indicates that steel overflows along the bottom of an oscillation mark from the slab corner. Phosphorus segregation is clearly observed at the end of the overflow region, although it is not observed in the longitudinal cross section. It is unlikely that the segregation is due solely to interdendritic flow through the semi-solid shell because this would require a relatively uniform segregation along the bottom of the oscillation mark. That the positive segregation was generated at the end of the overflow is probably a heat flow effect. The tip of the overflow close to the bottom of the oscillation mark is separated from the mould wall by a larger gap than overflow closer to the corner which fills more of the oscillation mark. The reduced heat transfer at the tip of the overflow will reduce the solidification rate and allow more time for segregation. This will be discussed theoretically in the next section.

5.3.5 Summary Of Metallurgical Investigations Of Positive Segregation

Positive segregation was found in the subsurface structure adjacent to oscillation marks both in the presence and in the absence of hooks. P and Mn were detected in the segregation zone in the plain carbon steel slabs. In the case of stainless steel slabs the segregated elements are mainly Ni and P. The types of positive segregation observed in this investigation can be classified into four categories as shown in Fig. 5-32. Segregation type 1 is observed at the bottom of deep oscillation marks where overflow ends. In type 2 the segregation is associated with an overflow which is closer to the top of the oscillation marks. The segregation is weaker, appearing to be interdendritic in origin and following the hook. In type 3 the depth of the oscillation mark is shallow and segregation is almost the same as in type 2. Type 4 is observed at the bottom of oscillation marks which are not accompanied by a subsurface hook. The thickness of the segregation layer increases with increasing depth of oscillation marks.

Traces of flow through the semi-solidified shell was detected in this investigation. This supports the reported mechanism schematically explained by Tanaka et al.²⁹ Indeed, the segregation type 4 can be explained only by this mechanism. The metallographic examination of samples from the slab corner indicates that a nonuniform solidification rate due to the shape of oscillation marks plays a dominant role in regard to

segregation type 1.

5.4 Heat Transfer Analysis Of Solidification In The Mould In The Vicinity Of Oscillation Marks

5.4.1 Objectives And Description Of The Physical System

The metallurgical investigation described in previous sections clearly indicates the strong effect of nonuniform heat transfer, caused by the shape of oscillation marks, on transverse crack formation and positive segregation. Therefore a two-dimensional heat flow analysis in the mould, taking account of the shape of oscillation marks, was undertaken to determine the following:

- (1) Temperature distribution both in the steel and in the mould flux in the mark depression.
- (2) Temperature hysteresis of each region of the slab surface in the mould.
- (3) Influence of the shape of oscillation marks on the nonuniformity of the shell thickness.

The physical system for the mathematical modelling is shown in Fig. 5-33. It is assumed that the oscillation mark is formed just at the meniscus, but once formed, the mark retains its shape in the mould. The length of the system in the casting direction is equal to the pitch of the oscillation marks. The width of the system is taken to be a half width of the mould.

This system moves down at the casting speed from the meniscus to the outlet of the mould. There is a mould flux layer which acts as a thermal resistance between the mould wall and the solidified shell. The mould flux in the mark depression is additionally taken into account as a thermal resistance.

5.4.2 Mathematical Modeling

Fig. 5-34 shows the coordinate of the system under study. The x and y directions are the casting direction and the mould width direction respectively. The following assumptions have been made in the model formulation;

- [i]. The shape of oscillation mark is symmetric at $x=0$ and can be represented by a quadratic equation at $0 \leq x \leq x_1^*$, and beyond by a straight line parallel to the mould wall for simplicity. Thus the pitch and the depth of oscillation mark are $2x_1^*$ and y_1^* , respectively.
- [ii]. From the symmetry of the oscillation mark, there is no axial heat flow at $x=0$.
- [iii]. The depression created by the oscillation mark is filled with mould flux in the mould. The thermal resistance at the interface between the mould flux and slab surface is negligible.
- [iv]. Heat is extracted from the plane $y=0$. The measured heat flux¹⁸ is used as the boundary condition at this plane. As the shell moves down at the casting speed, this boundary condition also changes with drawing time from the meniscus to the outlet of the mould.

The governing heat conduction equations for the steel and the mould flux are two-dimensional and unsteady state.

$$\frac{\partial T_s}{\partial t} = \frac{\lambda_s}{\rho_s C_{ps}} \left(\frac{\partial^2 T_s}{\partial x^2} + \frac{\partial^2 T_s}{\partial y^2} \right) \quad (5-1)$$

$$\frac{\partial T_f}{\partial t} = \frac{\lambda_f}{\rho_f C_{pf}} \left(\frac{\partial^2 T_f}{\partial x^2} + \frac{\partial^2 T_f}{\partial y^2} \right) \quad (5-2)$$

The initial and boundary conditions are as follows;

$$t = 0, \quad 0 \leq x \leq x_1^*, \quad 0 \leq y \leq f(x) ; \quad T_f = T_{fi} \quad (5-3)$$

$$t = 0, \quad 0 \leq x \leq x_1^*, \quad y \geq f(x) ; \quad T_s = T_{si} \quad (5-4)$$

$$t = 0, \quad x_1^* < x \leq x_2^*, \quad y \geq 0 ; \quad T_s = T_{si} \quad (5-5)$$

$$t \geq 0, \quad 0 \leq x \leq x_1^*, \quad y = 0 ; \quad -\lambda_f \frac{\partial T_f}{\partial y} = q_o(x) \quad (5-6)$$

$$t \geq 0, \quad 0 \leq x \leq x_1^*, \quad y = f(x) ;$$

$$-\lambda_s \frac{\partial T_s}{\partial r} = -\lambda_f \frac{\partial T_f}{\partial r} = h_{s-f}(T_s - T_f) \quad (5-7)$$

$$t \geq 0, \quad x = 0, \quad 0 \leq y \leq y_1^* ; \quad -\lambda_f \frac{\partial T_f}{\partial x} = 0 \quad (5-8)$$

$$t \geq 0, \quad x_1^* < x \leq x_2^*, \quad y = 0 ; \quad -\lambda_s \frac{\partial T_s}{\partial y} = q_o(x) \quad (5-9)$$

$$t \geq 0, \quad x = 0, \quad y_1^* < y \leq y_2^* ; \quad -\lambda_s \frac{\partial T_s}{\partial y} = 0 \quad (5-10)$$

$$t \geq 0, \quad y = y_2, \quad 0 \leq x \leq x_2^* ; \quad -\lambda_s \frac{\partial T_s}{\partial y} = 0 \quad (5-11)$$

Additionally for the simplification of the heat flow calculation it is assumed that the longitudinal heat flow is negligible compared with the lateral heat flow at $x=\pm x_2^*$, represented as Eq. (5-12).

$$t \geq 0, \quad x = \pm x_2^*, \quad 0 \leq y \leq y_2^*; \quad -\lambda_s \frac{\partial T_s}{\partial y} = 0 \quad (5-12)$$

With respect to the mould heat-flux distribution in the casting direction, the measured results by Nakato et al,¹⁸ have been modified, especially in the vicinity of the meniscus, by the two-dimensional mould heat-transfer model described in a previous chapter. The mould heat flux distribution is expressed by the following polynomials as a function of time in the mould under the condition of 1) casting speed is 1 m/min and 2) length of the mould is 0.8m.

$$0 \leq t \leq 12; \quad q_0^*(t) = 251.04 - 23.341t + 1.9618t^2 - 0.066233t^3 \quad (5-13)$$

$$12 \leq t \leq 48; \quad q_0^*(t) = 251.04 - 16.899t + 0.8250t^2 - 0.018468t^3 + 1.5616 \times 10^{-4}t^4 \quad (5-14)$$

However this heat flux distribution does not apply at oscillation marks. Therefore another assumption was made for the computation of solidification which is affected by the shape of the oscillation marks. The heat flux at the depression is assumed to decrease in proportion to the thickness of the layer of mould flux in the depression. The thickness of mould flux, which effectively reduces the heat flux by half, is defined as Y_H . Based on this assumption, the local distribution of heat

flux is expressed by the following equations.

$$t = t_i \quad ; \quad \int_0^{x_1} q_f(x)dx + \int_{x_1}^{x_2} q_s(x)dx = \int_0^{x_2} q_0^*(t_i)dx \quad (5-15)$$

$$q_f(x) = (1 - f(x)/2y_H)q_0^*(t_i) \quad (5-16)$$

Equations (5-1) and (5-2) were solved, subject to the initial and boundary conditions, Eqs. (5-3) to (5-16), using the explicit finite-difference method. Triangular volume elements have been employed to simulate the curvature of the oscillation marks, as was the case in the computation of meniscus heat transfer in Chapter 4. The release of latent heat of solidification has been incorporated by adjusting the specific heat between the solidus and liquidus temperature. Calculations were performed for a plate grade steel using the heat flux profile presented in Eqs. (5-13) to (5-16). The composition of steel and data employed in the computation are given in Table VIII. Note that the superheat of steel is taken to be 5°C, the initial temperature of the mould flux is 1500°C,¹² and y_H is 0.05 cm.

5.4.3 Calculated Results

5.4.3.1 Temperature Distribution In Mould Flux And Steel

Figs. 5-35 and 36 show the temperature distribution both in the steel and the mould flux in the oscillation mark depression after 10s and 48s respectively. Those two results correspond to locations 16.7 and 80cm beneath the meniscus for

the casting speed of 1.0m/min. In this calculation the pitch (l) and the depth (d) of the oscillation mark are 1.0cm and 0.1cm respectively; The ratio of the length of the depression to the pitch of oscillation mark, viz x_1^*/x_2^* is 0.5. In Fig. 5-35 (10s after the meniscus) the mould flux remains liquid except for a solidified layer close to the mould wall. The melting point of mould flux applied in this computation is estimated to be about 1100°C. A nonuniformity of temperature distribution is observed in the steel which results from the presence of the mould flux in the oscillation-mark depression. A temperature difference of about 150°C was calculated between the top (less than 1200°C) and the bottom (about 1350°C) of the oscillation mark. Even after 48s, liquid mould flux still exists at the bottom of the oscillation mark. Thus the bottom of the oscillation mark is always in contact with liquid mould flux so that if a crack opens up at the bottom of the oscillation mark anywhere inside the mould, the liquid mould flux easily penetrates into the crack. This finding agrees well with the observation reported earlier, ie the mould flux was detected on the dendritic crack surface, Fig. 5-14. At the end of the mould, the temperature difference between the top and the bottom of the oscillation mark is about 100°C, about half as large as the difference just below the meniscus. This result, however, is only valid provided that the oscillation mark depression is filled with mould flux; but this may not be the case lower in the mould. There, mould flux may flow downward to form an air gap and/or may solidify and again form the air gap to increase

the thermal resistance at the shell-flux interface. In this event heat extraction may not proceed completely by conduction alone but by both conduction and radiation. Consequently the nonuniformity of temperature distribution increases further. However the calculated shell profile in the mould is in good agreement with the measured profile by Nakato et al.¹⁸ using tracers. This indicates the validity of the calculation despite the numerous assumptions.

5.4.3.2 The Effect Of Oscillation-mark Shape On The Nonuniformity Of Shell Thickness

Thus it is seen that the mould flux and/or the air gap in the depression of the oscillation marks strongly affects the temperature distribution in the subsurface of the adjacent steel. This implies that there is also a nonuniformity in the shell thickness. To study this effect further, more calculations were carried out to estimate the effect of oscillation-mark shape on the nonuniformity of shell thickness in the absence of an air gap. Calculated shell profiles (fraction solid=1) adjacent to various shapes of oscillation marks after 5, 10, 20, and 30s are shown in Figs. 5-37 to 5-40 respectively. The ratio x_1^*/x_2^* was held constant at 0.5. Owing to symmetry of the system, only the lower part of the shell profiles is shown. Fig. 5-37 shows the change of shell profile with time when $l=1.0\text{cm}$ and $d=0.10\text{cm}$. A slight nonuniformity is found at the solidification front after 5s, but a uniformly thick shell is thereafter soon recovered. Even though the depth

increases to $d=0.15\text{cm}$, it does not much affect the nonuniformity of the solidification front at $l=1.0\text{cm}$, see Fig. 5-38. In these cases, the depth of oscillation marks is much larger than the locally reduced thickness of the solid shell. Fig. 5-39 represents the shell profiles when the oscillation-mark pitch is greater, $l=2.0\text{cm}$, and $d=0.10\text{cm}$. The reduction in shell thickness in the vicinity of the bottom of oscillation mark clearly increases as compared with the short pitch ($l=1.0\text{cm}$). A uniformly thick shell cannot be attained even after 30s. In the case of $l=2.0\text{cm}$, the locally thin shell is exacerbated with an increase in the depth of oscillation marks, Fig. 5-40.

Next the ratio x_1^*/x_2^* , see Fig. 5-34, was changed from 0.3 to 0.7, where the pitch and the depth of marks were kept constant ($l=2.0\text{cm}$, $d=0.10\text{cm}$). Comparison of Fig. 5-41 ($x_1^*/x_2^*=0.7$) and Fig. 5-42 ($x_1^*/x_2^*=0.3$) clearly indicates that increasing the flat part of the surface significantly improves the uniformity of shell thickness.

These calculated results reveal that both the pitch and the depth of oscillation marks are important factors which influence the nonuniformity of the shell thickness, see Fig. 5-43. Particularly, it should be noted that the heat conduction in steel in the casting direction plays an important role in the uniformity of shell profile. As mentioned in Chapter 4 the shape of oscillation marks is affected by the carbon content of the steel. The oscillation marks on slabs having 0.10% carbon are deep and curved, while they are relatively flat and shallow

on higher carbon slabs; these were explained by the carbon dependent-deformability of the shell. Such characteristic shapes of the oscillation mark suggests that the variation in shell thickness in casting of about 0.10% carbon slabs is more severe.

Another factor influencing the shape of oscillation mark is mould reciprocation frequency. High-frequency mould oscillation has been reported to drastically improve the surface quality of slabs, especially with respect to transverse cracks. The depth of oscillation marks is reduced by higher frequency of mould oscillation, for which a mechanism was proposed in Chapter 4. Furthermore this higher frequency decreases the pitch of oscillation marks. Heat flow analysis predicts that both of these phenomena yield a more uniformly thick shell. As mentioned in a previous section, the transverse cracks might have been initiated in the mould where the stress and/or strain are concentrated at the thinner part of the shell, viz in the vicinity of the bottom of oscillation marks. It is therefore inferred that the formation of transverse cracks is reduced by making the shell thickness uniform with increasing the oscillation frequency.

5.4.3.3 Cooling Rate Distribution Near The Oscillation Marks

It has been seen that oscillation marks in the mould cause a nonuniform temperature distribution on the slab surface and consequently strongly affect the shell profile. This fact indicates that there might be large differences in the cooling

rate between the top and the bottom of oscillation marks. Fig. 5-44 shows this to be the case for oscillation marks of different shape. As described previously, not only reducing the oscillation-mark depth but also decreasing the mark pitch reduces these temperature differences. Fig. 5-45 shows the change of cooling rate with time when $l=1.0\text{cm}$ and $d=0.10\text{cm}$. The cooling rates at both locations after 5s are almost same, while they are very different before 5s. It is well known that the cooling rate affects the primary solidification structure, especially the secondary dendrite arm spacing. The relationship between these variables as measured by Suzuki¹⁰⁴ is shown in Fig. 5-46. The average value of the secondary dendrite arm spacing measured in the present work, described in Chapter 4, are also given in this figure. Cooling rates from the data of Suzuki are consistent with the calculated values.

The shell growth rates have also been calculated to assess the effect of the shape of the oscillation mark. Fig. 5-47 shows the change of the shell thickness with time both at the bottom and at the top of an oscillation mark, when $l=1.0\text{cm}$ and $d=0.10\text{cm}$. The shell thickness does not show the general linear relationship with $t^{0.5}$ but rather is linear with $t^{0.75}$ as reported by Kumai et al.¹⁰⁵ using a radio isotope in the mould. A large difference of solidification rate is not found at the two locations but there is a difference in the time at which solidification commences. The time delay for solidification at the top of oscillation marks is due mainly to the superheat of the steel; at the bottom of the mark the

thermal resistance of the mould flux layer further contributes to make the time delay longer. The change of shell thickness with time is shown for an oscillation mark having $l=2.0\text{cm}$ and $d=0.10\text{cm}$, Fig. 5-48, and $l=2.0\text{cm}$ and $d=0.15\text{cm}$, Fig. 5-49. Thus the longer the mark pitch and/or the deeper the mark depth, the greater the difference in solidification start time between the top and the bottom of the oscillation marks. These findings help to explain segregation observed near subsurface hooks reported earlier. The overflow region on the hook at the bottom of the oscillation mark is expected to have a certain time delay before solidification commences compared to the top of the mark. The solute elements are thus concentrated at the final solidification point, namely at the bottom of the oscillation mark.

5.5 Discussion On The Formation Of Positive Segregation

A large area of positive segregation is found adjacent to oscillation marks having subsurface hooks when the following three conditions are satisfied: a) The angle of the hook to the slab surface is not large and a narrow and long overflow region is formed over the hook, b) the overflow region is located at the bottom of oscillation marks, and c) the oscillation mark is deep. The concentrated liquid steel segregates at the end of the overflow, since it solidifies later than the remainder of the region between the hook and steel-flux interface. This mechanism is supported by the positive segregation found at the

end of the overflow from the slab corner along the bottom of the oscillation mark, Fig. 5-31. Furthermore, the mechanism is consistent with the results of the heat transfer model.

On the other hand the positive-segregation layer on the bottom of the oscillation marks having no subsurface hooks cannot be explained by such a heat transfer effect because there is no overflow. In this case, it has been postulated that the weak shell caused by high superheat or high carbon content etc. is drawn back to the mould wall by the negative pressure generated in the mould flux channel during the upward motion of the mould. The top of the shell is in the semi-solid state and hence it is conceivable that interdendritic liquid could be drawn out to the surface by the negative pressure.

To investigate this possibility, the negative pressure force generated in the flux channel during upward mould motion was estimated by combining meniscus heat transfer with lubrication theory as described in a previous chapter. Computations were carried out for the seventeen different oscillation conditions. The calculated pressure distribution $P(x)$ was converted to average pressure P_a by the following equation.

$$P_a = \frac{1}{l_f} \int_0^{l_f} P(x) dx \quad (5-17)$$

The results are shown in Fig. 5-50. Thus the average negative pressure increases with increasing negative strip time. As

suggested this may cause interdendritic flow, the velocity of which can be estimated from D'arcy's Law:¹⁰⁶

$$v_L = - \frac{k}{\mu_s L_c g_L} (P_a + \Delta P_s) \quad (5-18)$$

In this case the static pressure difference ΔP_s is almost negligible compared with the magnitude of P_a . Assuming that the fraction liquid, g_L , is approximately 0.5 because the top of the shell is semi-solid state at the meniscus, the permeability K can be estimated to be about 10^{-8}cm^2 based on Piwonka's data¹⁰⁷ shown in Fig. 5-51. The length of channel L_c can be regarded as the shell thickness ($g_L=0.5$). Therefore L_c is roughly estimated to be 0.05cm from the calculated results of the meniscus heat transfer. With the viscosity of molten steel at 7cP,¹⁵ the flow velocity V_L is computed to be approximately 0.6cm/s, which suggests that the interdendritic liquid can move outward to the shell surface within a period of one mould oscillation. This mechanism is consistent with observed data in industrial plants, that the frequency and the thickness of surface segregation increase with increasing negative-strip time,²⁷ and also with the investigated result shown in Fig. 5-21.

Also in the case of the oscillation marks having subsurface hooks, this interdendritic flow likely takes place in addition to the heat transfer effect, as shown in Fig. 5-17. Tanaka et al.²⁹ have reported that positive segregation of phosphorus was observed along the outside of the hook, while negative segregation exists below the positive segregation line. This

result is explained by the mechanism proposed here, although Tanaka et al assumed that the interdendritic flow occurs during downward motion of the mould. The interdendritic flow should be more significant in the case of oscillation marks having no subsurface hooks, since the rigidity of the shell is likely to be less than that of the shell when hooks form due to overflow at the meniscus.

Table IX - Casting Conditions of Samples for Metallurgical Study of Transverse Cracks

Samp No.	Comp	Chemical Composition (%)							Casting Conditions					
		C	Mn	Si	P	S	Al	N	Tc (°C)	Vs (m/min)	S (mm)	f(cpm)	Type of Nozzle	Type of Mould Flux
A1	B	0.10	0.41	0.06	0.007	0.013	0.042	0.164	1538	1.57	11	95	7.5' up	b
A2	B	"	"	"	"	"	"	"	1541	1.37	"	"	"	b
A3	C	0.07	0.33	0.03	0.003	0.012	0.062	0.0080	1547	0.91	5.8	64	15' up	c1

Tc : Casting temperature of steel in tundish
 Vs : Casting speed
 S : Stroke of mould oscillation
 f : Frequency of mould oscillation

Table X - Casting Conditions of Samples for Metallurgical Study of Positive Segregation

Samp No.	Comp	Chemical Composition (%)									Casting Condition					
		C	Mn	Si	P	S	Al	Cr	Ni	N	Tc(°C)	Vs (m/min)	S(mm)	f(cpm)	Type of Nozzle	Type of Mould Flux
B1	A	0.09	0.79	0.24	0.008	0.014	0.033	-	-	0.0080	1538	0.94	12.7	44	25° dwn	a
B2	B	0.10	0.41	0.06	0.007	0.013	0.042	-	-	0.0164	1538	1.57	11	95	7.5° dwn	b
B3	A	0.09	0.79	0.24	0.008	0.014	0.033	-	-	0.0080	1541	0.91	12.7	43	25° dwn	a
B4	A	0.26	0.76	0.22	"	0.012	0.001	-	-	0.0070	1538	0.89	"	42	"	a
B5	A	"	"	"	"	"	"	-	-	"	1532	1.02	"	48	"	a
B6	F	0.10	1.03	0.67	0.033	0.004	-	16.82	7.64	0.0200	1491	1.00	12.7	60	15° up	f

Tc : Casting temperature of steel in tundish

Vs : Casting speed

S : Stroke of mould oscillation

f : Frequency of mould oscillation

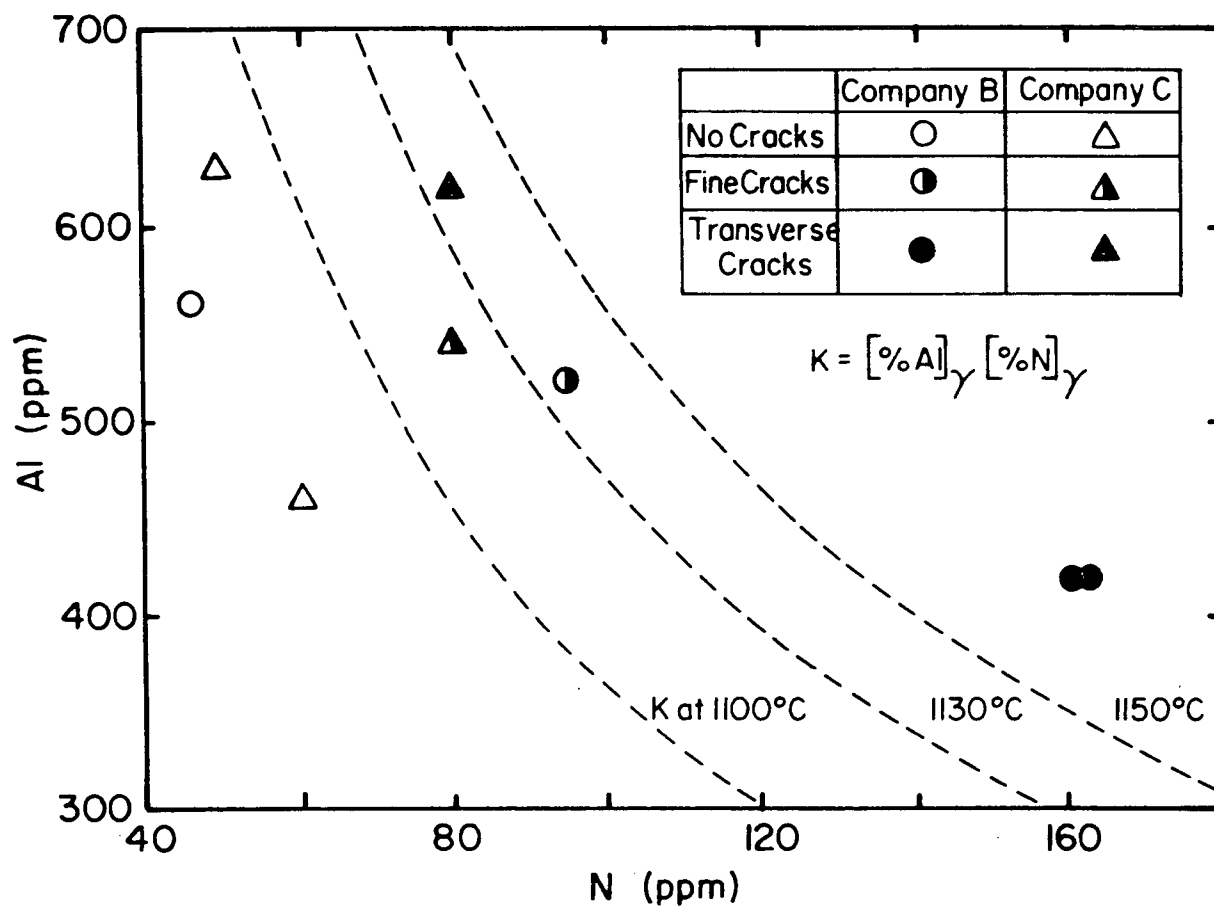


Fig. 5-1 Effect of N content on the formation of transverse cracks.
 Note: equilibrium constant $K = [\%Al]_{\gamma} [\%N]_{\gamma}$ by L.S. Darken et al.¹⁰⁸

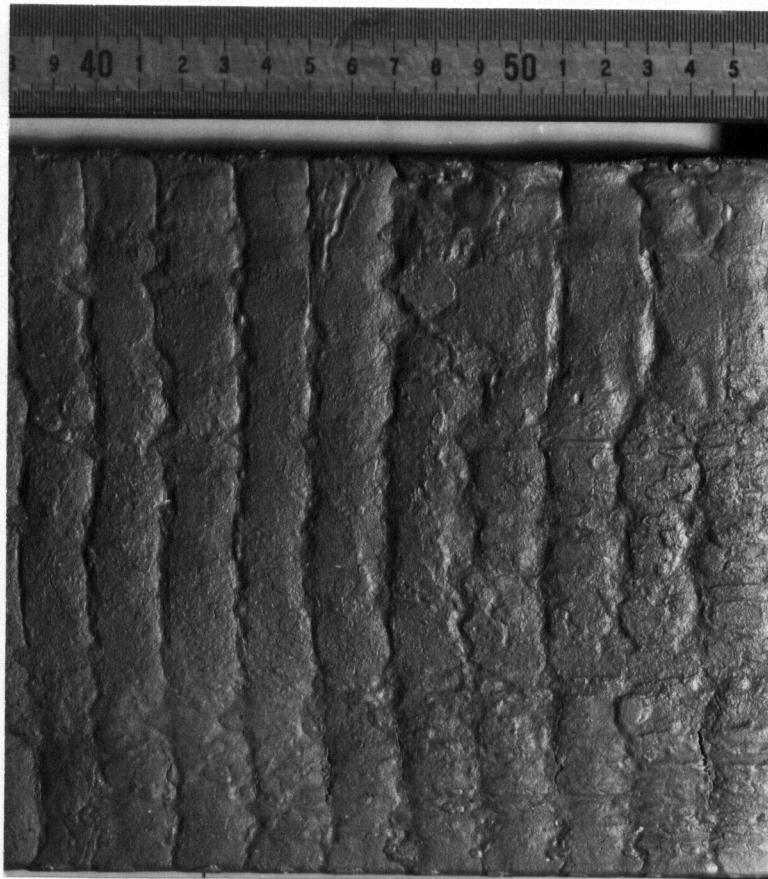


Fig. 5-2 Appearance of transverse cracks (i) (Company B).

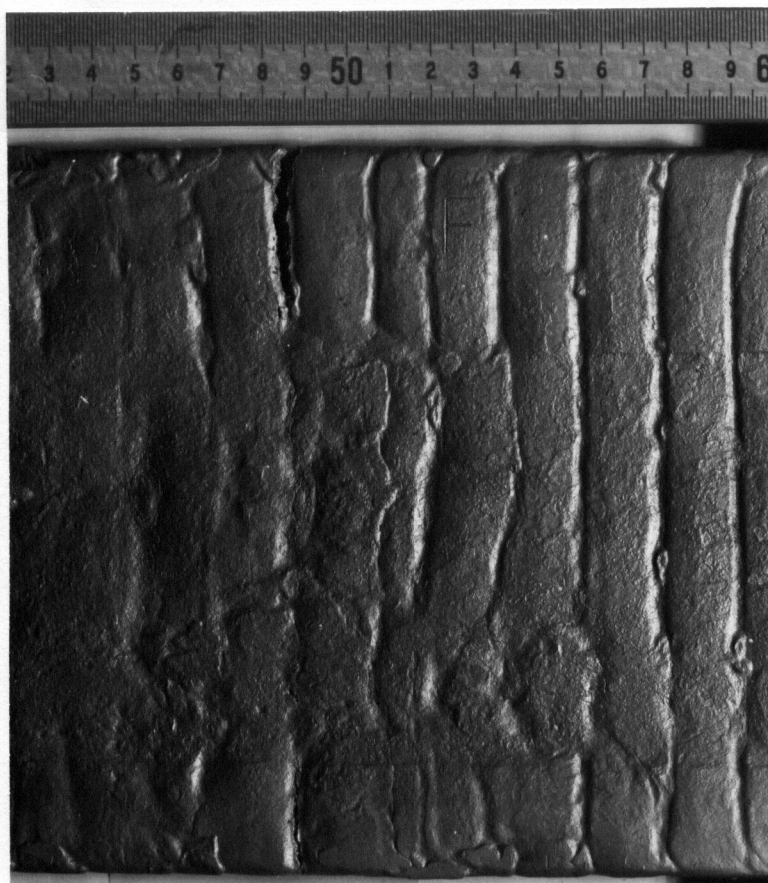


Fig. 5-3 Appearance of transverse cracks (ii) (Company B).

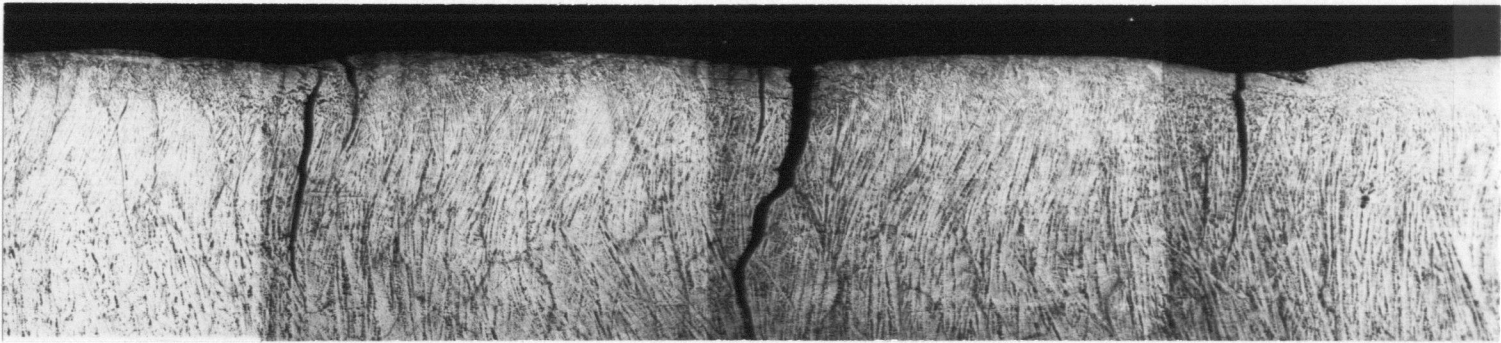


Fig. 5-4 Transverse cracks formed at the bottom of
oscillation marks; picral etching (Company B).
(x3.6)

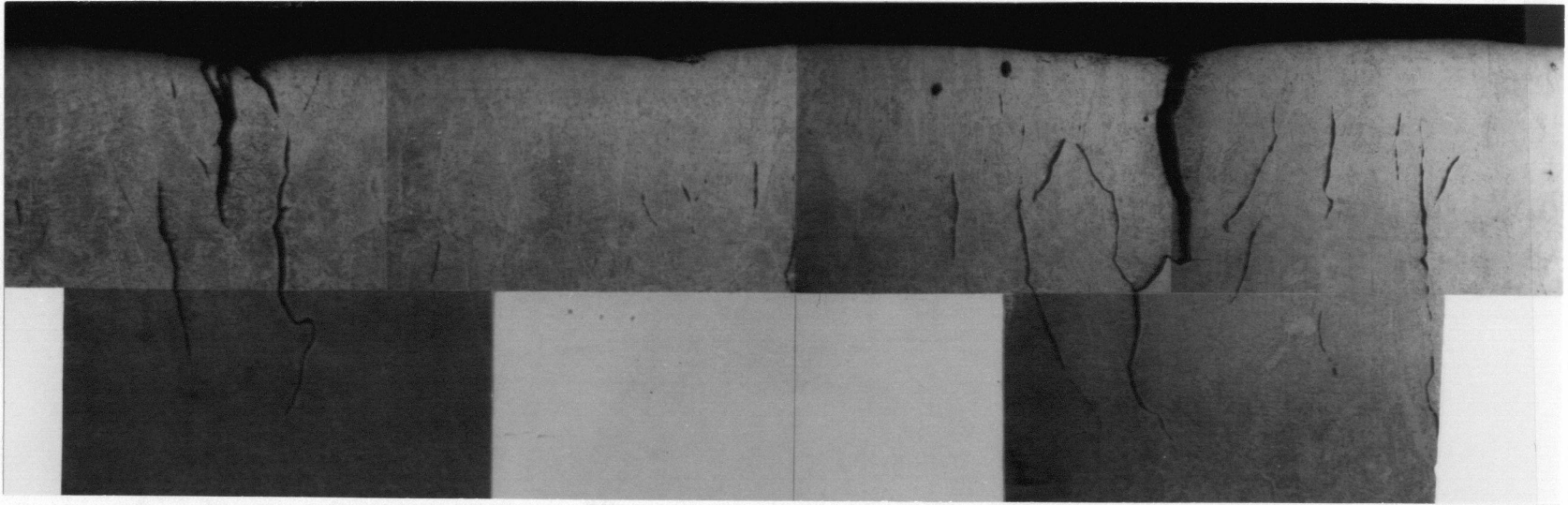
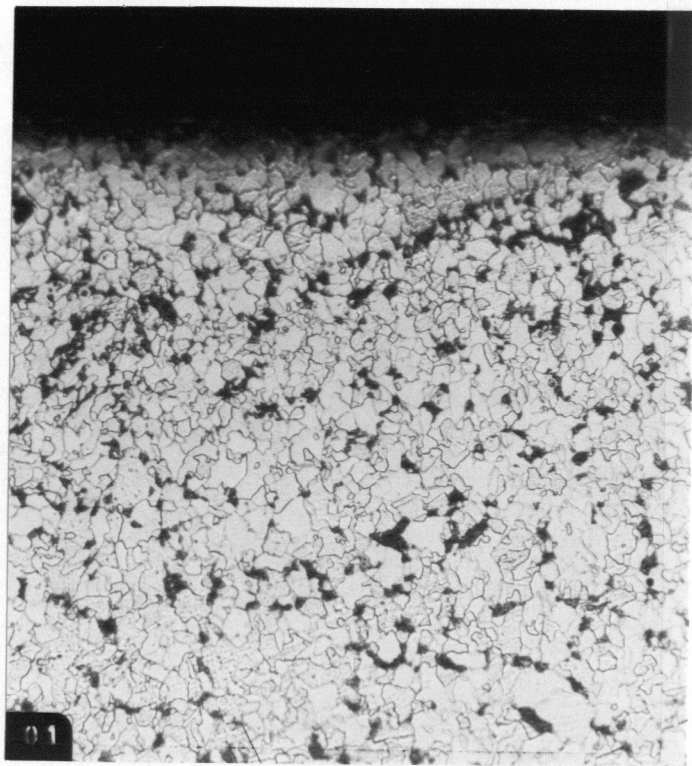
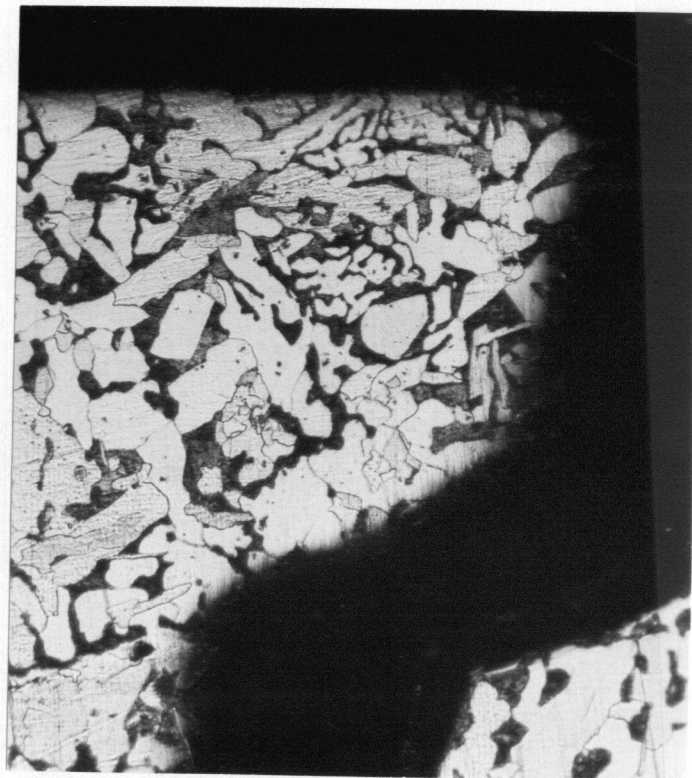


Fig. 5-5 Transverse cracks formed at the bottom of oscillation marks; nital etching (Company B). (x3.6)

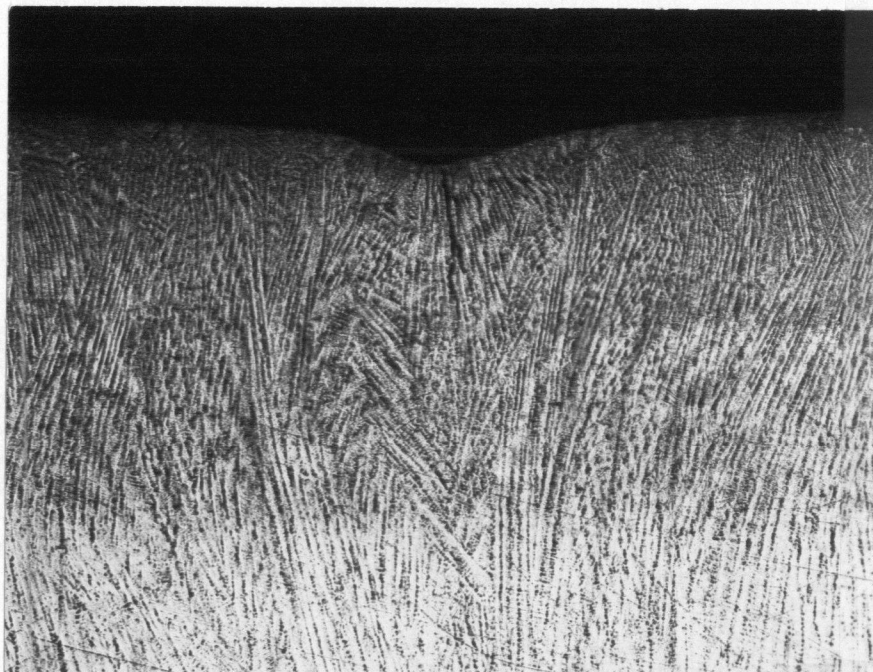


(a)

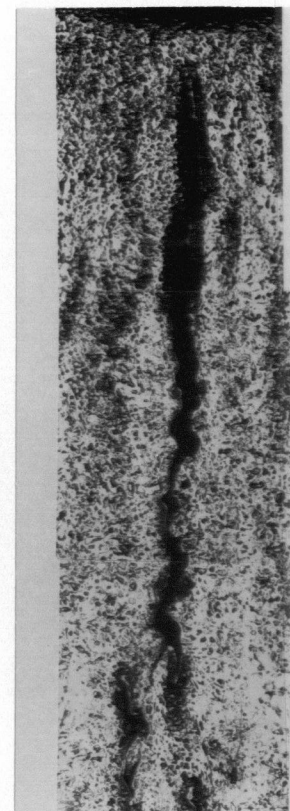


(b)

Fig. 5-6 Ferrite-pearlite structure (a) at the top and (b) at the bottom of an oscillation mark; nital etching (Company B). (x146)

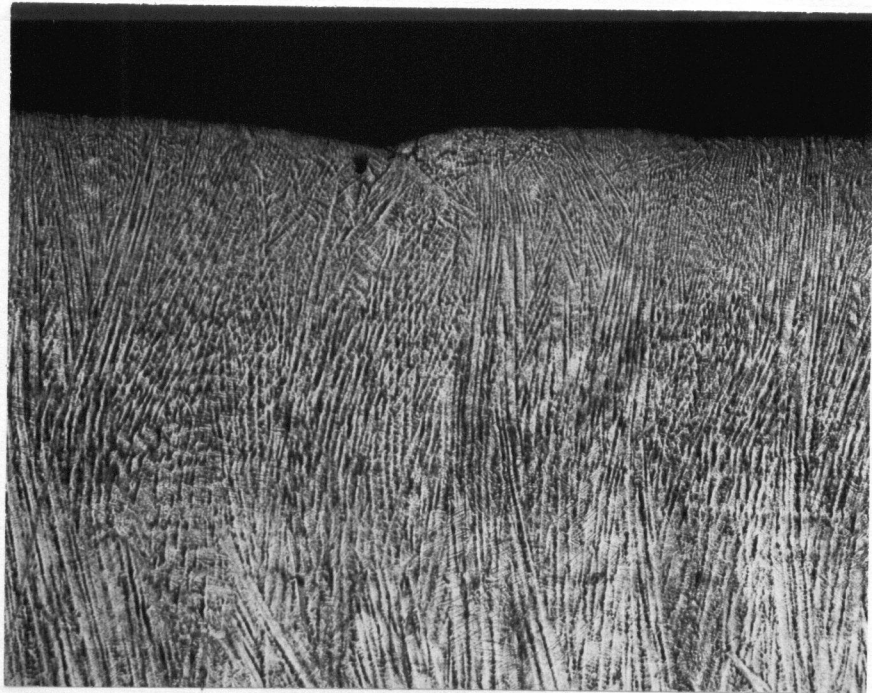


(a)

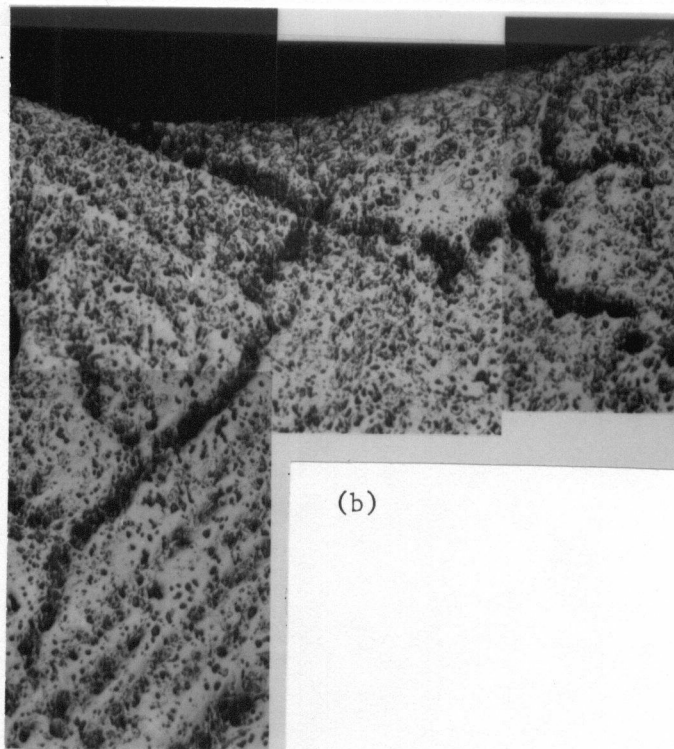


(b)

Fig. 5-7 Interdendritic cracks at the bottom of oscillation marks; picral etching (Company B). (a):x6.5, (b):x32.



(a)



(b)

Fig. 5-8 Small crack observed along and near the subsurface hook; picral etching (Company B). (a):x6.5, (b):x43.

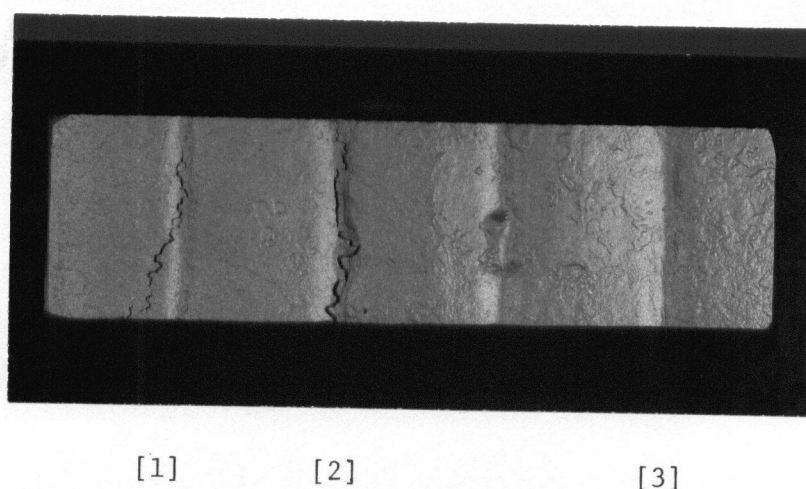
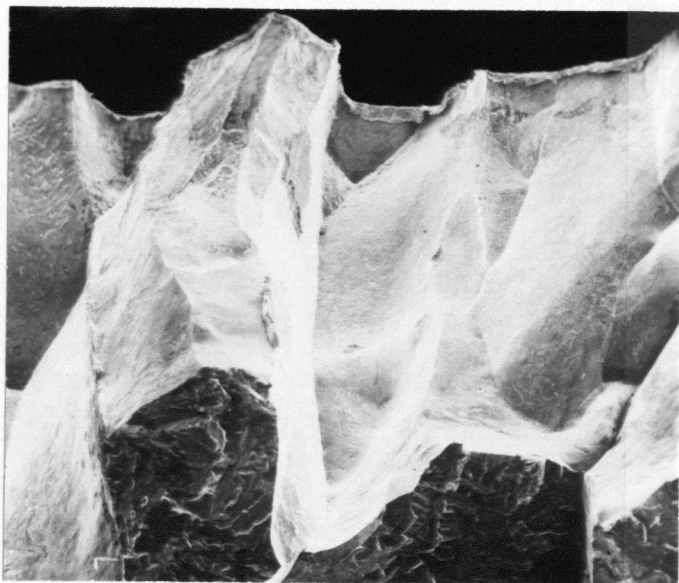
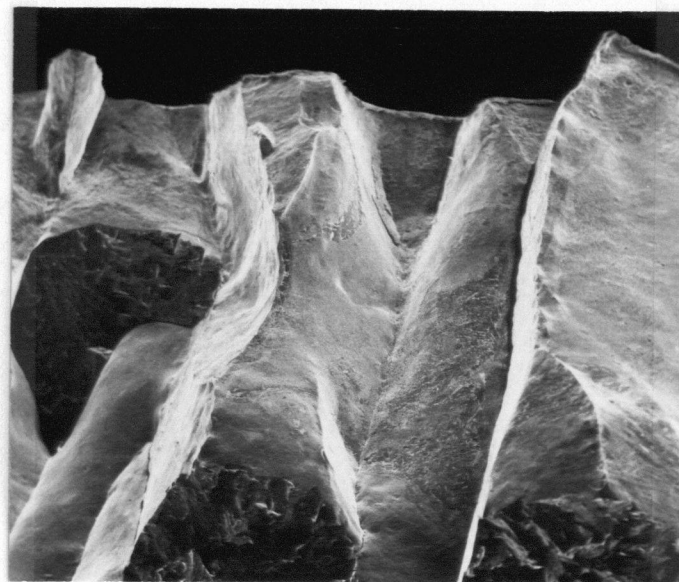


Fig. 5-9 Transverse cracks on the surface of a slab sample from Company B. (x1.18)

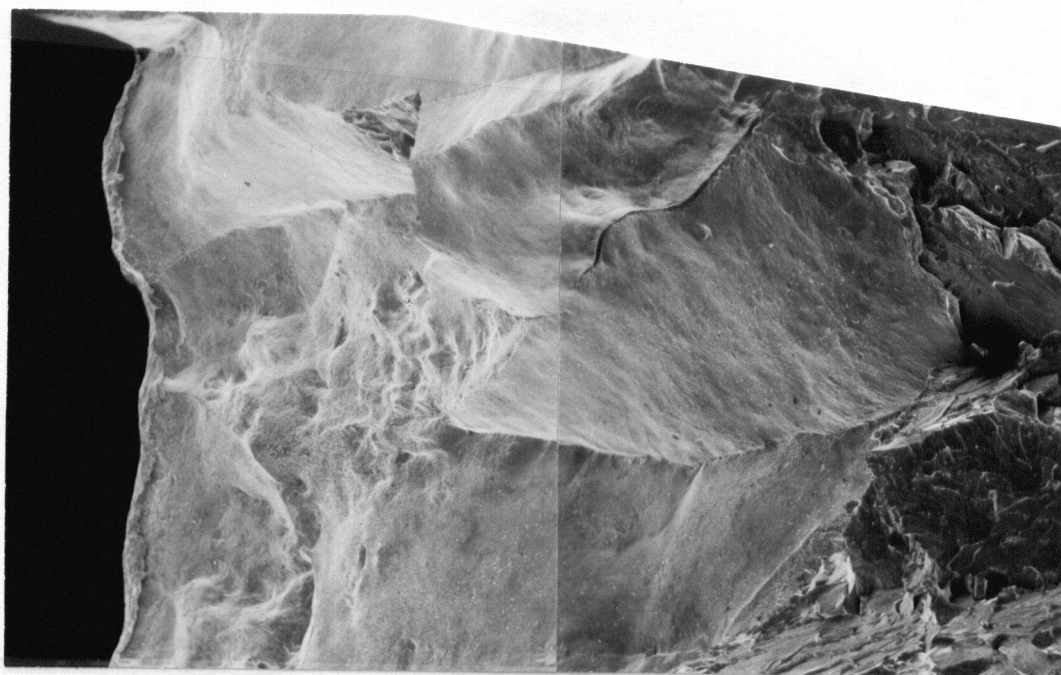


(a)



(b)

Fig. 5-10 Surface of transverse cracks [1] from Company B.
(x20)

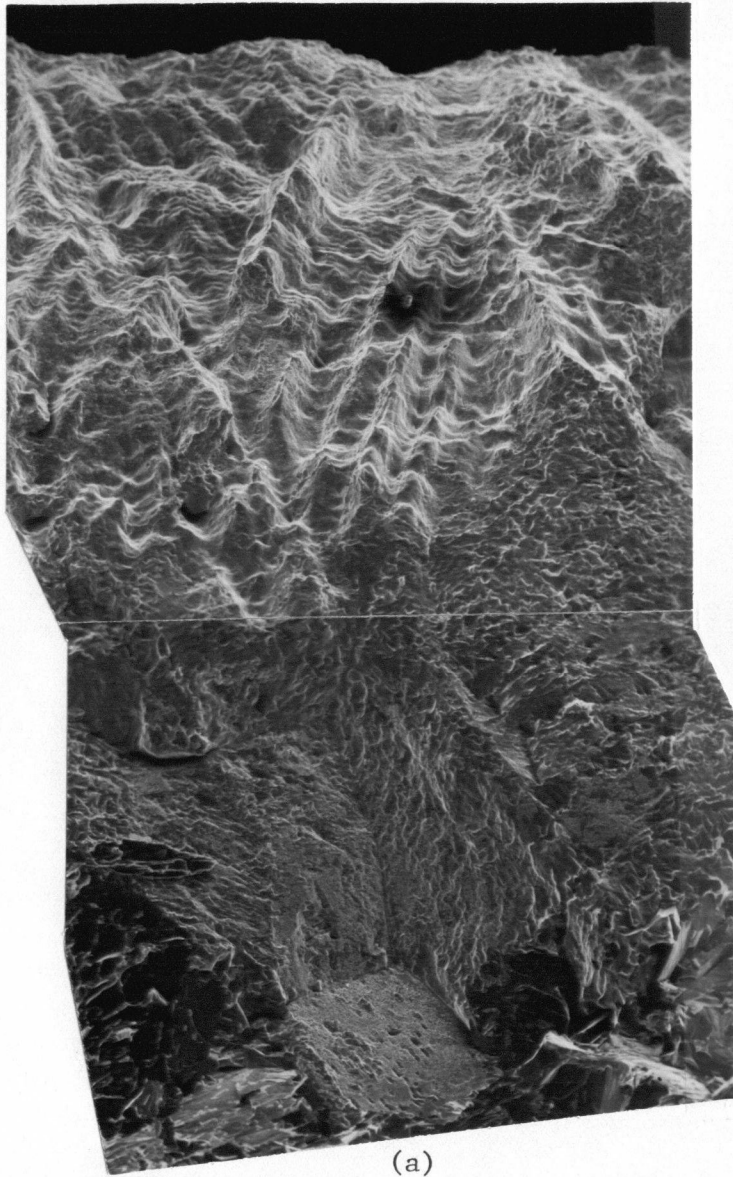


(b)

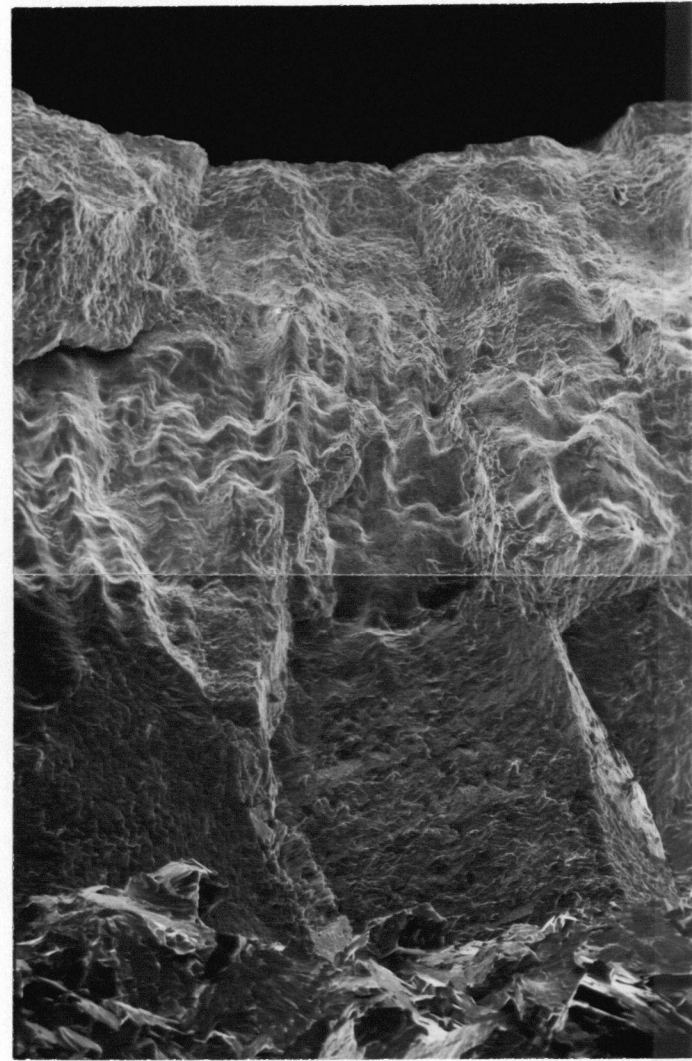


(a)

Fig. 5-11 Surfaces of transverse crack [2] from Company B.
(x20)

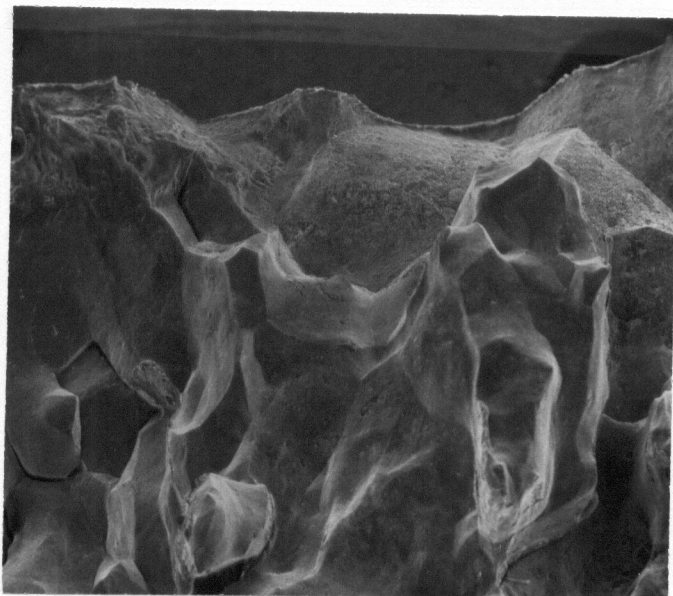


(a)

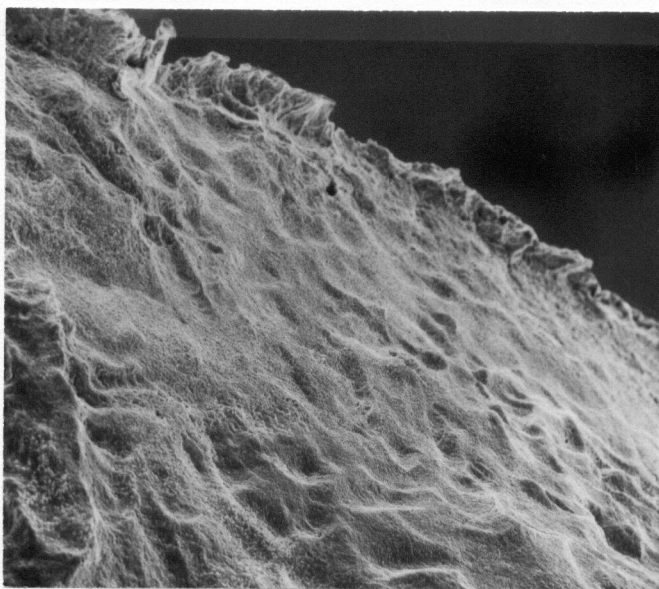


(b)

Fig. 5-12 Surface of transverse crack [3] from Company B.
(x40)



(a)



(b)

Fig. 5-13 Surface of transverse crack from Company C.
(a):x40, (b):x200.

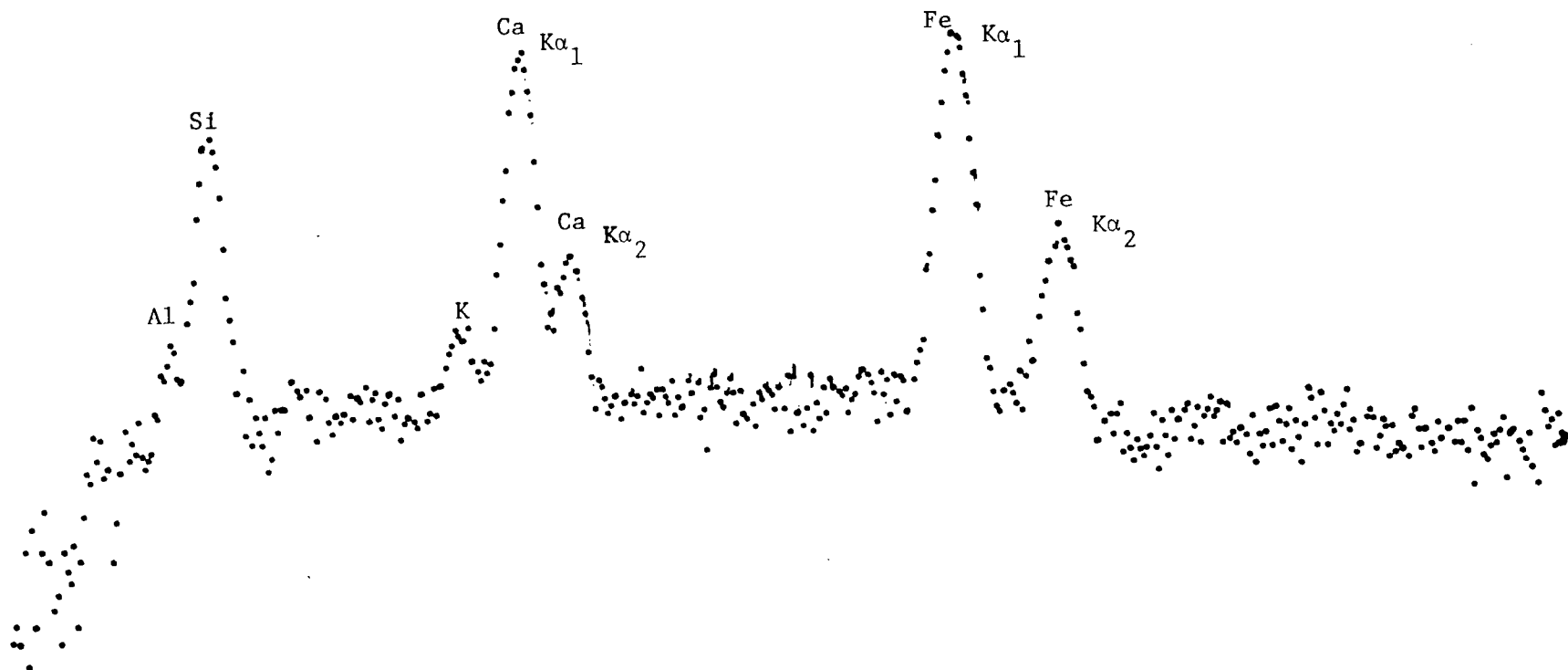


Fig. 5-14 X-ray spectrograph of adherent material on the surface of transverse crack, Company C.

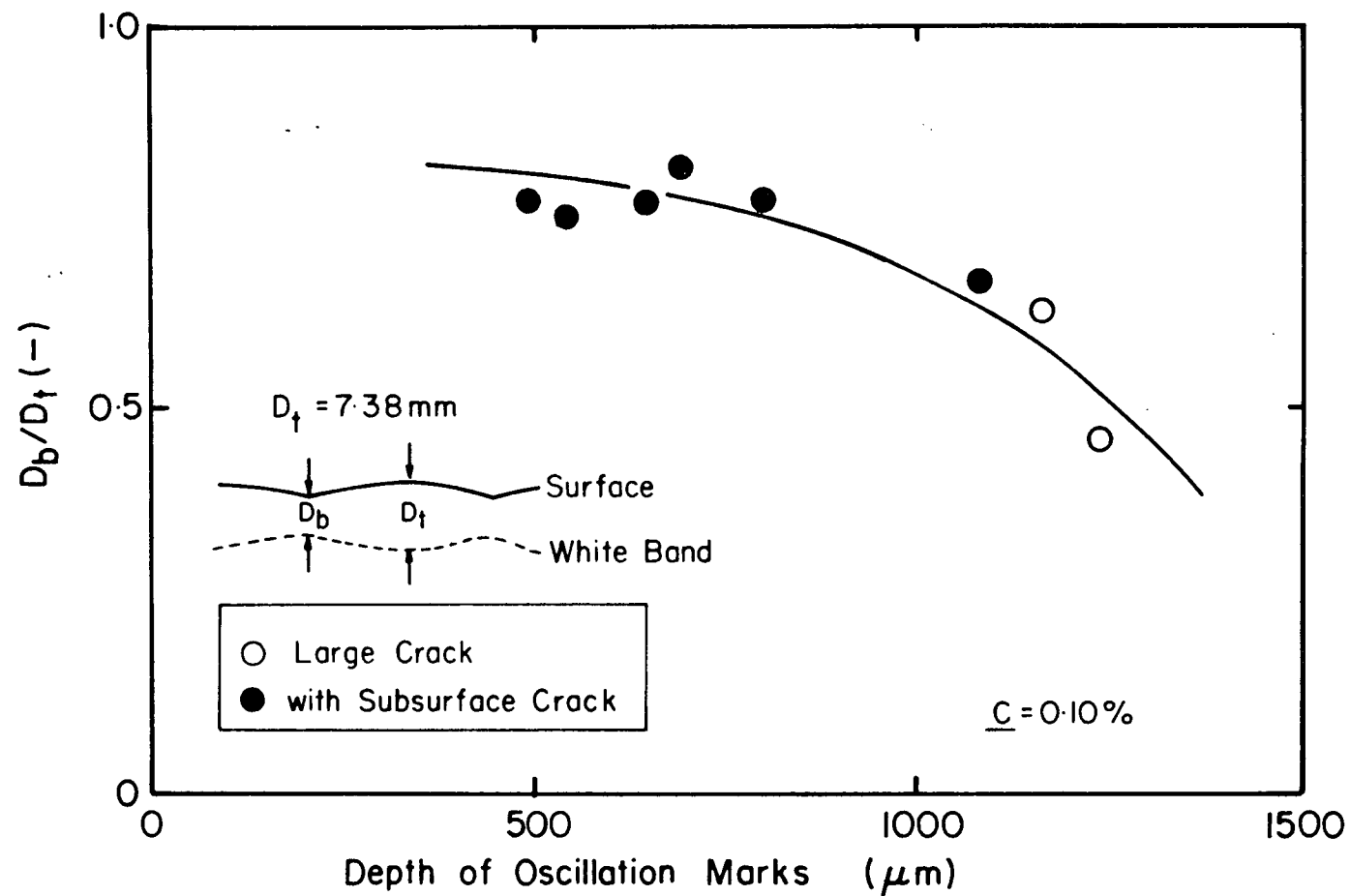


Fig. 5-15 Relationship between the depth of oscillation marks and the nonuniformity of the shell thickness (Company B).

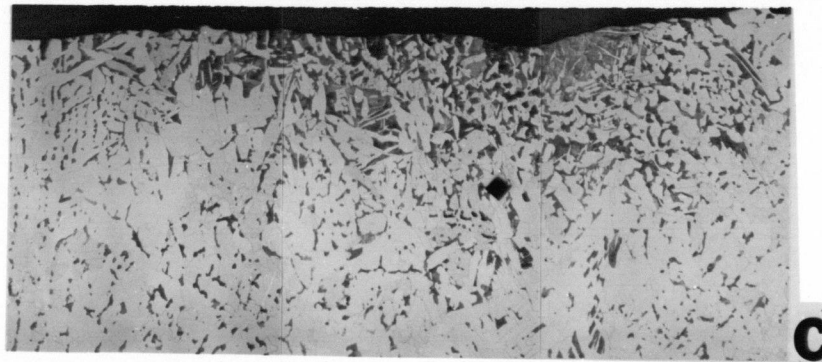
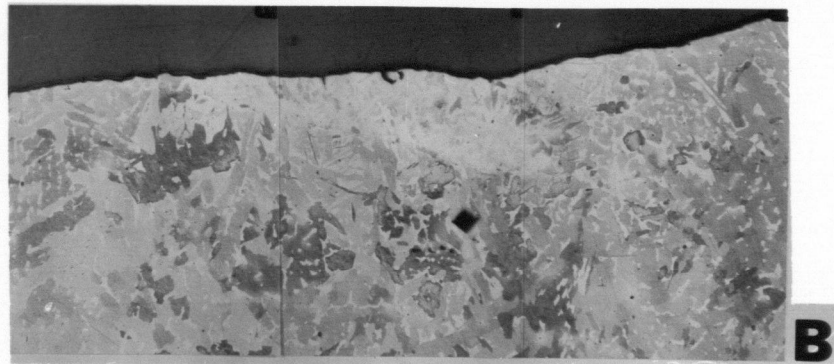
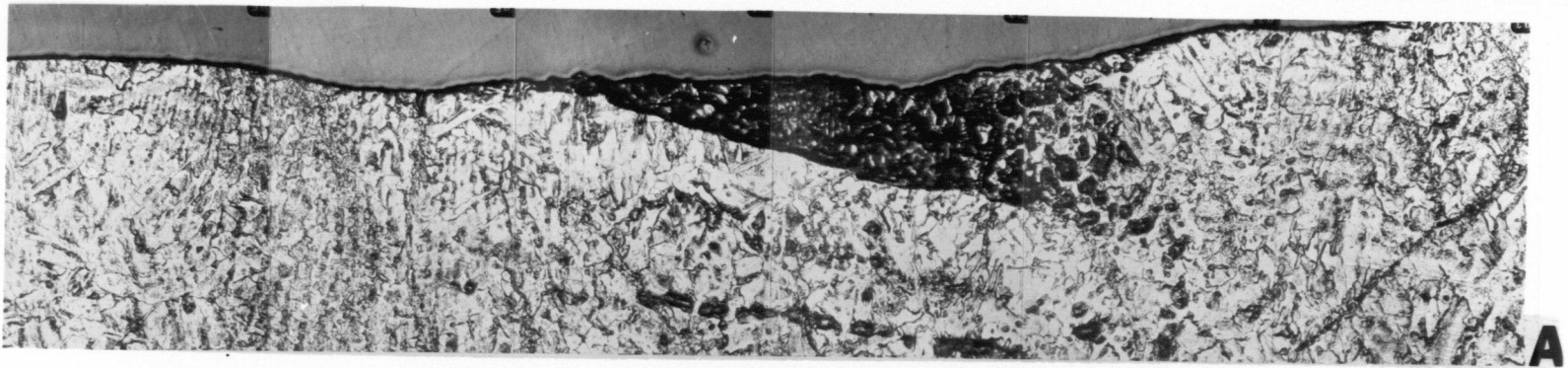
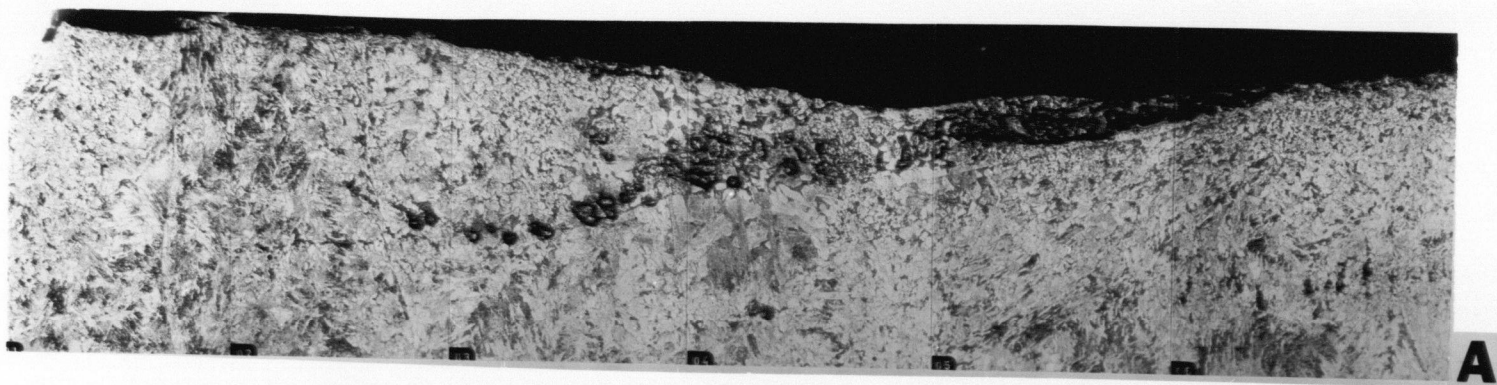
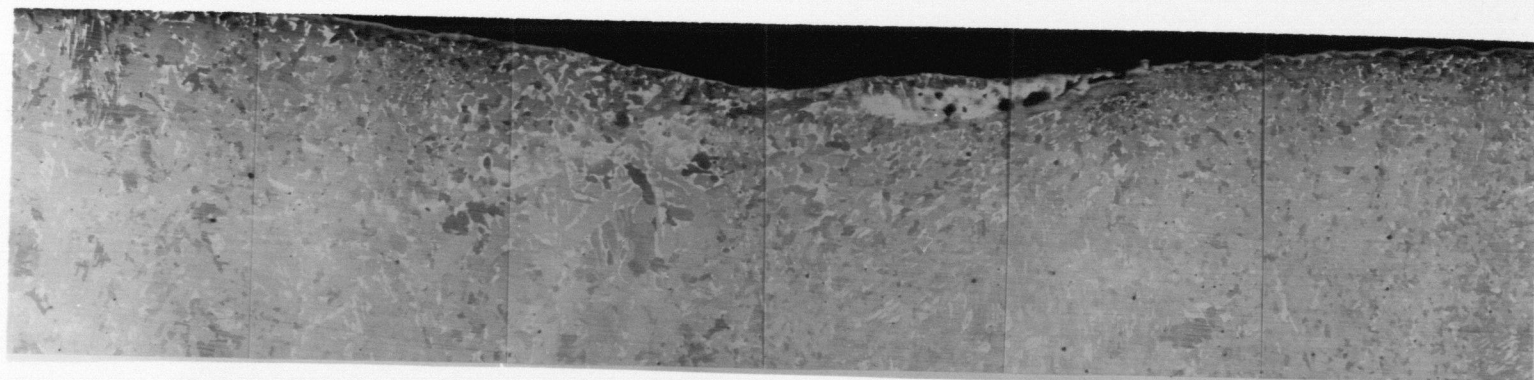


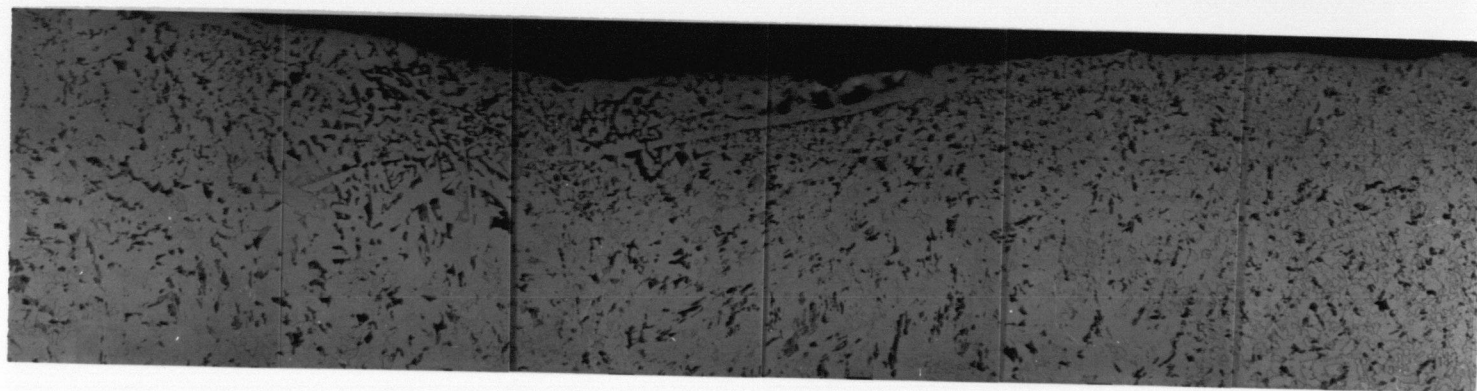
Fig. 5-16 Subsurface structure near positive segregation
(Sample B1). (x38.7)



A



B



C

Fig. 5-17 Subsurface structure near positive segregation (Sample B2). (x38.7)

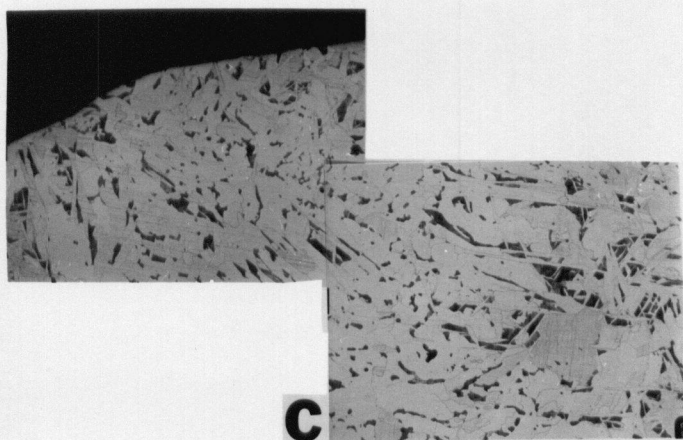
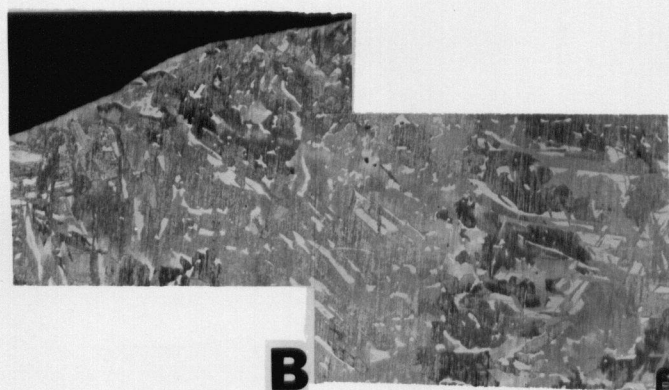
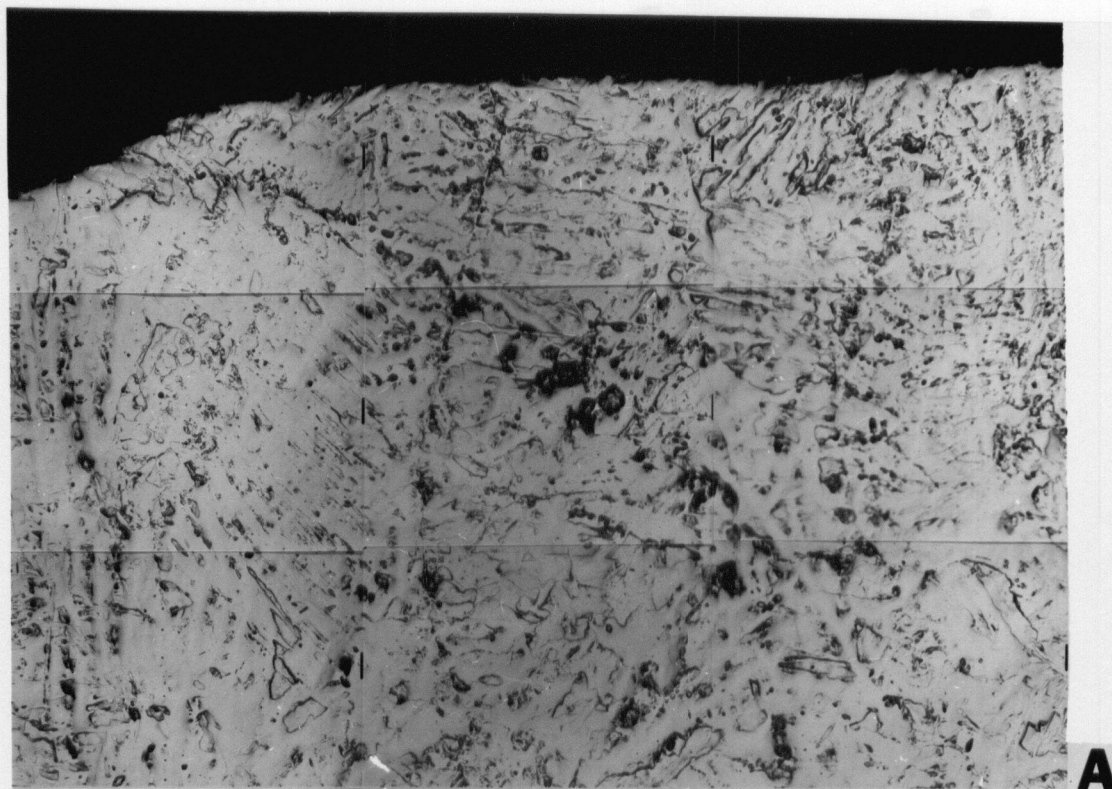


Fig. 5-18 Subsurface structure near a hook; $C \approx 0.10\%$ (Sample B3). (x38.7)

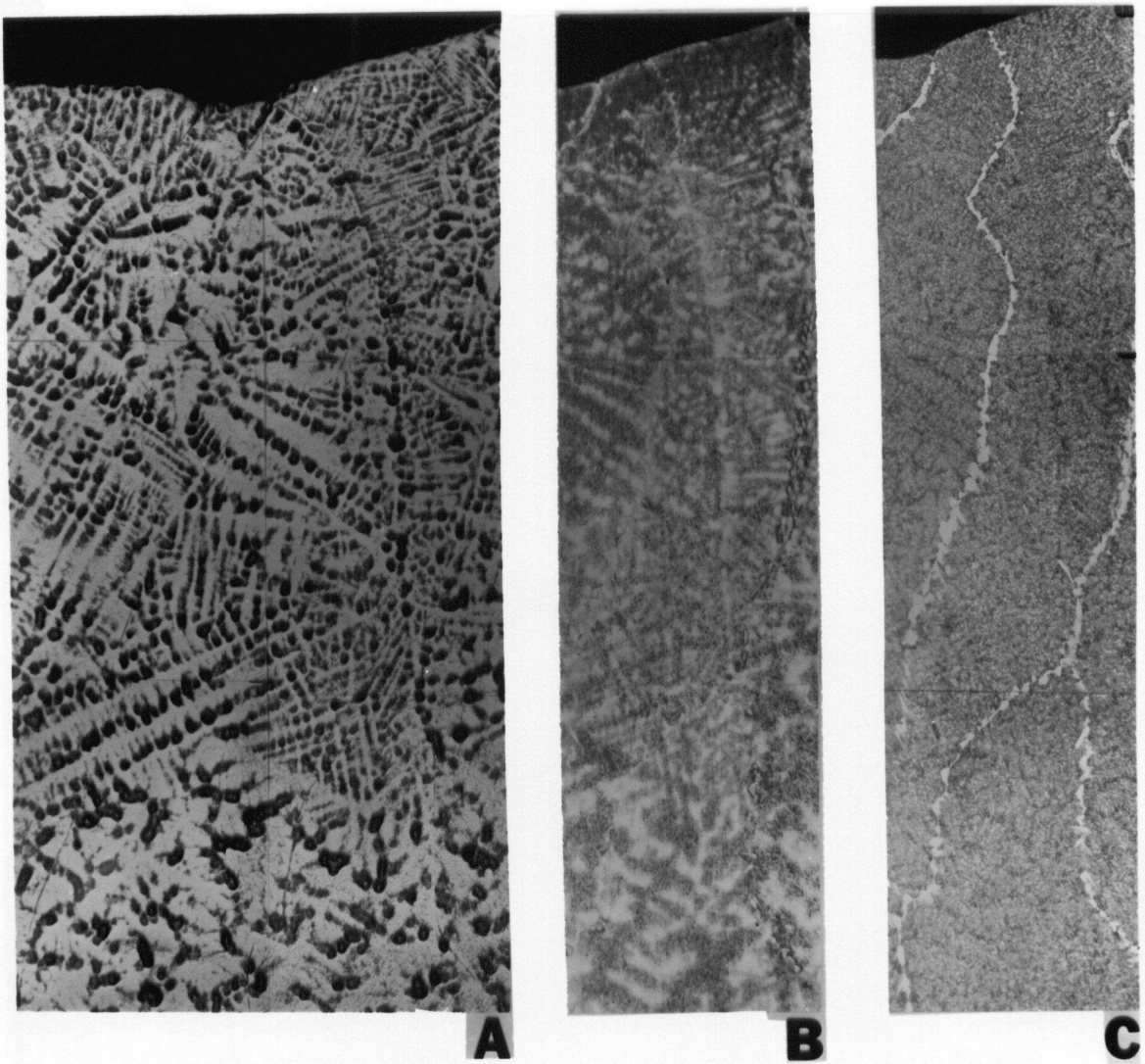
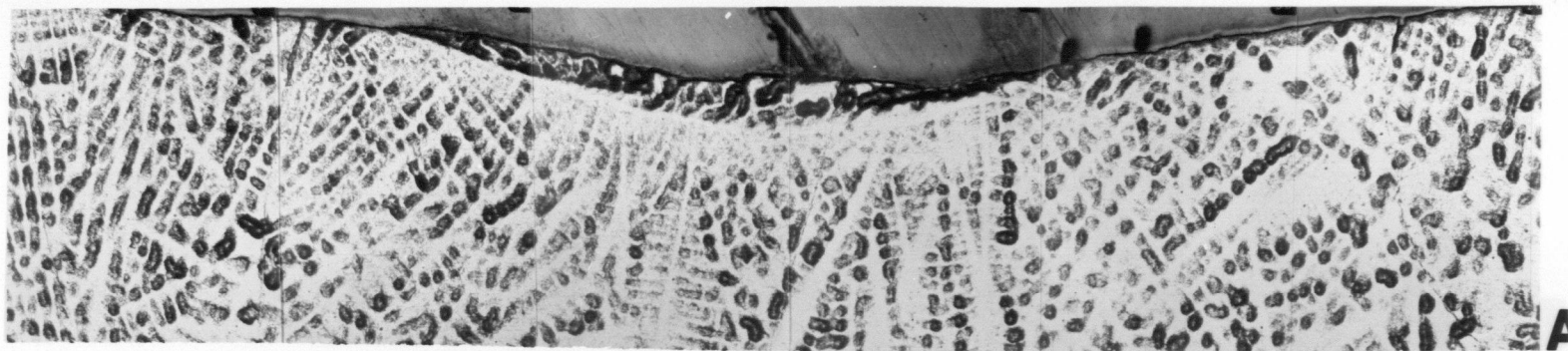
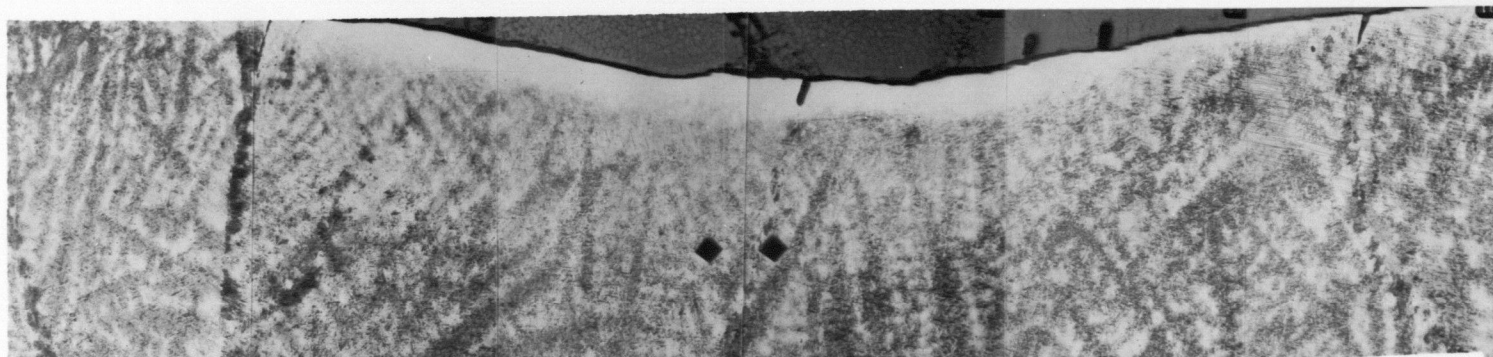


Fig. 5-19 Subsurface structure near a hook; $C \approx 0.26\%$ (Sample B4). (x38.7)



A



B



C

Fig. 5-20 Subsurface structure in the vicinity of positive segregation layer with hooks absent (Sample B5). (x38.7)

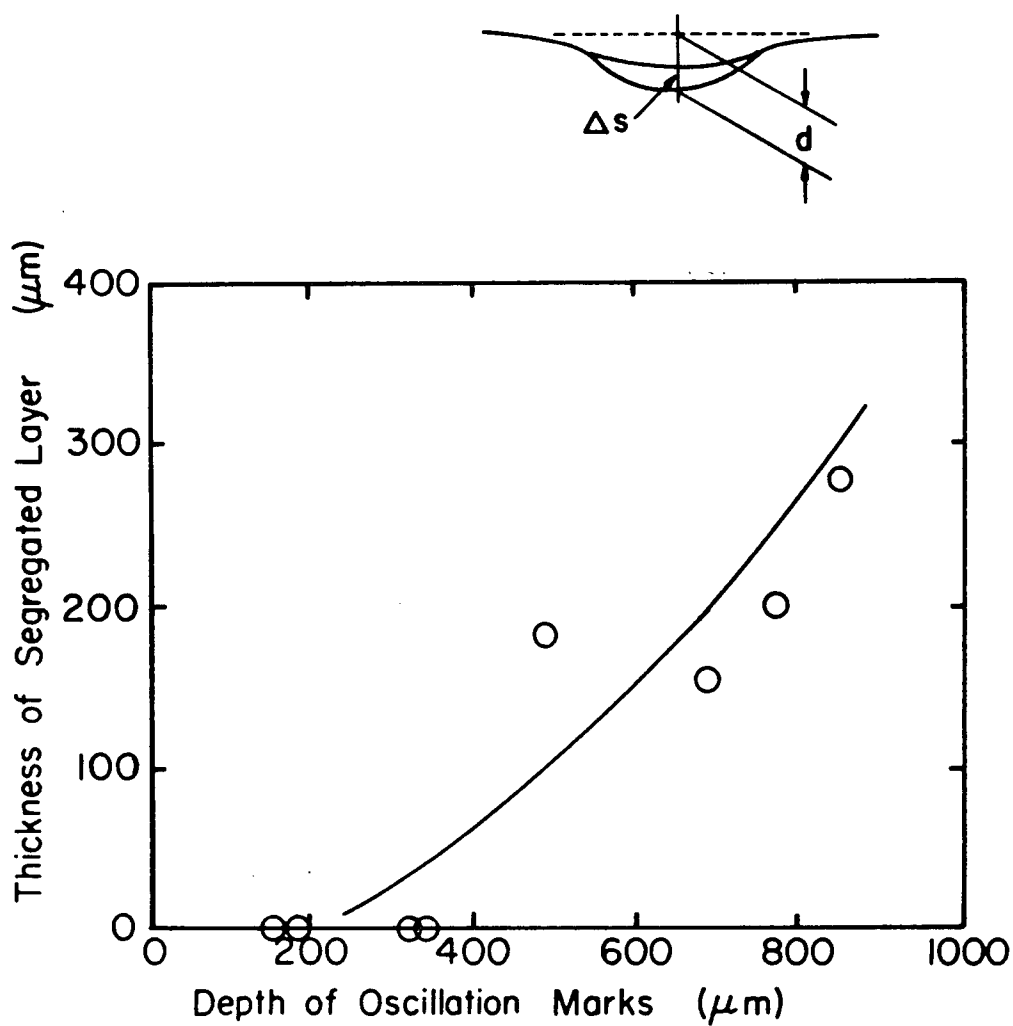


Fig. 5-21 Relationship between the depth of oscillation marks and the thickness of segregation layer (Company A).

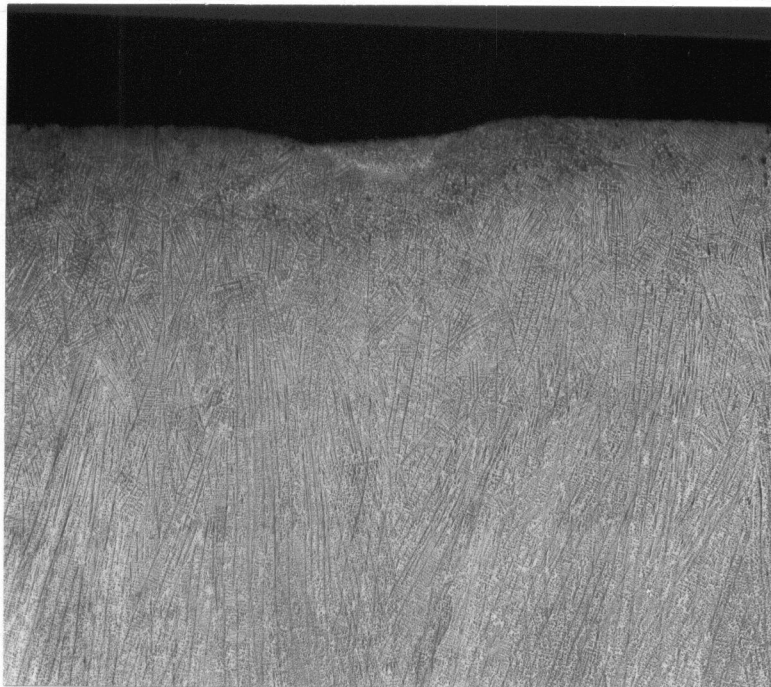
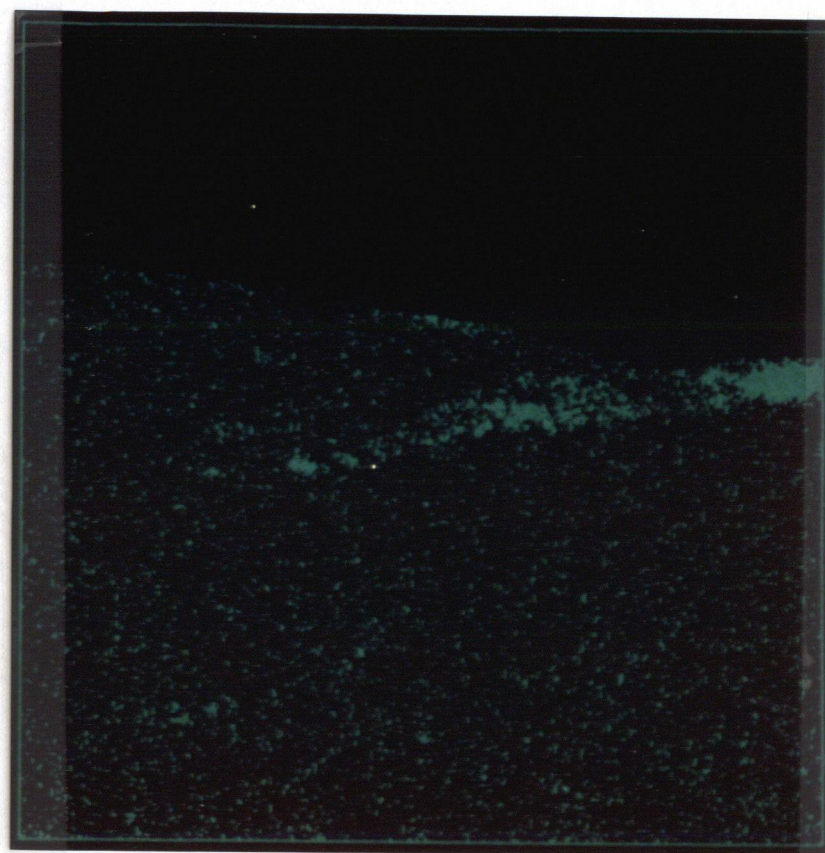


Fig. 5-22 Positive segregation at the bottom of oscillation mark in stainless steel slab (Sample B6). (x6)



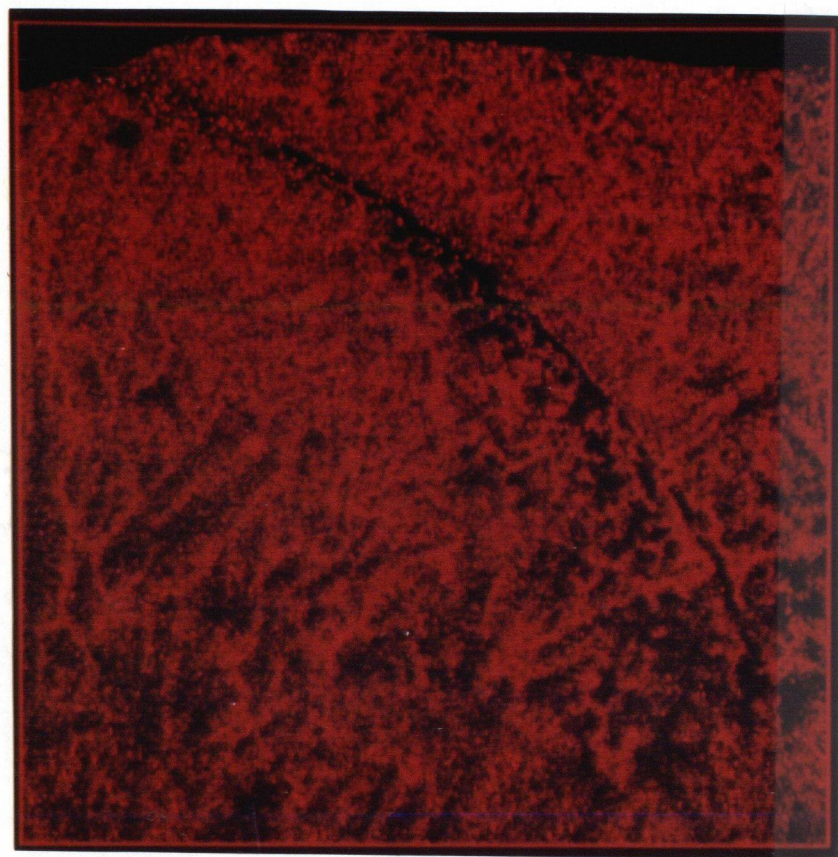
Mn



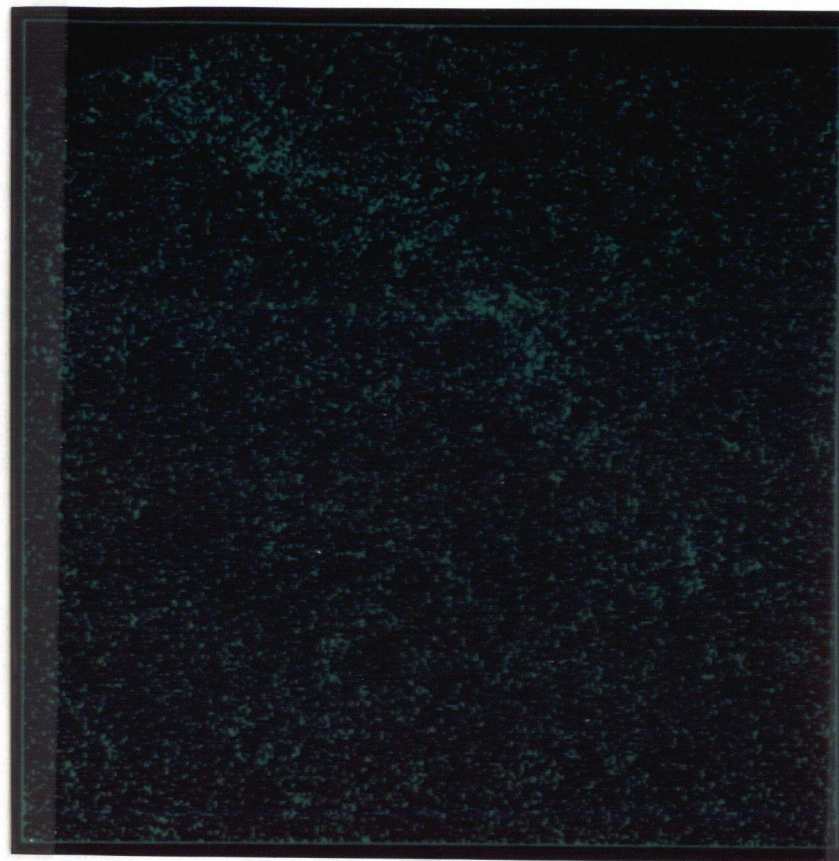
P

0 1.0 (mm)

Fig. 5-23 Segregation of Mn and P in the subsurface area of the oscillation mark determined by CMA (Sample B2).



Mn



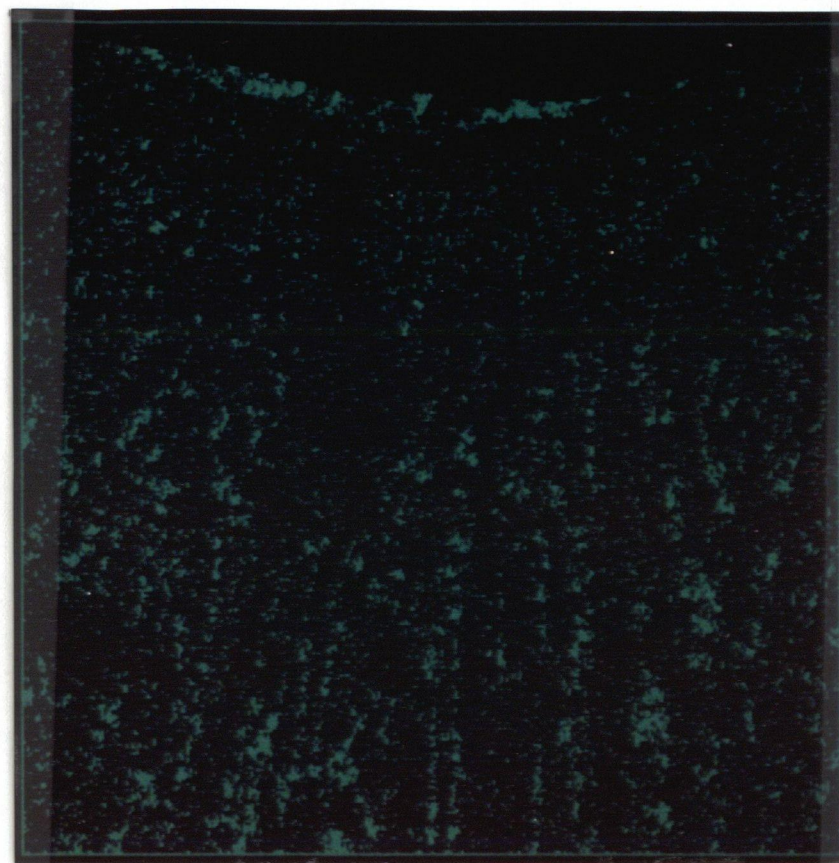
P

0 1.0 (mm)

Fig. 5-24 Segregation of Mn and P in the subsurface area of the oscillation mark determined by CMA (Sample B3).



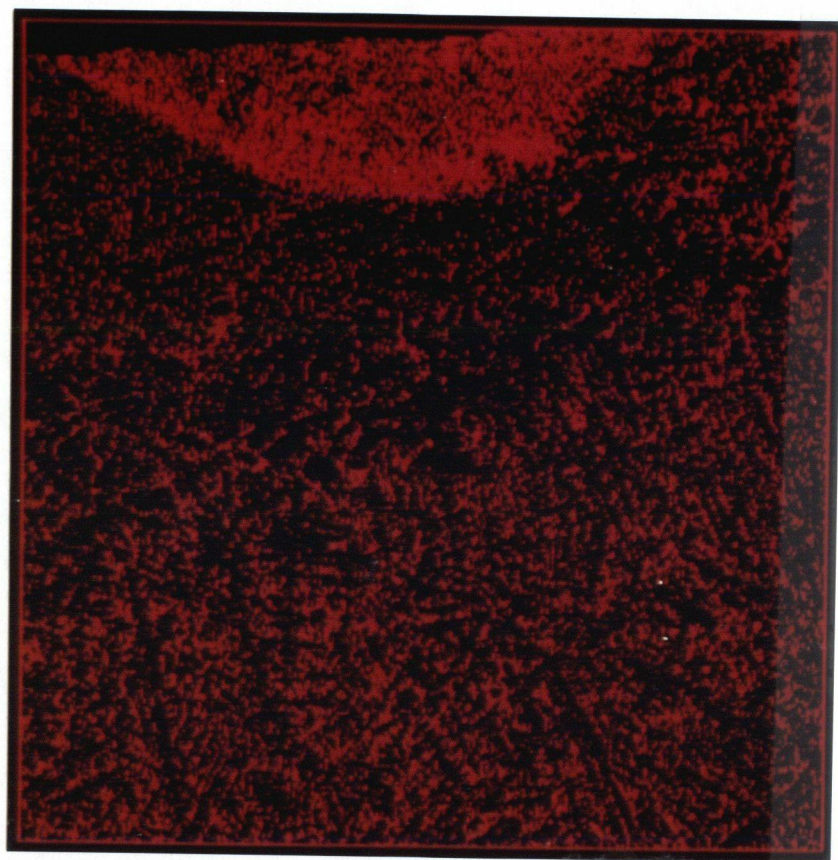
Mn



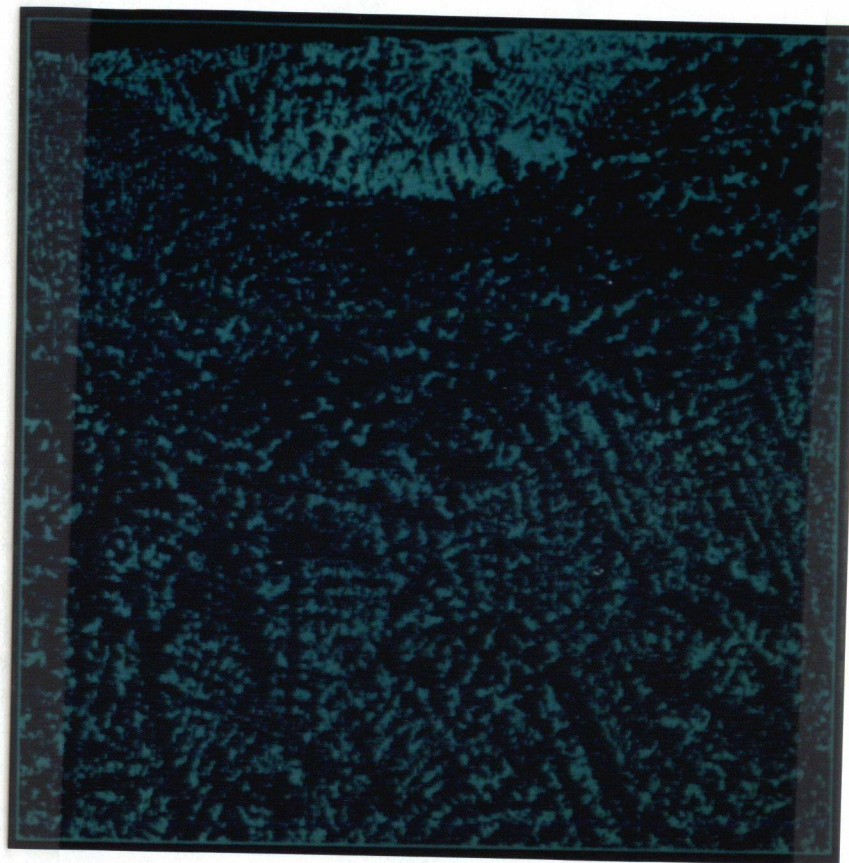
P

0 1.0 (mm)

Fig. 5-25 Segregation of Mn and P in the subsurface area of the oscillation mark determined by CMA (Sample B5).



Ni



P

0 1.0 (mm)

Fig. 5-26 Segregation of Ni and P in the subsurface area of the oscillation mark determined by CMA (Sample B6).

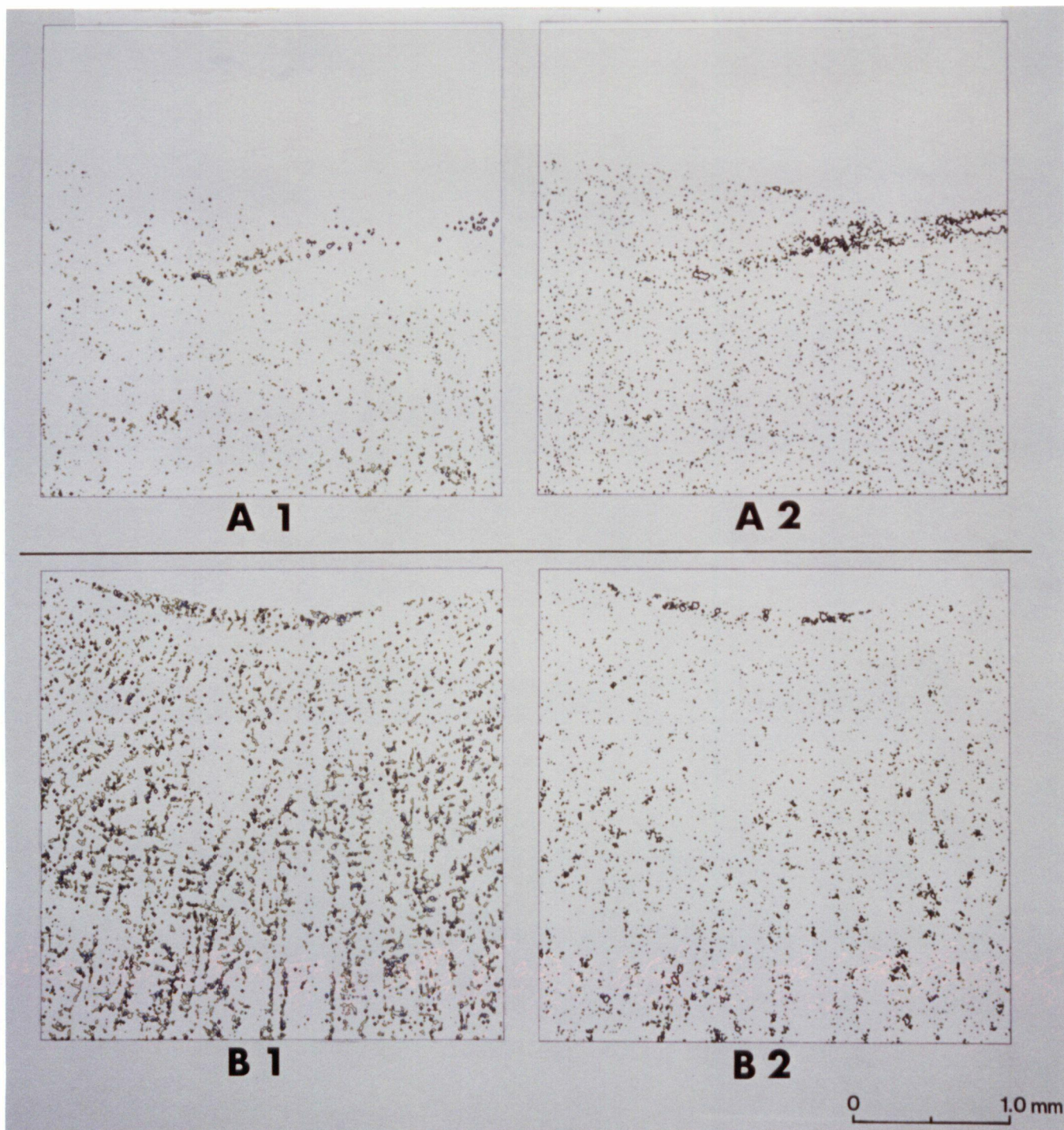


Fig. 5-27 Contour map of the segregation ratios, R , for (1) Mn and (2) P in (A) Sample B7 and (B) Sample B5.

Mn: Red/ R =1.4	P: Red/ R =3.0
Blue/ R =1.2	Blue/ R =1.2
Green/ R =1.1	Green/ R =1.1

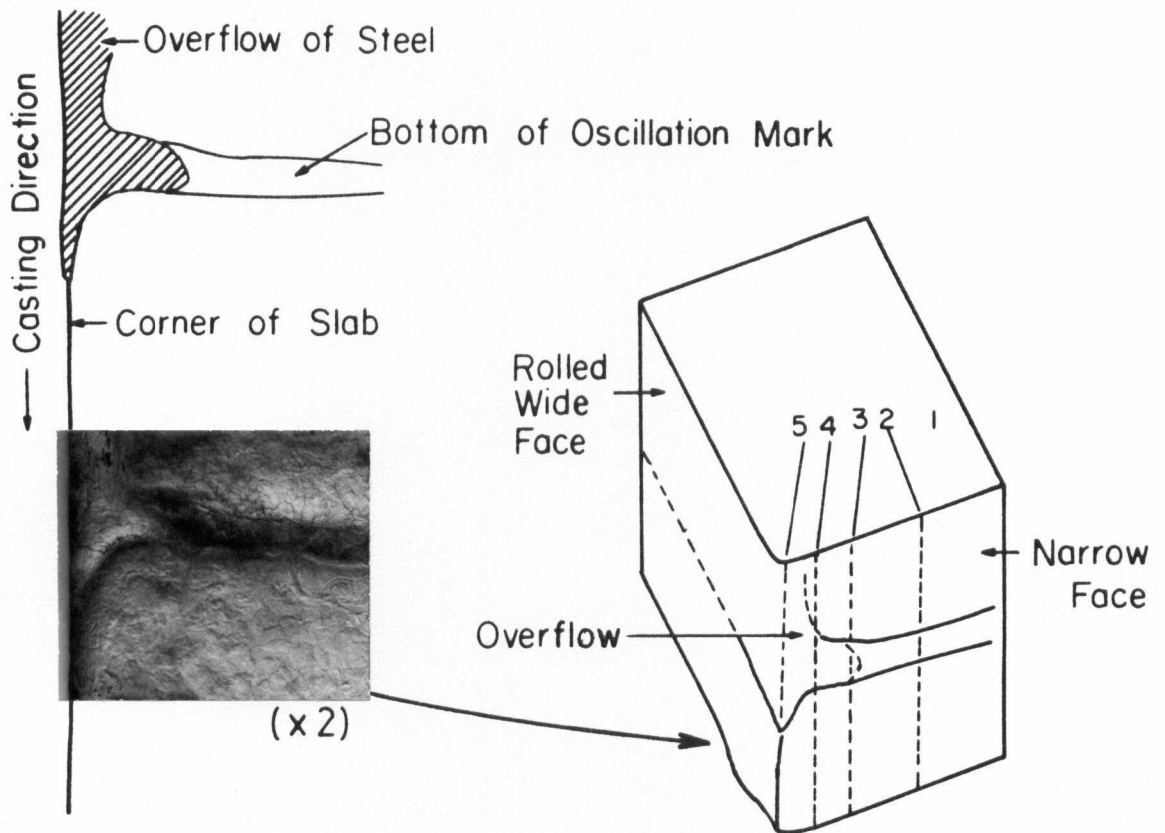


Fig. 5-28 Appearance of overflow at the slab corner and the location of cross section for metallographic inspection, Company A.

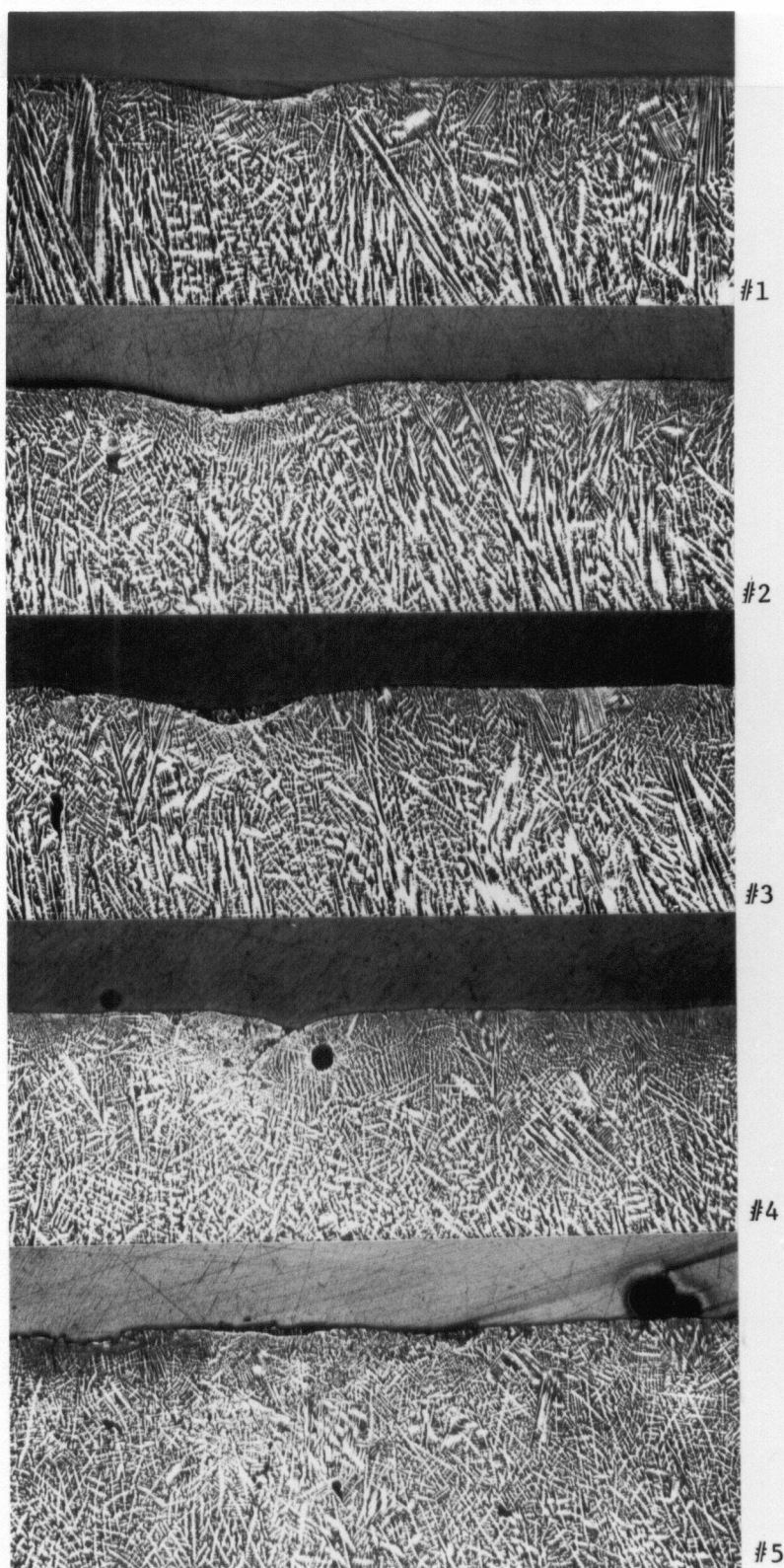


Fig. 5-29 Subsurface structure in each longitudinal cross section shown in Fig. 5-28; picral etching (Company A). (x5.4)

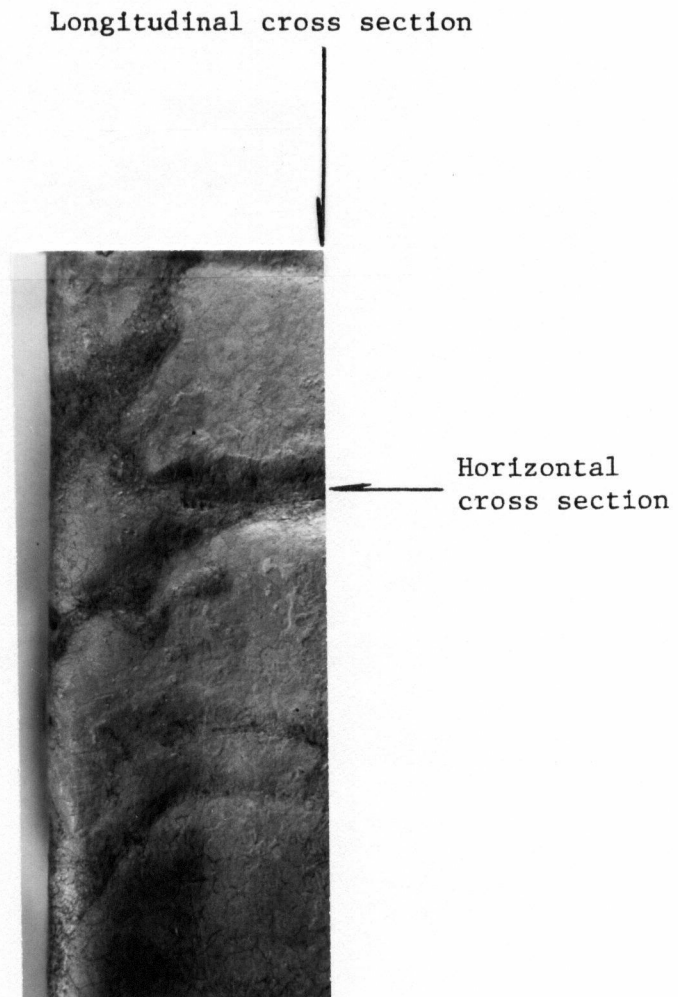
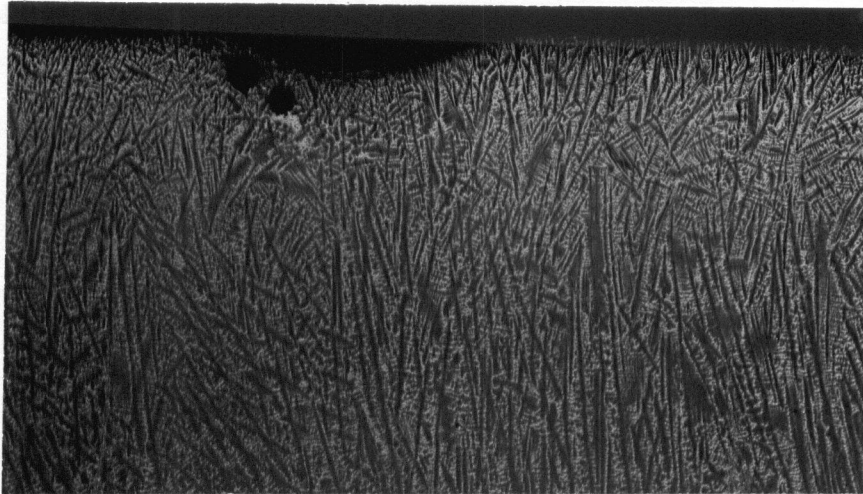
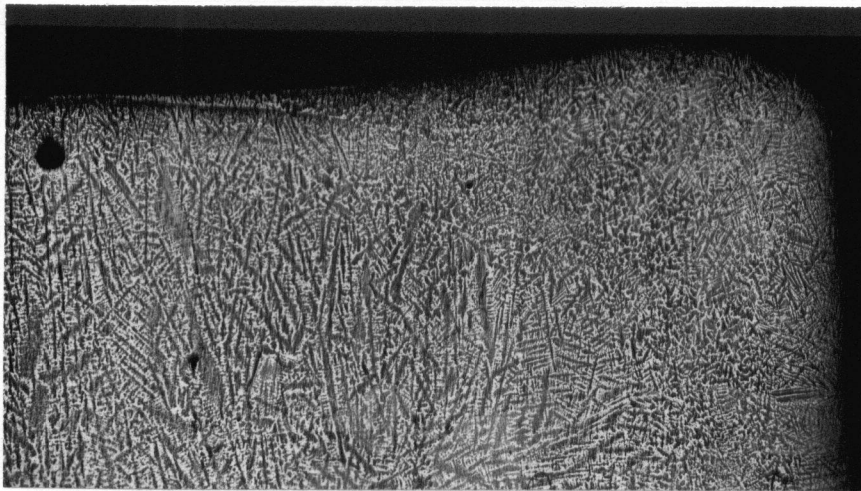


Fig. 5-30 Slab corner sample for the investigation into the structure in the horizontal cross section (Company A). (x2)



(a)



(b)

Fig. 5-31 Subsurface structure (a) in longitudinal cross section, and (b) in horizontal cross section of the sample shown in Fig. 5-30; Oberhoffer etch (Company A). (a):x6.5, (b):x6.


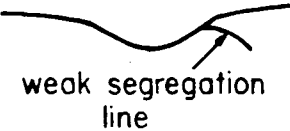
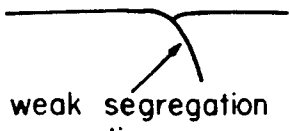

Types of Oscillation Mark	Types of Positive Segregation		
Hooks in subsurface structure	Type 1  large segregation area	Type 2  weak segregation line	Type 3  weak segregation line
Hooks absent in subsurface structure	Type 4  segregation layer		

Fig. 5-32 Classification of positive segregation.

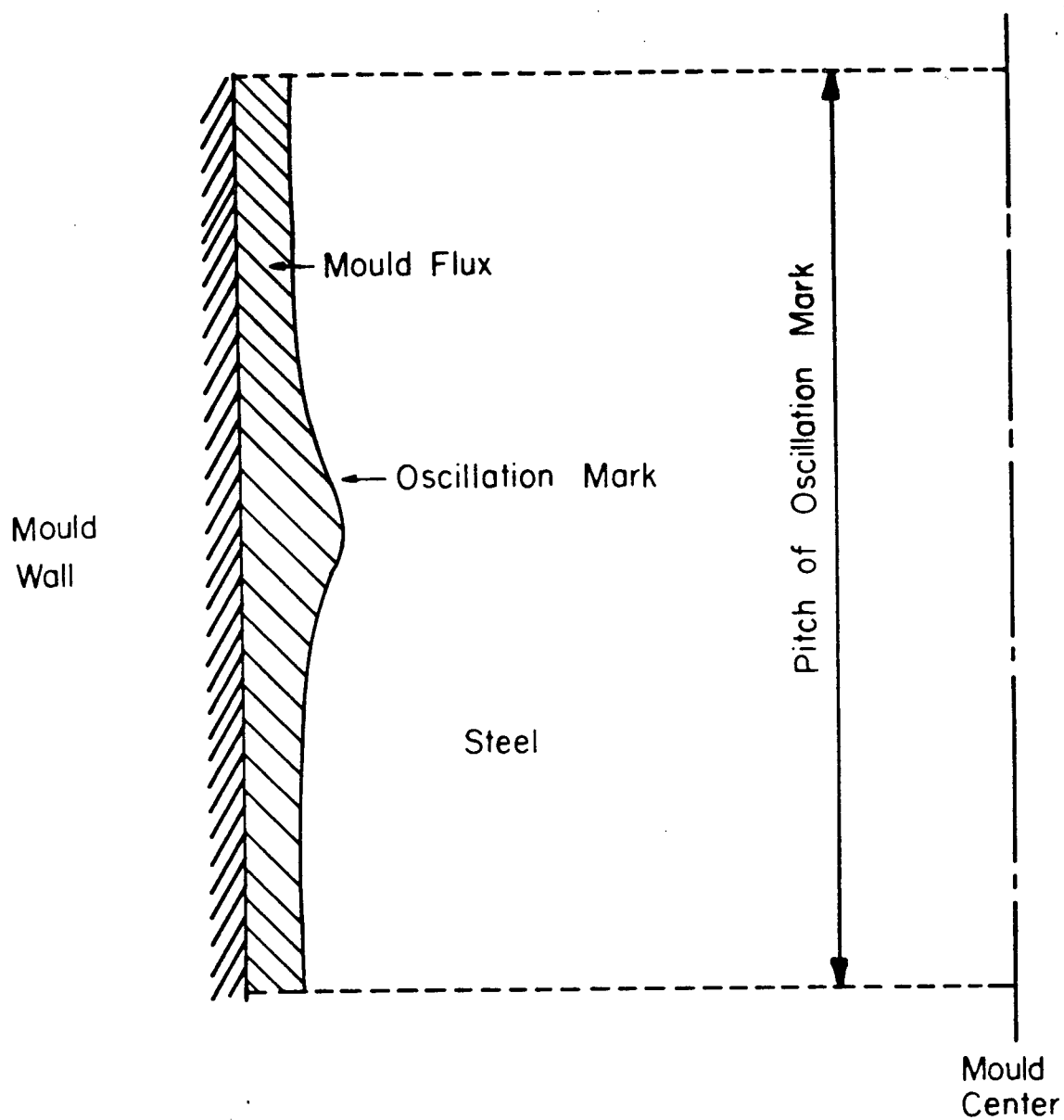
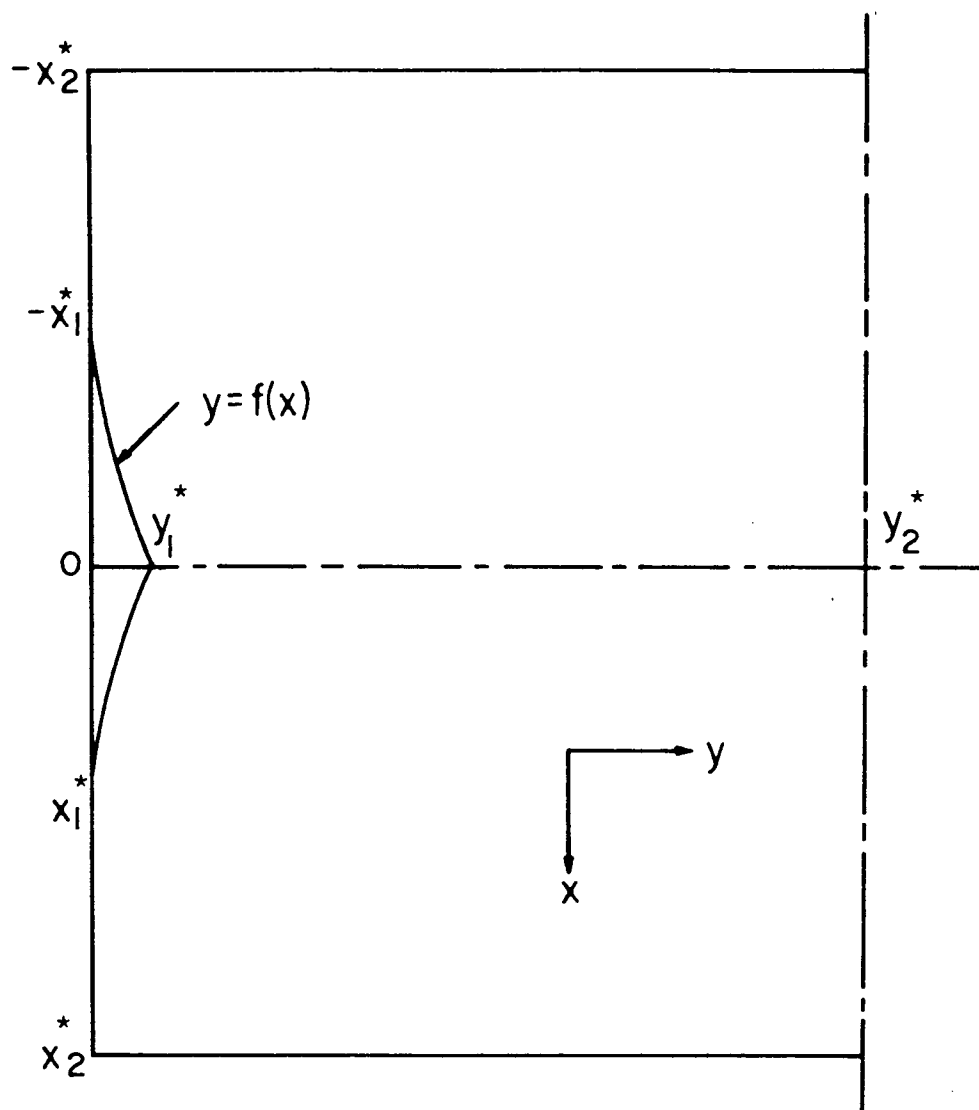


Fig. 5-33 Physical system for mathematical model of heat flow in the vicinity of the oscillation mark.



x_1^* : half length of mark depression

x_2^* : half pitch of oscillation marks

y_1^* : depth of oscillation mark

y_2^* : half width of the mould

Fig. 5-34 Coordinate of the controlled system (symmetric system).

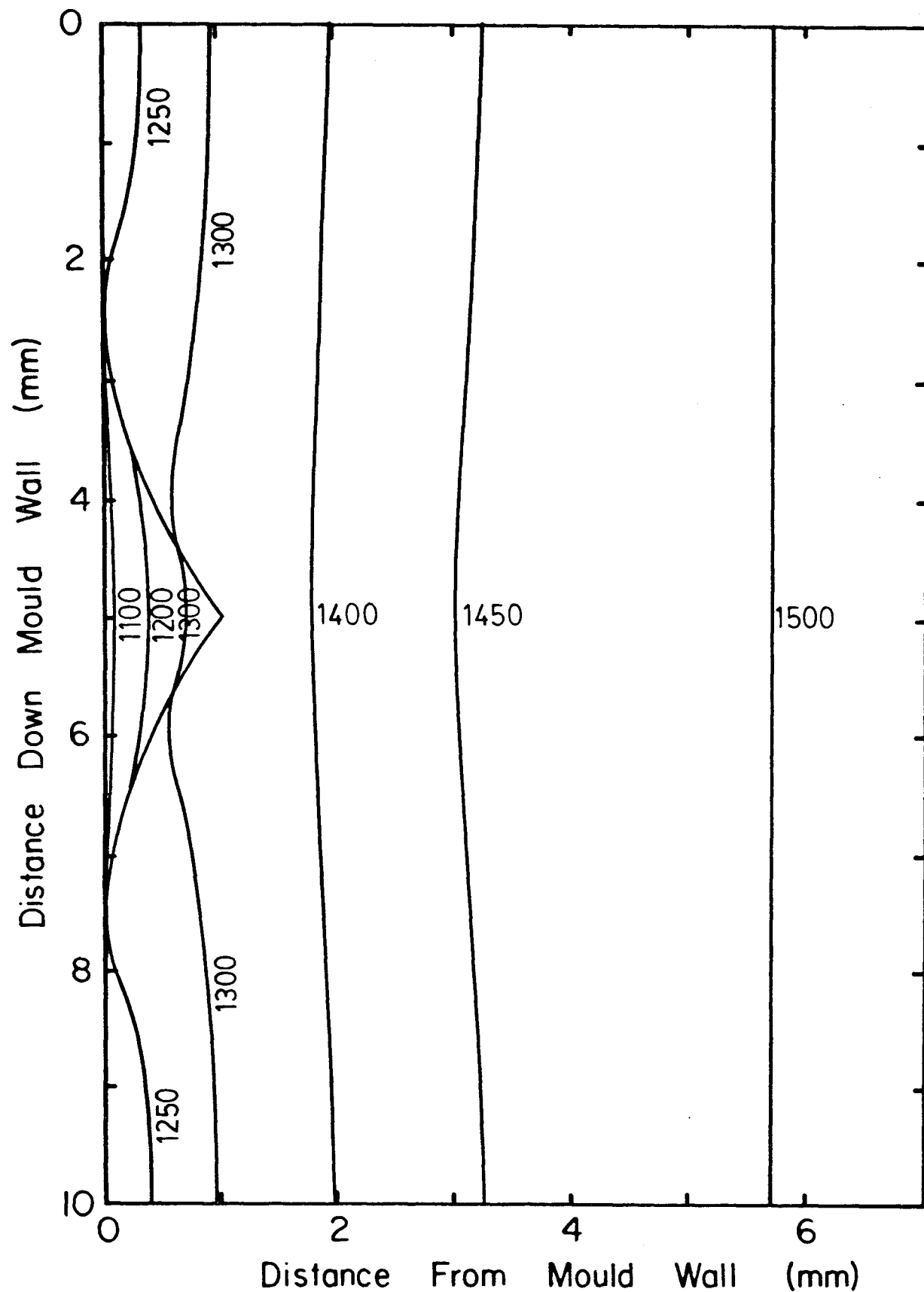


Fig. 5-35 Temperature distribution in mould flux and steel after 10s.

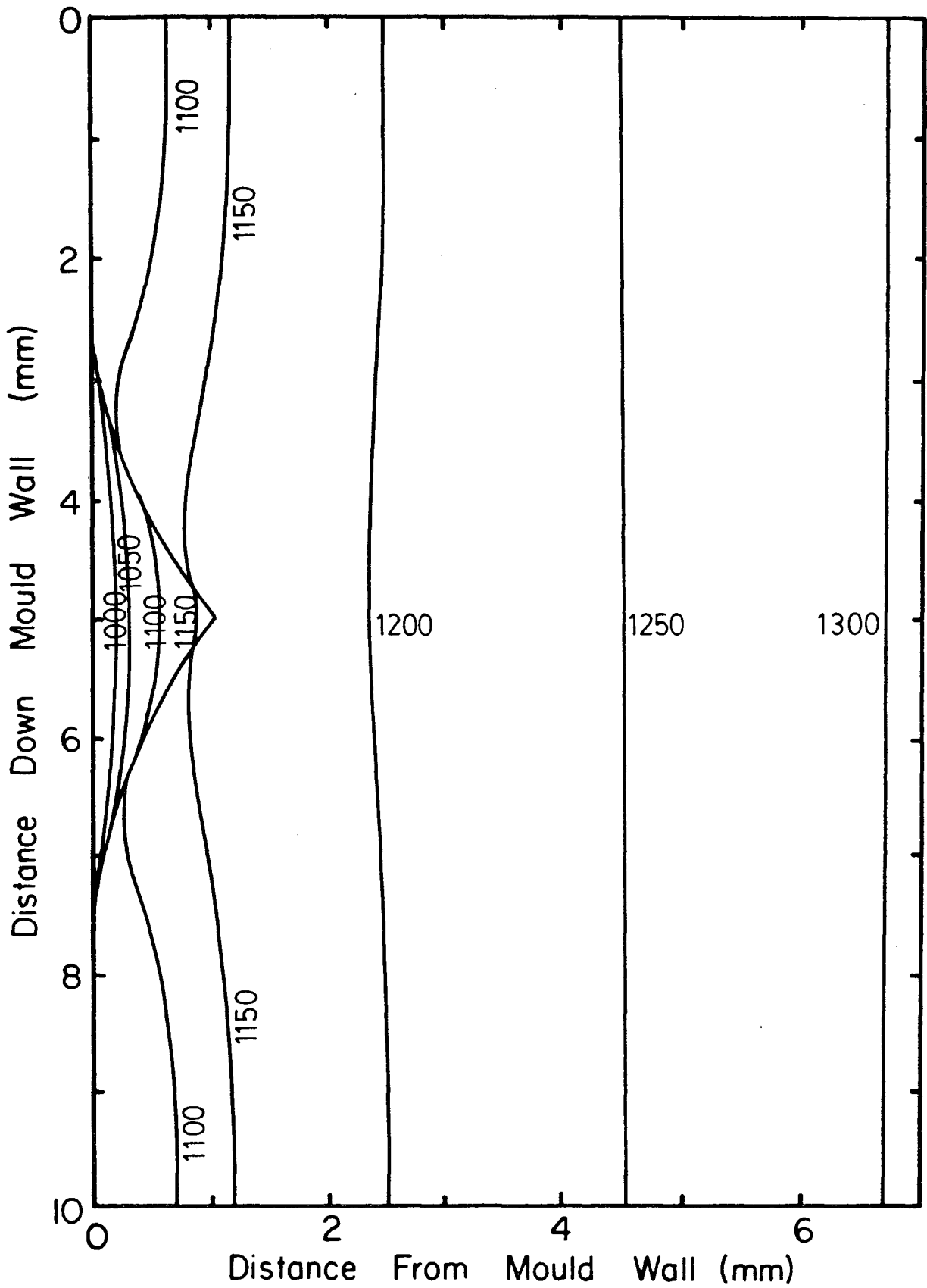


Fig. 5-36 Temperature distribution in mould flux and steel after 48s.

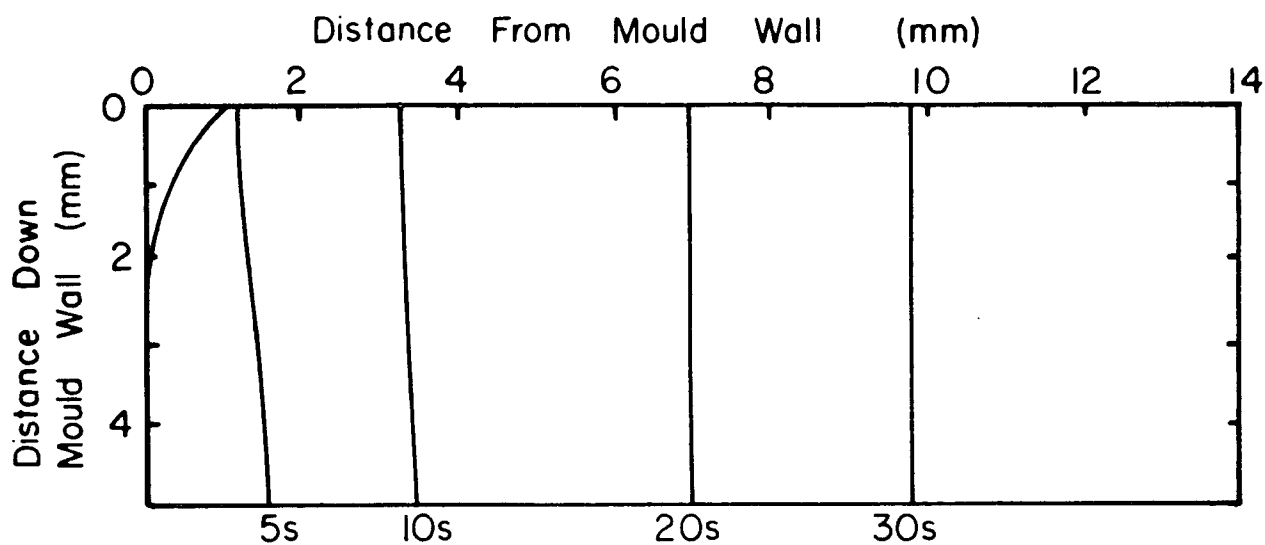


Fig. 5-37 Change of shell profile with time.
 ($l=1.0\text{cm}$, $d=0.10\text{cm}$, $x_1^*/x_2^*=0.5$)

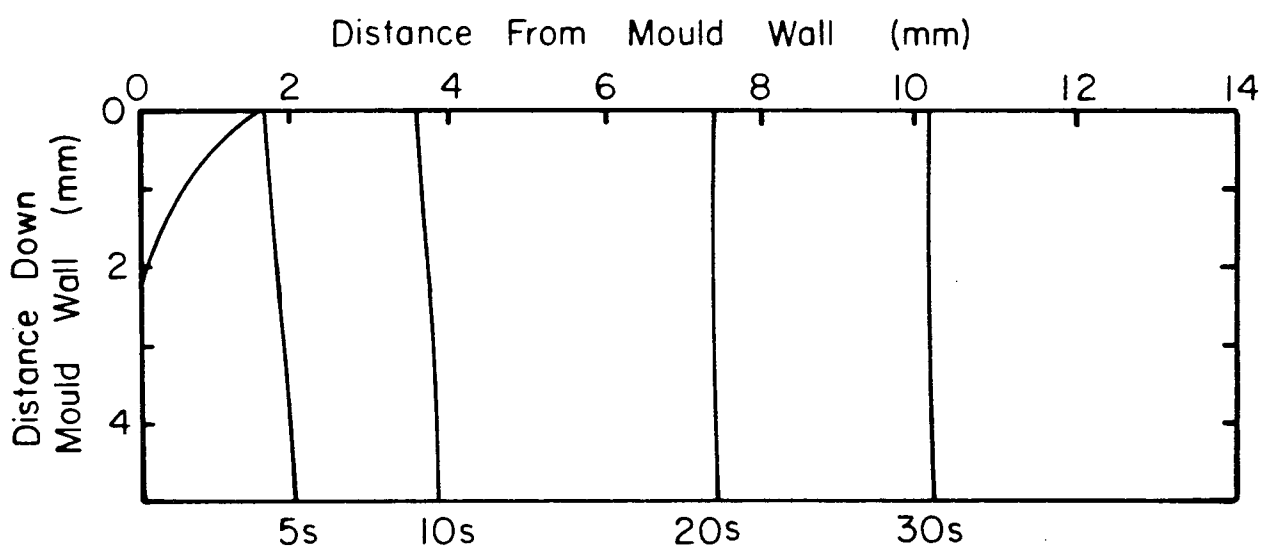


Fig. 5-38 Change of shell profile with time.
 ($l=1.0\text{cm}$, $d=0.15\text{cm}$, $x_1^*/x_2^*=0.5$)

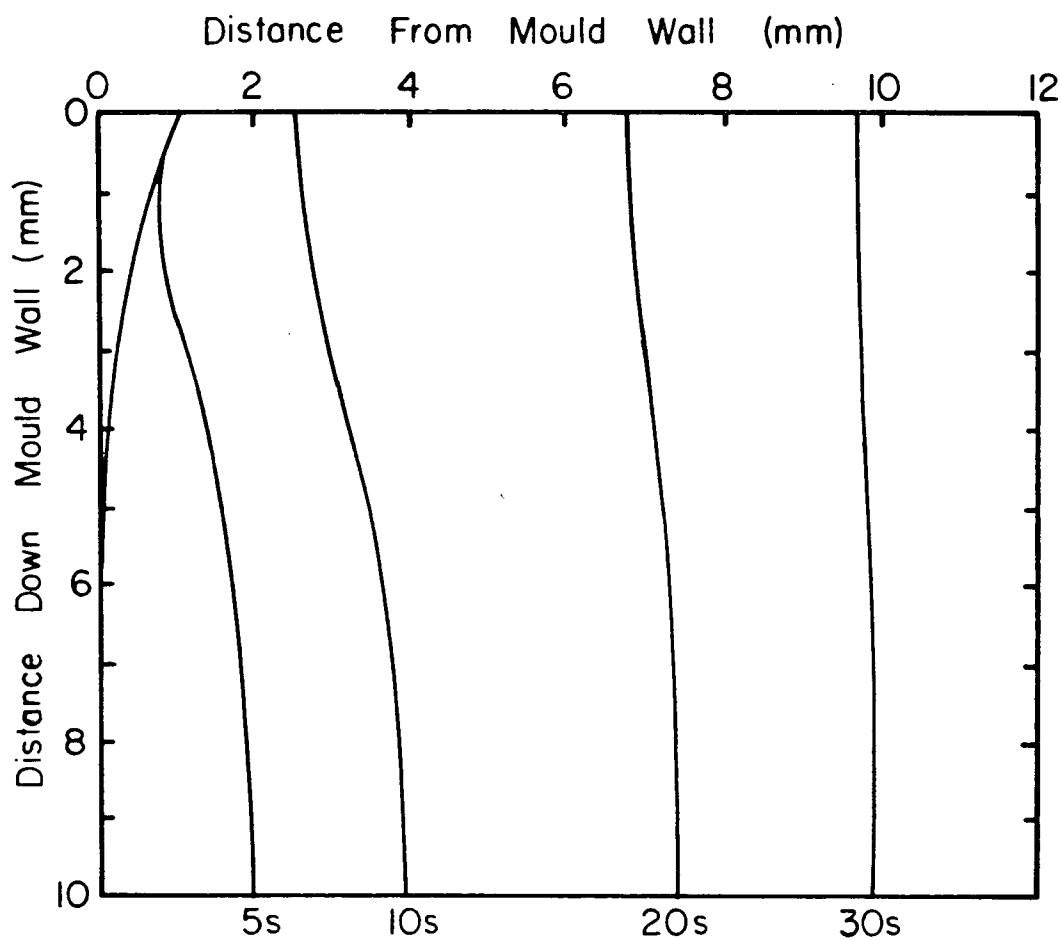


Fig. 5-39 Change of shell profile with time.
 ($l=2.0\text{cm}$, $d=0.10\text{cm}$, $x_1^*/x_2^*=0.5$)

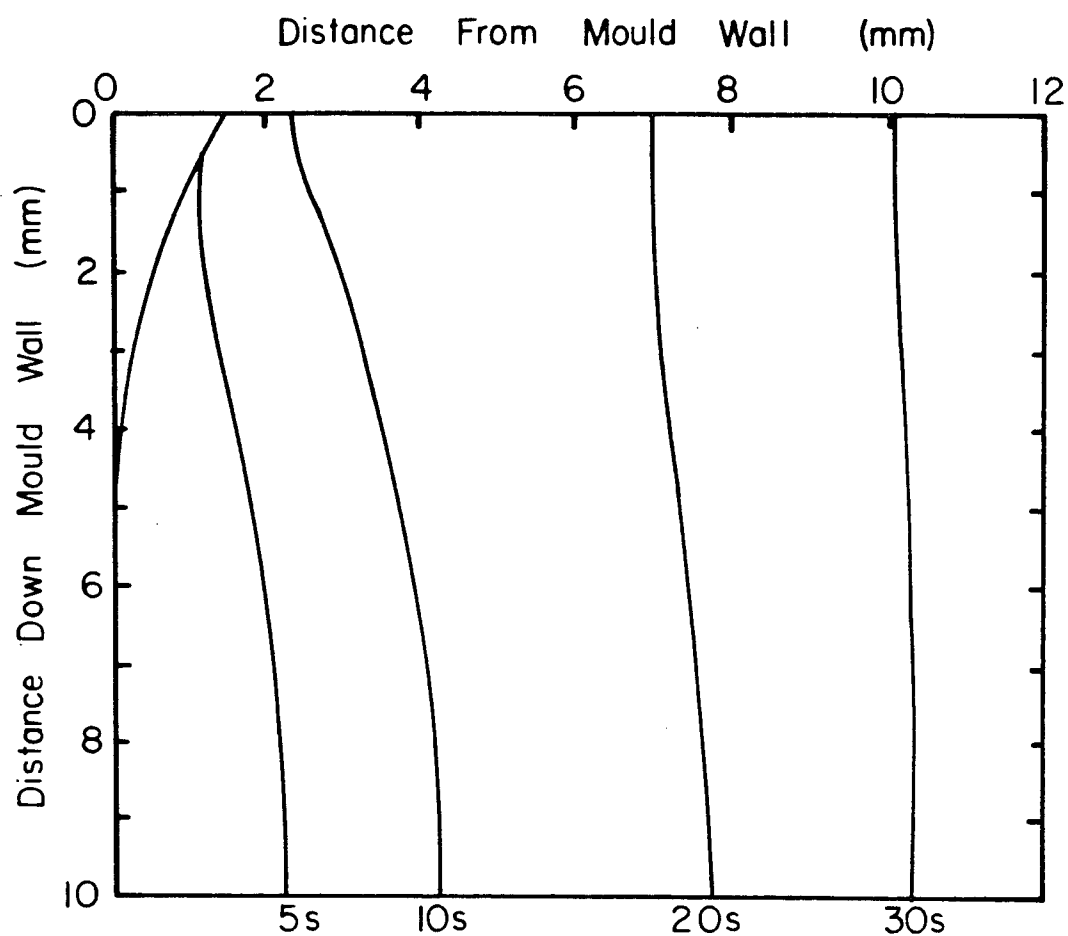


Fig. 5-40 Change of shell profile with time.
 ($l=2.0\text{cm}$, $d=0.15\text{cm}$, $x_1^*/x_2^*=0.5$)

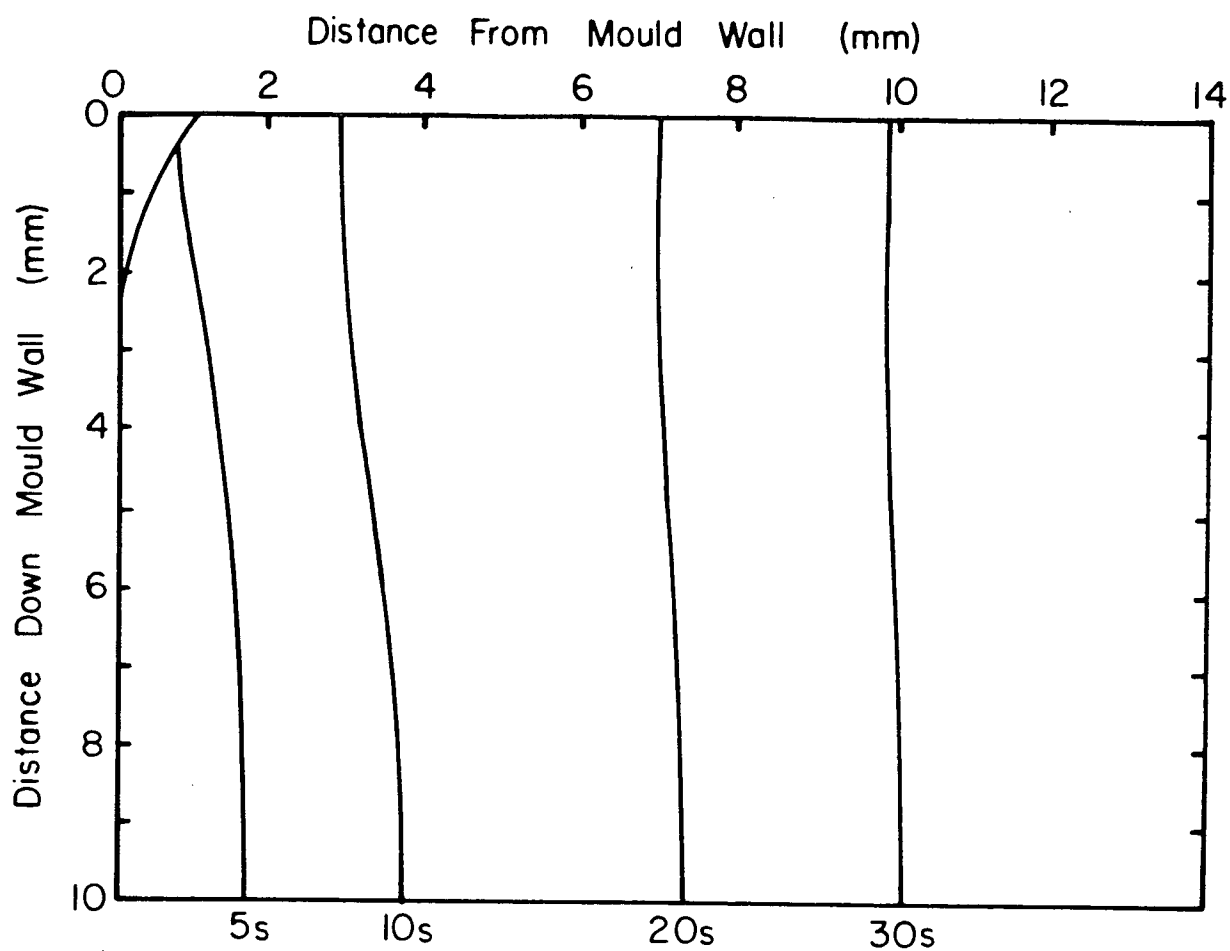


Fig. 5-41 Change of shell profile with time.
 ($l=2.0\text{cm}$, $d=0.10\text{cm}$, $x_1^*/x_2^*=0.3$)

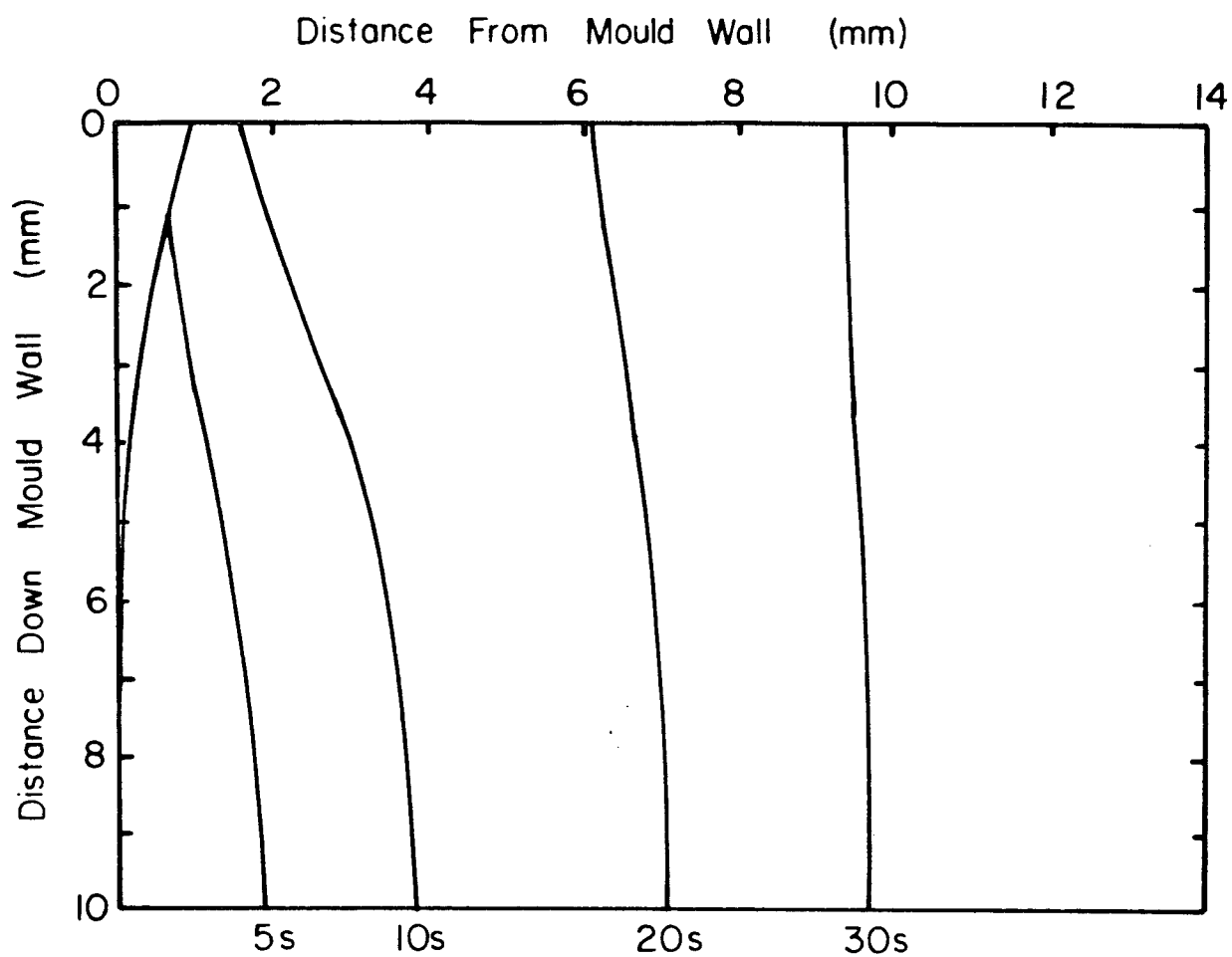


Fig. 5-42 Change of shell profile with time.
 ($l=2.0\text{cm}$, $d=0.10\text{cm}$, $x_1^*/x_2^*=0.7$)

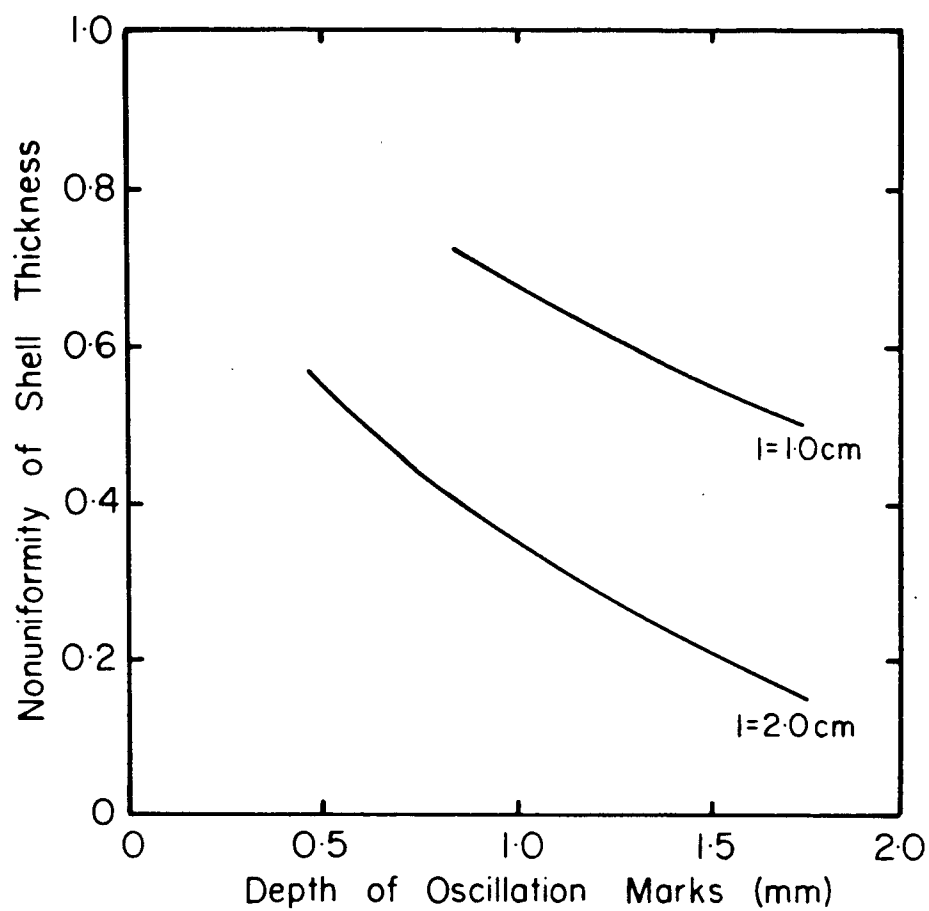


Fig. 5-43 Effect of the shape of oscillatin mark on the nonuniformity of shell thickness after 10s.
($x_1^*/x_2^*=0.5$)

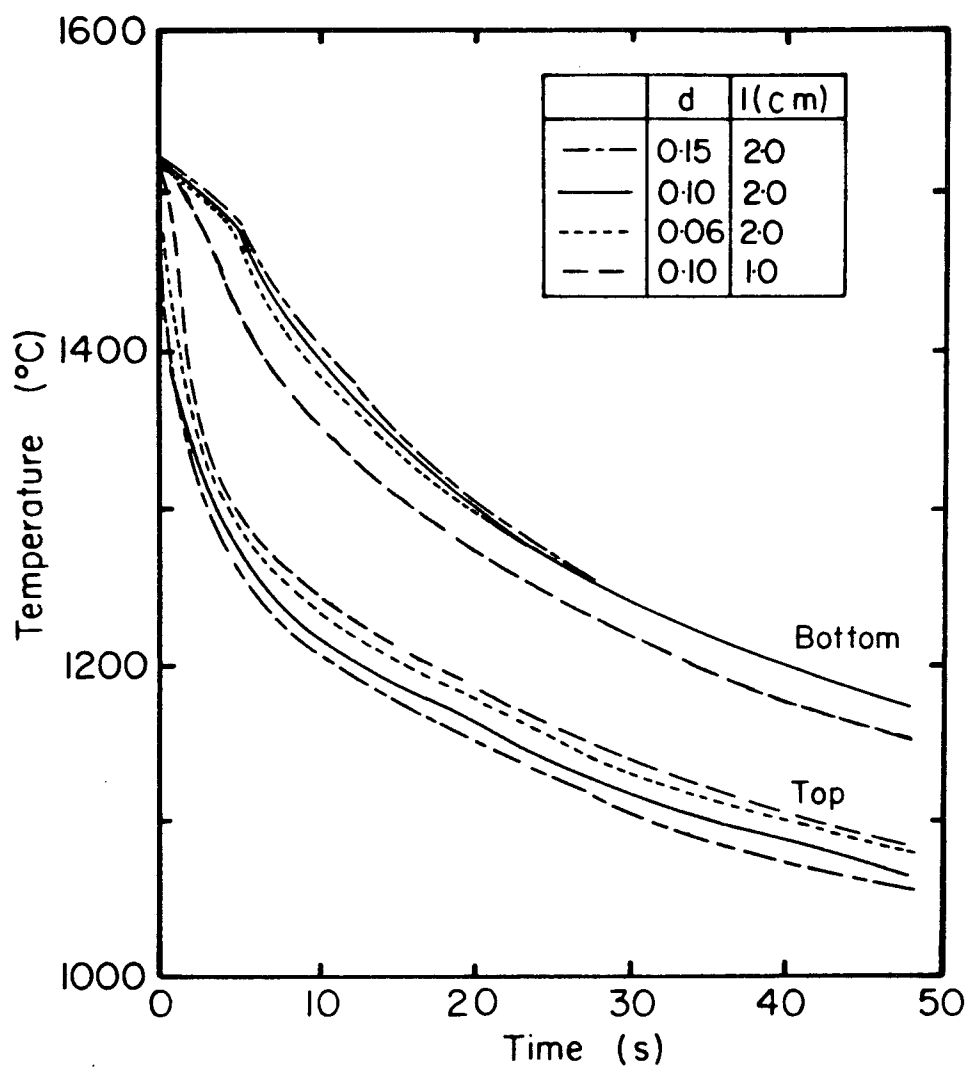


Fig. 5-44 Change of temperature with time at the bottom and at the top of oscillation marks.

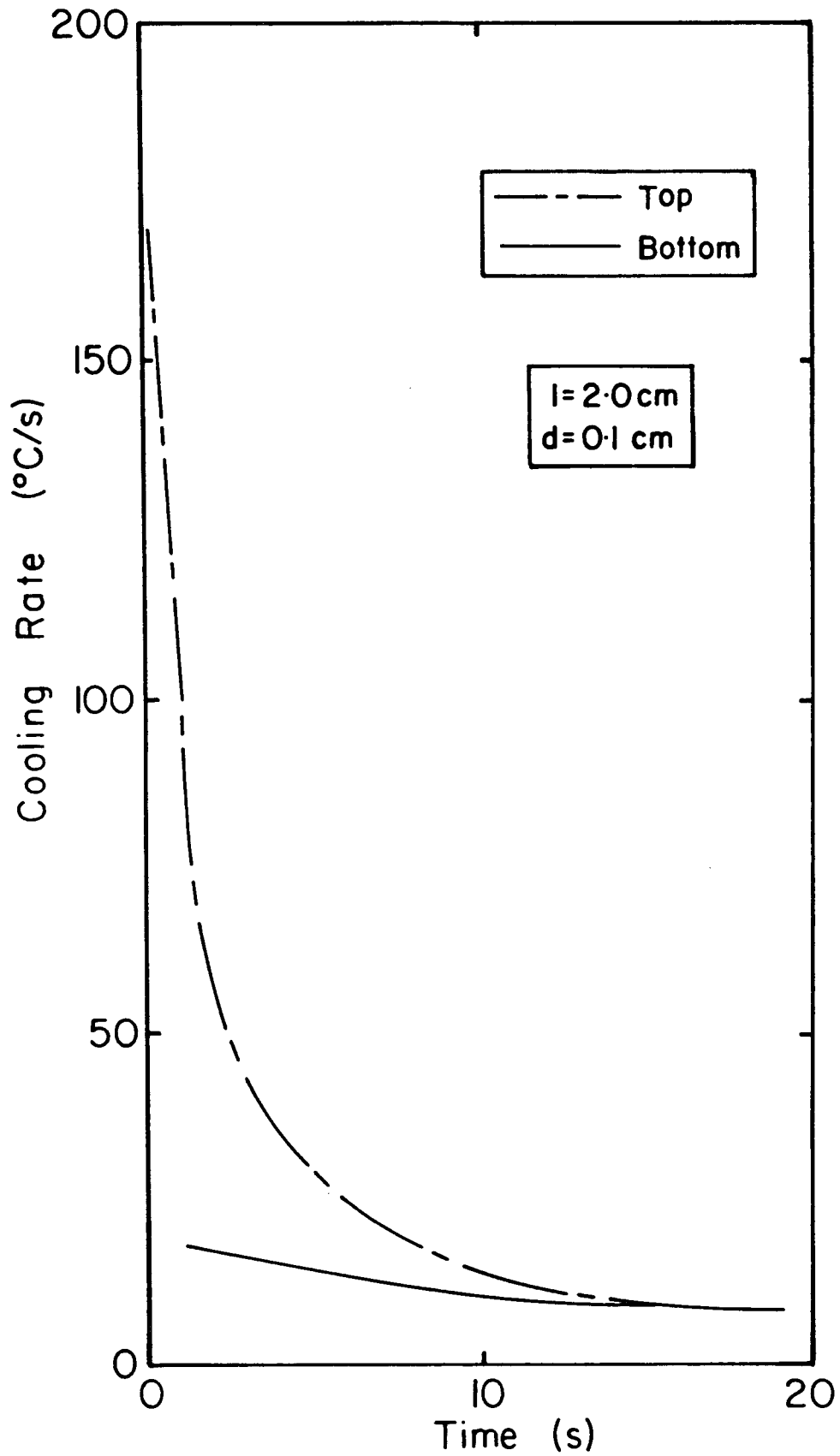


Fig. 5-45 Change of cooling rate with time at the top and at the bottom of oscillation mark. ($l=2.0\text{cm}$, $d=0.10\text{cm}$)

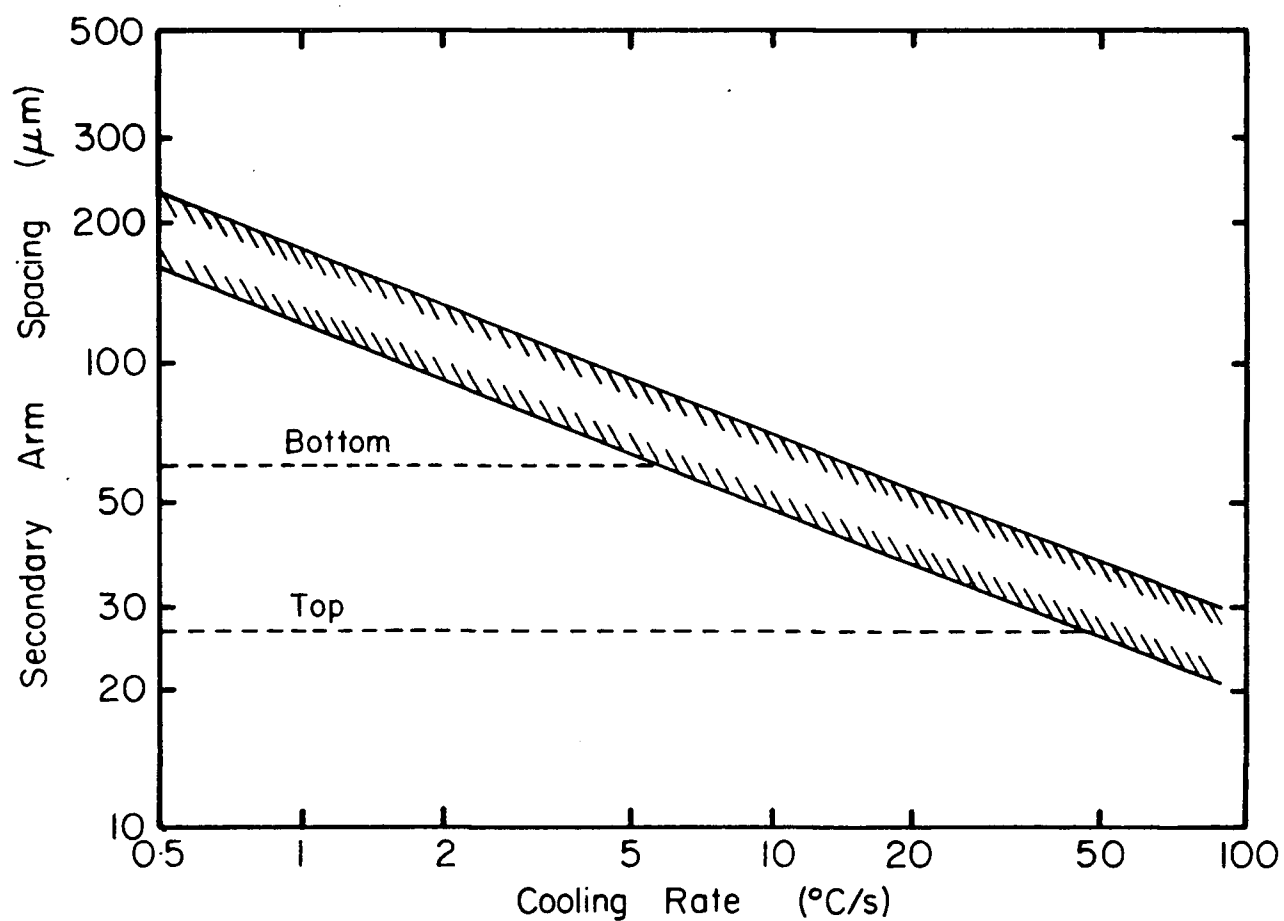


Fig. 5-46 Relationship between cooling rate and the secondary dendrite arm spacing by A. Suzuki et al.¹⁰⁴
 Note: Measured average values of secondary arm spacing at the top and at the bottom of oscillation mark are indicated.

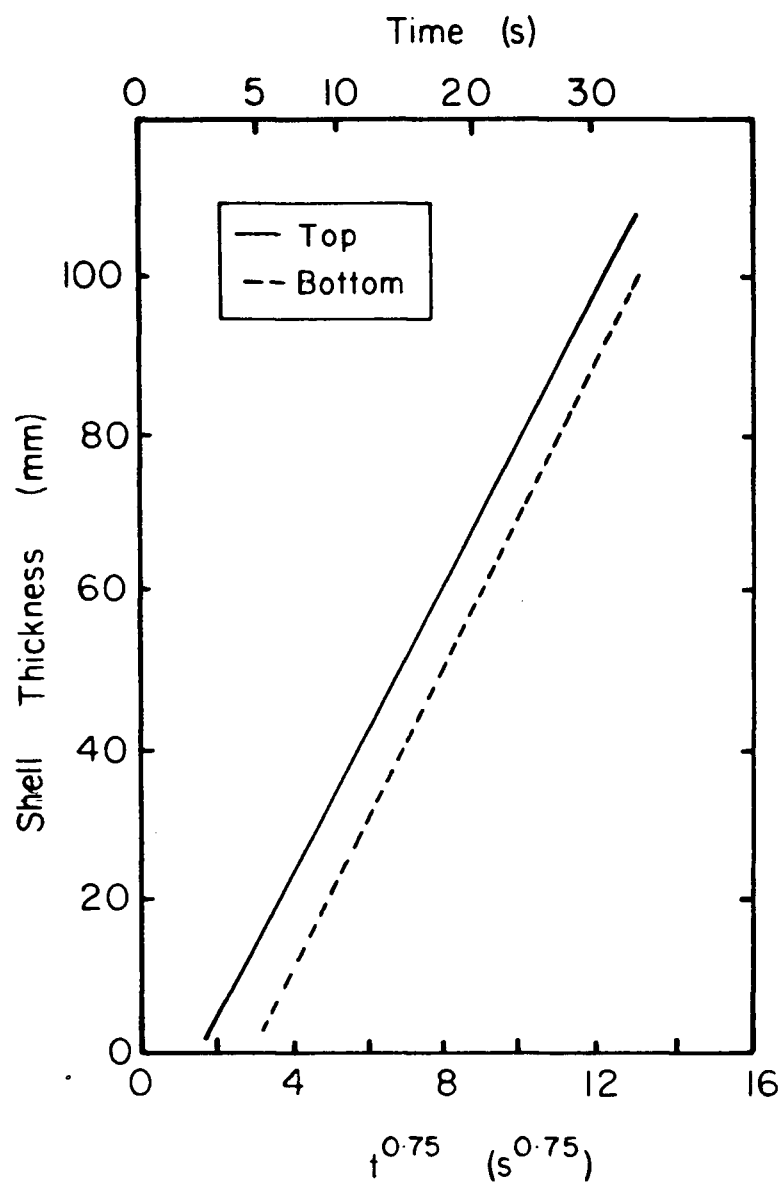


Fig. 5-47 Relationship between shell thickness and time.
($l=1.0\text{cm}$, $d=0.10\text{cm}$)

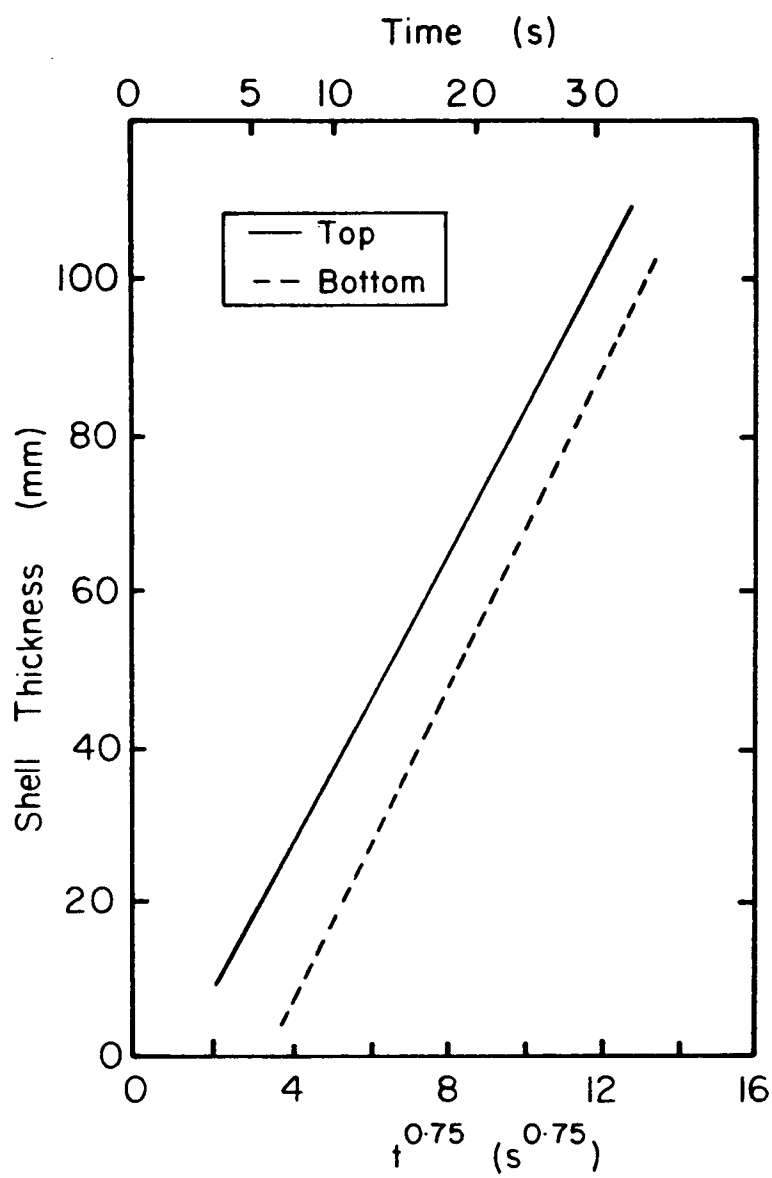


Fig. 5-48 Relationship between shell thickness and time.
($l=2.0\text{cm}$, $d=0.10\text{cm}$)

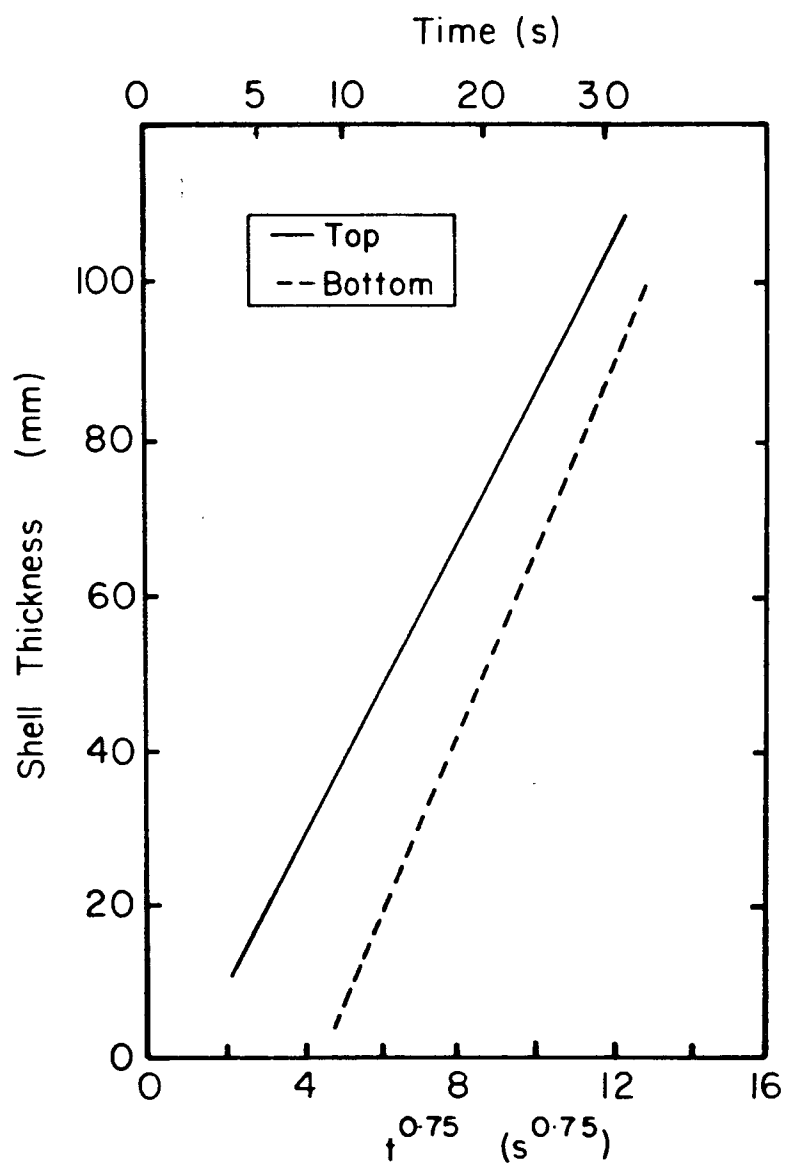


Fig. 5-49 Relationship between shell thickness and time.
($l=2.0\text{cm}$, $d=0.15\text{cm}$)

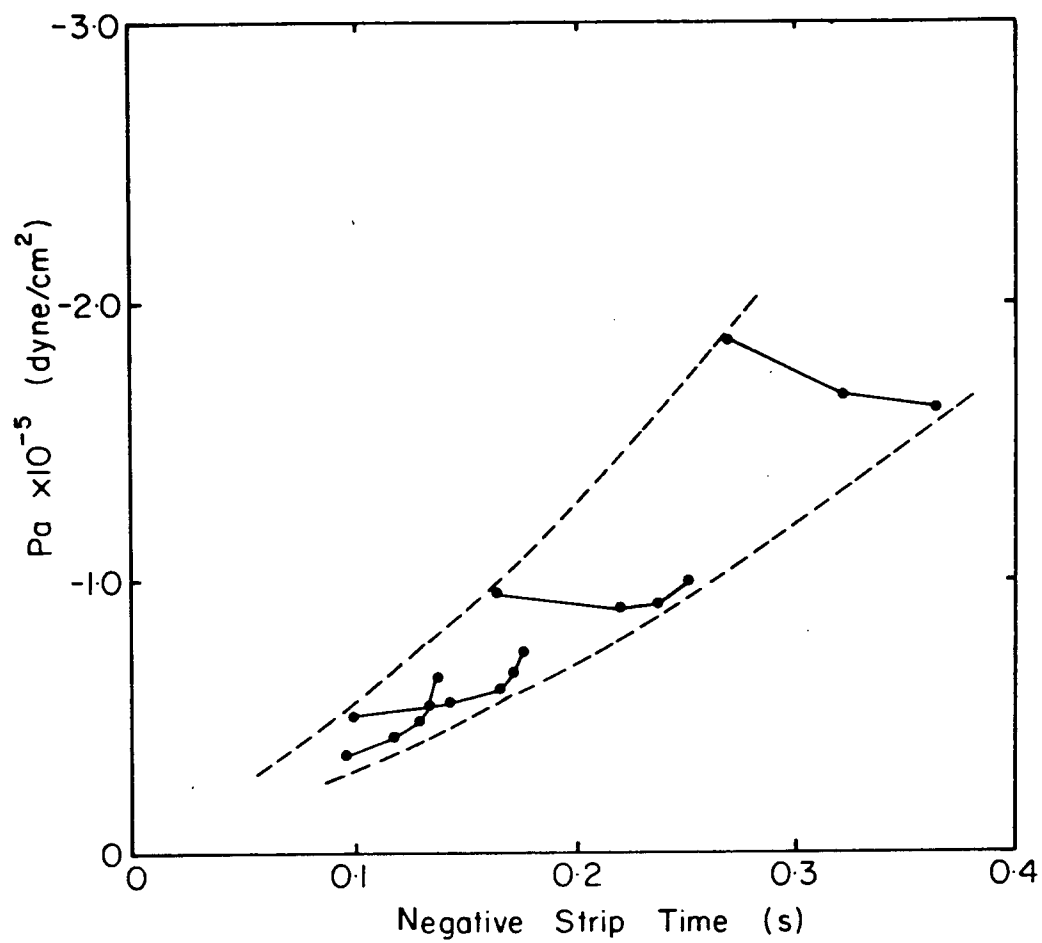


Fig. 5-50 Relationship between Pa and negative-strip time.

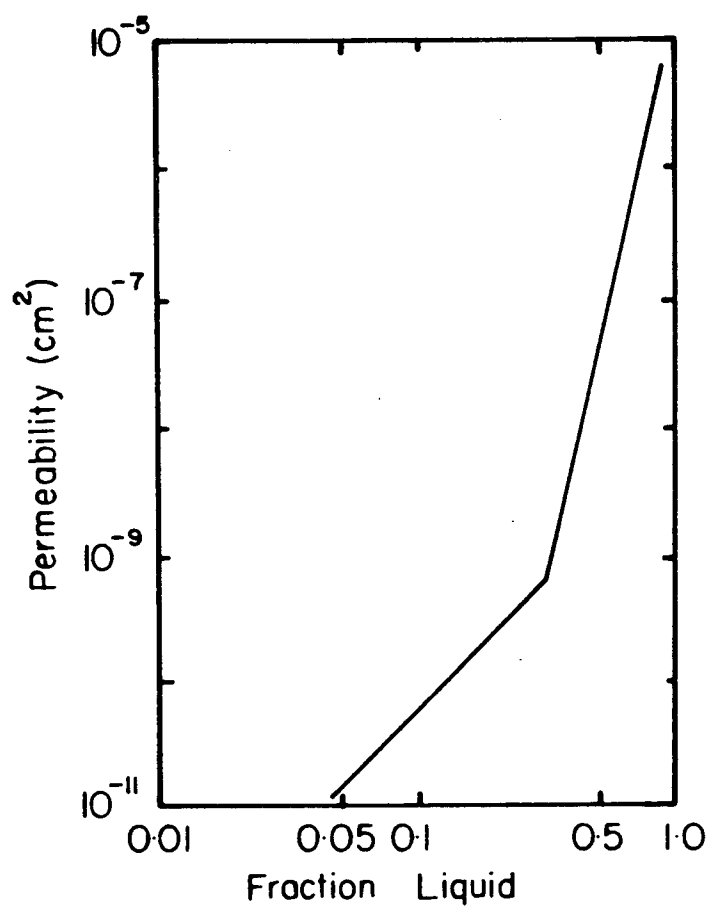


Fig. 5-51 Relationship between permeability and fraction liquid from Piwonka et al.¹⁰⁷

6. CONCLUSIONS AND SUGGESTIONS FOR FUTURE WORK

6.1 Conclusions

Initial solidification phenomena in the continuous casting slab mould have been studied by metallurgically examining slab samples and by undertaking a series of theoretical analyses. Firstly an investigation has been conducted to elucidate the mechanism of oscillation-mark formation. The metallurgical investigation has revealed the following:

- [i] As reported by previous workers, oscillation marks were found with and without hooks in the adjacent subsurface structure.
- [ii] Hooks in the subsurface structure of 0.09%-carbon slabs form a smaller angle with the surface than in 0.26%-carbon slabs.
- [iii] Slabs having oscillation marks without subsurface hooks characteristically also contained inert-gas blowholes, which suggest that fluid flow of steel caused by argon gas injection through the submerged nozzle had influenced the meniscus solidification. In other cases, the multi-port practice and electromagnetic stirring in the mould suppressed meniscus solidification due to rapid convection in the meniscus region.
- [iv] The depth of oscillation marks with subsurface hooks is

greater in low-carbon (0.09%) than in medium-carbon (0.26%) slabs. Oscillation marks without hooks do not show a carbon dependence of depth. In low-carbon slabs the depth of oscillation marks with subsurface hooks is slightly greater when the steel is killed with aluminum than when killed with silicon.

The theoretical analyses contributed new knowledge on meniscus phenomena.

- [i] Prediction of the temperature distribution in the meniscus region, using experimental heat fluxes, showed that partial solidification at the meniscus, to form a thin rigid skin, depends strongly on both local convection and superheat. A low-temperature region was also predicted in the mould flux adjacent to the mould wall.
- [ii] A fluid-flow analysis has shown that, owing to the shape of the flux channel between the meniscus and mould wall, pressure is generated in the flux by the mould oscillation. The pressure is positive when the mould is moving downward faster than the strand (negative strip) and is negative during the positive-strip period. The pressure is much larger than the shear stress acting in the flux channel.
- [iii] Calculation of the meniscus shape (in the absence of a rigid skin) has indicated that the meniscus is pushed away from the mould wall during the negative-strip period when positive pressure is generated in the flux

and is drawn back toward the mould wall by negative flux pressure during positive strip. Overflow thus may occur at the beginning of the positive-strip period.

The mechanism of oscillation mark-formation is based upon the generation of pressure in the flux channel and the presence of a rigid or semi-rigid skin at the meniscus. If the skin is rigid, overflow at the commencement of positive-strip causes a subsurface hook to form; whereas if the skin is semi-rigid it moves with the meniscus toward the mould, and overflow does not occur and hooks do not form. This mechanism and a resulting first-generation meniscus model can explain observations of oscillation marks made in this work and in other studies.

Secondly, extensive studies have been made on the mechanism of transverse crack formation and positive segregation at the surface of slabs, which are closely tied to oscillation-mark formation.

[i] A large area of positive segregation was found adjacent to deep oscillation marks having subsurface hooks when a narrow and long overflow region formed over the hooks.

[ii] A two-dimensional, heat-flow analysis, taking into account the shape of oscillation marks, predicts a local delay of cooling at the bottom of oscillation marks. If the end of the overflow region is located at the bottom of the oscillation marks, positive segregation forms at the point where solidification is delayed.

[iii] Another type of positive segregation was found in a layer on the bottom of oscillation marks having no subsurface hooks. The thickness of the segregation layer increases with increasing depth of oscillation marks. This event cannot be explained by the heat-transfer model, but instead can be rationalized by a penetration model, in which interdendritic, enriched liquid is drawn out by the negative pressure generated in the mould flux channel during the upward motion of the mould.

In both types of positive segregation, the segregation of phosphorus was characteristically detected.

[iv] As reported in previous studies, transverse cracks formed along the bottom of oscillation marks and are affected largely by the Al and N content in steel.

[v] In the subsurface structure of slabs, transverse cracks were observed along the austenite grain boundary, in the interdendritic region, and in the region of positive segregation near the bottom of the oscillation marks. However almost all of the transverse crack surfaces exhibited a partially interdendritic surface in the vicinity of the slab surface. Some of the cracks contained mould flux.

[vi] Nonuniformity of the shell profile in the mould was detected from the white band caused by the stream of steel from the submerged nozzle. The shell was thinnest adjacent to deep oscillation marks.

Transverse cracks form at this thinnest part of the shell.

- [vii] A heat flow analysis has revealed that the shape of oscillation marks, viz. not only the depth but also the pitch, is largely responsible for the nonuniformity of the shell profile. Therefore increasing the frequency of the mould oscillation effectively improves the uniformity of the shell thickness, and consequently reduces the sites of transverse cracks.

The results of these studies offer new information for the better understanding of initial solidification phenomena, especially in the vicinity of the meniscus of the continuous-casting slab mould, where several interrelated phenomena take place simultaneously.

6.2 Suggestions For Future Work

In the present work a mathematical model describing oscillation-mark formation has helped to explain the metallographic results obtained as well as previously reported industrial data. However it is a first-generation model which is based on many assumptions. In the future an extensive programme is required to enhance the ability of the model to simulate initial solidification phenomena more accurately. This would include the following:

- [A] Most important is the experimental measurement of heat flux in the vicinity of the meniscus including the

mould flux zone. This measurement could be undertaken using an array of thermocouples imbedded into the mould wall. Measured temperatures would be converted to a heat-flux distribution by two-dimensional, heat-flow analysis. The effects of the casting condition such as the superheat, casting speed, type of steel, type of mould flux, oscillation stroke, and oscillation frequency on the amount of heat flux would be examined. Simultaneously the subsurface structure of slabs and the consumption rate of mould flux would be investigated. The detection of the meniscus shell profile using tracers such as sulphur or radioactive Au^{198} are also quite important from the standpoint of determining the rigidity of the shell.

- [B] Secondly, an extension of the present work would be to develop a theoretical analysis of mould-flux consumption in which heat and fluid flow should be coupled and solved simultaneously. This subject is of great interest in the steel industry which is striving to continuously cast slabs with high surface quality at high speed. The analysis could be based on the proposed model of oscillation mark formation. The measurement of mould friction force also would be useful for this theoretical analysis.

BIBLIOGRAPHY

1. N.A. McPherson and S. Henderson: Ironmaking and Steelmaking, 1983, vol. 10, no. 6, pp. 259-268.
2. Proc. of 2nd Process Technology Conf. on Continuous Casting of Steel, Chicago, ISS-AIME, 1981, vol.2.
3. Special Issue on Continuous Casting of Steel (II), Tetsu-to-Hagane', 1981, vol.67, no.8.
4. Y. Takemura, S. Mizoguchi, O. Tsubakihara, T. Kuwabara, and M. Saito: Nippon Steel Tech. Report, 1983, no. 21, pp. 189-201.
5. T. Kohno, T. Shima, T. Kuwabara, S. Mizoguchi, T. Yamamoto, H. Misumi, and S. Tsuneoka: Tetsu-to-Hagane', 1981, vol. 86, no. 13, ppl 1764-1772.
6. N.A. McPherson and R.E. Mercer: Ironmaking and Steelmaking, 1980, vol 7, pp. 167-179.
7. Y. Nuri, T. Ohashi, N. Miyasaka, K. Shima, and Y. Uchida: Tetsu-to-Hagane', 1979, vol. 65, p. S701.
8. T. Okazaki, H. Tomono, T. Ozaki, and Y. Akabane: Tetsu-to-Hagane', 1982, vol. 68, no. 11, p. S929.
9. T.Emi, H. Nakato, Y. Iida, K. Emoto, R. Tachibana, T. Imai, and H. Bada: Proc. 61st NOH-BOSC, 1978, pp. 350-361.
10. P.V. Riboud and M. Larrecq: Proc. 62nd NOH-BOSC, 1979, pp. 78-92.
11. R. Gray and H. Marston: Proc. 62nd NOH-BOSC, 1979, pp. 93-102.
12. T. Sakuraya, T. Emi, T. Imai, K. Emoto, and M. Kodama: Tetsu-to-Hagane', 1981, vol. 67, no. 8, pp. 1220-1228.
13. T. Nakano, M. Fuji, K. Nagano, S. Mizoguchi, T. Yamamoto, and K. Asano: Tetsu-to-Hagane', 1981, vol. 67, no. 8, pp. 1210-1219.
14. M.D. Lanyi and C.J. Rosa: Proc. 2nd Process Tech. Conf., 1981, pp. 133-140.
15. A Hand Book on Property of Liquid Iron and Slag, The Iron and Steel Institue of Japan, 1971.

16. K. Sorimachi, H. Yamakawa, M. Kuga, H. Shitaka, and M. Saigusa: in Proc. of Modeling of Casting and Welding Process, Engineering Foundation, New York, 1983, pp. 195-198.
17. A. Nishiwaki and K. Ogino: 140th Committee, The Japan Society for the Promotion of Science, Dec. 1979.
18. H. Nakato and I. Muchi: Tetsu-to-Hagane', 1980, vol. 66, pp. 33-42.
19. K. Ogino, A. Nishiwaki, and K. Yamamoto: Tetsu-to-Hagane', 1979, no. 65, p. S683.
20. W.C.K. Boemer and A.G. Raper: JISI, 1970, vol. 208, pp. 18-27.
21. T. Kuwano, N. Shigematsu, F. Hoshi, and H. Ogiwara: Ironmaking and Steelmaking, 1983, vol. 10, pp. 75-81.
22. H. Oka, Y. Eda, T. Koshikawa, H. Nakato, T. Nozaki, and Y. Hato: Tetsu-to-Hagane', 1983, vol. 69, p. S932.
23. M. Hashio, T. Watanabe, T. Yamamoto, M. Marukawa, and M. Kawasaki: Tetsu-to-Hagane', 1982, vol. 68, p. S981.
24. S. Mizoguchi, H. Misumi, and S. Tanaka: in preprint of Japan - US Joint Seminar on Solidification Processing, June, 1983, Boston.
25. N.A. McPherson, A.W. Hardie, and G. Patric: ISS Transactions, 1983, vol. 3, pp. 21-36.
26. I. Saucedo, J. Beech, and G.J. Davis: Proc. 6th Intl. Vacuum Metallurgy Conf., 1979, pp. 885-904.
27. H. Takeuchi, S. Matsumura, and Y. Ikegami: Tetsu-to-Hagane', 1983, vol. 69, no. 16, pp. 1995-2001.
28. S. Tanaka, H. Misumi, S. Mizoguchi, and H. Horiguchi: Tetsu-to-Hagane', 1981, vol. 67, p. S172.
29. S. Tanaka, H. Misumi, H. Kibe, T. Ohta, and S. Mizoguchi: Tetsu-to-Hagane', 1981, vol. 67, p. S852.
30. R. Sato: Proc. 62nd NOH-BOSC, ISS-AIME, 1979, pp. 48-67.
31. J. Savage and W.H. Pritchard: J. Iron Steel Inst., 1954, vol. 178, pp. 269-277.

32. H. Tomono, H. Ackermann, W. Kurz, and W. Heinemann: in Casting of Small Section, TMS-AIME, Warrendale, PA., 1982, pp. 55-73.
33. T. Araki and Y. Sugitani: Tetsu-to-Hagane', 1973, vol. 59, pp. A17-A20.
34. R. Schoeffmann: Iron and Steel Engr., 1972, vol. 49, pp. 25-36.
35. H.P Jung, K.J. Kremer, H. Spitzer, H. Voge, and R. Hentrich: Stahl u. Eisen, 1984, vol. 104, no. 4, pp. 197-204.
36. K. Kawakami, T. Kitagawa, H. Mizukami, H. Uchibori, S. Miyahara, M. Suzuki, and Y. Shiratani: Tetsu-to-Hagane', 1981, vol. 67, no. 8, pp. 1190-1199.
37. H. Takeuchi, S. Matsumura, R. Hidaka, Y. Nagano, and Y. Suzuki: Tetsu-to-Hagane', 1983, vol. 69, no. 2, pp. 248-253.
38. I. Saucedo, J. Beech, and G.J. Davies: Metal Tech., 1982, vol.9, pp. 282-291.
39. H. Nakato, Y. Habu, T. Emi, K. Sorimachi, T. Koshikawa, and H. Kojima: Tetsu-to-Hagane', 1981, vol. 67, p. S908.
40. R. Alberny, A. Leclercq, D. Amaury, and M. Lahousse: Rev. Met., 1976, vol. 73, pp. 545-557.
41. M. Wolf: Trans. ISIJ, 1980, vol. 20, pp. 710-717.
42. H. Nakato, Y. Habu, T. Emi, K. Kinoshita, Y. Tomura, N. Ueda, and T. Imai: Tetsu-to-Hagane', 1976, vol. 62, p. S506.
43. T. Saeki, S. Ohguchi, S. Mizoguchi, T. Yamamoto, H. Misumi, and S. Tsuneoka: Tetsu-to-Hagane', 1982, vol. 68, pp. 1773-1781.
44. S.N. Shingh and K.E. Blazek: J. Metals, 1974, vol. 26, pp. 17-27.
45. K. Kinoshita, T. Emi, and M. Kasai: Tetsu-to-Hagane', 1979, vol. 65, no. 14, pp. 2022-2031.
46. I.V. Samarasekera and J.K. Brimacombe: Can. Met. Quart., 1979, vol. 18, pp. 251-266.

47. T. Nakano, K. Koyama, S. Nakamori, H. Misumi, and T. Naito: *Tetsu-to-Hagane'*, 1983, vol. 69, no. 12, p. S1036.
48. H. Nakato, M. Ozawa, K. Kinoshita, Y. Habu, and T. Emi: *Tetsu-to-Hagane'*, 1981, vol. 67, no. 8, pp. 1200-1209.
49. H. Yamakawa, J. Ikeda, T. Nishiya, and S. Ando: *Tetsu-to-Hagane'*, 1983, vol. 69, no. 4, p. S164.
50. M. Wolf: *Tetsu-to-Hagane'*, 1981, vol. 67, p. S904.
51. K. Hamagami, H. Bada, M. Enomoto, M. Kuga, and S. Ohmiya: *Tetsu-to-Hagane'*, 1983, vol. 69, no. 4, p. S162.
52. H. Bada, K. Mamagami, M. Kuga, and M. Enomoto: *Tetsu-to-Hagane'*, 1983, vol. 69, no. 14, p. S1031.
53. H. Mizukami, M. Komatsu, T. Kitagawa, K. Kawakami, H. Uchibori, and H. Miyano: *Tetsu-to-Hagane'*, 1983, vol. 69, no. 14, p. S1032.
54. K. Tokiwa, F. Kataoka, S. Tsuneoka, Y. Nakamori, and Y. Fujigake: *Tetsu-to-Hagane'*, 1983, vol. 69, no. 14, p. S1033.
55. Y. Miyawaki, M. Hanmyo, S. Uchida, T. Teraoka, Y. Shiratani, and Y. Ishida: *Tetsu-to-Hagane'*, 1984, vol. 70, no. 4, p. S143.
56. Y. Miyawaki, M. Hanmyo, S. Uchida, T. Mori, Y. Shiratani, and Y. Ishida: *Tetsu-to-Hagane'*, 1984, vol. 70, no. 4, p. S144.
57. Y. Nagano, K. Koyama, T. Nakano, T. Mukai, T. Komai, and S. Kaneko: *Tetsu-to-Hagane'*, 1984, vol. 70, no. 4, p. S145.
58. Y. Mimura, F. Yamaguchi, T. Takahashi, N. Ogibayashi, H. Yamaguchi, and K. Koyama: *Tetsu-to-Hagane'*, 1984, vol. 70, no. 4, p. S146.
59. K. Koyama, Y. Nagano, T. Nakano, H. Yamaguchi, N. Ogibayashi, and Y. Mimura: *Tetsu-to-Hagane'*, 1984, vol. 70, no. 4, p. S147.
60. T. Koyama, M. Yamaguchi, H. Sakai, A. Yamagami, and C. Matsumura: *Tetsu-to-Hagane'*, 1984, vol. 70, no. 4, p. S148.

61. H. Nakato, T. Nozaki, Y. Habu, H. Oka, N. Ueda, and H. Bada: *Tetsu-to-Hagane'*, 1984, vol. 70, no. 4, p. S149.
62. K. Tokiwa, F. Kataoka, S. Tsuneoka, Y. Nakamori, and Y. Fujigake: *Tetsu-to-Hagane'*, 1984, vol. 70, no. 4, p. S150.
63. H. Mizukami, T. Kitagawa, and K. Kawakami: *Tetsu-to-Hagane'*, 1984, vol. 70, no. 4, p. S151.
64. Y. Nakamori, O. Ichiko, Y. Mimura, Y. Eda, and M. Ohta: *Tetsu-to-Hagane'*, 1984, vol. 70, no. 4, p. S152.
65. Y. Nakamori, O. Ichiko, T. Washitani, M. Ohta, Y. Mimura: *Tetsu-to-Hagane'*, 1984, vol. 70, no. 4, p. S153.
66. H. Mizukami, M. Komatsu, T. Kitagawa, K. Kawakami, H. Uchibori, and H. Miyano: *Tetsu-to-Hagane'*, 1983, vol. 69, no. 14, p. S1032.
67. K. Tokiwa, T. Okazaki, T. Shirai, Y. Nakamori, and Y. Fuigake: *Tetsu-to-Hagane'*, 1983, vol. 69, no. 12, p. S1034.
68. Y. Komatsu, Y. Uchida, Y. Shiratani, S. Miyahara, M. Suzuki, J. Fukumi, T. Doihara, and O. Nomura: *Tetsu-to-Hagane'*, 1982, vol. 68, p. S928.
69. G.J.W. Kor: in *Proc. of 2nd Process Technology Conf. on Continuous Casting of Steel*, Chcago, ISS-AIME, 1981, vol. 2, pp. 124-132.
70. Y. Nuri and T. Ohashi: *Tetsu-to-Hagane'*, 1979, vol. 65, p. S702.
71. Y. Nuri and T. Ohashi: *Tetsu-to-Hagane'*, 1979, vol. 65, p. S703.
72. M. Komatsu, T. Kitagawa, and K. Kawakami: *Tetsu-to-Hagane'*, 1982, vol. 68, p. S927.
73. T. Kimura, T. Ozaki, Y. Akabane, M. Nakamura, and Y. Shiraishi: *Tetsu-to-Hagane'*, 1984, vol. 70, p. S154.
74. Y. Nakamori, O. Ichiko, K. Tokiwa, and F. Kataoka: *Tetsu-to-Hagane'*, 1983, vol. 69, p. S1035.
75. S. Ohmiya, H. Nakato, Y. Habu, T. Emi, K. Hamagami, H. Bada, and Y. Fukuhara: *Tetsu-to-Hagane'*, 1982, vol. 68, p. S926.

76. M. Hashio, M. Kawasaki, T. Watanabe, Y. Ohtani, and J. Murayama: *Tetsu-to-Hagane'*, 1980, vol. 66, p. s757.
77. C. Offerman, C. Dacker, and C. Enstrom: *Scandinavian J. of Metallurgy*, 1981, vol. 10, pp. 115-119.
78. L. Schmidt and A. Josefsson: *Scandinavian J. of Metallurgy*, 1974, vol. 3, pp. 193-199.
79. T. Mukai, N. Ogibayashi, R. Tsujino, T. Naito, H. Suzuki, Y. Abe, and S. Nagata: *Tetsu-to-Hagane'*, 1982, vol. 68, pp. A161-164.
80. H. Suzuki, S. Nishimura, J. Imamura, and Y. Nakamura: *Tetsu-to-Hagane'*, 1981, vol. 67, no. 8, pp. 1180-1189.
81. Y. Iida, K. Moriwaki, N. Ueda, and Y. Habu: *Tetsu-to-Hagane'*, 1973, vol. 59, p. S89.
82. Y. Miyashita, M. Suzuki, K. Taguchi, S. Uchida, H. Sato, and M. Yamamura: *Nippon Kokan Tech. Report*, 1982, no. 36, pp. 1-10.
83. J. Fukumi, Y. Miyawaki, M. Hanmyo, M. Ishikawa, and Y. Ishida: *Tetsu-to-Hagane'*, 1982, vol. 68, p. S985.
84. T. Sugitani: in preprint of CONCAST Slab Seminar, 1973, Zurich.
85. M. Yamaki et al.: *Tetsu-to-Hagane'*, 1974, vol. 60, p. S455.
86. H. Takeuchi, S. Matsumura, T. Yanai, and Y. Ikehara: *Tetsu-to-Hagane'*, 1984, vol. 70, no. 7, pp. 687-693.
87. Y. Fukuda, S. Mizoguchi, T. Matsumiya, H. Hamada, T. Miyazaki, and R. Sasaki: *Tetsu-to-Hagane'*, 1984, vol. 70, no. 4, p. S282.
88. E. Takeuchi, H. Fujii, T. Ohashi, H. Tanno, S. Tokao, I. Furugaki, and H. Kitamura: *Tetsu-to-Hagane'*, 1983, vol. 69, no. 14, pp. 1615-1622.
89. T. Nakano, M. Fugii, T. Kishi, K. Koyama, T. Komai, and T. Naito: *Tetsu-to-Hagane'*, 1983, vol. 69, S163.
90. W. H. McAdam: "Heat Transmission", 3ed., 1954, New York, McGraw-Hill.
91. R. Higbie: *Trans. Am. Inst. Chem. Eng.*, 1935, vol. 31, pp. 365-389.

92. J. Szekely and N.J. Themelis: "Rate Phenomena in Process Metallurgy", Wiley-Interscience, 1971, pp. 427-431.
93. B. Carnahan, H.A. Luther, and J.O. Wilkes: "Applied Numerical Method", Wiley, New York, 1969, pp. 432-433.
94. T. Matsumiya, T. Saeki, J. Tanaka, and T. Ariyoshi: "Tetsu-to-Hagane", 1982, vol. 68, p. 1782-1791.
95. M. Ishiguro, K. Kawakami, M. Ito, and S. Miyoshi: "Tetsu-to-Hagane", 1974, vol. 60, p. S885.
96. J. Harris: "Rheology and Non-Newtonian Flow", Longmans, 1977, pp. 280-289.
97. J.J. Biderman: "Physical Surfaces", Academic Press, 1970, p.12.
98. E. Matijevic: "Surface and Colloid Science", Wiley-Interscience, 1969, vol. 1, p.81.
99. F. Kreith and W.Z. Black: "Basic Heat Transfer", 1980, New York, Harper & Row.
100. Private Communication, Nippon Steel Corporation.
101. K. Kawakami, T. Kitagawa, K. Murakami, Y. Miyashita, Y. Tsuchida, and K. Kawawa: "Nippon Kokan Tech. Report", 1983, no. 93, pp. 149-163.
102. J.K. Brimacombe, F. Weinberg, and E.B. Hawbolt: "Met. Trans. B", 1979, vol 10B, pp. 279-292.
103. H. Takeuchi, S. Matsumura, Y. Ikehara, T. Komano, and T. Yanai: "Tetsu-to-Hagane", 1983, vol. 69, no. 1, pp. 73-79.
104. A. Suzuki and Y. Nagaoka: "J. Japan Inst. Metals", 1969, vol. 33, pp. 658.
105. H. Kumai, K. Asano, T. Ohashi, E. Nomura, and H. Fujii: "Tetsu-to-Hagane", 1974, vol. 60, no. 7, pp. 894-914.
106. M.C. Flemings: "Solidification Processing", 1974, New York, McGraw-Hill, pp. 234-239.
107. T.S. Piwonka and M.C. Flemings: "Transactions of the Metallurgical Society of AIME", 1966, vol. 236, pp. 1157-1165.

108. L.S. Darken, R.W. Gurry: "Physical Chemistry of Metals", 1953, New York, McGraw-Hill.
109. W.A. Fischer and H. Frye: Arch. Eisenhüttenw., 1970, vol. 41, pp.293.

APPENDIX I

NODAL EQUATIONS FOR THE HEAT FLOW CALCULATION
IN THE MOULD WALL

Nodal equations for each type of node are as follows:

$$< \text{type 1} > \frac{(T_{1,0} - T_{0,0})}{\Delta x^2} + \frac{(T_{0,1} - T_{0,0})}{\Delta y^2} + \frac{h_w}{\Delta y \lambda_M} (T_w - T_{0,0}) = 0 \quad (\text{A-1-1})$$

$$< \text{type 2} > \frac{(T_{0,n-1} - 2 T_{0,n} + T_{0,n+1})}{2 \Delta y^2} + \frac{(T_{1,n} - T_{0,n})}{\Delta x^2} = 0 \quad (\text{A-1-2})$$

$$< \text{type 3} > \frac{(T_{0,n-1} - T_{0,n})}{\Delta y^2} + \frac{(T_{1,n} - T_{0,n})}{\Delta x^2} + \frac{q_o(x)}{\Delta y \lambda_M} = 0 \quad (\text{A-1-3})$$

$$< \text{type 4} > \frac{(T_{m-1,0} - 2 T_{m,0} + T_{m+1,0})}{2 \Delta x^2} + \frac{(T_{m,1} - T_{m,0})}{\Delta y^2} + \frac{h_w}{\Delta y \lambda_M} \\ \cdot (T_w - T_{m,0}) = 0 \quad (\text{A-1-4})$$

$$< \text{type 5} > \frac{(T_{m-1,n} - 2 T_{m,n} + T_{m+1,n})}{\Delta x^2} + \frac{(T_{m,n-1} - 2 T_{m,n} + T_{m,n+1})}{\Delta y^2} = 0 \quad (\text{A-1-5})$$

$$< \text{type 6} > \frac{(T_{m-1,n} - 2 T_{m,n} + T_{m+1,n})}{2 \Delta x^2} + \frac{(T_{m,n-1} - T_{m,n})}{\Delta y^2} + \frac{q_o(x)}{\Delta y \lambda_M} = 0 \quad (\text{A-1-6})$$

$$< \text{type 7} > \frac{(T_{m-1,0} - T_{m,0})}{\Delta x^2} + \frac{(T_{m,1} - T_{m,0})}{\Delta y^2} + \frac{h_w}{\Delta y \lambda_M} (T_w - T_{m,0}) = 0 \quad (\text{A-1-7})$$

$$< \text{type 8} > \frac{(T_{m,n-1} - 2 T_{m,n} + T_{m,n+1})}{2\Delta y^2} + \frac{(T_{m-1,n} - T_{m,n})}{\Delta x^2} = 0 \quad (\text{A-1-8})$$

$$< \text{type 9} > \frac{(T_{m,n-1} - T_{m,n})}{\Delta y^2} + \frac{(T_{m-1,n} - T_{m,n})}{\Delta x^2} + \frac{q_o(x)}{\Delta y \lambda_M} = 0 \quad (\text{A-1-9})$$

These simultaneous equations are rewritten in a matrix system, which can be solved with the Gauss-Siedel method under the given conditions.

APPENDIX II

NODAL EQUATIONS FOR THE TEMPERATURE DISTRIBUTION IN
THE MENISCUS REGION

	Node	Q_1	Q_2	Q_3	Q_4
flux region	a	0	$q_o(x)$	Q30	Q40
	b	0	Q20	Q30	Q40
	c	0	Q20	Q30	$(T_f = T_{f1})$
	d	Q10	$q_o(x)$	Q30	Q40
	e	Q10	Q20	Q30	Q40
	f	Q10	Q20	Q30	$(T_f = T_{f1})$
	g	Q10	Q20	Q31	Q40
	h	Q10	Q20	Q32	Q40
	i	Q10	Q20	Q32	$(T_f = T_{f1})$
	j	Q10	Q20	Q31	Q41
	k	Q11	Q21	Q33	-
steel	l	-	Q22	Q34	Q41
	m	Q12	Q23	Q30	Q40
	n	Q12	Q20	Q30	Q40
	o	Q12	Q20	Q30	$(T_s = T_{s1})$
	p	Q13	Q23	Q30	Q40
flux	q	Q10	$q_o(x)$	Q31	Q41
	r	Q10	$q_o(x)$	Q33	-
	s	Q13	Q23	Q30	Q40
steel region	t	Q13	$q_o(x)$	Q30	Q40
	u	Q10	Q20	Q30	Q40
	v	Q10	Q20	Q30	$(T_s = T_{s1})$
	w	Q10	$q_o(x)$	Q30	Q40
	x	Q10	$q_o(x)$	0	Q40
	y	Q10	Q20	0	Q40
	z	Q10	Q20	0	$(T_s = T_{s1})$

Nodal equations for each type of node are as follows:

$$Q_{10} = \frac{\Delta y (T_{m-1,n} - T_{m,n})}{\frac{\Delta y_{m-1}}{2\lambda_{m-1,n}} + \frac{\Delta x_m}{2\lambda_{m,n}}} \quad (A-2-1)$$

$$Q_{11} = \frac{\Delta y (\lambda_{m-1,n} + \lambda_{m,n})(T_{m+1,n} - T_{m,n})(\Delta x_{m-1}/2 + \Delta x_m/3)}{2\{(\Delta y/6)^2 + (\Delta x_m/3 + \Delta x_{m-1}/2)^2\}} \quad (A-2-2)$$

$$Q12 = \frac{\Delta y (T_{m-1,n}^{\text{flux}} - T_{m,n})}{\frac{\Delta x_{m-1}}{2\lambda_{m,n}^{\text{flux}}} + \frac{1}{h_{s-f}} + \frac{\Delta x_m}{2\lambda_{m,n}}} \quad (\text{A-2-3})$$

$$Q13 = \frac{(\lambda_{m-1,n} + \lambda_{m,n}) \Delta y (T_{m-1,n} - T_{m,n}) (\Delta x_m/2 + \Delta x_{m-1}/3)}{2 \{ (\Delta y/6)^2 + (\Delta x_{m-1}/3) + (\Delta x_m/2)^2 \}} \quad (\text{A-2-4})$$

$$Q20 = \frac{\Delta x_m (\lambda_{m,n-1} + \lambda_{m,n}) (T_{m,n-1} - T_{m,n})}{2 \Delta y} \quad (\text{A-2-5})$$

$$Q21 = \frac{15 \Delta y \Delta x_m (\lambda_{m,n-1} + \lambda_{m,n}) (T_{m,n-1} - T_{m,n})}{25 \Delta y^2 + \Delta x_m^2} \quad (\text{A-2-6})$$

$$Q22 = \frac{2 \Delta y \Delta x_m (T_{m,n}^{\text{flux}} - T_{m,n}) / \sqrt{\Delta x_m^2 + \Delta y^2}}{\sqrt{\Delta x_m^2 + \Delta y^2} / 12 \lambda_{m,n}^{\text{flux}} + \sqrt{\Delta x_m^2 + \Delta y^2} / 12 \lambda_{m,n} + 1/h_{s-f}} \quad (\text{A-2-7})$$

$$Q23 = \frac{15 \Delta y \Delta x_m (\lambda_{m,n-1} + \lambda_{m,n}) (T_{m,n-1} + T_{m,n})}{25 \Delta y^2 + \Delta x_m^2} \quad (\text{A-2-8})$$

$$Q30 = \frac{\Delta y (T_{m+1,n} - T_{m,n})}{\frac{\Delta x_{m+1}}{2\lambda_{m+1,n}} + \frac{\Delta x_m}{2\lambda_{m,n}}} \quad (\text{A-2-9})$$

$$Q31 = \frac{\Delta x (\lambda_{m+1,n} + \lambda_{m,n}) (T_{m+1,n} - T_{m,n}) (\Delta x_m/2 + \Delta x_{m+1}/3)}{2 \{ (\Delta y/6)^2 + (\Delta x_{m+1}/3 + \Delta x_m/2)^2 \}} \quad (A-2-10)$$

$$Q32 = \frac{\Delta y (T_{m+1,n} - T_{m,n})}{\frac{\Delta x_{m+1}}{2\lambda_{m+1,n}} + \frac{1}{h_{s-f}} + \frac{\Delta x_m}{2\lambda_{m,n}}} \quad (A-2-11)$$

$$Q33 = \frac{2\Delta y \Delta x_m (T_{m,n}^{\text{steel}} - T_{m,n}) / \sqrt{\Delta x_m^2 + \Delta y^2}}{\sqrt{\Delta x_m^2 + \Delta y^2} / 12 \lambda_{m,n} + \sqrt{\Delta x_m^2 + \Delta y^2} / 12 \lambda_{m,n}^{\text{steel}} + 1/h_{s-f}} \quad (A-2-12)$$

$$Q34 = \frac{(\lambda_{m+1,n} + \lambda_{m,n}) \Delta y (T_{m+1,n} - T_{m,n}) (\Delta x_{m+1}/2 + \Delta x_m/2)}{2 \{ (\Delta y/6)^2 + (\Delta x_m/3 + \Delta x_{m+1}/2)^2 \}} \quad (A-2-13)$$

$$Q40 = \frac{\Delta x_m (\lambda_{m,n+1} + \lambda_{m,n}) (T_{m,n+1} - T_{m,n})}{2\Delta y} \quad (A-2-14)$$

$$Q41 = \frac{15\Delta y \Delta x_m (\lambda_{m,n+1} + \lambda_{m,n}) (T_{m,n+1} - T_{m,n})}{25\Delta y^2 + \Delta x_m^2} \quad (A-2-15)$$

Finally temperature of element (m,n) after Δt is,

$$T'_{m,n} = T_{m,n} + \frac{\Sigma Q_i}{C\rho\Delta y \cdot \Delta x_m} \Delta t \quad (A-2-16)$$

for the triangle element (m,n) after Δt is calculated by,

$$T''_{m,n} = \frac{2\Sigma Q_i}{C\rho\Delta y \cdot \Delta x_m} \Delta t \quad (A-2-17)$$

APPENDIX III

SHAPE OF MENISCUS

Generally the geometry of the steel droplet in molten flux is expressed with Eq.(A-3-1):

$$\sigma \left(\frac{1}{r_1} + \frac{1}{r_2} \right) = \Delta P \quad (\text{A-3-1})$$

The meniscus system can be expressed by the equation of meridional and cylindrical curvature respectively.

$$\frac{1}{r_1} = \frac{d\phi}{ds} \quad (\text{A-3-2})$$

$$\frac{1}{r_2} = \frac{\sin \phi}{y} \quad (\text{A-3-3})$$

In the case of the meniscus in the continuous casting mould, however, r_2 is so large that the two dimensional external meniscus can be applicable.

$$\frac{d\phi}{ds} = \frac{\Delta P}{\sigma} \quad (\text{A-3-4})$$

Also following relations can be obtained from Fig. 4-39.

$$\frac{dy}{ds} = \cos \phi \quad (\text{A-3-5})$$

$$\frac{dx}{ds} = - \sin \phi \quad (\text{A-3-6})$$

The pressure difference ΔP is expressed by Eq.(A-3-7) when the fluid pressure $P^*(x)$ exists in the flux layer.

$$\Delta P = (\rho_s - \rho_f)gx - P^*(x) \quad (\text{A-3-7})$$

From equations as above,

$$\sin \phi \frac{d\phi}{dx} = \frac{(\rho_s - \rho_f)gx - P^*(x)}{\sigma} \quad (\text{A-3-8})$$

With the boundary condition,

$$\phi = 0; \quad x = 0 \quad (\text{A-3-9})$$

$$\int_0^\phi \sin \phi d\phi = \int_0^x \frac{(\rho_s - \rho_f)gx - P^*(x)}{\sigma} dx \quad (\text{A-3-10})$$

$$\therefore \cos \phi = 1 - \frac{(\rho_s - \rho_f)g}{2\sigma} x^2 + \frac{R(x)}{\sigma} \quad (\text{A-3-11})$$

$$\text{where} \quad R(x) = \int_0^x P^*(x) dx = \int_0^x \{P(x) - \rho_f gx\} dx \quad (\text{A-3-12})$$

From Eqs.(A-3-5),(6) and (11)

$$\frac{dy}{dx} = - \frac{2\sigma(\rho_s - \rho_f)gx^2 - 4\sigma\{R(x) + \sigma\}}{[\rho_s - \rho_f]^2 g^2 x^4 - 4(\rho_s - \rho_f)\{R(x) + \sigma\}gx^2 + 4R(x)\{R(x) + 2\sigma\}]^{1/2}} \quad (\text{A-3-13})$$

Static shape of the meniscus can be calculated analytically by Eq. (A-3-13) when $R(x) = 0$. Variation of equation is as follows:

$$\frac{dy}{dx} = - \frac{a^2 - x^2}{x\sqrt{2a^2 - x^2}} \quad (\text{A-3-14})$$

where a^2 is a capillar constant

$$a^2 = \frac{2\sigma}{g(\rho_s - \rho_f)} \quad (\text{A-3-15})$$

Integration of Eq.(A-3-14) is

$$\int dy = \int \left(- \frac{a^2 - x^2}{x\sqrt{2a^2 - x^2}} \right) dx \quad (\text{A-3-16})$$

$$= a^2 \int \frac{dx}{x\sqrt{2a^2 - x^2}} - \int \frac{\sqrt{2a^2 - x^2}}{x} dx \quad (\text{A-3-17})$$

$$\begin{aligned} \therefore y &= a^2 \left(-\frac{1}{\sqrt{2a}} \ln \frac{\sqrt{2a^2} + \sqrt{2a^2 - x^2}}{x} \right) - (\sqrt{2a^2 - x^2} - \sqrt{2a^2}) \\ &\quad \cdot \ln \frac{\sqrt{2a^2} + \sqrt{2a^2 - x^2}}{x} + C_0 \end{aligned} \quad (\text{A-3-18})$$

$$= -\sqrt{2a^2 - x^2} + \frac{\sqrt{2a^2}}{2} \ln \frac{\sqrt{2a^2} + \sqrt{2a^2 - x^2}}{x} + C_0 \quad (\text{A-3-19})$$

$$= -\sqrt{2a^2} \cos \frac{\phi}{2} + \frac{\sqrt{2a^2}}{2} \ln \frac{1 + \cos \frac{\phi}{2}}{\sin \frac{\phi}{2}} + C_0 \quad (\text{A-3-20})$$

With the boundary condition,

$$\phi = \pi/2; \quad y = 0 \quad (\text{A-3-21})$$

$$y = -\sqrt{2a^2} \cos \frac{\phi}{2} + \frac{\sqrt{2a^2}}{2} \ln \frac{1 + \cos \frac{\phi}{2}}{\sin \frac{\phi}{2}} + 0.3768 a \quad (\text{A-3-22})$$

$$= -\sqrt{2a^2 - x^2} + \frac{\sqrt{2a^2}}{2} \ln \frac{\sqrt{2a^2} + \sqrt{2a^2 - x^2}}{x} + 0.3768 a \quad (\text{A-3-23})$$

On the other hand change of meniscus shape by dynamic pressure in the flux channel is calculated in the following way.

- (i) The dynamic pressure is calculated by the meniscus shape at $t = t_1$, assuming that the shape is expressed as the second order of a curve.
- (ii) Calculated pressure profile is modified to a simple form by Eq.(A-3-24), thus the meniscus shape at $t = t_{i+1}$ is calculated by Eq.(A-3-13).

$$R(x)/R(x_c, t_{i+1}) = x^2/x_{c, t_{i+1}}^2 \quad (\text{A-3-24})$$

$$t_{i+1} = t_1 + \Delta t \quad (\text{A-3-25})$$

$x_{c, t_{i+1}}$ is the "contact point" of meniscus with the mould wall and is obtained from Eq.(A-3-11).

$$x_{c,t_{i+1}} = \frac{2\sigma}{g(\rho_s - \rho_f)} \left\{ 1 + \frac{R(x_{c,t_{i+1}})}{\sigma} \right\} \quad (\text{A-3-26})$$

Computation of (i) and (ii) are iterated by the time step Δt for one cycle of the mould oscillation.

APPENDIX IV

DYNAMIC PRESSURE IN THE MOULD FLUX CHANNEL

The solution to Eqs. (4-26) and (4-27) for the pressure profile and velocity distribution in the mould flux channel has been obtained as follows. Equation (4-26) was integrated with respect to y , with limits set by B.C.'s (4-29) and (4-30), to obtain

$$u_x = (v_m - v_s)(1 - \frac{y}{h}) - \frac{h^2}{2\mu_f} \left(\frac{dP}{dx} + \rho_f g \right) \frac{y}{h} \left(1 - \frac{y}{h} \right) \quad (A-4-1)$$

Then Eq.(A-4-1) was substituted into Eq.(4-27) which was integrated, and rearranged to give

$$\frac{dP}{dx} = \frac{6\mu_f(v_m - v_s)}{h^2} + \rho_f g - \frac{12\mu_f}{h^3} Q_R \quad (A-4-2)$$

Q_R , the relative flux consumption rate, was evaluated by rearranging Eq.(A-4-2) and integrating from $x = 0$ to $x = \lambda_f$ (Fig. 4-35).

$$Q_R = \frac{\rho_f g \lambda_f - (P_f - P_i) + 6\mu_f(v_m - v_s) \varepsilon(\lambda_f)}{12\mu_f \zeta(\lambda_f)} \quad (A-4-3)$$

where

$$\varepsilon(\lambda_f) = \int_0^{\lambda_f} \frac{dx}{h^2(x)} \quad (A-4-4)$$

$$\zeta(\lambda_f) = \int_0^{\lambda_f} \frac{dx}{h^3(x)} \quad (A-4-5)$$

Eqs.(A-4-3) and (A-4-5) were substituted into Eq.(A-4-2) which was integrated again from 0 to x , giving

$$\begin{aligned} P(x) = P_i + \rho_f g x + 6\mu_f(v_m - v_s) \varepsilon(x) - \{ \rho_f g \lambda_f - (P_i - P_f) \\ + 6\mu_f(v_m - v_s) \varepsilon(\lambda_f) \} \frac{\zeta(x)}{\zeta(\lambda_f)} \end{aligned} \quad (A-4-6)$$

where $\varepsilon(x)$ and $\zeta(x)$ are defined as in Eqs.(A-4-4) and (A-4-5).

The relative velocity distribution was obtained by combining Eqs.(A-4-1) - (A-4-5) to yield

$$u_x = (v_m - v_s)(1 - \frac{y}{h}) - \frac{1}{2\mu_f} (\frac{y}{h} - \frac{y}{h^2}) \{6\mu_f(v_m - v_s)\} \\ - \frac{\rho_f g l_f - (P_f - P_1) + 6\mu_f(v_m - v_s) \varepsilon(l_f)}{h\zeta(\lambda_f)} \quad (A-4-7)$$

The expressions for $\varepsilon(y)$ and $\zeta(y)$ depend on the function used to approximate the segment of the meniscus under consideration. If a linear function is adopted, eg.

$$h(x) = \alpha x + \beta \quad (A-4-8)$$

then

$$\varepsilon(x) = -\frac{1}{\alpha} \left[\frac{1}{h(x)} - \frac{1}{\beta} \right] \quad (A-4-9)$$

$$\zeta(x) = -\frac{1}{2\alpha} \left[\frac{1}{\{h(x)\}^2} - \frac{1}{\beta^2} \right] \quad (A-4-10)$$

For the physical system in Fig. 4-35

$$\alpha = \frac{h_f - h_1}{l_f} \quad (A-4-11)$$

and

$$\beta = h_1 \quad (A-4-12)$$

Substitution of Eqs.(A-4-9) - (A-4-12) into Eqs.(A-4-6) and (A-4-7) leads to Eqs.(A-4-9) and (A-4-10) respectively.

On the other hand, if a quadratic function for the lower part of the meniscus region is chosen, viz.

$$h(x) = ax^2 + bx + c \quad (a, b, c \text{ const.}) \quad (A-4-13)$$

the evaluation of $\varepsilon(x)$ and $\zeta(x)$ depends on the value of $K = 4ac - b^2$. If $K > 0$

$$\varepsilon(x) = \frac{1}{K} \left(\frac{2ax + b}{h(x)} - \frac{b}{c} \right) + \frac{4a}{K^{3/2}} \left\{ \arctan \left(\frac{2ax + b}{K^{1/2}} \right) - \arctan \frac{b}{K^{1/2}} \right\} \quad (A-4-14)$$

$$\begin{aligned} \zeta(x) = & \frac{1}{2K^2} \left\{ \frac{(2ax + b)(K + 6ah(x))}{h^2(x)} - \frac{b(K + 6ac)}{c^2} \right\} \\ & + \frac{12a^2}{K^{5/2}} \left(\arctan \left(\frac{2ax + b}{K^{1/2}} \right) - \arctan \frac{b}{K^{1/2}} \right) \end{aligned} \quad (A-4-15)$$

but if $K < 0$

$$\begin{aligned} \varepsilon(x) = & \frac{1}{K} \left(\frac{2ax + b}{h(x)} - \frac{b}{c} \right) + \frac{2a}{(-K)^{3/2}} \ln \left\{ \frac{(2ax + b - \sqrt{-K})(b + \sqrt{-K})}{(2ax + b + \sqrt{-K})(b - \sqrt{-K})} \right\} \end{aligned} \quad (A-4-16)$$

$$\begin{aligned} \zeta(x) = & \frac{1}{2K^2} \left\{ \frac{(2ax + b)(K + 6ah(x))}{h^2(x)} - \frac{b(K + 6ac)}{c^2} \right\} \\ & + \frac{6a^2}{(-K)^{5/2}} \ln \left\{ \frac{(2ax + b - \sqrt{-K})(b + \sqrt{-K})}{(2ax + b + \sqrt{-K})(b - \sqrt{-K})} \right\} \end{aligned} \quad (A-4-17)$$

This refinement of the fluid flow calculations has not been pursued further in the present study.

COMPUTER PROGRAM FOR THE TEMPERATURE PREDICTION

IN THE MENISCUS REGION

```

*****
TWO-DIMENSIONAL UNSTEADY STATE FINITE DIFFERENCE HEAT TRANSFER PROGRAM
AT MENISCUS FEATURED TRIANGULAR NODES
*****
PROGRAM FILE NAME : HEAT333
DATA FILE NAME : DATA333
*****
LIST OF SYMBOLS
US TEMPERATURE OF STEEL
UF TEMPERATURE OF MOULD FLUX
US2 NEW TEMPERATURE OF STEEL
UF2 NEW TEMPERATURE OF MOULD FLUX
DX SIZE OF NODE IN X DIRECTION
DZ SIZE OF NODE IN Z DIRECTION (CASTING DIRECTION)
RAMF THERMAL CONDUCTIVITY OF MOULD FLUX
RAMS THERMAL CONDUCTIVITY OF STEEL
CS SPECIFIC HEAT OF STEEL
CF SPECIFIC HEAT OF MOULD FLUX
ROUS DENSITY OF STEEL
ROUF DENSITY OF MOULD FLUX
LMS STATE OF STEEL
LNS STATE OF STEEL ; LIQUID,MUSHY,SOLID
Q(N) HEAT FLUX DISTRIBUTION
N1 NUMBER OF NODE IN FLUX REGION IN Z DIRECTION
N2 NUMBER OF NODE IN CURVED REGION OF MENISCUS IN Z DIRECTION
N3 NUMBER OF NODE IN STEEL REGION IN Z DIRECTION
M1 NUMBER OF NODE IN CURVED REGION OF MENISCUS IN X DIRECTION
M2 NUMBER OF NODE IN FLAT REGION OF MENISCUS IN X DIRECTION
Z1 THICKNESS OF MOULD FLUX ON MENISCUS
Z2 LENGTH OF CURVED REGION OF MENISCUS IN Z DIRECTION
Z3 LENGTH OF STEEL REGION IN Z DIRECTION
X1 LENGTH OF CURVED REGION IN X DIRECTION
DT TIME STEP
UFI INITIAL TEMPERATURE OF MOULD FLUX
USI INITIAL TEMPERATURE OF STEEL
TLIQUID LIQUIDUS TEMPERATURE OF STEEL
TSOLID SOLIDUS TEMPERATURE OF STEEL
TP POURING TEMPERATURE OF STEEL
H HEAT TRANSFER COEFFICIENT BETWEEN STEEL AND MOULD FLUX
CFL SPECIFIC HEAT OF LIQUID FLUX
CFS SPECIFIC HEAT OF SOLIDIFIED FLUX
CSL SPECIFIC HEAT OF LIQUID STEEL
CSS SPECIFIC HEAT OF SOLIDIFIED STEEL
ROUFL DENSITY OF LIQUID FLUX
ROUSL DENSITY OF LIQUID STEEL
ROUFS DENSITY OF SOLIDIFIED FLUX
ROUSSL DENSITY OF SOLIDIFIED STEEL
RAMFL THERMAL CONDUCTIVITY OF LIQUID FLUX
RAMSL THERMAL CONDUCTIVITY OF LIQUID STEEL
RAMFS THERMAL CONDUCTIVITY OF SOLIDIFIED FLUX
RAMSSL THERMAL CONDUCTIVITY OF SOLIDIFIED STEEL
HALTS HALTS LATENT HEAT OF STEEL
QEF HEAT FLUX IN MOULD FLUX REGION
QES PEAK HEAT-FLUX IN STEEL REGION
*****

```

```

C*****
C    DIMENSION
C*****
C
C    DIMENSION US(100,100),UF(100,100),US2(100,100),UF2(100,100),DZ(
A100),RAMF(100,100),RAMS(100,100),CS(100,100),CF(100,100),ROUS(100
A,100),ROUF(100,100),LMF(100,100),LNF(100,100),LMS(100,100),LNS(100
A,100),Q(100)
C
C
C*****
C    READ DATA
C*****
C
C    READ(5,500) N1,N2,N3,M1,M2,Z1,Z2,Z3,X1,DT
500 FORMAT(5I4,4F8.4,F10.6)
    READ(5,501) UFI,USI,TLIQF,TLIQS,TSOLF,TSOLS,TP,H
501 FORMAT(8F10.5)
    READ(5,502) CFL,CSL,ROUFL,ROUSL,RAMFL,RAMSL,HLATF,HLATS
502 FORMAT(8F10.5)
    READ(5,503) CFS,CSS,ROUFS,ROUSS,RAMFS,RAMSS,QEF,QES
503 FORMAT(8F10.5)
C
C
C*****
C    WRITE DATA
C*****
C
C    WRITE(6,2000) N1,N2,N3,M1,M2,Z1,Z2,Z3,X1,DT
2000 FORMAT(10H N1      = , I4/10H N2      = , I4/10H N3      = , I4
A/10H M1      = , I4/10H M2      = , I4/10H Z1      = , F12.6/
A10H Z2      = , F12.6/10H Z3      = , F12.6/10H X1      = , F12.6
A/10H DT      = , F12.6)
    WRITE(6,2001) UFI,USI,TLIQF,TLIQS,TSOLF,TSOLS,TP,H
2001 FORMAT(10H UFI      = , F12.6/10H USI      = , F12.6/10H TLIQF      = ,
AF12.6/10H TLIQS      = , F12.6/10H TSOLF      = , F12.6/10H TSOLS      = ,
AF12.6/10H TP        = , F12.6/10H H          = , F12.6)
    WRITE(6,2002) CFL,CSL,ROUFL,ROUSL,RAMFL,RAMSL,HLATF,HLATS
2002 FORMAT(10H CFL      = , F12.6/10H CSL      = , F12.6/10H ROUFL      = ,
AF12.6/10H ROUSL      = , F12.6/10H RAMFL      = , F12.6/10H RAMSL      = ,
AF12.6/10H HLATF      = , F12.6/10H HLATS      = , F12.6)
    WRITE(6,2003) CFS,CSS,ROUFS,ROUSS,RAMFS,RAMSS,QEF,QES
2003 FORMAT(10H CFS      = , F12.6/10H CSS      = , F12.6/10H ROUFS      = ,
AF12.6/10H ROUSS      = , F12.6/10H RAMFS      = , F12.6/10H RAMSS      = ,
AF12.6/10H QEF        = , F12.6/10H QES        = , F12.6)
C
C
C*****
C    OUTPUT TIME SET
C*****
C
C
END1=0.160
END1A=END1+DT
END2=0.162
END2A=END2+DT

```

END3=O. 164
END3A=END3+DT
END4=O. 165
END4A=END4+DT
END5=O. 168
END5A=END5+DT
END6=O. 169
END6A=END6+DT
END7=O. 173
END7A=END7+DT
END8=O. 179
END8A=END8+DT
END9=O. 181
END9A=END9+DT
END10=O. 192
END10A=END10+DT
END11=O. 203
END11A=END11+DT
END12=O. 216
END12A=END12+DT
END13=O. 221
END13A=END13+DT
END14=O. 227
END14A=END14+DT
END15=O. 234
END15A=END15+DT
END16=O. 238
END16A=END16+DT
END17=O. 256
END17A=END17+DT
END18=O. 300
END18A=END18+DT
END19=O. 339
END19A=END19+DT
END20=O. 348
END20A=END20+DT
END21=O. 358
END21A=END21+DT
END22=O. 362
END22A=END22+DT
END23=O. 374
END23A=END23+DT
END24=O. 375
END24A=END24+DT
END25=O. 378
END25A=END25+DT
END26=O. 395
END26A=END26+DT
END27=O. 402
END27A=END27+DT
END28=O. 422
END28A=END28+DT
END29=O. 432
END29A=END29+DT
END30=O. 466
END30A=END30+DT
END31=O. 494
END31A=END31+DT
END32=O. 542
END32A=END32+DT


```

END33=0.600
END33A=END33+DT
END34=0.609
END34A=END34+DT
END35=0.637
END35A=END35+DT
END36=0.640
END36A=END36+DT
END37=0.667
END37A=END37+DT
END38=0.678
END38A=END38+DT
END39=0.716
END39A=END39+DT
END40=0.720
END40A=END40+DT
END41=0.731
END41A=END41+DT
END42=0.793
END42A=END42+DT
END43=0.967

C
C
C*****
C      DIMENSION OF SYSTEM
C*****
C
C
C
      NZ=N1+N2+N3
      MX=M1+M2
      N11=N1+1
      N21=N1+N2
      N20=N21-1
      N22=N21+1
      M10=M1-1
      M12=M1+1
      DX=X1/FLOAT(M1)
      X2=DX*FLOAT(M2)
      T=0.0
      IF(M1-N2) 800,801,800
800  WRITE(6,850)
850  FORMAT(1H0,20H  M1=N2 NOT EQUAL  )
      GO TO 1500
801  CONTINUE
      DO 200 N=1,N1
200  DZ(N)=Z1/FLOAT(N1)
      DO 201 N=N11,N21
201  DZ(N)=SQRT(Z2**2/X1*(X1-DX*FLOAT(N-N1-1)))-SQRT(Z2**2/X1*(X1-
      ADX*FLOAT(N-N1)))
      DO 202 N=N22,NZ
202  DZ(N)=Z3/FLOAT(N3)
C
C
C*****
C      PROFILE OF HEAT FLUX
C*****
C
C
C
      DO 701 N=1,N1

```

```

701 Q(N)=QEF
    DO 702 N=N11,N21
702 Q(N)=-QES*QEF*((N2+1)**2)/(N22*SQRT(-QES)-N1*SQRT(-QEF)
    A=N*(SQRT(-QES)-SQRT(-QEF))**2
    DO 703 N=N22,NZ
703 Q(N)=QES
C
C
C*****
C    INITIAL CONDITION ETC.
C*****
C
C
C
DO 205 N=1,NZ
DO 205 M=1,MX
UF(M,N)=UFI
US(M,N)=USI
LMF(M,N)=O
LNF(M,N)=O
LMS(M,N)=O
LNS(M,N)=O
CF(M,N)=CFL
CS(M,N)=CSL
ROUF(M,N)=ROUFL
ROUS(M,N)=ROUSL
RAMF(M,N)=RAMFL
205 RAMS(M,N)=RAMSL
CFF=HLATF/(TLIQF-TSOLF)+CFL
CSF=HLATS/(TLIQS-TSOLS)+CSL
ROUFF=(ROUFL+ROUFS)/2.0
RAMFF=(RAMFL+RAMFS)/2.0
ROUSF=(ROUSL+ROUSS)/2.0
RAMSF=(RAMSL+RAMSS)/2.0
GXF=RAMFL*DT/(CFL*ROUFL*DX**2)
GXS=RAMSL*DT/(CSL*ROUSL*DX**2)
GZ1F=RAMFL*DT/(CFL*ROUFL*DZ(1)**2)
GZ2F=RAMFL*DT/(CFL*ROUFL*DZ(N11)**2)
GZ2S=RAMSL*DT/(CSL*ROUSL*DZ(N11)**2)
GZ3=RAMSL*DT/(CSL*ROUSL*DZ(N22)**2)
IF(GXF-0.5) 560,570,570
560 IF(GXS-0.5) 561,570,570
561 IF(GZ1F-0.5) 562,570,570
562 IF(GZ2F-0.5) 563,570,570
563 IF(GZ2S-0.5) 564,570,570
564 IF(GZ3-0.5) 565,570,570
570 WRITE(6,575)
575 FORMAT(1H0,46HG IS MORE THAN 0.5, CANNOT PERFORM CALCULATION)
    GO TO 1500
565 CONTINUE
C
C
C*****
C    TIME INCREASES
C*****
C
C
C    T=T+DT
C
C
C*****

```

```

C      HEAT FLUX CALCULATION IN EACH TYPE OF NODE
C*****
C
C
1  CONTINUE
   DO 999 N=1,NZ
   DO 999 M=1,MX
   IF(N-1) 10,10,15
10  IF(M-1) 12,12,11
12  CALL SUB1(DX,DZ(N),DZ(N+1),RAMF(M,N),RAMF(M+1,N),RAMF(M,N+1),UF(M,
   AN+1),UF(M,N),UF(M+1,N),QF,Q(N))
   US(M,N)=0
   GO TO 991
11  IF(M-MX) 13,14,14
13  CALL SUB2(DX,DZ(N),DZ(N+1),RAMF(M-1,N),RAMF(M,N),RAMF(M+1,N),
   ARAMF(M,N+1),UF(M-1,N),UF(M,N),UF(M,N+1),UF(M+1,N),QF)
   US(M,N)=0
   GO TO 991
14  CALL SUB3(DX,DZ(N),DZ(N+1),RAMF(M-1,N),RAMF(M,N),RAMF(M,N+1),
   AUF(M-1,N),UF(M,N),UF(M,N+1),UFI,QF)
   US(M,N)=0
   GO TO 991
C
C*****
C
15  IF(N-N1) 16,18,38
16  IF(M-1) 17,17,19
17  CALL SUB4(DX,DZ(N-1),DZ(N),DZ(N+1),RAMF(M+1,N),RAMF(M,N),RAMF(M,N-
   A1),RAMF(M,N+1),UF(M,N-1),UF(M,N),UF(M,N+1),UF(M+1,N),QF,Q(N))
   US(M,N)=0
   GO TO 991
19  IF(M-MX) 20,50,50
20  CALL SUB5(DX,DZ(N-1),DZ(N),DZ(N+1),RAMF(M-1,N),RAMF(M,N),
   ARAMF(M+1,N),RAMF(M,N-1),RAMF(M,N+1),UF(M,N-1),UF(M,N),UF(M-1,N),
   AUF(M,N+1),UF(M+1,N),QF)
   US(M,N)=0
   GO TO 991
50  CALL SUB6(DX,DZ(N-1),DZ(N),DZ(N+1),RAMF(M-1,N),RAMF(M,N),RAMF(M,N-
   A1),RAMF(M,N+1),UF(M,N-1),UF(M,N),UF(M-1,N),UF(M,N+1),UFI,QF)
   US(M,N)=0
   GO TO 991
C
C*****
C
18  IF(M-1) 51,51,52
51  CALL SUB4(DX,DZ(N-1),DZ(N),DZ(N+1),RAMF(M+1,N),RAMF(M,N),RAMF(M,N-
   A1),RAMF(M,N+1),UF(M,N-1),UF(M,N),UF(M,N+1),UF(M+1,N),QF,Q(N))
   US(M,N)=0
   GO TO 991
52  IF(M-M1) 25,21,22
25  CALL SUB5(DX,DZ(N-1),DZ(N),DZ(N+1),RAMF(M-1,N),RAMF(M,N),
   ARAMF(M+1,N),RAMF(M,N-1),RAMF(M,N+1),UF(M,N-1),UF(M,N),UF(M-1,N),
   AUF(M,N+1),UF(M+1,N),QF)
   US(M,N)=0
   GO TO 991
21  CALL SUB7(DX,DZ(N-1),DZ(N),DZ(N+1),RAMF(M-1,N),RAMF(M,N),RAMF(M,N+
   A1),RAMF(M+1,N),RAMF(M,N-1),UF(M,N-1),UF(M,N),UF(M-1,N),UF(M,N+1),
   AUF(M+1,N),QF)
   US(M,N)=0
   GO TO 991

```

```

22 IF(M-MX) 23,24,24
23 CALL SUB8(DX,DZ(N-1),DZ(N),DZ(N+1),RAMF(M-1,N),RAMF(M,N),RAMF(M+1,
  AN),RAMF(M,N-1),RAMS(M,N+1),UF(M,N-1),UF(M,N),UF(M-1,N),US(M,N+1),
  AUF(M+1,N),H,QF)
  US(M,N)=0
  GO TO 991
24 CALL SUB9(DX,DZ(N-1),DZ(N),DZ(N+1),RAMF(M-1,N),RAMF(M,N),RAMF(M,N-
  A1),RAMS(M,N+1),UF(M,N-1),UF(M,N),UF(M-1,N),US(M,N+1),UFI,H,QF)
  US(M,N)=0
  GO TO 991
C
C*****
C
38 IF(N-N11) 39,39,40
39 IF(M-1) 26,26,27
26 CALL SUB4(DX,DZ(N-1),DZ(N),DZ(N+1),RAMF(M+1,N),RAMF(M,N),RAMF(M,N-
  A1),RAMF(M,N+1),UF(M,N-1),UF(M,N),UF(M,N+1),UF(M+1,N),QF,Q(N))
  US(M,N)=0
  GO TO 991
27 IF(M-M10) 30,31,32
30 CALL SUB5(DX,DZ(N-1),DZ(N),DZ(N+1),RAMF(M-1,N),RAMF(M,N),
  ARAMF(M+1,N),RAMF(M,N-1),RAMF(M,N+1),UF(M,N-1),UF(M,N),UF(M-1,N),
  AUF(M,N+1),UF(M+1,N),QF)
  US(M,N)=0
  GO TO 991
31 CALL SUB10(DX,DZ(N-1),DZ(N),DZ(N+1),RAMF(M-1,N),RAMF(M,N),RAMF(M,N
  A+1),RAMF(M+1,N),RAMF(M,N-1),UF(M,N-1),UF(M,N),UF(M-1,N),UF(M,N+1),
  AUF(M+1,N),QF)
  US(M,N)=0
  GO TO 991
32 IF(M-M12) 33,34,35
33 CALL SUB11(DX,DZ(N-1),DZ(N),RAMF(M,N-1),RAMF(M,N),RAMF(M-1,N),RAMS
  A(M,N),UF(M,N-1),UF(M,N),UF(M-1,N),US(M,N),H,QF)
  CALL SUB12(DX,DZ(N),DZ(N+1),RAMF(M,N),RAMS(M,N+1),RAMS(M,N),
  ARAMS(M+1,N),UF(M,N),US(M,N),US(M,N+1),US(M+1,N),H,QS)
  GO TO 990
34 CALL SUB13(DX,DZ(N-1),DZ(N),DZ(N+1),RAMF(M,N-1),RAMS(M-1,N),RAMS(M
  A,N),RAMS(M+1,N),RAMS(M,N+1),UF(M,N-1),US(M,N),US(M-1,N),US(M,N+1),
  AUS(M+1,N),H,QS)
  UF(M,N)=0
  GO TO 992
35 IF(M-MX) 62,63,63
62 CALL SUB14(DX,DZ(N-1),DZ(N),DZ(N+1),RAMF(M,N-1),RAMS(M-1,N),RAMS(M
  A,N),RAMS(M+1,N),RAMS(M,N+1),UF(M,N-1),US(M,N),US(M-1,N),US(M,N+1),
  AUS(M+1,N),H,QS)
  UF(M,N)=0
  GO TO 992
63 CALL SUB15(DX,DZ(N-1),DZ(N),DZ(N+1),RAMF(M,N-1),RAMS(M-1,N),RAMS(M
  A,N),RAMS(M,N+1),UF(M,N-1),US(M,N),US(M-1,N),US(M,N+1),TP,H,QS)
  UF(M,N)=0
  GO TO 992
C
C*****
C
40 IF(N-N20) 69,70,80
69 MC1=M1-(N-N1)
  MC2=MC1+2
  IF(M-1) 41,41,42
41 CALL SUB4(DX,DZ(N-1),DZ(N),DZ(N+1),RAMF(M+1,N),RAMF(M,N),RAMF(M,N-
  A1),RAMF(M,N+1),UF(M,N-1),UF(M,N),UF(M,N+1),UF(M+1,N),QF,Q(N))

```

```

      US(M,N)=0
      GO TO 991
42 IF(M-MC1) 43,44,45
43 CALL SUB5(DX,DZ(N-1),DZ(N),DZ(N+1),RAMF(M-1,N),RAMF(M,N),
      ARAMF(M+1,N),RAMF(M,N-1),RAMF(M,N+1),UF(M,N-1),UF(M,N),UF(M-1,N),
      AUF(M,N+1),UF(M+1,N),QF)
      US(M,N)=0
      GO TO 991
44 CALL SUB10(DX,DZ(N-1),DZ(N),DZ(N+1),RAMF(M-1,N),RAMF(M,N),RAMF(M,N
      A+1),RAMF(M+1,N),RAMF(M,N-1),UF(M,N-1),UF(M,N),UF(M-1,N),UF(M,N+1),
      AUF(M+1,N),QF)
      US(M,N)=0
      GO TO 991
45 IF(M-MC2) 46,47,48
46 CALL SUB11(DX,DZ(N-1),DZ(N),RAMF(M,N-1),RAMF(M,N),RAMF(M-1,N),RAMS
      A(M,N),UF(M,N-1),UF(M,N),UF(M-1,N),US(M,N),H,QF)
      CALL SUB12(DX,DZ(N),DZ(N+1),RAMF(M,N),RAMS(M,N+1),RAMS(M,N),
      ARAMS(M+1,N),UF(M,N),US(M,N),US(M,N+1),US(M+1,N),H,QS)
      GO TO 990
47 CALL SUB16(DX,DZ(N-1),DZ(N),DZ(N+1),RAMS(M,N-1),RAMS(M,N),
      ARAMS(M-1,N),RAMS(M+1,N),RAMS(M,N+1),US(M,N-1),US(M,N),US(M-1,N),
      AUS(M,N+1),US(M+1,N),QS)
      UF(M,N)=0
      GO TO 992
48 IF(M-MX) 49,60,60
49 CALL SUB5(DX,DZ(N-1),DZ(N),DZ(N+1),RAMS(M-1,N),RAMS(M,N),
      ARAMS(M+1,N),RAMS(M,N-1),RAMS(M,N+1),US(M,N-1),US(M,N),US(M-1,N),
      AUS(M,N+1),US(M+1,N),QS)
      UF(M,N)=0
      GO TO 992
60 CALL SUB23(DX,DZ(N-1),DZ(N),DZ(N+1),RAMS(M-1,N),RAMS(M,N),
      ARAMS(M,N-1),RAMS(M,N+1),US(M,N-1),US(M,N),US(M-1,N),
      AUS(M,N+1),TP,QS)
      UF(M,N)=0
      GO TO 992
C
C*****
C
70 IF(M-1) 71,71,72
71 CALL SUB17(DX,DZ(N-1),DZ(N),DZ(N+1),RAMF(M,N+1),RAMF(M,N),RAMF(M+1
      A,N),RAMF(M,N-1),UF(M,N-1),UF(M,N),UF(M,N+1),UF(M+1,N),
      AQF,Q(N))
      US(M,N)=0
      GO TO 991
72 IF(M-3) 73,74,75
73 CALL SUB11(DX,DZ(N-1),DZ(N),RAMF(M,N-1),RAMF(M,N),RAMF(M-1,N),RAMS
      A(M,N),UF(M,N-1),UF(M,N),UF(M-1,N),US(M,N),H,QF)
      CALL SUB12(DX,DZ(N),DZ(N+1),RAMF(M,N),RAMS(M,N+1),RAMS(M,N),
      ARAMS(M+1,N),UF(M,N),US(M,N),US(M,N+1),US(M+1,N),H,QS)
      GO TO 990
74 CALL SUB16(DX,DZ(N-1),DZ(N),DZ(N+1),RAMS(M,N-1),RAMS(M,N),
      ARAMS(M-1,N),RAMS(M+1,N),RAMS(M,N+1),US(M,N-1),US(M,N),US(M-1,N),
      AUS(M,N+1),US(M+1,N),QS)
      UF(M,N)=0
      GO TO 992
75 IF(M-MX) 76,77,77
76 CALL SUB5(DX,DZ(N-1),DZ(N),DZ(N+1),RAMS(M-1,N),RAMS(M,N),
      ARAMS(M+1,N),RAMS(M,N-1),RAMS(M,N+1),US(M,N-1),US(M,N),US(M-1,N),
      AUS(M,N+1),US(M+1,N),QS)
      UF(M,N)=0

```

```

      GO TO 992
77 CALL SUB23(DX,DZ(N-1),DZ(N),DZ(N+1),RAMS(M-1,N),RAMS(M,N),
  ARAMS(M,N-1),RAMS(M,N+1),US(M,N-1),US(M,N),US(M-1,N),
  AUS(M,N+1),TP,QS)
      UF(M,N)=0
      GO TO 992
C
C*****
C
80 IF(N-N22) 81,90,100
81 IF(M-2) 82,83,84
82 CALL SUB18(DX,DZ(N-1),DZ(N),RAMF(M,N-1),RAMF(M,N),RAMS(M,N),
  AUF(M,N-1),UF(M,N),US(M,N),H,QF,Q(N))
  CALL SUB12(DX,DZ(N),DZ(N+1),RAMF(M,N),RAMS(M,N+1),RAMS(M,N),
  ARAMS(M+1,N),UF(M,N),US(M,N),US(M,N+1),US(M+1,N),H,QS)
      GO TO 990
83 CALL SUB16(DX,DZ(N-1),DZ(N),DZ(N+1),RAMS(M,N-1),RAMS(M,N),
  ARAMS(M-1,N),RAMS(M+1,N),RAMS(M,N+1),US(M,N-1),US(M,N),US(M-1,N),
  AUS(M,N+1),US(M+1,N),QS)
      UF(M,N)=0
      GO TO 992
84 IF(M-MX) 85,86,86
85 CALL SUB5(DX,DZ(N-1),DZ(N),DZ(N+1),RAMS(M-1,N),RAMS(M,N),
  ARAMS(M+1,N),RAMS(M,N-1),RAMS(M,N+1),US(M,N-1),US(M,N),US(M-1,N),
  AUS(M,N+1),US(M+1,N),QS)
      UF(M,N)=0
      GO TO 992
86 CALL SUB23(DX,DZ(N-1),DZ(N),DZ(N+1),RAMS(M-1,N),RAMS(M,N),
  ARAMS(M,N-1),RAMS(M,N+1),US(M,N-1),US(M,N),US(M-1,N),
  AUS(M,N+1),TP,QS)
      UF(M,N)=0
      GO TO 992
C
C*****
C
90 IF(M-1) 91,91,92
91 CALL SUB19(DX,DZ(N-1),DZ(N),DZ(N+1),RAMS(M,N-1),RAMS(M,N),
  ARAMS(M+1,N),RAMS(M,N+1),US(M,N-1),US(M,N),US(M,N+1),US(M+1,N),
  AQS,Q(N))
      UF(M,N)=0
      GO TO 992
92 IF(M-MX) 93,94,94
93 CALL SUB5(DX,DZ(N-1),DZ(N),DZ(N+1),RAMS(M-1,N),RAMS(M,N),
  ARAMS(M+1,N),RAMS(M,N-1),RAMS(M,N+1),US(M,N-1),US(M,N),US(M-1,N),
  AUS(M,N+1),US(M+1,N),QS)
      UF(M,N)=0

      GO TO 992
94 CALL SUB23(DX,DZ(N-1),DZ(N),DZ(N+1),RAMS(M-1,N),RAMS(M,N),
  ARAMS(M,N-1),RAMS(M,N+1),US(M,N-1),US(M,N),US(M-1,N),
  AUS(M,N+1),TP,QS)
      UF(M,N)=0
      GO TO 992
C
C*****
C
100 IF(N-NZ) 101,110,110
101 IF(M-1) 102,102,103
102 CALL SUB24(DX,DZ(N-1),DZ(N),DZ(N+1),RAMS(M+1,N),RAMS(M,N),RAMS
  A(M,N-1),RAMS(M,N+1),US(M,N-1),US(M,N),US(M,N+1),US(M+1,N),QS,Q(N))

```

```

      UF(M,N)=0
      GO TO 992
103 IF(M-MX) 104,105,105
104 CALL SUB5(DX,DZ(N-1),DZ(N),DZ(N+1),RAMS(M-1,N),RAMS(M,N),
      ARAMS(M+1,N),RAMS(M,N-1),RAMS(M,N+1),US(M,N-1),US(M,N),US(M-1,N),
      AUS(M,N+1),US(M+1,N),QS)
      UF(M,N)=0
      GO TO 992
105 CALL SUB23(DX,DZ(N-1),DZ(N),DZ(N+1),RAMS(M-1,N),RAMS(M,N),
      ARAMS(M,N-1),RAMS(M,N+1),US(M,N-1),US(M,N),US(M-1,N),
      AUS(M,N+1),TP,QS)
      UF(M,N)=0
      GO TO 992
C
C*****
C
110 IF(M-1) 111,111,120
111 CALL SUB20(DX,DZ(N-1),DZ(N),RAMS(M+1,N),RAMS(M,N),RAMS(M,N-1),
      AUS(M,N-1),US(M,N),US(M+1,N),QS,Q(N))
      UF(M,N)=0
      GO TO 992
120 IF(M-MX) 121,122,122
121 CALL SUB21(DX,DZ(N-1),DZ(N),RAMS(M-1,N),RAMS(M,N),RAMS(M+1,N),
      ARAMS(M,N-1),US(M,N-1),US(M,N),US(M-1,N),US(M+1,N),QS)
      UF(M,N)=0
      GO TO 992
122 CALL SUB22(DX,DZ(N-1),DZ(N),RAMS(M-1,N),RAMS(M,N),RAMS(M,N-1),
      AUS(M,N-1),US(M,N),US(M-1,N),TP,QS)
      UF(M,N)=0
      GO TO 992
C
C
C*****
C      NEW TEMPERATURE CALCULATION
C*****
C
C
990 UF2(M,N)=UF(M,N)+2.O*DT*QF/(CF(M,N)*ROUF(M,N)*DX*DZ(N))
      US2(M,N)=US(M,N)+2.O*DT*QS/(CS(M,N)*ROUS(M,N)*DX*DZ(N))
      GO TO 999
991 UF2(M,N)=UF(M,N)+DT*QF/(CF(M,N)*ROUF(M,N)*DX*DZ(N))
      US2(M,N)=US(M,N)
      GO TO 999
992 US2(M,N)=US(M,N)+DT*QS/(CS(M,N)*ROUS(M,N)*DX*DZ(N))
      UF2(M,N)=UF(M,N)
      GO TO 999
999 CONTINUE
C
C
C*****
C      TEMPERATURE CHANGE
C*****
C
C
DO 150 N=1,NZ
DO 150 M=1,MX
      UF(M,N)=UF2(M,N)
150 US(M,N)=US2(M,N)
DO 175 N=1,N21
DO 175 M=1,MX

```

```

      IF(LNF(M,N)) 175,199,175
199  IF(UF(M,N).GT.TLIQF) GO TO 175
      IF(LMF(M,N)) 173,174,173
174  UF(M,N)=TLIQF-CFL*(TLIQF-UF(M,N))/CFF
      CF(M,N)=CFF
      ROUF(M,N)=ROUFF
      RAMF(M,N)=RAMFF
      LMF(M,N)=1
173  IF(UF(M,N).GT.TSOLF) GO TO 175
      ROUF(M,N)=ROUFS
      CF(M,N)=CFS
      RAMF(M,N)=RAMFS
      LNF(M,N)=1
175  CONTINUE
      DO 275 N=N11,NZ
      DO 275 M=1,MX
      IF(LNS(M,N)) 275,299,275
299  IF(US(M,N).GT.TLIQS) GO TO 275
      IF(LMS(M,N)) 273,274,273
274  US(M,N)=TLIQS-CSL*(TLIQS-US(M,N))/CSF
      CS(M,N)=CSF
      ROUS(M,N)=ROUSF
      RAMS(M,N)=RAMSF
      LMS(M,N)=1
273  IF(US(M,N).GT.TSOLS) GO TO 275
      ROUS(M,N)=ROUSS
      CS(M,N)=CSS
      RAMS(M,N)=RAMSS
      LNS(M,N)=1
275  CONTINUE
C
C
C*****
C      OUTPUT
C*****
C
C
      IF(T-END1) 565,1000,9001
9001 IF(T-END1A) 1000,9002,9002
9002 IF(T-END2) 565,1000,9003
9003 IF(T-END2A) 1000,9004,9004
9004 IF(T-END3) 565,1000,9005
9005 IF(T-END3A) 1000,9006,9006
9006 IF(T-END4) 565,1000,9007
9007 IF(T-END4A) 1000,9008,9008
9008 IF(T-END5) 565,1000,9009
9009 IF(T-END5A) 1000,9010,9010
9010 IF(T-END6) 565,1000,9011
9011 IF(T-END6A) 1000,9012,9012
9012 IF(T-END7) 565,1000,9013
9013 IF(T-END7A) 1000,9014,9014
9014 IF(T-END8) 565,1000,9015
9015 IF(T-END8A) 1000,9016,9016
9016 IF(T-END9) 565,1000,9017
9017 IF(T-END9A) 1000,9018,9018
9018 IF(T-END10) 565,1000,9019
9019 IF(T-END10A) 1000,9020,9020
9020 IF(T-END11) 565,1000,9021
9021 IF(T-END11A) 1000,9022,9022
9022 IF(T-END12) 565,1000,9023

```


9023 IF(T-END12A) 1000,9024,9024
9024 IF(T-END13) 565,1000,9025
9025 IF(T-END13A) 1000,9026,9026
9026 IF(T-END14) 565,1000,9027
9027 IF(T-END14A) 1000,9028,9028
9028 IF(T-END15) 565,1000,9029
9029 IF(T-END15A) 1000,9030,9030
9030 IF(T-END16) 565,1000,9031
9031 IF(T-END16A) 1000,9032,9032
9032 IF(T-END17) 565,1000,9033
9033 IF(T-END17A) 1000,9034,9034
9034 IF(T-END18) 565,1000,9035
9035 IF(T-END18A) 1000,9036,9036
9036 IF(T-END19) 565,1000,9037
9037 IF(T-END19A) 1000,9038,9038
9038 IF(T-END20) 565,1000,9039
9039 IF(T-END20A) 1000,9040,9040
9040 IF(T-END21) 565,1000,9041
9041 IF(T-END21A) 1000,9042,9042
9042 IF(T-END22) 565,1000,9043
9043 IF(T-END22A) 1000,9044,9044
9044 IF(T-END23) 565,1000,9045
9045 IF(T-END23A) 1000,9046,9046
9046 IF(T-END24) 565,1000,9047
9047 IF(T-END24A) 1000,9048,9048
9048 IF(T-END25) 565,1000,9049
9049 IF(T-END25A) 1000,9050,9050
9050 IF(T-END26) 565,1000,9051
9051 IF(T-END26A) 1000,9052,9052
9052 IF(T-END27) 565,1000,9053
9053 IF(T-END27A) 1000,9054,9054
9054 IF(T-END28) 565,1000,9055
9055 IF(T-END28A) 1000,9056,9056
9056 IF(T-END29) 565,1000,9057
9057 IF(T-END29A) 1000,9058,9058
9058 IF(T-END30) 565,1000,9059
9059 IF(T-END30A) 1000,9060,9060
9060 IF(T-END31) 565,1000,9061
9061 IF(T-END31A) 1000,9062,9062
9062 IF(T-END32) 565,1000,9063
9063 IF(T-END32A) 1000,9064,9064
9064 IF(T-END33) 565,1000,9065
9065 IF(T-END33A) 1000,9066,9066
9066 IF(T-END34) 565,1000,9067
9067 IF(T-END34A) 1000,9068,9068
9068 IF(T-END35) 565,1000,9069
9069 IF(T-END35A) 1000,9070,9070
9070 IF(T-END36) 565,1000,9071
9071 IF(T-END36A) 1000,9072,9072
9072 IF(T-END37) 565,1000,9073
9073 IF(T-END37A) 1000,9074,9074
9074 IF(T-END38) 565,1000,9075
9075 IF(T-END38A) 1000,9076,9076
9076 IF(T-END39) 565,1000,9077
9077 IF(T-END39A) 1000,9078,9078
9078 IF(T-END40) 565,1000,9079
9079 IF(T-END40A) 1000,9080,9080
9080 IF(T-END41) 565,1000,9081
9081 IF(T-END41A) 1000,9082,9082
9082 IF(T-END42) 565,1000,9083

```

9083 IF(T-END42A) 1000,9084,9084
9084 IF(T-END43) 565,1000,1000

```

```

1000 CONTINUE
      WRITE(6,300) T
300  FORMAT(10H  TIME  =,F10.7)
      WRITE(6,303) END1,END2,END3,END4,END5,END6,END7,END8,END9,END10
303  FORMAT(4F10.7)
      WRITE(6,301)
301  FORMAT(5H U-1 ,5H U-2 ,5H U-3 ,5H U-4 ,5H U-5 ,5H U-6 ,5H U-7
A,5H U-8 ,5H U-9 ,5H U-10,5H U-11,5H U-12,5H U-13,5H U-14,5H U-15,5
AH U-16,5H U-17,5H U-18,5H U-19,5H U-20,5H U-21,5H U-22,5H U-23)
      DO 350 N=1,40
      WRITE(6,3350) (UF(M,N),M=1,23)
3350 FORMAT(23F5.0)
350  CONTINUE
      WRITE(6,302)
302  FORMAT(5H U-1 ,5H U-2 ,5H U-3 ,5H U-4 ,5H U-5 ,5H U-6 ,5H U-7
A,5H U-8 ,5H U-9 ,5H U-10,5H U-11,5H U-12,5H U-13,5H U-14,5H U-15,5
AH U-16,5H U-17,5H U-18,5H U-19,5H U-20,5H U-21,5H U-22,5H U-23)
      DO 351 J=1,40
      WRITE(6,3510) (US(M,J),M=1,23)
3510 FORMAT(23F5.0)
351  CONTINUE
      IF(T-END43) 565,1500,1500
1500 STOP
      END

```

```

C
C
C
C*****
C      SUBROUTINE
C*****
C
C

```

```

      SUBROUTINE SUB1(DX,DZ1,DZ2, RAM11, RAM21, RAM12, U12, U11, U21, Q, Q10)
      RAM=(RAM11+RAM21)/2.0
      Q2=Q10*DZ1
      Q3=DX*(U12-U11)/(DZ2/(2.0*RAM12)+DZ1/(2.0*RAM11))
      Q4=RAM*DZ1*(U21-U11)/DX
      Q=Q2+Q3+Q4
      RETURN
      END

```

```

C
C
      SUBROUTINE SUB2(DX,DZ1,DZ2, RAM01, RAM11, RAM21, RAM12, U01, U11,
AU12, U21, Q)
      RAM1=(RAM01+RAM11)/2.0
      RAM2=(RAM11+RAM21)/2.0
      Q2=RAM1*DZ1*(U01-U11)/DX
      Q3=DX*(U12-U11)/(DZ2/(2.0*RAM12)+DZ1/(2.0*RAM11))
      Q4=RAM2*DZ1*(U21-U11)/DX
      Q=Q4+Q2+Q3
      RETURN
      END

```

```

C
C
      SUBROUTINE SUB3(DX,DZ1,DZ2, RAM01, RAM11, RAM12, U01, U11, U12, UFI, Q)
      RAM=(RAM01+RAM11)/2.0
      Q2=RAM*DZ1*(U01-U11)/DX

```

```

Q3=DX*(U12-U11)/(DZ2/(2.O*RAM12)+DZ1/(2.O*RAM11))
Q4=2.O*RAM11*DZ1*(UFI-U11)/DX
Q=Q2+Q3+Q4
RETURN
END

```

C
C

```

SUBROUTINE SUB4(DX,DZO,DZ1,DZ2,RAM21,RAM11,RAM10,RAM12,U10,U11,U12
A,U21,Q,Q10)
RAM=(RAM21+RAM11)/2.O
Q1=DX*(U10-U11)/(DZO/(2.O*RAM10)+DZ1/(2.O*RAM11))
Q2=Q10*DZ1
Q3=DX*(U12-U11)/(DZ2/(2.O*RAM12)+DZ1/(2.O*RAM11))
Q4=RAM*DZ1*(U21-U11)/DX
Q=Q1+Q2+Q3+Q4
RETURN
END

```

C
C

```

SUBROUTINE SUB5(DX,DZO,DZ1,DZ2,RAMO1,RAM11,RAM21,RAM10,RAM12,U10,U
A11,UO1,U12,U21,Q)
RAM1=(RAMO1+RAM11)/2.O
RAM2=(RAM21+RAM11)/2.O
Q1=DX*(U10-U11)/(DZO/(2.O*RAM10)+DZ1/(2.O*RAM11))
Q2=RAM1*DZ1*(UO1-U11)/DX
Q3=DX*(U12-U11)/(DZ2/(2.O*RAM12)+DZ1/(2.O*RAM11))
Q4=RAM2*DZ1*(U21-U11)/DX
Q=Q1+Q2+Q3+Q4
RETURN
END

```

C
C

```

SUBROUTINE SUB6(DX,DZO,DZ1,DZ2,RAMO1,RAM11,RAM10,RAM12,U10,U11,
AUO1,U12,UFI,Q)
RAM=(RAMO1+RAM11)/2.O
Q1=DX*(U10-U11)/(DZO/(2.O*RAM10)+DZ1/(2.O*RAM11))
Q2=RAM*DZ1*(UO1-U11)/DX
Q3=DX*(U12-U11)/(DZ2/(2.O*RAM12)+DZ1/(2.O*RAM11))
Q4=2.O*RAM11*DZ1*(UFI-U11)/DX
Q=Q1+Q2+Q3+Q4
RETURN
END

```

C
C

```

SUBROUTINE SUB7(DX,DZO,DZ1,DZ2,RAMO1,RAM11,RAM12,RAM21,RAM10,
AU10,U11,UO1,U12,U21,Q)
RAM1=(RAMO1+RAM11)/2.O
RAM2=(RAM12+RAM11)/2.O
RAM3=(RAM21+RAM11)/2.O
Q1=DX*(U10-U11)/(DZO/(2.O*RAM10)+DZ1/(2.O*RAM11))
Q2=RAM1*DZ1*(UO1-U11)/DX
Q3=RAM2*DX*(U12-U11)*(DZ1/2.O+DZ2/3.O)/((DX/6.O)**2+(DZ2/3.O+
ADZ1/2.O)**2)
Q4=RAM3*DZ1*(U21-U11)/DX
Q=Q1+Q2+Q3+Q4
RETURN
END

```

C
C

```

SUBROUTINE SUB8(DX,DZO,DZ1,DZ2,RAMO1,RAM11,RAM21,RAM10,RAMS,U10,

```

```

AU11,UO1,U12,U21,H,Q)
  RAM1=(RAMO1+RAM11)/2.O
  RAM2=(RAM21+RAM11)/2.O
  Q1=DX*(U1O-U11)/(DZO/(2.O*RAM1O)+DZ1/(2.O*RAM11))
  Q2=RAM1*DZ1*(UO1-U11)/DX
  Q3=DX*(U12-U11)/(DZ1/(2.O*RAM11)+1.O/H+DZ2/(2.O*RAMS))
  Q4=RAM2*DZ1*(U21-U11)/DX
  Q=Q1+Q2+Q3+Q4
  RETURN
  END

```

C
C

```

SUBROUTINE SUB9(DX,DZO,DZ1,DZ2,RAMO1,RAM11,RAM1O,RAMS,U1O,U11,
AUO1,U12,UFI,H,Q)
  RAM=(RAMO1+RAM11)/2.O
  Q1=DX*(U1O-U11)/(DZO/(2.O*RAM1O)+DZ1/(2.O*RAM11))
  Q2=RAM*DZ1*(UO1-U11)/DX
  Q3=DX*(U12-U11)/(DZ1/(2.O*RAM11)+1.O/H+DZ2/(2.O*RAMS))
  Q4=2.O*RAM11*DZ1*(UFI-U11)/DX
  Q=Q1+Q2+Q3+Q4
  RETURN
  END

```

C
C

```

SUBROUTINE SUB10(DX,DZO,DZ1,DZ2,RAMO1,RAM11,RAM12,RAM21,RAM1O,
AU1O,U11,UO1,U12,U21,Q)
  RAM1=(RAMO1+RAM11)/2.O
  RAM2=(RAM12+RAM11)/2.O
  RAM3=(RAM21+RAM11)/2.O
  Q1=DX*(U1O-U11)/(DZO/(2.O*RAM1O)+DZ1/(2.O*RAM11))
  Q2=RAM1*DZ1*(UO1-U11)/DX
  Q3=RAM2*DX*(U12-U11)*(DZ1/2.O+DZ2/3.O)/((DX/6.O)**2+
A(DZ2/3.O+DZ1/2.O)**2)
  Q4=3O.O*DX*DZ1*RAM3*(U21-U11)/(25.O*DX**2+DZ1**2)
  Q=Q1+Q2+Q3+Q4
  RETURN
  END

```

C
C

```

SUBROUTINE SUB11(DX,DZO,DZ1,RAM1O,RAM11,RAMO1,RAMS,U1O,U11,UO1,
AUS11,H,Q)
  RAM1=(RAM1O+RAM11)/2.O
  RAM2=(RAMO1+RAM11)/2.O
  Q1=DX*RAM1*(U1O-U11)*(DZO/2.O+DZ1/3.O)/((DX/6.O)**2+(DZ1/3.O+
ADZO/2.O)**2)
  Q2=3O.O*DX*DZ1*RAM2*(UO1-U11)/(25.O*DX**2+DZ1**2)
  Q3=(2.O*DX*DZ1*(US11-U11)/SQRT(DZ1**2+DX**2))/(SQRT(DZ1**2+DX**2)/
A(12.O*RAM11)+1.O/H+SQRT(DZ1**2+DX**2)/(12.O*RAMS))
  Q=Q1+Q2+Q3
  RETURN
  END

```

C
C

```

SUBROUTINE SUB12(DX,DZ1,DZ2,RAMF,RAM12,RAM11,RAM21,
AUF11,U11,U12,U21,H,Q)
  RAM1=(RAM12+RAM11)/2.O
  RAM2=(RAM21+RAM11)/2.O
  Q2=2.O*DX*DZ1*(UF11-U11)/SQRT(DZ1**2+DX**2)/(SQRT(DZ1**2+DX**2)/
A(12.O*RAMF)+1.O/H+SQRT(DZ1**2+DX**2)/(12.O*RAM11))
  Q3=RAM1*DX*(U12-U11)*(DZ2/2.O+DZ1/3.O)/((DX/6.O)**2+(DZ1/3.O+DZ2/

```

```

A2.O)**2)
Q4=30.O*DX*DZ1*RAM2*(U21-U11)/(25.O*DX**2+DZ1**2)
Q=Q2+Q3+Q4
RETURN
END

```

C
C

```

SUBROUTINE SUB13(DX,DZO,DZ1,DZ2,RAMF,RAMO1,RAM11,RAM21,RAM12,
AUF10,U11,UO1,U12,U21,H,Q)
RAM1=(RAMO1+RAM11)/2.O
RAM2=(RAM21+RAM11)/2.O
Q1=DX*(UF10-U11)/(DZO/(2.O*RAMF)+1.O/H+DZ1/(2.O*RAM11))
Q2=30.O*DX*DZ1*RAM1*(UO1-U11)/(25.O*DX**2+DZ1**2)
Q3=DX*(U12-U11)/(DZ2/(2.O*RAM12)+DZ1/(2.O*RAM11))
Q4=RAM2*DZ1*(U21-U11)/DX
Q=Q1+Q2+Q3+Q4
RETURN
END

```

C
C

```

SUBROUTINE SUB14(DX,DZO,DZ1,DZ2,RAMF,RAMO1,RAM11,RAM21,RAM12,
AUF10,U11,UO1,U12,U21,H,Q)
RAM1=(RAMO1+RAM11)/2.O
RAM2=(RAM21+RAM11)/2.O
Q1=DX*(UF10-U11)/(DZO/(2.O*RAMF)+1.O/H+DZ1/(2.O*RAM11))
Q2=RAM1*DZ1*(UO1-U11)/DX
Q3=DX*(U12-U11)/(DZ2/(2.O*RAM12)+DZ1/(2.O*RAM11))
Q4=RAM2*DZ1*(U21-U11)/DX
Q=Q1+Q2+Q3+Q4
RETURN
END

```

C
C

```

SUBROUTINE SUB15(DX,DZO,DZ1,DZ2,RAMF,RAMO1,RAM11,RAM12,
AUF10,U11,UO1,U12,TP,H,Q)
RAM=(RAMO1+RAM11)/2.O
Q1=DX*(UF10-U11)/(DZO/(2.O*RAMF)+1.O/H+DZ1/(2.O*RAM11))
Q2=RAM*DZ1*(UO1-U11)/DX
Q3=DX*(U12-U11)/(DZ2/(2.O*RAM12)+DZ1/(2.O*RAM11))
Q4=2.O*RAM11*DZ1*(TP-U11)/DX
Q=Q1+Q2+Q3+Q4
RETURN
END

```

C
C

```

SUBROUTINE SUB16(DX,DZO,DZ1,DZ2,RAM10,RAM11,RAMO1,RAM21,RAM12,
AU10,U11,UO1,U12,U21,Q)
RAM1=(RAM10+RAM11)/2.O
RAM2=(RAMO1+RAM11)/2.O
RAM3=(RAM21+RAM11)/2.O
Q1=RAM1*DX*(U10-U11)*(DZ1/2.O+DZO/3.O)/((DX/6.O)**2+
A(DZO/3.O+DZ1/2.O)**2)
Q2=30.O*DX*DZ1*RAM2*(UO1-U11)/(25.O*DX**2+DZ1**2)
Q3=DX*(U12-U11)/(DZ2/(2.O*RAM12)+DZ1/(2.O*RAM11))
Q4=RAM3*DZ1*(U21-U11)/DX
Q=Q1+Q2+Q3+Q4
RETURN
END

```

C
C

```

SUBROUTINE SUB17(DX,DZO,DZ1,DZ2, RAM12, RAM11, RAM21, RAM10,
AU10, U11, U12, U21, Q, Q10)
  RAM1=(RAM12+RAM11)/2.0
  RAM2=(RAM21+RAM11)/2.0
  Q1=DX*(U10-U11)/(DZO/(2.0*RAM10)+DZ1/(2.0*RAM11))
  Q2=Q10*DZ1
  Q3=RAM1*DX*(U12-U11)*(DZ1/2.0+DZ2/3.0)/((DX/6.0)**2+
A(DZ2/3.0+DZ1/2.0)**2)
  Q4=30.0*DX*DZ1*RAM2*(U21-U11)/(25.0*DX**2+DZ1**2)
  Q=Q1+Q2+Q3+Q4
  RETURN
C
C
  END
SUBROUTINE SUB18(DX,DZO,DZ1, RAM10, RAM11, RAMS, U10, U11, US11, H, Q,
AQ10)
  RAM=(RAM10+RAM11)/2.0
  Q1=DX*RAM*(U10-U11)*(DZO/2.0+DZ1/3.0)/((DX/6.0)**2
A+(DZ1/3.0+DZO/2.0)**2)
  Q2=Q10*DZ1
  Q3=(2.0*DX*DZ1*(US11-U11)/SQRT(DZ1**2+DX**2))/(SQRT(DZ1**2+DX**2)
A/(12.0*RAM11)+1.0/H+SQRT(DZ1**2+DX**2)/(12.0*RAMS))
  Q=Q1+Q2+Q3
  RETURN
  END
C
C
SUBROUTINE SUB19(DX,DZO,DZ1,DZ2, RAM10, RAM11, RAM21, RAM12,
AU10, U11, U12, U21, Q, Q10)
  RAM1=(RAM10+RAM11)/2.0
  RAM2=(RAM21+RAM11)/2.0
  Q1=RAM1*DX*(U10-U11)*(DZ1/2.0+DZO/3.0)/((DX/6.0)**2+(DZO/3.0+
ADZ1/2.0)**2)
  Q2=Q10*DZ1
  Q3=DX*(U12-U11)/(DZ2/(2.0*RAM12)+DZ1/(2.0*RAM11))
  Q4=RAM2*DZ1*(U21-U11)/DX
  Q=Q1+Q2+Q3+Q4
  RETURN
  END
C
C
SUBROUTINE SUB20(DX,DZO,DZ1, RAM21, RAM11, RAM10, U10, U11, U21, Q, Q10)
  RAM=(RAM21+RAM11)/2.0
  Q1=DX*(U10-U11)/(DZO/(2.0*RAM10)+DZ1/(2.0*RAM11))
  Q2=Q10*DZ1
  Q4=RAM*DZ1*(U21-U11)/DX
  Q=Q1+Q2+Q4
  RETURN
  END
C
C
SUBROUTINE SUB21(DX,DZO,DZ1, RAM01, RAM11, RAM21, RAM10, U10, U11, U01,
AU21, Q)
  RAM1=(RAM01+RAM11)/2.0
  RAM2=(RAM21+RAM11)/2.0
  Q1=DX*(U10-U11)/(DZO/(2.0*RAM10)+DZ1/(2.0*RAM11))
  Q2=RAM1*DZ1*(U01-U11)/DX
  Q4=RAM2*DZ1*(U21-U11)/DX
  Q=Q1+Q2+Q4
  RETURN

```

```

END
C
C
SUBROUTINE SUB22(DX,DZO,DZ1,RAM01,RAM11,RAM10,U10,U11,U01,TP,Q)
  RAM=(RAM01+RAM11)/2.0
  Q1=DX*(U10-U11)/(DZO/(2.0*RAM10)+DZ1/(2.0*RAM11))
  Q2=RAM*DZ1*(U01-U11)/DX
  Q4=2.0*RAM11*DZ1*(TP-U11)/DX
  Q=Q1+Q2+Q4
  RETURN
END ...

C
C
SUBROUTINE SUB23(DX,DZO,DZ1,DZ2,RAM01,RAM11,RAM10,RAM12,U10,U11,
AU01,U12,TP,Q)
  RAM=(RAM01+RAM11)/2.0
  Q1=DX*(U10-U11)/(DZO/(2.0*RAM10)+DZ1/(2.0*RAM11))
  Q2=RAM*DZ1*(U01-U11)/DX
  Q3=DX*(U12-U11)/(DZ2/(2.0*RAM12)+DZ1/(2.0*RAM11))
  Q4=2.0*RAM*DZ1*(TP-U11)/DX
  Q=Q1+Q2+Q3+Q4
  RETURN
END

C
C
SUBROUTINE SUB24(DX,DZO,DZ1,DZ2,RAM21,RAM11,RAM10,RAM12,U10,U11,U12,
AU21,Q,Q10)
  RAM=(RAM21+RAM11)/2.0
  Q1=DX*(U10-U11)/(DZO/(2.0*RAM10)+DZ1/(2.0*RAM11))
  Q2=Q10*DZ1
  Q3=DX*(U12-U11)/(DZ2/(2.0*RAM12)+DZ1/(2.0*RAM11))
  Q4=RAM*DZ1*(U21-U11)/DX
  Q=Q1+Q2+Q3+Q4
  RETURN
END

```

APPENDIX VI
COMPUTER PROGRAM FOR THE CALCULATION OF FLUID PRESSURE
IN THE FLUX CHANNEL

```

C*****
C    DYMANIC PRESSURE ACTING ON THE SHELL
C*****
C
C    PROGRAM FILE NAME : FLOW44
C    DATA FILE NAME   : DATA33
C*****
C
C    LIST OF SYMBOLS
C
C    P      PRESSURE DISTRIBUTION
C    RAM    INTEGRATION OF P
C    ARAM   INTEGRATED AVERAGE OF P
C    BM     BENDING MOMENT
C    MU     VISCOSITY OF MOULD FLUX
C    XHI    X-COORDINATE OF INLET OF FLUX CHANNEL
C    YHI    Y-COORDINATE OF INLET OF FLUX CHANNEL
C    XHF    X-COORDINATE OF OUTLET OF FLUX CHANNEL
C    YHF    Y-COORDINATE OF OUTLET OF FLUX CHANNEL
C    RF     DENSITY OF MOULD FLUX
C    RS     DENSITY OF STEEL
C    VS     VELOCITY OF SLAB
C    VM     VELOCITY OF MOULD
C    Q      FLUX CONSUMPTION
C    QQ     RELATIVE FLUX-CONSUMPTION
C*****
C
C    IMPLICIT REAL*8(A-H,O-Z)
C    REAL MU
C    DIMENSION P(3000),RAM(3000),BM(3000)
C
C
C    READ(5,100) XHI,YLI,XHF,YLF
C    READ(5,110) RF,RS,MU,VS,VM
C 100 FORMAT(4F10.7)
C 110 FORMAT(5F10.5)
C
C
C    WRITE(6,200) XHI,YLI,XHF,YLF
C    WRITE(6,210) RF,RS,MU,VS,VM
C 200 FORMAT(10H HI      = , F12.6/ 10H LI      = , F12.6
C / 10H HF      = , F12.6/ 10H LF      = , F12.6)
C 210 FORMAT(10H RF      = , F12.6/ 10H RS      = , F12.6
C / 10H MU      = , F12.6/ 10H VS      = , F12.6
C / 10H VM      = , F12.6)
C
C
C*****
C    SHAPE OF FLUX CHANNEL : X=A*Y+B
C*****
C
C
C    A=(XHI-XHF)/(YLI-YLF)
C    B=(XHF*YLI-XHI*YLF)/(YLI-YLF)
C
C
C    EPLF=-(1/A)*(1/XHF-1/B)

```



```

      ZELF=- (1/2./A)*(1/(XHF**2)-1/(B**2))
C
C
      Q=((2*RF-RS)*980*YLF+6*MU*(VM+VS)*EPLF)/(12*MU*ZELF)
C
      WRITE(6,330) Q
330  FORMAT(10H Q      = , F12.6)
C
C
      QQ=((2*RF-RS)*980*YLF+6*MU*(VM+VS)*EPLF)/(12*MU*ZELF)
C
C
      II=(YLF-YLI+0.001)*1000.0
      DO 405 I=1,II
      Y=FLOAT(I)/1000.0
      G=A*Y+B
      EPY=- (1/A)*(1/G-1/B)
      ZEY=-1/(2*A)*(1/(G**2)-1/(B**2))
C
      P(I)=(2*RF-RS)*980*Y+6*MU*(VM+VS)*EPY-12*MU*QQ*ZEY
405  CONTINUE
C
      RAM(1)=0.0
      BM(1)=0.0
      DO 600 I=2,II
      RAM(I)=RAM(I-1)+P(I)*0.0010
      BM(I)=BM(I-1)+P(I)*0.0010*(II-I)/1000
600  CONTINUE
C
C
      WRITE(6,610) II
610  FORMAT(10H II      = , I5)
      WRITE(6,620) RAM(II)
620  FORMAT(10H RAM(II)= , F15.6)
      ARAM=RAM(II)/(YLF-YLI)
      WRITE(6,630) ARAM
630  FORMAT(10H ARAM   = , F15.6)
      WRITE(6,650) BM(II)
650  FORMAT(10H BM(II) = , F15.6)
      STOP
      END

```

APPENDIX VII
COMPUTER PROGRAM FOR THE CALCULATION OF THE CHANGE
OF MENISCUS SHAPE

```

C *****
C   CHANGE OF MENISCUS SHEPE
C *****
C
C   PROGRAM FILE NAME : MENISCUS10
C   DATA FILE NAME   : DATA33M
C
C *****
C
C   LIST OF SYMBOLS
C
C   P   PRESSURE DISTRIBUTION
C   RAM  INTEGRATION OF P
C   MU   VISCOSITY OF MOULD FLUX
C   XHI  COORDINATE OF INLET OF FLUX CHANNEL
C   YHI  COORDINATE OF INLET OF FLUX CHANNEL
C   XHM  COORDINATE OF MIDDLE POINT OF FLUX CHANNEL
C   YHM  COORDINATE OF MIDDLE POINT OF FLUX CHANNEL
C   XHF  COORDINATE OF OUTLET OF FLUX CHANNEL
C   YHF  COORDINATE OF OUTLET OF FLUX CHANNEL
C   RF   DENSITY OF MOULD FLUX
C   RS   DENSITY OF STEEL
C   VS   VELOCITY OF SLAB
C   VM   VELOCITY OF MOULD
C   Q    FLUX CONSUMPTION
C   QQ   RELATIVE FLUX-CONSUMPTION
C   SIGMA INTERFACIAL TENSION
C   CAP  CAPILLARY CNSTANT
C   CAPMODMODIFIED CAPILLARY CONSTANT
C   XX(I) CALCULATED SHAPE OF MENISCUS
C   YY(I) CALCULATED SHAPE OF MENISCUS
C *****
C
C
C   IMPLICIT REAL*8(A-H,O-Z)
C   REAL MU
C   DIMENSION P(3000),RAM(3000),XX(1000),YY(1000)
C
C *****
C
C   READ AND WRITE DATA
C *****
C
C   READ(5,100) XHI,YLI,XHM,YLM,XHF,YLF
C   READ(5,110) RF,RS,MU,VS,VM
C 100 FORMAT(6F10.7)
C 110 FORMAT(5F10.5)
C
C *****
C
C   WRITE(6,200) XHI,YLI,XHM,YLM
C   WRITE(6,210) XHF,YLF,RF,RS
C   WRITE(6,220) MU,VS,VM
C 200 FORMAT(10H HI      = , F12.6/ 10H LI      = , F12.6/ 10H HM      = ,

```

```

      C F12.6/ 10H LM      = , F12.6)
210  FORMAT(10H HF      = , F12.6/ 10H LF      = , F12.6/ 10H RF      = ,
      C F12.6/ 10H RS      = , F12.6)
220  FORMAT(10H MU      = , F12.6/ 10H VS      = , F12.6/ 10H VM      = ,
      C F12.6)
C
C
C*****
C
C      APPLOXIMATED SHAPE OF MENISCUS  X=A*Y**2.+B*Y+C
C*****
C
C      A=((XHI-XHM)*(YLI-YLF)-(XHI-XHF)*(YLI-YLM))/((YLI-YLM)*(YLI-YLF)
C*(YLM-YLF))
C      B=((XHI-XHM)*(YLF**2.-YLI**2.)+(XHI-XHF)*(YLI**2.-YLM**2.))/
C((YLI-YLM)*(YLI-YLF)*(YLM-YLF))
C      C=XHI-(YLI*YLF*(YLF-YLI)*(XHI-XHM)-YLI*YLM*(YLM-YLI)
C*(XHI-XHF))/((YLI-YLM)*(YLI-YLF)*(YLM-YLF))
C
C
C*****
C
C      D=4*A*C-B**2
C
C
C*****
C
C      E=2*A*YLF+B
C      F=A*YLF**2+B*YLF+C
C
C
C*****
C
C      IF(D-0) 310,300,300
C
C
C*****
C
C      300  EPLF=(1/D)*(E/F-B/C)+4*A/D**1.5*(DATAN(E/D**0.5)
C-DATAN(B/D**0.5))
C      ZELF=(1/2./D**2.)*(E*(D+6*A*F)/F**2.-B*(D+6*A*C)/C**2.)
C+12.*A**2./D**2.5*(DATAN(E/D**0.5)-DATAN(B/D**0.5))
C      GO TO 320
C
C
C*****
C
C      310  EPLF=(1/D)*(E/F-B/C)+2*A/(-D)**1.5*DLOG((E-(-D)**0.5)
C*(B+(-D)**0.5)/(E+(-D)**0.5)/(B-(-D)**0.5))
C      ZELF=(1/2./D**2.)*(E*(D+6*A*F)/F**2.-B*(D+6.*A*C)/C**2.)
C+6.*A**2./(-D)**2.5*DLOG((E-(-D)**0.5)*(B+(-D)**0.5)
C/(E+(-D)**0.5)/(B-(-D)**0.5))
C

```

```

C
C*****
C
C
320 Q=((2.*RF-RS)*980*YLF+6.*MU*(VM+VS)*EPLF)/(12.*MU*ZELF)
C
C*****
C
C      WRITE(6,330) Q
330 FORMAT(10H Q      = , F12.6)
C
C*****
C
C      QQ=((2.*RF-RS)*980*YLF+6.*MU*(VM-VS)*EPLF)/(12.*MU*ZELF)
C
C*****
C
C      IF(D-0) 410,400,400
C
C*****
C
400 II=(YLF+0.0001)*1000.0
   DO 405 I=1,II
   Y=FLOAT(I)/1000.0
   G=2.*A*Y+B
   H=A*Y**2.+B*Y+C
   EPY=(1/D)*(G/H-B/C)+4.*A/D**1.5*(DATAN(G/D**0.5)-DATAN(B/D**0.5))
   ZEY=(1/2./D**2.)*(G*(D+6.*A*H)/H**2.-B*(D+6.*A*C)/C**2)
   C+12.*A**2./D**2.5*(DATAN(G/D**0.5)-DATAN(B/D**0.5))
C
C
C*****
C
C      P(I)=(2.*RF-RS)*980*Y+6*MU*(VM-VS)*EPY-12.*MU*QQ*ZEY
C
C*****
C
C
405 CONTINUE
   GO TO 500
C
C*****
C
C
410 II=(YLF+0.0001)*1000.0
   DO 415 I=1,II
   Y=FLOAT(I)/1000.0
   G=2.*A*Y+B
   H=A*Y**2.+B*Y+C

```

```

      EPY=(1/D)*(G/H-B/C)+2.*A/(-D)**1.5*DLOG((G-(-D)**0.5)
      C*(B+(-D)**0.5)/(G+(-D)**0.5)/(B-(-D)**0.5))
      ZEY=(1/2./D**2.)*(G*(D+6.*A*H)/H**2.-B*(D+6.*A*C)/C**2.)
      C+6.*A**2./(-D)**2.5*DLOG((G-(-D)**0.5)*(B+(-D)**0.5)
      C/(G+(-D)**0.5)/(B-(-D)**0.5))
C
C
C*****
C
C
      P(I)=(2.*RF-RS)*980*Y+6.*MU*(VM-VS)*EPY-12.*MU*QQ*ZEY
C
C
C*****
C
C
      415 CONTINUE
C
C
C*****
C
C
      500 RAM(1)=0.0
      DO 600 I=2,II
      RAM(I)=RAM(I-1)+P(I)*0.0010
      600 CONTINUE
      WRITE(6,610) II
      610 FORMAT(10H II      = , I5)
      WRITE(6,615) (I,I, P(I), I, RAM(I), I=1,II)
      615 FORMAT(14,3X,'P(',I4,') = ', F16.6,3X,'RAM(',I4,') = ',F16.6)
C
C
C*****
C
C
      READ(5,1000) SIGMA,YMIN,H
      1000 FORMAT(3F8.5)
      CAP=2.*SIGMA/(RS-RF)/980.
      IF(RAM(II)-0.) 1010,1020,1020
      1010 YMAX=0.000
      CAPMOD=2.*SIGMA/((RS-RF)*980.-2.*RAM(II)/YLF**2)
      GO TO 1030
      1020 YMAX=(CAP*(1.+RAM(II)/SIGMA))**0.5
      CAPMOD=2.*SIGMA/((RS-RF)*980.-2.*RAM(II)/YMAX**2)
      1030 WRITE(6,1100) SIGMA,YMIN,H
      1100 FORMAT( 10H SIGMA = ,F12.6/ 10H YMIN = ,F12.6/ 10H H      = ,
      CF12.6)
      WRITE(6,1200) CAP,YMAX,CAPMOD
      1200 FORMAT( 10H CAP = ,F12.6/ 10H YMAX = ,F12.6/ 10H CAPMOD = ,
      CF12.6/ 1H ,6X, 1HX,15X, 1HY, 1H )
C
C
C*****
C
C
      YY(1)=YMIN
      N=1
      1300 XX(N)=-((2.*CAPMOD-YY(N)**2)**0.5
      C+(CAPMOD/2.)*0.5*DLOG(((2.*CAPMOD)**0.5
      C+(2.*CAPMOD-YY(N)**2)**0.5)/YY(N))

```

```
C+0.3768*CAPMOD**0.5
N=N+1
YY(N)=YY(N-1)+H
YF=(2.*CAPMOD)**0.5
IF(YF-YY(N)) 1400,1300,1300
1400 M=N-1
WRITE(6,1500) (XX(I),YY(I),I=1,M)
1500 FORMAT( 1H , F10.6, F16.6)
STOP
END
```

APPENDIX VIII
COMPUTER PROGRAM FOR THE CALCULATION OF NONUNIFORMITY
OF SHELL PROFILE IN THE MOULD

```

C*****
C    TWO-DIMENSIONAL UNSTEADY STATE FINITE DIFFERENCE HEAT TRANSFER PROGRAM
C    OF SOLIDIFICATION NEAR OSCILLATION MARKS FEATURED TRIANGULAR NODES
C*****
C
C    PROGRAM FILE NAME : TRANSVERSE2
C    DATA FILE NAME   : DATA555
C
C*****
C
C    LIST OF SYMBOLS
C
C    US    TEMPERATURE OF STEEL
C    UF    TEMPERATURE OF MOULD FLUX
C    US2   NEW TEMPERATURE OF STEEL
C    UF2   NEW TEMPERATURE OF MOULD FLUX
C    DX    SIZE OF NODE IN X DIRECTION
C    DZ    SIZE OF NODE IN Z DIRECTION (CASTING DIRECTION)
C    RAMF  THERMAL CONDUCTIVITY OF MOULD FLUX
C    RAMS  THERMAL CONDUCTIVITY OF STEEL
C    CS    SPECIFIC HEAT OF STEEL
C    CF    SPECIFIC HEAT OF MOULD FLUX
C    ROUS  DENSITY OF STEEL
C    ROUF  DENSITY OF MOULD FLUX
C    LMS   STATE OF STEEL
C    LNS   STATE OF STEEL ; LIQUID,MUSHY,SOLID
C    N1    NUMBER OF NODE IN CURVED REGION OF O.M. IN Z DIRECTION
C    N2    NUMBER OF NODE IN FLAT REGION OF O.M. IN Z DIRECTION
C    M1    NUMBER OF NODE OF FLUX LAYER IN X DIRECTION
C    M2    NUMBER OF NODE OF SLAB WIDTH IN X DIRECTION - M1
C    Z1    LENGTH OF CURVED REGION OF O.M. IN Z DIRECTION
C    X1    DEPTH OF OSCILLATION MARK
C    X2    WIDTH OF SLAB - X1
C    DT    TIME STEP
C    UFI   INITIAL TEMPERATURE OF MOULD FUX
C    USI   INITIAL TEMPERATURE OF STEEL
C    TLIQS LIQUIDUS TEMPERATURE OF STEEL
C    TSOLS SOLIDUS TEMPERATURE OF STEEL
C    TP    POURING TEMPERATURE OF STEEL
C    H     HEAT TRANSFER COEFFISIENT BETWEEN STEEL AND MOULD FLUX
C    CFL   SPECIFIC HEAT OF LIQUID FLUX
C    CFS   SPECIFIC HEAT OF SOLIDIFIED FLUX
C    CSL   SPECIFIC HEAT OF LIQUID STEEL
C    CSS   SPECIFIC HEAT OF SOLIDIFIED STEEL
C    ROUFL DENSITY OF LIQUID FLUX
C    ROUSL DENSITY OF LIQUID STEEL
C    ROUFS DENSITY OF SOLIDIFIED FLUX
C    ROUSS DENSITY OF SOLIDIFIED STEEL
C    RAMFL THERMAL CONDUCTIVITY OF LIQUID FLUX
C    RAMSL THERMAL CONDUCTIVITY OF LIQUID STEEL
C    RAMFS THERMAL CONDUCTIVITY OF SOLIDIFIED FLUX
C    RAMSS THERMAL CONDUCTIVITY OF SOLIDIFIED STEEL
C    HALTS LATENT HEAT OF STEEL
C    Q(N)  HEAT FLUX DISTRIBUTION ALONG OSCILLATION MARK
C    QQ1   HEAT FLUX DISTRIBUTION DOWN MOULD WALL
C    XHV   THICKNESS OF FLUX LAYER THAT REDUCES HEAT FLUX AS HALF
C
C
C*****
C    DIMENSION

```

```

C*****
C
C
C      DIMENSION US(60,10),UF(60,10),US2(60,10),UF2(60,10),DZ(
A10),RAMF(60,10),RAMS(60,10),CS(60,10),CF(60,10),ROUS(60
A,10),ROUF(60,10),LMF(60,10),LNF(60,10),LMS(60,10),LNS(60
A,10),Q(10),DX(60)
C
C
C*****
C      READ DATA
C*****
C
C      READ(5,500) N1,N2,M1,M2,Z1,Z2,X1,X2,DT
500 FORMAT(4I4,4F8.4,F10.6)
      READ(5,501) UFI,USI,TLIQF,TLIQS,TSOLF,TSOLS,TP,H
501 FORMAT(8F10.5)
      READ(5,502) CFL,CSL,ROUFL,ROUSL,RAMFL,RAMSL,HLATF,HLATS
502 FORMAT(8F10.5)
      READ(5,503) CFS,CSS,ROUFS,ROUSS,RAMFS,RAMSS
503 FORMAT(6F10.5)
C
C
C*****
C      WRITE DATA
C*****
C
C      WRITE(6,2000) N1,N2,M1,M2,Z1,Z2,X1,X2,DT
2000 FORMAT(10H N1      = , I4/10H N2      = , I4
A/10H M1      = , I4/10H M2      = , I4/10H Z1      = , F12.6/
A10H Z2      = , F12.6/10H X1      = , F12.6/10H X2      = , F12.6
A/10H DT      = , F12.6)
      WRITE(6,2001) UFI,USI,TLIQF,TLIQS,TSOLF,TSOLS,TP,H
2001 FORMAT(10H UFI      = , F12.6/10H USI      = , F12.6/10H TLIQF      = ,
AF12.6/10H TLIQS      = , F12.6/10H TSOLF      = , F12.6/10H TSOLS      = ,
AF12.6/10H TP      = , F12.6/10H H      = , F12.6)

      WRITE(6,2002) CFL,CSL,ROUFL,ROUSL,RAMFL,RAMSL,HLATF,HLATS
2002 FORMAT(10H CFL      = , F12.6/10H CSL      = , F12.6/10H ROUFL      = ,
AF12.6/10H ROUSL      = , F12.6/10H RAMFL      = , F12.6/10H RAMSL      = ,
AF12.6/10H HLATF      = , F12.6/10H HLATS      = , F12.6)
      WRITE(6,2003) CFS,CSS,ROUFS,ROUSS,RAMFS,RAMSS
2003 FORMAT(10H CFS      = , F12.6/10H CSS      = , F12.6/10H ROUFS      = ,
AF12.6/10H ROUSS      = , F12.6/10H RAMFS      = , F12.6/10H RAMSS      = ,
AF12.6)
C
C
C*****
C      OUTPUT TIME SET
C*****
C
C
C      END1=0.30
      END1A=END1+DT
      END2=0.60
      END2A=END2+DT
      END3=0.90
      END3A=END3+DT

```


END4=1.20
END4A=END4+DT
END5=1.50
END5A=END5+DT
END6=1.80
END6A=END6+DT
END7=2.10
END7A=END7+DT
END8=2.40
END8A=END8+DT
END9=2.70
END9A=END9+DT
END10=3.0
END10A=END10+DT
END11=4.0
END11A=END11+DT
END12=5.0
END12A=END12+DT
END13=6.0
END13A=END13+DT
END14=7.0
END14A=END14+DT
END15=8.0
END15A=END15+DT
END16=9.0
END16A=END16+DT
END17=10.0
END17A=END17+DT
END18=11.0
END18A=END18+DT
END19=12.0
END19A=END19+DT
END20=13.0
END20A=END20+DT
END21=14.0
END21A=END21+DT
END22=15.0
END22A=END22+DT
END23=16.0
END23A=END23+DT
END24=17.0
END24A=END24+DT
END25=18.0
END25A=END25+DT
END26=19.0
END26A=END26+DT
END27=20.0
END27A=END27+DT
END28=21.0
END28A=END28+DT
END29=22.0
END29A=END29+DT
END30=23.0
END30A=END30+DT
END31=24.0
END31A=END31+DT
END32=26.0
END32A=END32+DT
END33=28.0
END33A=END33+DT

```

END34=30.O
END34A=END34+DT
END35=32.O
END35A=END35+DT
END36=34.O
END36A=END36+DT
END37=36.O
END37A=END37+DT
END38=38.O
END38A=END38+DT
END39=40.O
END39A=END39+DT
END40=42.O
END40A=END40+DT
END41=44.O
END41A=END41+DT
END42=46.O
END42A=END42+DT
END43=48.O

C
C
C*****
C  DIMENSION OF SYSTEM
C*****
C
C

M21=M1+M2
N10=N1-1
N11=N1+1
N21=N1+N2
M10=M1-1
M11=M1+1
T=0.O
IF(M1-N1) 800,801,800
800 WRITE(6,850)
850 FORMAT(1H0,20H M1=N1 NOT EQUAL )
GO TO 1500
801 CONTINUE
DO 200 M=1,M1
200 DX(M)=X1/FLOAT(M1)
DO 202 N=1,N1
202 DZ(N)=SQRT(Z1**2/X1*(X1-DX(1)*FLOAT(N-1)))
A-SQRT(Z1**2/X1*(X1-DX(1)*FLOAT(N)))
DO 201 M=M1,M21
201 DX(M)=X2/FLOAT(M2)
DO 203 N=N11,N21
203 DZ(N)=Z2/FLOAT(N2)

C
C
C*****
C  INITIAL CONDITION ETC.
C*****
C
C
DO 205 N=1,N21
DO 205 M=1,M21
UF(M,N)=UFI
US(M,N)=USI
LMF(M,N)=0

```

```

LNF(M,N)=O
LMS(M,N)=O
LNS(M,N)=O
CF(M,N)=CFL
CS(M,N)=CSL
ROUF(M,N)=ROUFL
ROUS(M,N)=ROUSL
RAMF(M,N)=RAMFL
205 RAMS(M,N)=RAMSL
CFF=HLATF/(TLIQF-TSOLF)+CFL
CSF=HLATS/(TLIQS-TSOLS)+CSL
ROUFF=(ROUFL+ROUFS)/2.0
RAMFF=(RAMFL+RAMFS)/2.0
ROUSF=(ROUSL+ROUSS)/2.0
RAMSF=(RAMSL+RAMSS)/2.0
GXF=RAMFL*DT/(CFL*ROUFL*DX(1)**2)
GXS=RAMSL*DT/(CSL*ROUSL*DX(1)**2)
GZ1F=RAMFL*DT/(CFL*ROUFL*DZ(1)**2)
GZ2F=RAMFL*DT/(CFL*ROUFL*DZ(N11)**2)
GZ2S=RAMSL*DT/(CSL*ROUSL*DZ(1)**2)
GZ3=RAMSL*DT/(CSL*ROUSL*DZ(N11)**2)
IF(GXF-0.5) 560,570,570
560 IF(GXS-0.5) 561,570,570
561 IF(GZ1F-0.5) 563,570,570
563 IF(GZ2S-0.5) 564,570,570
564 IF(GZ3-0.5) 565,570,570
570 WRITE(6,575)
575 FORMAT(1H0,46HG IS MORE THAN 0.5, CANNOT PERFORM CALCULATION)
GO TO 1500
565 CONTINUE
GO TO 710
599 T=T+DT
C
C
C*****
C    PROFILE OF HEAT FLUX  (NOTE ; M1=N1=3)
C*****
C
C
710 CONTINUE
XHV=0.05
DZZ1=DZ(1)*(XHV/(XHV+2.5*DX(1)))
DZZ2=DZ(2)*(XHV/(XHV+1.5*DX(1)))
DZZ3=DZ(3)*(XHV/(XHV+0.5*DX(1)))
IF(T-12.0) 701,701,705
701 QQ1=-1.0*(60.0-5.5786*T+0.46889*T**2-0.01583*T**3)
QQ2=QQ1*(Z1+Z2)/(DZZ1+DZZ2+DZZ3+Z2)
DO 702 N=1,N1
702 Q(N)=(XHV/(XHV+(3.5-N)*DX(1)))*QQ2
DO 703 N=N11,N21
703 Q(N)=QQ2
GO TO 720
705 QQ1=-1.0*(60.0-4.0389*T+0.19717*T**2
A-4.4139E-03*T**3+3.5889E-05*T**4)
QQ2=QQ1*(Z1+Z2)/(DZZ1+DZZ2+DZZ3+Z2)
DO 706 N=1,N1
706 Q(N)=(XHV/(XHV+(3.5-N)*DX(1)))*QQ2
DO 707 N=N11,N21
707 Q(N)=QQ2
720 CONTINUE

```

```

C
C
C*****
C      HEAT FLUX CALCULATION IN EACH TYPE OF NODE
C*****
C
C
C
1 CONTINUE
  DO 999 N=1,N21
  DO 999 M=1,M21
38 IF(N-1) 39,39,40
39 IF(M-1) 26,26,27
26 CALL SUB1(DX(M),DZ(N),DZ(N+1),RAMF(M+1,N),RAMF(M,N),
  ARAMF(M,N+1),UF(M,N),UF(M,N+1),UF(M+1,N),QF,Q(N))
  US(M,N)=0
  GO TO 991
27 IF(M-M1) 31,32,32
31 CALL SUB10A(DX(M),DZ(N),DZ(N+1),RAMF(M-1,N),RAMF(M,N),RAMF(M,N
  A+1),RAMF(M+1,N),UF(M,N),UF(M-1,N),UF(M,N+1),
  AUF(M+1,N),QF)
  US(M,N)=0
  GO TO 991
32 IF(M-M11) 33,34,35
33 CALL SUB11A(DX(M),DZ(N),RAMF(M,N),RAMF(M-1,N),RAMS
  A(M,N),UF(M,N),UF(M-1,N),US(M,N),H,QF)
  CALL SUB12A(DX(M),DX(M+1),DZ(N),DZ(N+1),RAMF(M,N),RAMS(M,N+1),
  ARAMS(M,N),RAMS(M+1,N),UF(M,N),US(M,N),US(M,N+1),US(M+1,N),H,QS)
  GO TO 990
34 CALL SUB13A(DX(M-1),DX(M),DZ(N),DZ(N+1),RAMS(M-1,N),RAMS(M
  A,N),RAMS(M+1,N),RAMS(M,N+1),US(M,N),US(M-1,N),US(M,N+1),
  AUS(M+1,N),H,QS)
  UF(M,N)=0
  GO TO 992
35 IF(M-M21) 62,63,63
62 CALL SUB14A(DX(M),DZ(N),DZ(N+1),RAMS(M-1,N),RAMS(M
  A,N),RAMS(M+1,N),RAMS(M,N+1),US(M,N),US(M-1,N),US(M,N+1),
  AUS(M+1,N),H,QS)
  UF(M,N)=0
  GO TO 992
63 CALL SUB15A(DX(M),DZ(N),DZ(N+1),RAMS(M-1,N),RAMS(M
  A,N),RAMS(M,N+1),US(M,N),US(M-1,N),US(M,N+1),TP,H,QS)
  UF(M,N)=0
  GO TO 992
C
C*****
C
40 IF(N-N10) 70,70,80
70 IF(M-1) 71,71,72
71 CALL SUB17(DX(M),DZ(N-1),DZ(N),DZ(N+1),RAMF(M,N+1),RAMF(M,N),
  ARAMF(M+1,N),RAMF(M,N-1),UF(M,N-1),UF(M,N),UF(M,N+1),UF(M+1,N),
  AQF,Q(N))
  US(M,N)=0
  GO TO 991
72 IF(M-3) 73,74,75
73 CALL SUB11(DX(M),DZ(N-1),DZ(N),RAMF(M,N-1),RAMF(M,N),RAMF(M-1,N),
  ARAMS(M,N),UF(M,N-1),UF(M,N),UF(M-1,N),US(M,N),H,QF)
  CALL SUB12A(DX(M),DX(M+1),DZ(N),DZ(N+1),RAMF(M,N),
  ARAMS(M,N+1),RAMS(M,N),
  ARAMS(M+1,N),UF(M,N),US(M,N),US(M,N+1),US(M+1,N),H,QS)

```

```

      GO TO 990
74 CALL SUB16A(DX(M),DX(M+1),DZ(N-1),DZ(N),DZ(N+1),RAMS(M,N-1),
  ARAMS(M,N),
  ARAMS(M-1,N),RAMS(M+1,N),RAMS(M,N+1),US(M,N-1),US(M,N),US(M-1,N),
  AUS(M,N+1),US(M+1,N),QS)
  UF(M,N)=0
  GO TO 992
75 IF(M-M21) 76,77,77
76 CALL SUB5A(DX(M-1),DX(M),DX(M+1),DZ(N-1),DZ(N),DZ(N+1),
  ARAMS(M-1,N),RAMS(M,N),
  ARAMS(M+1,N),RAMS(M,N-1),RAMS(M,N+1),US(M,N-1),US(M,N),US(M-1,N),
  AUS(M,N+1),US(M+1,N),QS)
  UF(M,N)=0
  GO TO 992
77 CALL SUB23A(DX(M),DZ(N-1),DZ(N),DZ(N+1),RAMS(M-1,N),RAMS(M,N),
  ARAMS(M,N-1),RAMS(M,N+1),US(M,N-1),US(M,N),US(M-1,N),
  AUS(M,N+1),TP,QS)
  UF(M,N)=0
  GO TO 992
C
C*****
C
80 IF(N-N11) 81,90,100
81 IF(M-2) 82,83,84
82 CALL SUB18(DX(M),DZ(N-1),DZ(N),RAMF(M,N-1),RAMF(M,N),RAMS(M,N),
  AUF(M,N-1),UF(M,N),US(M,N),H,QF,Q(N))
  CALL SUB12A(DX(M),DX(M+1),DZ(N),DZ(N+1),RAMF(M,N),RAMS(M,N+1),
  ARAMS(M,N),
  ARAMS(M+1,N),UF(M,N),US(M,N),US(M,N+1),US(M+1,N),H,QS)
  GO TO 990
83 CALL SUB16A(DX(M),DX(M+1),DZ(N-1),DZ(N),DZ(N+1),RAMS(M,N-1),
  ARAMS(M,N),
  ARAMS(M-1,N),RAMS(M+1,N),RAMS(M,N+1),US(M,N-1),US(M,N),US(M-1,N),
  AUS(M,N+1),US(M+1,N),QS)
  UF(M,N)=0
  GO TO 992
84 IF(M-M21) 85,86,86
85 CALL SUB5A(DX(M-1),DX(M),DX(M+1),DZ(N-1),DZ(N),DZ(N+1),
  ARAMS(M-1,N),RAMS(M,N),
  ARAMS(M+1,N),RAMS(M,N-1),RAMS(M,N+1),US(M,N-1),US(M,N),US(M-1,N),
  AUS(M,N+1),US(M+1,N),QS)
  UF(M,N)=0
  GO TO 992
86 CALL SUB23A(DX(M),DZ(N-1),DZ(N),DZ(N+1),RAMS(M-1,N),RAMS(M,N),
  ARAMS(M,N-1),RAMS(M,N+1),US(M,N-1),US(M,N),US(M-1,N),
  AUS(M,N+1),TP,QS)
  UF(M,N)=0
  GO TO 992
C
C*****
C
90 IF(M-1) 91,91,92
91 CALL SUB19(DX(M),DZ(N-1),DZ(N),DZ(N+1),RAMS(M,N-1),RAMS(M,N),
  ARAMS(M+1,N),RAMS(M,N+1),US(M,N-1),US(M,N),US(M,N+1),US(M+1,N),
  AQS,Q(N))
  UF(M,N)=0
  GO TO 992
92 IF(M-M21) 93,94,94
93 CALL SUB5A(DX(M-1),DX(M),DX(M+1),DZ(N-1),DZ(N),DZ(N+1),
  ARAMS(M-1,N),RAMS(M,N),

```

```

      ARAMS(M+1,N),RAMS(M,N-1),RAMS(M,N+1),US(M,N-1),US(M,N),US(M-1,N),
      AUS(M,N+1),US(M+1,N),QS)
      UF(M,N)=0
      GO TO 992
94  CALL SUB23A(DX(M),DZ(N-1),DZ(N),DZ(N+1),RAMS(M-1,N),RAMS(M,N),
      ARAMS(M,N-1),RAMS(M,N+1),US(M,N-1),US(M,N),US(M-1,N),
      AUS(M,N+1),TP,QS)
      UF(M,N)=0
      GO TO 992
C
C*****
C
100 IF(N-N21) 101,110,110
101 IF(M-1) 102,102,103
102 CALL SUB24(DX(M),DZ(N-1),DZ(N),DZ(N+1),RAMS(M+1,N),RAMS(M,N),RAMS
      A(M,N-1),RAMS(M,N+1),US(M,N-1),US(M,N),US(M,N+1),US(M+1,N),QS,Q(N))
      UF(M,N)=0
      GO TO 992
103 IF(M-M21) 104,105,105
104 CALL SUB5A(DX(M-1),DX(M),DX(M+1),DZ(N-1),DZ(N),DZ(N+1),RAMS(M-1,N),
      A,RAMS(M,N),
      ARAMS(M+1,N),RAMS(M,N-1),RAMS(M,N+1),US(M,N-1),US(M,N),US(M-1,N),
      AUS(M,N+1),US(M+1,N),QS)
      UF(M,N)=0
      GO TO 992
105 CALL SUB23A(DX(M),DZ(N-1),DZ(N),DZ(N+1),RAMS(M-1,N),RAMS(M,N),
      ARAMS(M,N-1),RAMS(M,N+1),US(M,N-1),US(M,N),US(M-1,N),
      AUS(M,N+1),TP,QS)
      UF(M,N)=0
      GO TO 992
C
C*****
C
110 IF(M-1) 111,111,120
111 CALL SUB20(DX(M),DZ(N-1),DZ(N),RAMS(M+1,N),RAMS(M,N),RAMS(M,N-1),
      AUS(M,N-1),US(M,N),US(M+1,N),QS,Q(N))
      UF(M,N)=0
      GO TO 992
120 IF(M-M21) 121,122,122
121 CALL SUB21A(DX(M-1),DX(M),DX(M+1),DZ(N-1),DZ(N),RAMS(M-1,N),
      ARAMS(M,N),RAMS(M+1,N),
      ARAMS(M,N-1),US(M,N-1),US(M,N),US(M-1,N),US(M+1,N),QS)
      UF(M,N)=0
      GO TO 992
122 CALL SUB22A(DX(M),DZ(N-1),DZ(N),RAMS(M-1,N),RAMS(M,N),RAMS(M,N-1),
      AUS(M,N-1),US(M,N),US(M-1,N),TP,QS)
      UF(M,N)=0
      GO TO 992
C
C
C*****
C      NEW TEMPERATURE CALCULATION
C*****
990 UF2(M,N)=UF(M,N)+2.0*DT*QF/(CF(M,N)*ROUF(M,N)*DX(M)*DZ(N))
      US2(M,N)=US(M,N)+2.0*DT*QS/(CS(M,N)*ROUS(M,N)*DX(M)*DZ(N))
      GO TO 999
991 UF2(M,N)=UF(M,N)+DT*QF/(CF(M,N)*ROUF(M,N)*DX(M)*DZ(N))
      US2(M,N)=US(M,N)
      GO TO 999
992 US2(M,N)=US(M,N)+DT*QS/(CS(M,N)*ROUS(M,N)*DX(M)*DZ(N))

```

```

      UF2(M,N)=UF(M,N)
      GO TO 999
999 CONTINUE
C
C
C*****
C      TEMPERATURE CHANGE
C*****
C
      DO 150 N=1,N21
      DO 150 M=1,M21
      UF(M,N)=UF2(M,N)
150  US(M,N)=US2(M,N)
      DO 175 N=1,N1
      DO 175 M=1,M21
      IF(LNF(M,N)) 175,199,175
199  IF(UF(M,N).GT.TLIQF) GO TO 175
      IF(LMF(M,N)) 173,174,173
174  UF(M,N)=TLIQF-CFL*(TLIQF-UF(M,N))/CFF
      CF(M,N)=CFF
      ROUF(M,N)=ROUFF
      RAMF(M,N)=RAMFF
      LMF(M,N)=1
173  IF(UF(M,N).GT.TSOLF) GO TO 175
      ROUF(M,N)=ROUFS
      CF(M,N)=CFS
      RAMF(M,N)=RAMFS
      LNF(M,N)=1
175  CONTINUE
      DO 275 N=1,N21
      DO 275 M=1,M21
      IF(LNS(M,N)) 275,299,275
299  IF(US(M,N).GT.TLIQS) GO TO 275
      IF(LMS(M,N)) 273,274,273
274  US(M,N)=TLIQS-CSL*(TLIQS-US(M,N))/CSF
      CS(M,N)=CSF
      ROUS(M,N)=ROUSF
      RAMS(M,N)=RAMSF
      LMS(M,N)=1
273  IF(US(M,N).GT.TSOLS) GO TO 275
      ROUS(M,N)=ROUSS
      CS(M,N)=CSS
      RAMS(M,N)=RAMSS
      LNS(M,N)=1
275  CONTINUE
C
C
C*****
C      OUTPUT
C*****
C
      IF(T-END1) 599,1000,9001
9001 IF(T-END1A) 1000,9002,9002
9002 IF(T-END2) 599,1000,9003
9003 IF(T-END2A) 1000,9004,9004
9004 IF(T-END3) 599,1000,9005
9005 IF(T-END3A) 1000,9006,9006
9006 IF(T-END4) 599,1000,9007
9007 IF(T-END4A) 1000,9008,9008

```

9008 IF(T-END5) 599,1000,9009
9009 IF(T-END5A) 1000,9010,9010
9010 IF(T-END6) 599,1000,9011
9011 IF(T-END6A) 1000,9012,9012
9012 IF(T-END7) 599,1000,9013
9013 IF(T-END7A) 1000,9014,9014
9014 IF(T-END8) 599,1000,9015
9015 IF(T-END8A) 1000,9016,9016
9016 IF(T-END9) 599,1000,9017
9017 IF(T-END9A) 1000,9018,9018
9018 IF(T-END10) 599,1000,9019
9019 IF(T-END10A) 1000,9020,9020
9020 IF(T-END11) 599,1000,9021
9021 IF(T-END11A) 1000,9022,9022
9022 IF(T-END12) 599,1000,9023
9023 IF(T-END12A) 1000,9024,9024
9024 IF(T-END13) 599,1000,9025
9025 IF(T-END13A) 1000,9026,9026
9026 IF(T-END14) 599,1000,9027
9027 IF(T-END14A) 1000,9028,9028
9028 IF(T-END15) 599,1000,9029
9029 IF(T-END15A) 1000,9030,9030
9030 IF(T-END16) 599,1000,9031
9031 IF(T-END16A) 1000,9032,9032
9032 IF(T-END17) 599,1000,9033
9033 IF(T-END17A) 1000,9034,9034
9034 IF(T-END18) 599,1000,9035
9035 IF(T-END18A) 1000,9036,9036
9036 IF(T-END19) 599,1000,9037
9037 IF(T-END19A) 1000,9038,9038
9038 IF(T-END20) 599,1000,9039
9039 IF(T-END20A) 1000,9040,9040
9040 IF(T-END21) 599,1000,9041
9041 IF(T-END21A) 1000,9042,9042
9042 IF(T-END22) 599,1000,9043
9043 IF(T-END22A) 1000,9044,9044
9044 IF(T-END23) 599,1000,9045
9045 IF(T-END23A) 1000,9046,9046
9046 IF(T-END24) 599,1000,9047
9047 IF(T-END24A) 1000,9048,9048
9048 IF(T-END25) 599,1000,9049
9049 IF(T-END25A) 1000,9050,9050
9050 IF(T-END26) 599,1000,9051
9051 IF(T-END26A) 1000,9052,9052
9052 IF(T-END27) 599,1000,9053
9053 IF(T-END27A) 1000,9054,9054
9054 IF(T-END28) 599,1000,9055
9055 IF(T-END28A) 1000,9056,9056
9056 IF(T-END29) 599,1000,9057
9057 IF(T-END29A) 1000,9058,9058
9058 IF(T-END30) 599,1000,9059
9059 IF(T-END30A) 1000,9060,9060
9060 IF(T-END31) 599,1000,9061
9061 IF(T-END31A) 1000,9062,9062
9062 IF(T-END32) 599,1000,9063
9063 IF(T-END32A) 1000,9064,9064
9064 IF(T-END33) 599,1000,9065
9065 IF(T-END33A) 1000,9066,9066
9066 IF(T-END34) 599,1000,9067
9067 IF(T-END34A) 1000,9068,9068


```

9068 IF(T-END35) 599,1000,9069
9069 IF(T-END35A) 1000,9070,9070
9070 IF(T-END36) 599,1000,9071
9071 IF(T-END36A) 1000,9072,9072
9072 IF(T-END37) 599,1000,9073
9073 IF(T-END37A) 1000,9074,9074
9074 IF(T-END38) 599,1000,9075
9075 IF(T-END38A) 1000,9076,9076
9076 IF(T-END39) 599,1000,9077
9077 IF(T-END39A) 1000,9078,9078
9078 IF(T-END40) 599,1000,9079
9079 IF(T-END40A) 1000,9080,9080
9080 IF(T-END41) 599,1000,9081
9081 IF(T-END41A) 1000,9082,9082
9082 IF(T-END42) 599,1000,9083
9083 IF(T-END42A) 1000,9084,9084
9084 IF(T-END43) 599,1000,1000
1000 CONTINUE
      WRITE(6,300) T,Q(1),Q(2),Q(3),Q(4),Q(5),Q(6)
300  FORMAT(10H TIME      =,F10.7/10H Q(1)      =,F10.5/10H Q(2)      =,
      AF10.5/10H Q(3)      =,F10.5/10H Q(4)      =,F10.5/10H Q(5)      =,
      AF10.5/10H Q(6)      =,F10.5)
      WRITE(6,301)
301  FORMAT(5H U-1 ,5H U-2 ,5H U-3 ,5H U-4 ,5H U-5 ,5H U-6 ,5H U-7
      A,5H U-8 ,5H U-9 ,5H U-10,5H U-11,5H U-12,5H U-13,5H U-14,5H U-15,5
      AH U-16,5H U-17,5H U-18,5H U-19,5H U-20,5H U-21,5H U-22,5H U-23)
      DO 350 N=1,6
      WRITE(6,3350) (UF(M,N),M=1,23)
3350 FORMAT(23F5.0)
350  CONTINUE
      WRITE(6,302)
302  FORMAT(5H U-1 ,5H U-2 ,5H U-3 ,5H U-4 ,5H U-5 ,5H U-6 ,5H U-7
      A,5H U-8 ,5H U-9 ,5H U-10,5H U-11,5H U-12,5H U-13,5H U-14,5H U-15,5
      AH U-16,5H U-17,5H U-18,5H U-19,5H U-20,5H U-21,5H U-22,5H U-23)
      DO 351 J=1,6
      WRITE(6,3510) (US(M,J),M=1,23)
3510 FORMAT(23F5.0)
351  CONTINUE
      IF(T-END43) 599,1500,1500
1500 STOP
      END

C
C
C
C*****
C      SUBROUTINE
C*****
C
C
C
      SUBROUTINE SUB1(DX1,DZ1,DZ2, RAM21, RAM11, RAM12, U11, U12, U21, Q, Q10)
      RAM=(RAM11+RAM21)/2.0
      Q2=Q10*DZ1
      Q3=DX1*(U12-U11)/(DZ2/(2.0*RAM12)+DZ1/(2.0*RAM11))
      Q4=RAM*DZ1*(U21-U11)/DX1
      Q=Q2+Q3+Q4
      RETURN
      END

C
C
      SUBROUTINE SUB5A(DX0,DX1,DX2,DZ0,DZ1,DZ2, RAM01, RAM11, RAM21, RAM10,

```

```
ARAM12,U10,U
```

```
A11,U01,U12,U21,Q)
```

```
RAM1=(RAM01+RAM11)/2.0
```

```
RAM2=(RAM21+RAM11)/2.0
```

```
Q1=DX1*(U10-U11)/(DZO/(2.0*RAM10)+DZ1/(2.0*RAM11))
```

```
Q2=RAM1*DZ1*(U01-U11)/(DX0/2+DX1/2)
```

```
Q3=DX1*(U12-U11)/(DZ2/(2.0*RAM12)+DZ1/(2.0*RAM11))
```

```
Q4=RAM2*DZ1*(U21-U11)/(DX1/2+DX2/2)
```

```
Q=Q1+Q2+Q3+Q4
```

```
RETURN
```

```
END
```

C
C

```
SUBROUTINE SUB10A(DX1,DZ1,DZ2,RAM01,RAM11,RAM12,RAM21,
```

```
AU11,U01,U12,U21,Q)
```

```
RAM1=(RAM01+RAM11)/2.0
```

```
RAM2=(RAM12+RAM11)/2.0
```

```
RAM3=(RAM21+RAM11)/2.0
```

```
Q2=RAM1*DZ1*(U01-U11)/DX1
```

```
Q3=RAM2*DX1*(U12-U11)*(DZ1/2.0+DZ2/3.0)/((DX1/6.0)**2+
```

```
A(DZ2/3.0+DZ1/2.0)**2)
```

```
Q4=30.0*DX1*DZ1*RAM3*(U21-U11)/(25.0*DX1**2+DZ1**2)
```

```
Q=Q2+Q3+Q4
```

```
RETURN
```

```
END
```

C
C

```
SUBROUTINE SUB11(DX1,DZO,DZ1,RAM10,RAM11,RAM01,RAMS,U10,U11,U01,
```

```
AUS11,H,Q)
```

```
RAM1=(RAM10+RAM11)/2.0
```

```
RAM2=(RAM01+RAM11)/2.0
```

```
Q1=DX1*RAM1*(U10-U11)*(DZO/2.0+DZ1/3.0)/((DX1/6.0)**2+(DZ1/3.0+
```

```
ADZO/2.0)**2)
```

```
Q2=30.0*DX1*DZ1*RAM2*(U01-U11)/(25.0*DX1**2+DZ1**2)
```

```
Q3=(2.0*DX1*DZ1*(US11-U11)/SQRT(DZ1**2+DX1**2))/(SQRT(DZ1**2+
```

```
ADX1**2)/
```

```
A(12.0*RAM11)+1.0/H+SQRT(DZ1**2+DX1**2)/(12.0*RAMS))
```

```
Q=Q1+Q2+Q3
```

```
RETURN
```

```
END
```

C
C

```
SUBROUTINE SUB11A(DX1,DZ1,RAM11,RAM01,RAMS,U11,U01,
```

```
AUS11,H,Q)
```

```
RAM2=(RAM01+RAM11)/2.0
```

```
Q2=30.0*DX1*DZ1*RAM2*(U01-U11)/(25.0*DX1**2+DZ1**2)
```

```
Q3=(2.0*DX1*DZ1*(US11-U11)/SQRT(DZ1**2+DX1**2))/(SQRT(DZ1**2+
```

```
ADX1**2)/
```

```
A(12.0*RAM11)+1.0/H+SQRT(DZ1**2+DX1**2)/(12.0*RAMS))
```

```
Q=Q2+Q3
```

```
RETURN
```

```
END
```

C
C

```
SUBROUTINE SUB12A(DX1,DX2,DZ1,DZ2,RAMF,RAM12,RAM11,RAM21,
```

```
AUF11,U11,U12,U21,H,Q)
```

```
RAM1=(RAM12+RAM11)/2.0
```

```
RAM2=(RAM21+RAM11)/2.0
```

```
Q2=2.0*DX1*DZ1*(UF11-U11)/SQRT(DZ1**2+DX1**2)/(SQRT(DZ1**2+
```

```
ADX1**2)/(12.0*RAMF)+1.0/H+SQRT(DZ1**2+DX1**2)/(12.0*RAM11))
```

```

Q3=RAM1*DX1*(U12-U11)*(DZ2/2.0+DZ1/3.0)/((DX1/6.0)**2+(DZ1/3.0
A+DZ2/2.0)**2)
Q4=(DZ1*(DX1/3+DX2/2)/((DX1/3+DX2/2)**2+(DZ1/6)**2))
A*RAM2*(U21-U11)

```

```

Q=Q2+Q3+Q4
RETURN
END

```

C
C

```

SUBROUTINE SUB13A(DX0,DX1,DZ1,DZ2,RAM01,RAM11,RAM21,RAM12,
AU11,UO1,U12,U21,H,Q)
RAM1=(RAM01+RAM11)/2.0
RAM2=(RAM21+RAM11)/2.0
Q2=(DZ1*(DX0/3+DX1/2)/((DX0/3+DX1/2)**2+(DZ1/6)**2))
A*RAM1*(UO1-U11)
Q3=DX1*(U12-U11)/(DZ2/(2.0*RAM12)+DZ1/(2.0*RAM11))
Q4=RAM2*DZ1*(U21-U11)/DX1
Q=Q2+Q3+Q4
RETURN
END

```

C
C

```

SUBROUTINE SUB14A(DX1,DZ1,DZ2,RAM01,RAM11,RAM21,RAM12,
AU11,UO1,U12,U21,H,Q)
RAM1=(RAM01+RAM11)/2.0
RAM2=(RAM21+RAM11)/2.0
Q2=RAM1*DZ1*(UO1-U11)/DX1
Q3=DX1*(U12-U11)/(DZ2/(2.0*RAM12)+DZ1/(2.0*RAM11))
Q4=RAM2*DZ1*(U21-U11)/DX1
Q=Q2+Q3+Q4
RETURN
END

```

C
C

```

SUBROUTINE SUB15A(DX1,DZ1,DZ2,RAM01,RAM11,RAM12,
AU11,UO1,U12,TP,H,Q)
RAM=(RAM01+RAM11)/2.0
Q2=RAM*DZ1*(UO1-U11)/DX1
Q3=DX1*(U12-U11)/(DZ2/(2.0*RAM12)+DZ1/(2.0*RAM11))
Q=Q2+Q3
RETURN
END

```

C
C

```

SUBROUTINE SUB16A(DX1,DX2,DZO,DZ1,DZ2,RAM10,RAM11,RAM01,RAM21,
ARAM12,U10,U11,UO1,U12,U21,Q)
RAM1=(RAM10+RAM11)/2.0
RAM2=(RAM01+RAM11)/2.0
RAM3=(RAM21+RAM11)/2.0
Q1=RAM1*DX1*(U10-U11)*(DZ1/2.0+DZO/3.0)/((DX1/6.0)**2+
A(DZO/3.0+DZ1/2.0)**2)
Q2=30.0*DX1*DZ1*RAM2*(UO1-U11)/(25.0*DX1**2+DZ1**2)
Q3=DX1*(U12-U11)/(DZ2/(2.0*RAM12)+DZ1/(2.0*RAM11))
Q4=RAM3*DZ1*(U21-U11)/(DX1/2+DX2/2)
Q=Q1+Q2+Q3+Q4
RETURN
END

```

C
C

```

SUBROUTINE SUB17(DX1,DZO,DZ1,DZ2, RAM12, RAM11, RAM21, RAM10,
AU10, U11, U12, U21, Q, Q10)
  RAM1=(RAM12+RAM11)/2.0
  RAM2=(RAM21+RAM11)/2.0
  Q1=DX1*(U10-U11)/(DZO/(2.0*RAM10)+DZ1/(2.0*RAM11))
  Q2=Q10*DZ1
  Q3=RAM1*DX1*(U12-U11)*(DZ1/2.0+DZ2/3.0)/((DX1/6.0)**2+
A(DZ2/3.0+DZ1/2.0)**2)
  Q4=30.0*DX1*DZ1*RAM2*(U21-U11)/(25.0*DX1**2+DZ1**2)
  Q=Q1+Q2+Q3+Q4
  RETURN
C
C
  END
SUBROUTINE SUB18(DX1,DZO,DZ1, RAM10, RAM11, RAMS, U10, U11, US11, H, Q,
AQ10)
  RAM=(RAM10+RAM11)/2.0
  Q1=DX1*RAM*(U10-U11)*(DZO/2.0+DZ1/3.0)/((DX1/6.0)**2
A+(DZ1/3.0+DZO/2.0)**2)
  Q2=Q10*DZ1
  Q3=(2.0*DX1*DZ1*(US11-U11)/SQRT(DZ1**2+DX1**2))/(SQRT(DZ1**2+
ADX1**2)/(12.0*RAM11)+1.0/H+SQRT(DZ1**2+DX1**2)/(12.0*RAMS))
  Q=Q1+Q2+Q3
  RETURN
  END
C
C
  SUBROUTINE SUB19(DX1,DZO,DZ1,DZ2, RAM10, RAM11, RAM21, RAM12,
AU10, U11, U12, U21, Q, Q10)
  RAM1=(RAM10+RAM11)/2.0
  RAM2=(RAM21+RAM11)/2.0
  Q1=RAM1*DX1*(U10-U11)*(DZ1/2.0+DZO/3.0)/((DX1/6.0)**2+(DZO/3.0+
ADZ1/2.0)**2)
  Q2=Q10*DZ1
  Q3=DX1*(U12-U11)/(DZ2/(2.0*RAM12)+DZ1/(2.0*RAM11))
  Q4=RAM2*DZ1*(U21-U11)/DX1
  Q=Q1+Q2+Q3+Q4
  RETURN
  END
C
C
  SUBROUTINE SUB20(DX1,DZO,DZ1, RAM21, RAM11, RAM10, U10, U11, U21, Q, Q10)
  RAM=(RAM21+RAM11)/2.0
  Q1=DX1*(U10-U11)/(DZO/(2.0*RAM10)+DZ1/(2.0*RAM11))
  Q2=Q10*DZ1
  Q4=RAM*DZ1*(U21-U11)/DX1
  Q=Q1+Q2+Q4
  RETURN
  END
C
C
  SUBROUTINE SUB21A(DX0, DX1, DX2, DZO, DZ1, RAM01, RAM11, RAM21, RAM10, U10,
AU11, U01, U21, Q)
  RAM1=(RAM01+RAM11)/2.0
  RAM2=(RAM21+RAM11)/2.0
  Q1=DX1*(U10-U11)/(DZO/(2.0*RAM10)+DZ1/(2.0*RAM11))
  Q2=RAM1*DZ1*(U01-U11)/(DX0/2+DX1/2)
  Q4=RAM2*DZ1*(U21-U11)/(DX1/2+DX2/2)
  Q=Q1+Q2+Q4
  RETURN

```

END

C
C

```
SUBROUTINE SUB22A(DX1,DZO,DZ1,RAM01,RAM11,RAM10,U10,U11,U01,TP,Q)
RAM=(RAM01+RAM11)/2.0
Q1=DX1*(U10-U11)/(DZO/(2.0*RAM10)+DZ1/(2.0*RAM11))
Q2=RAM*DZ1*(U01-U11)/DX1
Q=Q1+Q2
RETURN
END
```

C
C

```
SUBROUTINE SUB23A(DX1,DZO,DZ1,DZ2,RAM01,RAM11,RAM10,RAM12,U10,U11,
AU01,U12,TP,Q)
RAM=(RAM01+RAM11)/2.0
Q1=DX1*(U10-U11)/(DZO/(2.0*RAM10)+DZ1/(2.0*RAM11))
Q2=RAM*DZ1*(U01-U11)/DX1
Q3=DX1*(U12-U11)/(DZ2/(2.0*RAM12)+DZ1/(2.0*RAM11))
Q=Q1+Q2+Q3
RETURN
END
```

C
C

```
SUBROUTINE SUB24(DX1,DZO,DZ1,DZ2,RAM21,RAM11,RAM10,RAM12,U10,U11,
AU12,U21,Q,Q10)
RAM=(RAM21+RAM11)/2.0
Q1=DX1*(U10-U11)/(DZO/(2.0*RAM10)+DZ1/(2.0*RAM11))
Q2=Q10*DZ1
Q3=DX1*(U12-U11)/(DZ2/(2.0*RAM12)+DZ1/(2.0*RAM11))
Q4=RAM*DZ1*(U21-U11)/DX1
Q=Q1+Q2+Q3+Q4
RETURN
END
```

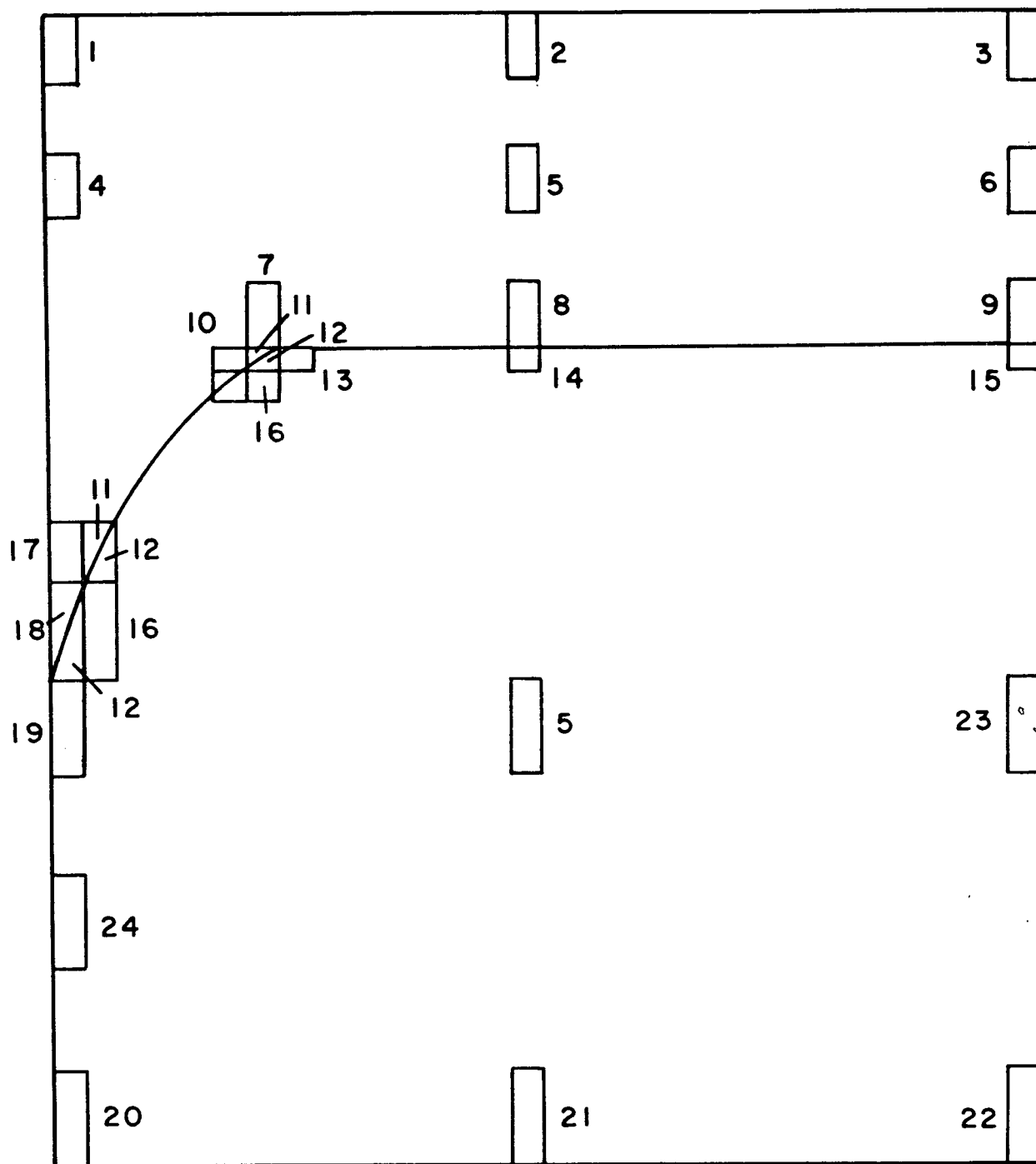


Fig. A1 Typical nodes and their number of subroutines in computer program for the calculation of temperature distribution at the meniscus

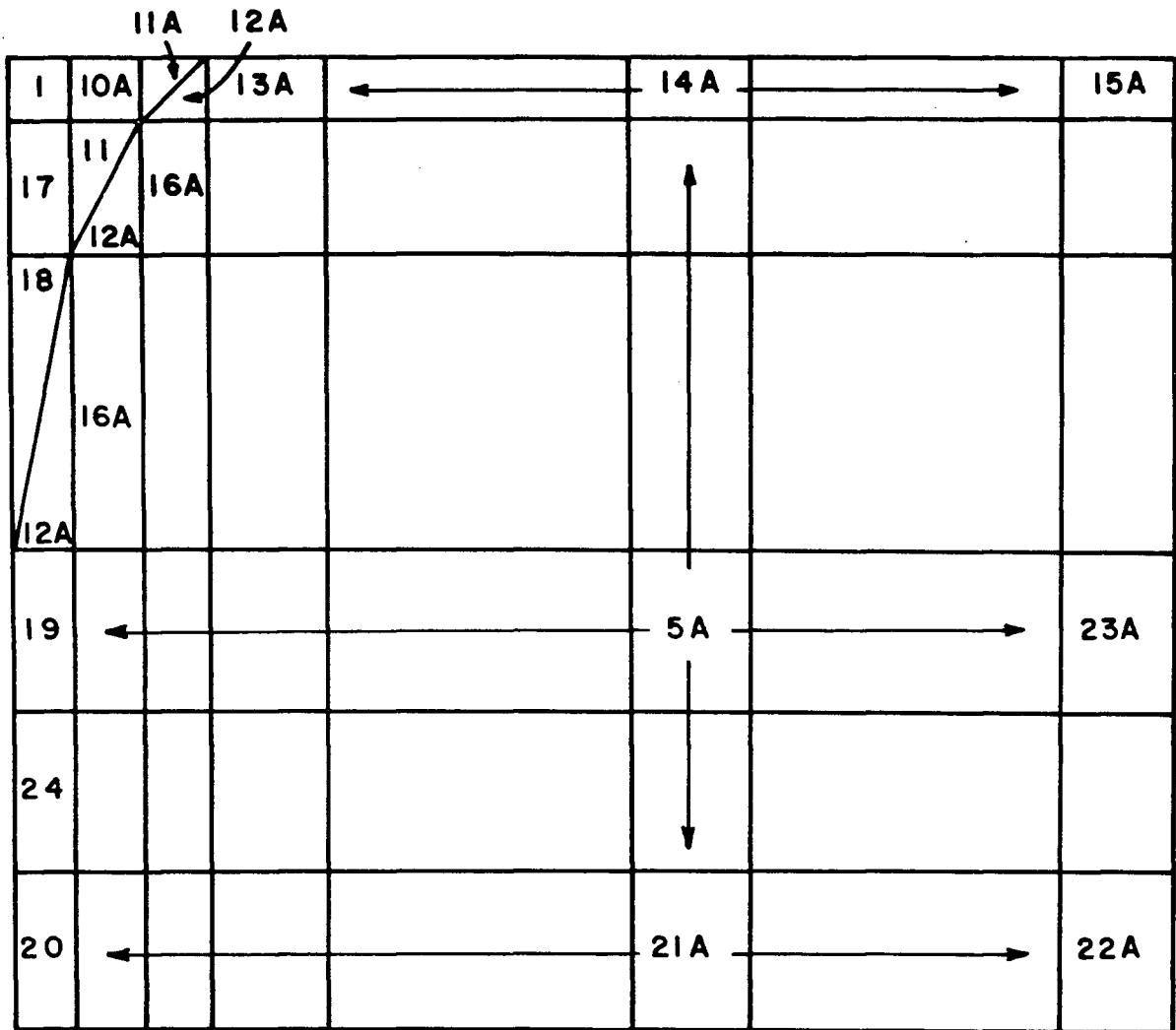


Fig. A2

Typical nodes and their number of subroutines in computer program for the calculation of nonuniformity of shell profile in the mould.